



POLITECNICO DI MILANO
DEPARTMENT OF MECHANICAL ENGINEERING

DOCTORAL PROGRAMME IN MECHANICAL ENGINEERING

Fiber-optic sensors for monitoring laser ablation thermal outcome in biological tissues

Doctoral Dissertation of:
Sanzhar Korganbayev

Supervisor:
Prof. Paola Saccomandi

Tutor:
Prof. Eduardo Sabioni

The Chair of the Doctoral Program:
Andrea Bernasconi

2019/2022–Cycle XXXIV (additional)

Abstract

Laser ablation (LA) is one of the tumor treatment techniques that can provide minimally invasive treatment in cases when conventional methods (surgical resection, chemotherapy, radiotherapy) are not recommended. The main principle of LA is based on the delivery of laser energy *via* a fiber optic cable to the tumor in order to induce local coagulation, necrosis, and apoptosis of cancer tissues. The main advantage of LA is based on two unique features that stem from the use of minimally-invasive fiber optic cable: immunity to electro-magnetic interference and flexibility of the applicator. Thus, the treatment can be used during magnetic-resonance and computed tomography imaging, and can reach deep-laying organs.

Nevertheless, LA cancer treatment is still limited due to the difficulty to guarantee complete destruction of the tumor and prevent collateral damage to the healthy tissues. The main reasons for it are the lack of accurate monitoring techniques and the use of an open-loop approach, i.e., laser parameters are set before the procedure. In this regard, my Ph.D. project is focused on investigation and development in the two main areas: (i) real-time temperature-based control techniques for extra- and intra-corporeal LA; and (ii) innovative fiber optics sensing methods to measure intra-tissue parameters (temperature, refractive index) during LA procedure.

For temperature-based LA control, FBG sensors were utilized in the development of different LA control techniques: (a) ON-OFF control for extracorporeal LA; (b) ON-OFF control for interstitial LA; and (c) proportional-integral-derivative (PID) control for interstitial LA. In addition, a pre-planning based on numerical simulations of the bioheat transfer has been developed to optimize the control parameters before the actual procedure. Moreover, the custom-made FBG sensors have been fabricated using point-by-point femtosecond laser inscription and optimized for LA procedures. In general, the obtained results that LA control allows controlling the margins of the ablated region, and, as a result, minimizes the damage to the surrounding healthy tissues. The novelty of the developed intraoperative platforms compared to currently available systems is that they also allow for quasi-distributed measurement of tissue temperature in two- and three-dimensional configurations, while retaining the minimally invasive nature of the procedure.

Regarding the innovative sensing methods for LA monitoring, the main investigated sensor was titled FBG (TFBG), a particular type of FBG with tilted FBG planes that allow coupling between the core and cladding modes. As a result, TFBG is sensitive to temperature, axial strain, pressure (as standard FBG), and also to outside medium parameters, such as surrounding refractive index (RI). In this regard, the experimental investigation of the increase of RI sensitivity by fiber etching has been performed. Analysis of step-wise etching and calibration in different RI solutions have provided the

best trade-off between wavelength and amplitude sensitivity, intensity level, and fiber thickness.

In addition, TFBG sensing modalities during LA of *ex-vivo* hepatic tissues have been investigated. The first modality is a measurement of the RI changes of the ablated tissue during LA. The second one – is the temperature sensing modality based on the core mode analysis using conventional peak tracking techniques (maximum tracking, X-dB Bandwidth, centroid methods) and the developed reconstruction algorithm. The developed algorithm allows the measurement of quasi-distributed spatial temperature profile along TFBG. In general, the results show that the main reliable sensing modality of TFBG during LA is temperature monitoring, which can be significantly improved by the proposed algorithm.

Future works should involve tumor tissues in *ex vivo* and *in vivo* experiments to assess the efficacy of the proposed methods and continue the investigations toward the clinical use of the discussed techniques.

This work was supported by the European Research Council (ERC) under the European Union's Horizon 2020 research and innovation program under Grant Agreement 759159.

Summary

My thesis work has been organized as follows.

In Chapter 1, a general overview of LA cancer treatment and its relation to different cancer therapies is provided. LA is discussed as an intersection between phototherapy, thermal therapy, and minimally-invasive therapy. After, the basic principles of laser ablation, information about monitoring during LA and related closed-loop feedback systems is provided. The last section of the introduction discusses a brief overview of the main equipment and instrumentation utilized in the thesis work: interrogators, FBG and TFBG sensors, and the diode laser used for experiments.

Chapter 2 describes the development of different FBG-based LA regulation techniques utilized for *ex vivo* experiments. Paper A reports the first step of the development of LA regulation, where a conventional controlling technique (ON-OFF controller) and extracorporeal positioning of the sensors (on the surface of the ablated tissue) are utilized. After, Paper B investigates LA control for an interstitial case and discusses the developed numerical COMSOL model as a tool for pre-treatment optimization of the procedure parameters (power, set temperature, controlling distance). Later, in Paper C we propose a PID controlling approach to avoid the oscillating errors which were present in the ON-OFF control works.

In Chapter 3, the results of the investigation of TFBG sensing aiming for tissue damage monitoring during LA are presented. Specifically, Paper D describes the chemical etching of the TFBG fiber and step-wise calibration in different sucrose concentrations used to optimize RI sensitivity, intensity level, and fiber thickness. Later, Paper E assesses the effectiveness of TFBG for real-time monitoring of intra-tissue parameters during LA of *ex vivo* hepatic tissue. TFBG's ability to accurately monitor temperature (point and quasi-distributed measurements) and RI of the tissue are analyzed.

The final discussion and future developments of my study are provided in Chapter 4. At the end of the thesis, a bibliography, scientific publications, and an appendix (Paper A – Paper E) are provided.

Content

Chapter 1 - State of the art: thermal ablation and monitoring	7
1.1. Introduction	7
1.2 Taxonomy of therapies	8
1.3 Laser ablation	11
1.4 Monitoring of laser therapies for cancer treatment	12
1.5 Laser ablation feedback systems	16
1.6 Equipment used in the experiments (Paper A – Paper E)	18
Chapter 2 – LA temperature-based control with FBG sensors	22
2.1 Paper A: ON-OFF non-invasive LA control	23
2.2 Paper B: ON-OFF interstitial LA control	29
2.3 Paper C: PID interstitial LA control	35
2.4 Discussion	39
Chapter 3 – Measurements of intra-tissue parameters during LA	41
3.1 Paper D. TFBG RI sensitivity increase	41
3.2 Paper E. TFBG measurements during laser ablation	47
3.3 Discussion	53
Chapter 4 – Discussion and future outlooks	54
Bibliography	56
Scientific productions	66
Appendix	71

Appendix:

Paper A: Closed-Loop Temperature Control Based on Fiber Bragg Grating Sensors for Laser Ablation of Hepatic Tissue [1].

Paper B: Quasi-distributed fiber optic sensor-based control system for interstitial laser ablation of tissue: theoretical and experimental investigations [2].

Paper C: PID Controlling Approach Based on FBG Array Measurements for Laser Ablation of Pancreatic Tissues [3].

Paper D: Optimization of Cladding Diameter for Refractive Index Sensing in Tilted Fiber Bragg Gratings [4].

Paper E: Tilted fiber Bragg grating measurements during laser ablation of hepatic tissues: quasi-distributed temperature reconstruction and cladding mode resonances analysis [5].

List of Abbreviations and Acronyms

APC	Antigen-presenting cells
CDAMP	Cell death-associated molecular patterns
CEM	Cumulative equivalent minute
CT	Computer tomography
CW	Continuous wave
DAMP	Damaged associated molecular patterns
EM	Electromagnetic
FBG	Fiber Bragg gratings
FD-PA	Frequency-domain photoacoustic
FEM	Finite element method
GL	Gauge length
GRP	Glucose-regulated proteins
HF	Hydrofluoric
HIFU	High-intensity focused ultrasound
HSP	heat shock proteins
IR	Infrared
IRE	Irreversible electroporation
LA	Laser ablation
MR	Magnetic resonance
MRE	Mean relative error
MRI	Magnetic resonance imaging
MRTI	Magnetic resonance thermometry imaging
MW	Microwave
OFDR	Optical frequency domain reflectometry
PA	Photoacoustic
PDT	Photodynamic therapy
PID	Proportional–integral–derivative
PIT	Photoimmune therapy
PRF	Proton resonance frequency
PTT	Photothermal therapy
RI	Refractive index
RIU	Refractive index units
ROS	Reactive oxygen species
RF	Radiofrequency
SNR	Signal to noise ratio
US	Ultrasound

Chapter 1. State of the art: thermal ablation and monitoring

1.1 Introduction

LA is a minimally-invasive thermal treatment of cancer, which is based on the laser–tissue interactions. Thus, LA can be described as an intersection of three fields of cancer treatment: 1) **phototherapy** – any techniques that involve light for cancer treatment; 2) **thermal therapy** – the main principle is based on temperature change (increase or decrease) to treat cancer; and 3) **minimally-invasive therapy** – any techniques related to cancer treatment with small applicator introduced into the target to induce thermal or non-thermal (chemical ablation, electroporation) cancer cell destruction (Fig. 1.1).

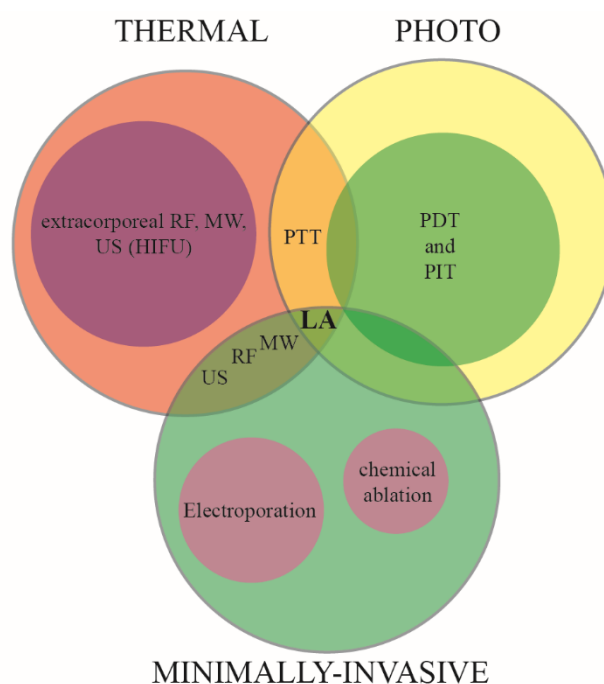


Fig. 1.1: Diagrams of classification for cancer treatment techniques: minimally-invasive, thermal, and photo therapies. RF – radiofrequency, MW – microwave, US – ultrasound, HIFU – high intensity focused ultrasound, PTT – photothermal therapy, PDT – photodynamic therapy. PIT – photoimmunotherapy.

Since the obtained knowledge, skills, and techniques proposed in this thesis can find a possible application in the three abovementioned areas, it is worth describing types of therapy in more detail. And, in general, it can be useful for a possible reader to know the overall context and place of the discussed thesis in the field of cancer treatment.

Thus, this Chapter will start with the concept of phototherapy and its subdivisions: photodynamic therapy (PDT), photoimmunotherapy (PIT), and photothermal therapy (PTT). In this context, LA can be considered as a PTT because the main effect is based on temperature increase.

Then, thermal treatments (with any level of invasiveness) will be discussed. Thermal treatments can be divided according to the **source of energy**: microwave (MW), radiofrequency (RF), ultrasound (US), laser, and cryotherapy; or according to the **interaction method**: interstitial or extracorporeal (contactless); or according to the **temperature values**: fever-range hyperthermia (39.5 °C – 41.5 °C), traditional hyperthermia (41.5 °C – 54 °C), and ablation (more than 60 °C) [6].

After, the introduction will cover minimally-invasive treatments as an alternative to conventional cancer treatment techniques. Later, the discussion will be narrowed to LA, its advantages and disadvantages, and the possibility of sensing and controlling techniques to improve the treatment. Finally, at the end of this section, the basics of fiber optic sensors and their application for LA will be discussed.

1.2 Taxonomy of therapies

1.2.1 Phototherapy

It is quite fascinating that the history of phototherapy can be considered to be started 3000 years ago, when, according to the sacred Hindu texts *Atharva Veda* (~ 1400 B.C.), people with vitiligo were given specific herb extracts (*Eclipta prostrata*) and then exposed to the sun to cure the disease. Very interesting and unexpected application of phototherapy a long time before the invention of light sources and lasers! [7].

Nowadays, with technological progress, the main principles and devices used for phototherapy are much more diverse and can be categorized into three main areas: PDT, PTT, and PIT. Each of them has distinctive damage mechanisms: interaction of light and light-sensitive medicine (porfimer sodium, aminolevulinic acid, benzoporphyrin derivatives, others) to destroy cancer cells for PDT, cancer cell death stemmed from the heat induced by light for PTT, and immune response for PIT [8], [9].

The main principle of PDT is based on the photochemical interaction of (1) nontoxic photosensitizer (PS), (2) oxygen in tumors, and (3) light. The light wavelength range suitable for PDT is defined by the limits of absorption by tissue chromophores and is approximately equal to 650 nm – 1200 nm [10]. PS is introduced in the tumor, then the targeted area is irradiated by a specific wavelength (corresponding to the absorbance band of PS) in the presence of oxygen, and, as a result, highly reactive oxygen species (ROS) are generated [11], [12]. Therefore, significant toxicity is present in the area, and consequent cancer cell death is achieved *via* apoptosis or necrosis [13]. It is important to note that the lifetime of singlet oxygen is short (less than 300 ns), so the related diffusion is limited up to 60 nm in cells [14]. In this regard, limited light penetration and PS targeting are important fields of research for PDT applications in recent decades.

PTT is based on the absorption of photon energy (of laser, visible light) by the

targetted tissue to induce thermal damage (local coagulation, necrosis, and apoptosis) to cancer cells [15]. It is worth mentioning, that nanoparticles (nanorods, nanoshells, nanocages based on gold, silver, copper sulfide (CuS) nanoparticles, carbon nanotubes, etc.) sometimes are utilized to increase the light energy absorption and increase the penetration depth of the light [16]. Moreover, the accumulation of nanoparticles only in the tumor and not in the surrounding healthy tissues can significantly improve the selectivity of the treatment (reduce collateral damage to healthy tissues).

PIT actually is based on PDT or PTT, but the main focus is not to create photochemical (ROS production) or photothermal reaction (heat), but to increase the immune response that stems from the release of damaged associated and cell death-associated molecular patterns (DAMPs and CDAMPs correspondingly) [7]. In particular, PTT or PDT induces the release of heat shock proteins (HSPs) and stress-inducible glucose-regulated proteins (GRPs) from cancer cells. After antigen-presenting cells (APCs) can capture the abovementioned antigens (HSPs, GRPs, etc.) and present them to T cells (thymus-derived cells), in other words, the APCs “teach” T cells. Thus, T cells become able to recognize tumor cells and kill them, thus leading to a systematic antitumor immune response [17].

1.2.2 Thermal therapy

Thermal therapy, as the name suggests, is based on thermal transfer into or out of the body to treat different diseases. Thermal treatments can have different sources of energy: **electromagnetic (EM) non-ionizing radiations**: RF (~100 kHz - few MHz), MW (~100 MHz - 10 GHz), laser (THz range); **mechanical** – US (2-20 MHz sound waves) [18].

For thermal treatments, the main effect on biological tissues is related to temperature and exposure time [6]. As a result, it is possible to categorize the treatment according to temperature levels: fever-range hyperthermia, traditional hyperthermia, and ablation [6]. Moreover, each temperature has its own distinctive effects on biological tissue, which are briefly summarized in Table 1.2.1.

TABLE 1.2.1. Effects of temperature on biological tissues for different temperature ranges

Temperature (°C)	Time	Results
< -50	>10 min	freezing, disruption of cell membrane
40 - 41	6 – 72 h	increased tissue blood flow, metabolism, accelerated repair
42 - 45	15 – 60 min	increased tumor blood flow and oxygen level, an increase of sensitivity to radiotherapy
> 50	> 5 min	protein denaturation, coagulation
60- 130	1 - 3 s	coagulation, ablation
100 - 300	1 - 3 s	vaporization
> 300	< 1 s	carbonization, smoke generation

Thermal therapies can also be categorized according to the application area: (1) **local** – the temperature is changed in the small area at the tumor region (treatment can be interstitial or extracorporeal); (2) **regional** – the target is organ or region of the body – mostly used for deep tumors. It is worth noting that such treatment is more complex because the treated area usually is not homogeneous (different tissues or organs) [19]; (3) **whole body hyperthermia** – the temperature is increased to 42-43 °C – mostly for advanced metastatic cancer or human immunodeficiency virus treatment. Also, it can utilize different methods such as hot water blankets or thermal chambers [20].

1.2.3 Minimally-invasive therapy

During minimally-invasive treatment, the tumor is locally destroyed *via* direct application of a chemical (non-energy) or energy-based therapy (nonthermal and thermal) [21]. As a result, the main advantage of such techniques is minimal invasiveness, which is possible with endoscopic or percutaneous guidance [22].

One of the non-energy-based minimally-invasive treatments is chemical ablation, during which cancer cell destruction stems from protein denaturation and cellular dehydration caused by an injection of chemical ablation agent (i.e., ethanol, acetic acid, urea) directly into the tumor [23]. Different routes can be utilized for chemical ablation: intravascular, interstitial, and intraarterial. Also, different types of delivery equipment (catheters), substances, and rates of injection (rapid or at a predefined rate) can be used.

Nonthermal energy-based therapy includes mainly irreversible electroporation (IRE), in which therapeutic result is achieved by means of repeated short-duration high-voltage pulses, which lead to electroporation - electrical breakdown of cell membranes and consequent cancer cell necrosis [24]. As the name suggests, after IRE the cell membrane pores are opened permanently leading to the demolition of physiological function and apoptosis [25]. Since electroporation is a nonthermal treatment, it is prone to a heat-sink effect that is a common problem for other thermal treatments.

The next type of energy-based minimally-invasive treatment is a thermal treatment, which is based on inducing of local temperature change of the tumor, either with heating or cooling, that leads to malignant cell death [26]. They are divided based on the principles that induce temperature change: RF [27], MW [28], laser [29], cryotherapy [30], and US [31]. It is worth to mention that ultrasound ablation is based on two effects: thermal (conversion of acoustic energy into heat) and mechanical (acoustically induced cavitation) It is important to highlight, that applicator used as a device used to guide the energy should have a small size in order to minimize the physical trauma to the patient (using percutaneous or endoscopic guidance). Depending on the energy source, the applicator can be called an antenna for MW, an electrode for RF, laser fiber for LA, and a cryoprobe for cryoablation.

1.2.4 Discussion

After the abovementioned categorization, it is easier to define the main challenges of the development of optimal therapy. Indeed, the main thermal therapy aspects to be optimized are: the definition of effective thermal dose, clinical trials to test the efficacy of thermal dose, instrumentation to precisely measure the thermal dose, and accurate delivery of the thermal dose [18]. Regarding phototherapy aspects, light-related parameters need to be optimized: wavelength and related penetration depth, irradiation profile, absorption and scattering properties of the targeted tissue. For effective minimal invasiveness of the treatment, it is important to solve the challenges related to the size, flexibility, and robustness of the applicator and sensing instrumentation, guiding aspects (under US or MRI imaging), and minimize the spread of remaining cancer cells during the removal of the applicator after treatment, etc.

In this regard, different works were performed during my Ph.D. for optimization of aspects of laser treatment but they will not be discussed in the thesis in detail. Thermal therapy-related investigations: numerical modeling [32], [33], comparison of different sensing techniques [34], [35], noninvasive imaging using MRI thermometry [36]. Phototherapy-related investigations are: nanoparticle fabrication and characterization [37]–[40], the use of applicators with different irradiation profiles (bare fiber, diffuser, tapered tip) and dimensions (200 μm – 600 μm), laser wavelength variations (808 nm, 940 nm, 970 nm, and 1064 nm). Investigated aspects related to minimal invasiveness mainly are catheterization of the laser fiber and sensing needle, bundling of the sensor and the laser fiber in one tubing, and the use of different laser fiber materials to improve flexibility.

The works discussed in this thesis mainly focus on thermal therapy aspects: the instrumentation to measure the thermal dose (different fiber optic sensing techniques) and accurate delivery of the thermal dose (LA temperature-based control methods discussed in Papers A - C). The definition of effective thermal dose *via* numerical modeling can be considered as a complementary instrument for treatment optimization (used in Papers B, C). Moreover, Papers D, E aimed to investigate not only thermal dose monitoring but also measurements of the ablated tissue changes (using RI measurements).

1.3 Laser ablation

LA is minimally-invasive photothermal therapy, an intersection of the three abovementioned therapies. Minimal invasiveness stems from the fact that a small flexible optical fiber is used to transport monochromatic light into the targeted tissue. The treatment is considered thermal because the main effect is the absorption of laser light energy and its conversion into heat to induce cancer cells' death. Also, due to the fact that the thermal dose is high, the treatment is called ablation (temperatures near the applicator are more than 60 °C).

The main unique features of LA over other thermal ablation techniques are: flexibility and small dimensions of the applicator (laser fiber diameter < 1 mm),

and immunity of the applicator to electromagnetic interference (laser fiber material is glass or plastic). As a result, LA can be considered one of the least invasive methods which can be used to treat deep-laying organs. In addition, a laser fiber is compatible with Magnetic Resonance (MRI) and computed tomography (CT) imaging, which can be important tools for treatment planning, positioning of the applicator, and monitoring of the targeted tissue properties [16]. Moreover, the short duration of the procedure, less pain, and reduced cost of therapy pave the way for more investigation of clinical applications of LA for cancer treatment.

The first application of LA for cancer treatment was performed by Bown in 1983 to treat brain carcinoma. Nowadays, investigations of LA for different organs have been reported: bones [41], thyroid [42], liver [43], pancreas [44]–[46], brain [47], [48], prostate [49], lung [50], and breast tissue [51].

The main disadvantage of LA is a smaller volume of the ablated region compared with other ablation techniques, which stem from the low penetration depth of the laser light. Indeed, for the treatment of medium or large-size tumors, RF and MW techniques are more developed and used in clinical scenarios [52]. Therefore, the main commercial and clinical interest is in the niche where minimal invasiveness of LA plays a crucial role (in the case of pancreas, brain, prostate), or MRI/CT compatibility of the applicator is needed.

Even in the niche, the uncertainty in the treatment results limits the clinical application of LA. The therapy outcome depends on different parameters: wavelength and power of the laser, applicator properties, tissue perfusion, and tissue thermal and optical properties. As a result, it is very difficult to accurately predict the thermal effect, guarantee complete tumor destruction and minimize cancer recurrences [53]. In this regard, it is important to accurately visualize and control in real-time the thermal outcome to selectively treat pathological tissue with safe margins for healthy tissues.

1.4 Monitoring of laser therapies for cancer treatment

In laser ablation (as in other thermal therapies), it is important to guarantee complete tumor destruction and reduce collateral damage to healthy tissues for the minimization of tumor recurrences [53]. The main steps to guarantee it are: **planning, targeting, monitoring, intraprocedural modifications** (also called feedback control), and **evaluation of treatment response** [54]. While planning and targeting are performed before the actual start of the ablation, and evaluation of treatment response after it; the other two steps (monitoring, and intraprocedural modifications) are performed in real-time. It is worth noting that monitoring can be considered as a base of feedback control of treatment [55].

Monitoring is usually divided into non-invasive (contactless) and invasive (contact) types [56]. For invasive techniques: IR imaging, US imaging, CT, MRI, and shear wave elastography [57]–[60] can be used for measuring ablation effects

via evaluating tissue changes in density, reflectivity, and phase [55]. It should be noted that non-invasive monitoring (**imaging**) can be categorized into two main types: (1) **visualization** – when the ablated volume is evaluated based on the tissue changes analysis; and (2) **thermometry** – tissue temperature measurements.

1.4.1 Non-invasive monitoring

Despite the noninvasiveness of these methods, different aspects limit the application of such techniques. For instance, only MR-compatible devices can be used in parallel with MRI monitoring, ionizing radiation limits CT application, and US imaging is not effective for a high range of temperatures [61]–[63].

US monitoring is based on the analysis of the reflected sound waves at the boundaries of tissues. US visualization can be used to evaluate the ablated region by assessing the echogenic zone that should increase in volume as the ablated volume increases [64]. This approach is popular among clinicians due to its simplicity, but it is only a rough estimation of the ablated margins and other techniques need to be implemented [65]. US thermometry relies on the dependency between temperature and frequency shift of US signal and related sound speed variation [66]. However, at high temperatures, US thermometry becomes less effective due to nonlinear temperature dependency, tissue phase changes, and the presence of cavitation bubbles [67].

CT imaging is based on the interaction between a series of X-rays that pass through the patient and the tissue properties. As a result, the image in which each pixel is related to the average attenuation of the tissue part can be obtained. To obtain thermometry information from CT images, the dependency between tissue physical density and temperature has to be analyzed [57], [68], [69]. However, exposure to X-ray radiation is one of the main limitations of CT imaging and related thermometry.

Infrared imaging is not used for tissue properties measurement, but directly for temperature monitoring which relies on the detection of infrared (900 nm - 14 μm) energy emitted from the surface of the monitored object [70]. Since it requires a line of sight between the camera and the ablated region, it is mainly utilized for skin ablation or ablation performed *via* open surgery [71].

During MRI imaging, strong magnetic fields force protons in the body to align to that field. Then, RF current is applied for a short period to spin the protons out of the equilibrium. Immediately after the RF signal, the protons realign back and release some energy. The analysis of this energy and time of realignment provides information about the monitored tissue properties [72]. It is important to highlight that MRI differs from CT – it does not use X-rays and ionizing radiation. The main principle of MRI thermometry is the dependency between temperature and MRI-related properties: the relaxation times, the diffusion coefficient, and the proton resonance frequency (PRF) shift [73].

Several clinical MRI thermometry systems have been already introduced to clinical scenarios of non-motion organs, such as the brain, prostate, and breast [74]–[76]. The main limitation of MRI thermometry for LA is the formation of gas bubbles at high temperatures that lead to magnetic susceptibility strong contrasts and related artifacts that decrease the accuracy of thermal mapping or can even lead to loss of thermal information in the vicinity of the laser applicator [73].

1.4.2 Invasive monitoring

For invasive approaches, the most used techniques are thermocouples, thermistors, and fiber optic sensors (fluoroptic sensors, distributed sensing, FBGs, etc.) [53]. The main disadvantage of invasive monitoring is the need to insert the sensor in the region of interest. However, the low cost, accuracy, and reliability, and the possibility in some cases to embed them into the applicator pave the way for the development of this approach.

The **thermocouple** working principle is based on the use of the electrical junction of two dissimilar conductors that produces a temperature-dependent voltage [21]. The main limitation of thermocouple use for LA is the light absorption by metallic conductors that can lead to the change of the heat profile and temperature overestimation (~ 20 °C near the laser applicator) [77]. **Thermistor** sensing is based on specific resistors that have temperature-dependent resistance. In addition, single-point measurements provided by thermocouples and thermistors do not allow proper temperature mapping during LA. Therefore, other techniques need to be investigated for optimal treatment monitoring.

Fiber optic monitoring can be considered a good alternative to conventional thermocouples and thermistors due to the small size and flexibility of optical fibers, immunity to electromagnetic interference, and biocompatibility [18].

Fluorescence optical sensors (fluoroptic) utilize the dependence between temperature and fluorescence decay time of the material (alexandrite, thulium, ruby, etc.): the material at the tip of the sensor is excited by a light pulse, and then the fluorescent signal exponentially decays [53]. The measured time constant of the decay allows reconstruction of the point temperature at the sensor tip.

For **distributed fiber optic sensing**, one of the widespread techniques is based on Rayleigh scattering phenomena: dependency between temperature and the spectra of each segment of the fiber [78]. Therefore, it is possible to reconstruct the temperature change profile along the fiber by comparing the measured spectra and spectra at the reference state (no temperature applied). The main limitations of Rayleigh-based sensing are the high cost of the interrogation device, low spatial resolution and low sampling frequencies (in comparison with FBG measurements).

Fiber Bragg grating sensors

FBG is a fiber-optic structure that consists of a periodic variation of the refractive index in the fiber core. In the case of sending a broadband light through the optical fiber into this structure, each line in the grating (line as a transition between two media with different refractive indices) reflects a small part of wavelength centered at λ_B , finally resulting in a high amplitude reflection centered at Bragg wavelength. In other words, self-backward coupling of the core mode occurs.

Bragg wavelength is, obviously (from the classical wave approach), proportional to the grating period Λ and, in addition, to n_{eff} since the wave is traveling in a specific medium (that has a specific refractive index n_{eff}):

$$\lambda_B = 2n_{eff}\Lambda \quad (\text{Eq. 1.1})$$

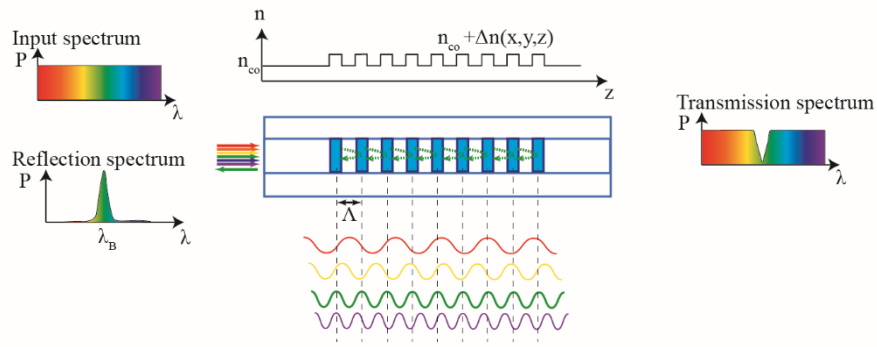


Figure 1.2: FBG principle: periodic change of refractive index in core ($n_{co} + \Delta n$) reflects only part of incident light. The reflected part is centered at Bragg wavelength λ_B .

FBG temperature sensing is based on the dependency of the material properties (thermal expansion and the temperature dependence of the refractive index) and Bragg wavelength [79]. As a result, it is possible to derive the equation between the Bragg wavelength shift and related temperature change:

$$\frac{\Delta\lambda_B}{\lambda_B} = \frac{\lambda_{B,\Delta T} - \lambda_{B,initial}}{\lambda_B} = \alpha\Delta T \quad (\text{Eq. 1.2})$$

where α ($^{\circ}\text{C}^{-1}$) is the thermal sensitivity of the grating.

It is important to note that FBG is also sensitive to strain due to FBG elongation (and related change in grating period), and the change in fiber index due to photoelastic effects. As a result, it is important to have constant strain (or compensate external strain perturbations) to have accurate FBG temperature measurements,

Moreover, it is possible to have multi-point measurements using an array of spatially-resolved FBGs, each with a different grating period, inscribed in one fiber. Incident broadband light reflects from each FBG at a distinctive Bragg wavelength. Thus, quasi-distributed measurement is possible by analyzing the Bragg wavelength shift of each reflected peak.

Tilted fiber Bragg grating sensors

There are several well-written reviews about tilted FBG (TFBG) [80], [81] that provide detailed theoretical background and application aspects of this sensor. In general, TFBG is a specific type of FBG. Thus, it is able to measure the same parameters as FBG: temperature, axial strain, and pressure. The main distinction between TFBG and FBG is the tilt of grating planes to the optical fiber axis.

Fig. 1.3 reports the transmission spectrum of custom-made TFBG with a 10° tilt angle. The dips on the transmission spectrum (resonances) can be clearly seen – they stem from the coupling of the forward-propagating core mode to a group of backward-propagating cladding modes.

It is worth noting, that tilt of FBG amplifies such coupling (small coupling can be noticed even without tilt, for example in standard FBG). Resonances of such coupling lead to dips on the TFBG transmission spectrum, also called cladding modes. Such cladding modes are sensitive not only to temperature and strain (as the core mode) but also to the variation of surrounding RI. As a result, TFBG can be used as an RI sensor, and, with additional modifications, for biosensing [81]–[84].

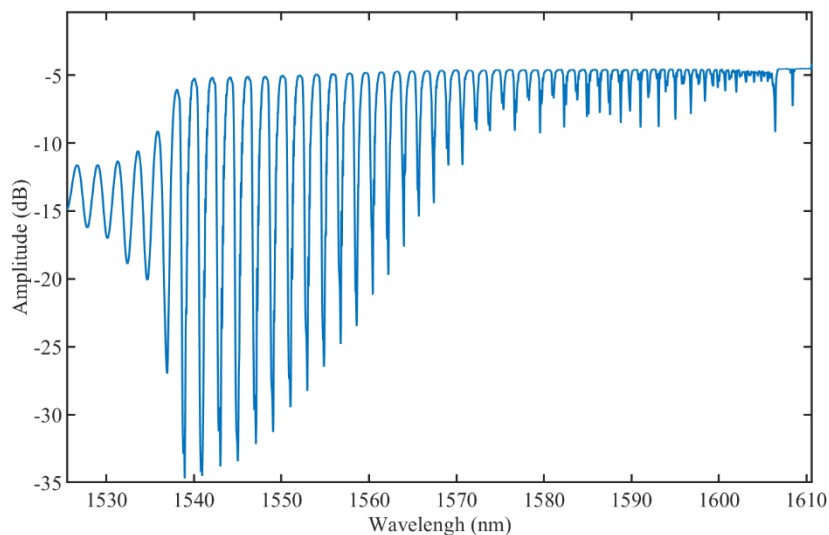


Figure 3: Transmission spectrum of TFBG (10° tilt, 1 cm length). Coupling to the cladding mode resonances leads to dips in the transmission spectrum.

1.5 Laser ablation feedback systems

Earlier attempts to develop a feedback system to regulate laser power and reduce the risk of excessive heating during LA have been based on the measurement of temperatures using thermistors, thermocouples, and IR imaging.

For **thermistor-based control**, ON-OFF temperature control with 43°C pre-set temperature was developed in [85]. In [86] a laser device has been designed to deliver high laser power to deep tissue areas embedding one thermistor. The temperature of the tissue in the border area was computed and used to control

the laser power automatically and to modulate it continuously in order not to exceed the critical temperature. It is worth noting that the control is performed dynamically with software support, triggered by the operator *via* a laser pedal. In [87] the temperature distribution was monitored by several thermistor probes. A Microprocessor controlled power regulation integrating a diode laser (805 nm wavelength). The temperature was controlled at one feedback thermistor positioned at a 5 mm distance from the fiber tip through stepwise changes in output power.

For **thermocouple-based control**, ON-OFF temperature control between 42 °C and 44 °C was used in [88]. As soon as the temperature was over the upper range the delivery of laser energy stopped. The system allowed for either continuous wave (CW) or pulse mode of laser energy delivery to be rapidly available in order to maintain the fine control of tissue temperature between the pre-set ranges. The pulse mode allowed more precise control than a continuous wave. In [89] ON-OFF temperature control is designed with two T-type thermocouples that measured the temperature during nanoparticles-mediated photothermal therapy. In [90], a thermocouple-assisted PID controller is employed during 980-nm LA with a radial diffusion applicator to attain the pre-determined temperature (80 °C) for tissue coagulation theoretically and experimentally.

Regarding **thermography-based control**, in [91] temperatures in a selected area including the irradiated spot were captured by the thermal sensor circuit and used to modulate the laser current and control the target temperature. While in [92], an IR camera was used for “low and slow” control – an open loop designed to control the temperature within a target range of 50° C -60 °C.

Later in [93], **a photo-optic probe** was used to measure the temperature as well as the applied energy at the laser tip continuously. The power of the laser source was dynamically controlled by the thermosensor so that the preselected temperature at the fiber tip was automatically kept constant. If the applied energy mismatches with the measured temperature on the application probe (fast increase in temperature at a relatively small applied laser power) and carbonization can be expected, a carbonization alarm was generated, and energy deposition was suspended.

Some of the emerging non-invasive thermometry methods were also investigated for control-loop implementation. Photoacoustic (PA) imaging is an emerging hybrid modality that has the contrast of optical imaging and the high resolution of ultrasound imaging. PA techniques have the advantages of better temperature sensitivity and the potential to extract absolute temperature at depths. For example, in [94] single CW-laser-based photothermal system with ultrafast frequency-domain photoacoustic (FD-PA) temperature feedback. By interleaving FD-PA temperature measurement into photothermal heating (therefore, time-sharing the laser) and incorporating closed-loop control, the photothermal temperature was self-regulated.

Assi *et al.* [95] proposed an automated control system for hyperthermia therapy that can accurately achieve a prescribed temperature for both surface heating

and deep-tissue heating. The control was based solely on real-time PA thermometry, without any invasive point thermometry. The laser power was controlled using a PID controller.

The general advantage of sensor-based systems is continuous real-time temperature measurement and, as a result, real-time LA control. While in an MRTI-based system, the image acquisition and update time define a delay between discrete temperature measurements. One of the disadvantages of the MRTI is bubble formation and the cavitation artifacts that can significantly reduce the accuracy of the measurements.

In general, thermocouples and thermistors usually rely on the use of single-point measurement to perform the temperature control strategy, hence leading to increased invasiveness when more sensors are needed for performing both control and monitoring in the tissue. In addition, metallic material absorbs the laser light and leads to temperature overestimation. Indeed, in the recent work focused on the PID regulation using thermocouple measurements, a 0.5 mm plastic plate was positioned between the laser applicator and the thermocouple to prevent laser light artifacts along with self-heating heating [90]. Paiella *et al.* performed clinical testing of immune-stimulating interstitial laser thermotherapy control based on thermistors measurements. The investigation shows unsatisfactory results in terms of device handling, safety, and feasibility [96]. In order to avoid such complications during LA, the use of electromagnetic immune fiber optic sensors for LA regulation receive more and more interest in recent times.

Recently, several works investigated the possibility to use fiber optic sensors for LA control: ON-OFF control for 1D [97], 2D superficial ablation [97], and interstitial ablations [2], and PID-based control for interstitial ablation [3].

1.6 Equipment used in the experiments (Paper A – Paper E)

1.6.1 Interrogators

Two main optical interrogators that were used in the works described in Papers A - E are MicronOptics si255 swept-laser interrogator (Micron Optics, Atlanta, USA) and optical backscatter reflectometer LUNA OBR 4600 (LUNA OBR 4600 from LunaInc, Blacksburg, VA, USA).

MicronOptics si255 was used for FBG arrays and TFBGs interrogation. It allows using 16 channels at the same time, the wavelength range is 1460 nm – 1620 nm and a wavelength resolution of 8 pm (20000 points per wavelength range), wavelength accuracy is 1 pm, and 1 kHz sampling rate. For FBG measurements, only peak data saving was utilized because temperature reconstruction is based only on the Bragg peaks shifts and the measurements of the whole spectra are not needed. For TFBG measurements, the spectral data saving modality was used because it was important to save the whole spectra with the core mode and

cladding mode resonances. In cases when both FBG and TFBG were connected to MicronOptics, the combination of both modalities of data saving was used.

TFBG interrogation in Paper D was performed with LUNA OBR 4600 at a wavelength range between 1525 nm and 1610 nm, sampling frequency ~ 0.3 Hz. Since in this work only RI calibration was done using single measurements, the low sampling rate did not affect the experiments. Moreover, the backscatter-level sensitivity of -130 dB allowed to measure the highly-etched TFBG states, which have very low intensity since part of the light leaves the fiber.

1.6.2 FBG and TFBG sensors

Temperature measurements discussed in this thesis were performed by the custom-made highly dense FBG arrays inscribed with femtosecond point-by-point writing technique [98]. ABL1000 air-bearing linear stage (*Aerotech Inc.*, Pittsburgh, PA, USA) was used for accurate fiber positioning during inscription. The properties of the femtosecond Pharos 6W laser system (*Light Conversion Ltd.*, Vilnius, Lithuania) are following: duration of 232 fs, 1000 Hz repetition rate, 0,1 μ J of pulse energy, and wavelength of 1026 nm (Fig. 1.4).

The design of FBG was optimized to have a wavelength separation between adjacent Bragg peaks of 4 nm (Fig. 1.5 reports FBG spectrum). As a result, 40 FBGs were possible to observe in the Micron Optics si255 wavelength range (1460 nm – 1620 nm). The resulting grating length is equal to 1.19 mm, and the edge-to-edge distance between gratings is 0.01 mm. Thus, the total sensing length is 48 mm with a spatial resolution of 1.2 mm.

For fiber, polyimide-coated single-mode fiber SM1500(9/125)P with a reduced coating diameter of 145 μ m (*Fibercore Ltd.*, Southampton, UK) was used. Since polyimide is transparent to IR femtosecond radiation, it was possible to inscribe gratings directly through the polyimide and avoid coating removal. Moreover, polyimide provides high thermal resistance (400 $^{\circ}$ C for polyimide coating vs. 80 $^{\circ}$ C for conventional acrylate coating), and low thermal conductivity [98]–[100]. The cost of FBG sensing is significantly smaller than MRI-thermometry [101], and it has better metrological characteristics (i.e., response time in the order of 0.1 s and accuracy of <1 $^{\circ}$ C).

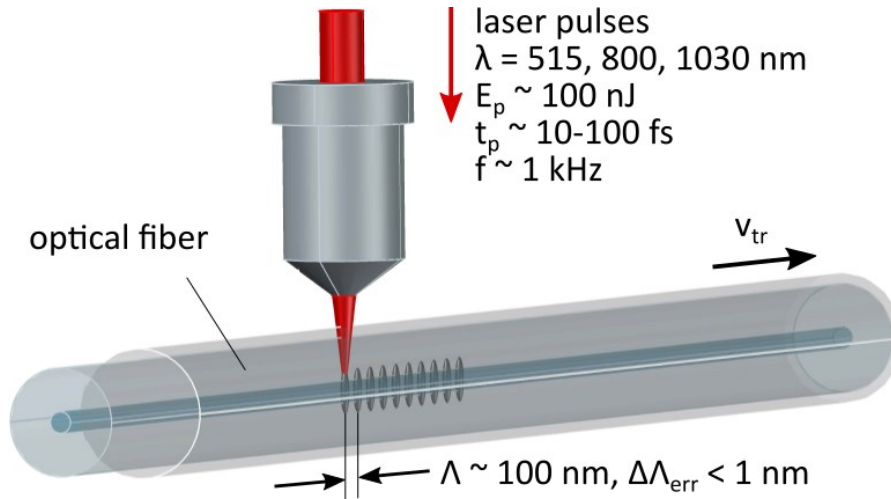


Figure 1.4: Femtosecond point-by-point FBG inscription in the polyimide-coated single-mode fiber. The ranges of the main laser and grating characteristics (wavelength, pulse energy, pulse duration, pulse repetition, grating period) are given.

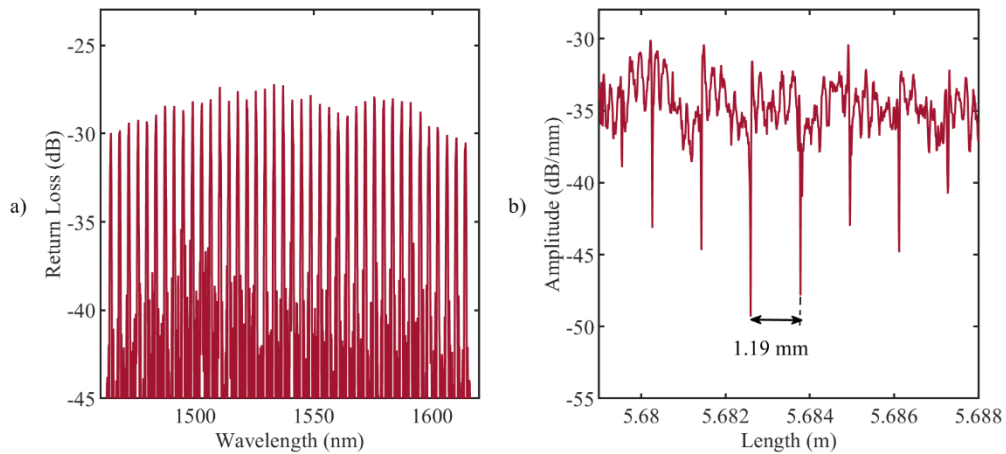


Figure 1.5: (a) Reflection spectrum of the custom-made FBG array (grating length is equal to 1.19 mm, and the edge-to-edge distance between gratings is 0.01 mm); (b) LUNA OBR 4600 backscattering signal: the distance between the ends of the gratings (drops in amplitude) is 1.19 mm.

Temperature calibration of FBG arrays was performed in the thermostatic calibrator (*Giussani Quartz*) in the range of 20 °C – 125 °C with a 10 °C step. The reference measurements were performed by a PT100 thermistor (± 0.15 °C accuracy). The resulting sensitivity of the arrays is $(7.43 \pm 0.01) \times 10^{-6}$ °C⁻¹ [1], [98].

Several variants of FBG arrays were fabricated and used in the experiments: an array of 25 FBGs (grating length 0.9 mm, edge-to-edge distance is 0.1 mm), an array of 40 FBGs (grating length 1.19 mm, edge-to-edge distance is 0.01 mm), and an array of 40 FBGs (grating length 1.15 mm, edge-to-edge distance is 0.05 mm). The two later options are more optimal for LA due to their sensing length (~ 48 mm) which allows for measuring the whole temperature profile and provides easier positioning of the sensing part near the applicator inside the ablated tissue.

1.6.3 Laser diode

For laser ablation, the continuous-wave diode laser (LuOcean Mini 4, Lumics, Berlin, Germany) was utilized. In the laboratory, four different diodes are available each having different wavelengths: 808 nm, 940 nm, 975 nm, and 1064 nm. All these wavelengths belong to the "therapeutic window" (650 nm – 1300 nm) that provides a good tradeoff between penetration depth and absorption of the laser by the tissue [102]. As a result, the most utilized wavelengths for soft tissue ablations are 800–980 nm and 1064 nm [29].

Chapter 2. LA temperature-based control with FBG sensors

As mentioned in the previous chapter, most of the works on LA control are based on temperature measurements provided by thermocouples and thermistors. The main disadvantages of these methods are the metallic material of the sensors and their low spatial resolution. Metallic material absorbs laser light and heat; thus, leading to an overestimation of temperature that can reach above 20 °C [56], [77]. The low spatial resolution of conventional sensors does not allow proper temperature reconstruction due to high thermal gradients, especially in the proximity of the applicator tip [103].

In this regard, fiber optic-based sensors can provide unique advantages, such as immunity to electromagnetic interference, small size, biocompatibility, and multi-point sensing. The following chapter covers works on LA control using fiber-optic sensors carried out during my Ph.D. studies and published by the research team. These are the first works available in the literature on the application of FBG technology for the real-time control of LA thermal therapy.

For all these works, my part was the development of a custom-made LabVIEW program for LA control, sensors calibration, experimental setup development, conduction of the experiments, critical data analysis, and paper writing. The main steps of the developed LabVIEW programs are: 1) monitoring of FBG peaks data by the optical interrogator and sending this data to the computer in a real-time mode; 2) temperature reconstruction on the computer; 3) Laser diode power modulation based on the measured temperature.

The order of presenting papers in this chapter follows the criterium of increased clinical applicability for interstitial ablation. Indeed, Paper A discusses the setup when the fibers are positioned on the tissue surface. This setup is far away from the interstitial application but can be an important tool to improve laser treatment of skin cancers, as an alternative to traditional non-invasive infrared imaging. Paper B can be considered as the first step for interstitial applications of fiber sensors for LA regulation and it introduces the numerical COMSOL model as a tool for pre-treatment optimization of the procedure parameters. Later, Paper C is an additional step in the development of accurate temperature regulation with a better controlling technique, i.e., the PID regulation.

2.1. Paper A: ON-OFF non-invasive LA control

Paper Title: “Closed-Loop Temperature Control Based on Fiber Bragg Grating Sensors for Laser Ablation of Hepatic Tissue” [1].

Paper Objective:

The first work towards the development of LA control using FBG measurements was presented by our group in the 2020 IEEE Workshop on Metrology for Industry 4.0 and IoT [97] by introducing the algorithm to measure temperature along one FBG array on the tissue surface and ON-OFF laser control. However, the setup of using only one FBG array (1D monitoring) for non-invasive ablations is not well appropriate for clinical applications. Indeed, recently IR imaging was used for 2D temperature mapping, for example during skin heating [92]. However, an IR camera is not immune to electromagnetic interference, so it can not be used in an MRI machine. Thus, fiber sensing can be a good option for 2D temperature mapping. Therefore, the main idea of Paper A was to develop the matrix of sensing points on the ablated tissue (using several parallel FBG arrays) for 2D mapping and perform ablated area regulation.

In this regard, the objective of Paper A was to develop and test the system (as a proof of concept) for ON-OFF temperature control of superficial laser ablation based on the use of custom-made highly-dense FBG arrays. Investigation of the relation between the controlled parameters (temperature and radius of the controlled thermal map) and thermal damage zone.

Methods:

The main idea of the work was to utilize the system of 3 parallel FBG arrays on the surface of the *ex vivo* porcine liver and to perform controlled superficial ablation based on FBG array measurements (Fig. 2.1.1). Collimator (*OZ Optics Ltd.*, Ottawa, Canada) positioned at a 7 cm distance above the tissue surface to guarantee small beam divergence: collimated beam diameter = 15.4 mm, the effect of divergence for 7 cm distance is 0.8 mm, the final beam diameter on the surface is 16.2 mm. FBG interrogation was performed by MicronOptics si255, then the data was transferred to PC and related temperature values were obtained. After, the laser diode was controlled based on the reconstructed temperature maps.

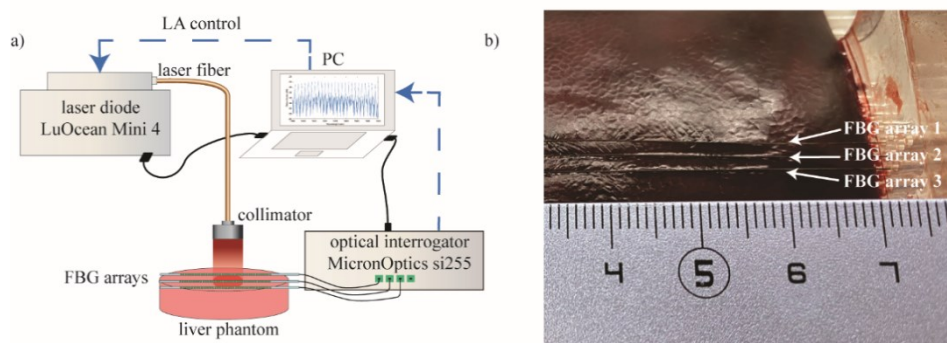


Fig. 2.1.1. Superficial ablation experiment: 3 parallel FBG arrays positioned on the liver surface. Laser diode control is based on FBG temperature measurements. (a) Schematics of the experiment; (b) Photo of the setup

The ON-OFF control logic was during tissue ablation utilized to perform a zone-control: the area of the ablation was regulated by adjusting the input parameters of the control algorithm (set temperature T_s and set radius r_s). Fig. 2.2.2 reports three main steps of the LabVIEW algorithm: (1) alignment phase, when peaks of the reconstructed Gaussian profiles were aligned at the beginning of ablation; (2) reconstruction of the two-dimensional temperature maps, and (3) real-time laser ablation control.

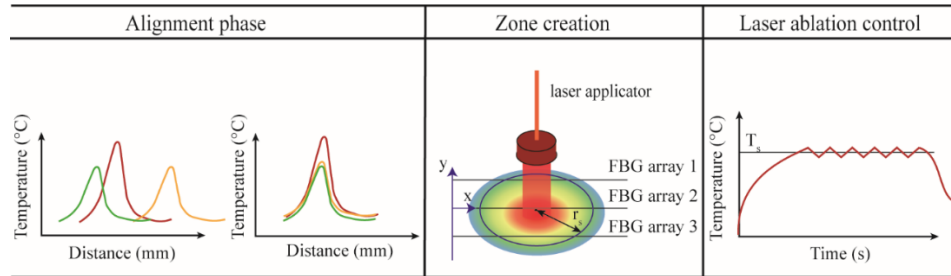


Fig. 2.1.2. Three stages of the developed LabVIEW algorithm for zone-control logic based on FBG array measurements.

Results:

The main results of the experiments can be divided into two main categories: a) temperature profiles vs. time for each array; and b) spatial temperature maps (x vs y-axis) reconstructed from the FBG array measurements. The first category reports that the maximum temperatures follow the set thresholds; moreover, a characteristic sawtooth-like shape is observed, due to the effect of the laser that is switched ON and OFF according to the set T_s and r_s . The second category shows a spatial temperature map and related thermal damage on the surface of the ablated tissue.

a) Temperature profiles vs. time for each array

The maximum temperature during the experiments corresponds to the center of the collimated beam on the tissue surface. As a result, the central FBG array experienced the highest temperature increase. The temperature profiles of this increase for each experiment (uncontrolled (green line) and controlled ones) are presented in Fig. 2.1.3. As can be seen, the maximum temperature oscillates near the set temperature T_s . Moreover, the magnitude of these oscillations (the average difference between the highest and lowest peaks, ΔT_p) is dependent on the set radius r_s .

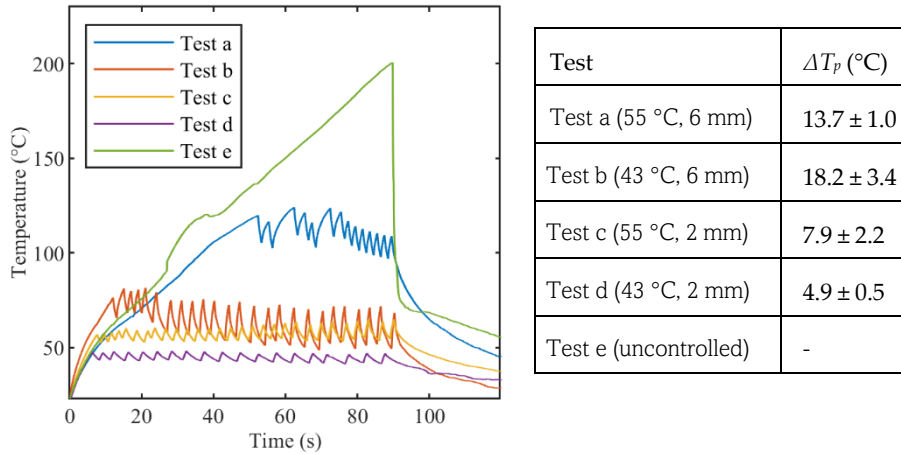


Fig. 2.1.3. Evolution of maximum measured temperature for each test: uncontrolled one, and controlled ablations with different input parameters (T_s and r_s). Table summarizes test inputs and measured magnitudes of oscillations.

Fig. 2.1.3 shows the temporal profile only of the maximum point measurement of the central FBG array. In this regard, it is important to utilize quasi-distributed sensing of FBGs and show spatial profile evolution: x-axis vs. time, where the x-axis corresponds to the distance along the sensing part of the fiber. Thus, Fig. 2.1.4 a-d report controlled tests, and Fig. 2.1.4 e – the test performed without any laser control. The effect of the control is clearly observable: during the uncontrolled case, heat is distributed towards the edges of the irradiated zone, and the width of the >100 °C is around 8 mm. Even after the switching of the laser, some heat is still dissipated around the zone. While more regular behavior can be observed in the controlled cases.

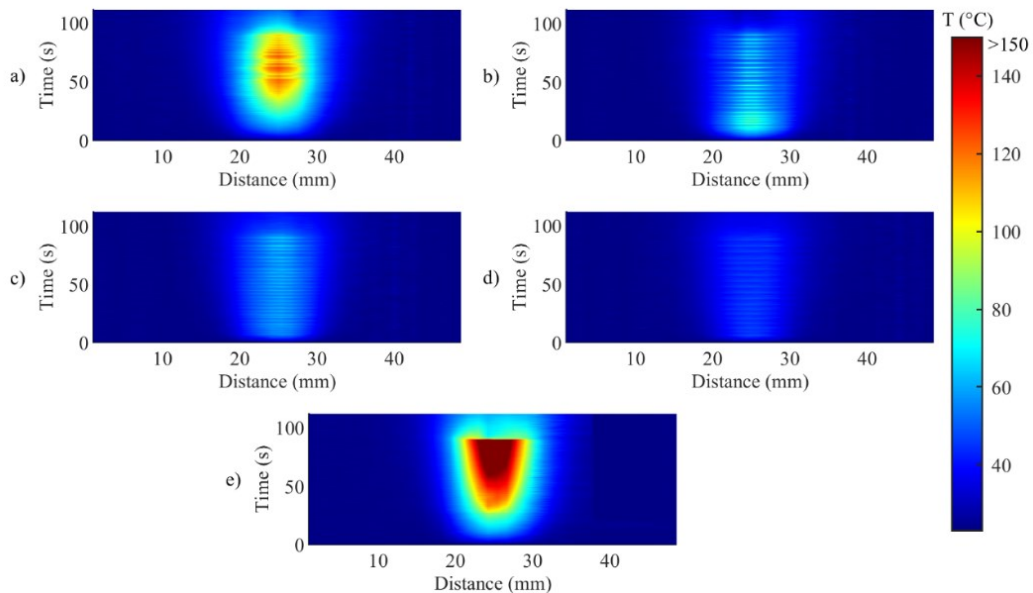


Fig. 2.1.4. Temperature profile evolutions (distance along the sensor vs. time) for controlled (a - d) and uncontrolled tests (e), where (a) 55 °C and 6 mm; (b) 43 °C and 6 mm; (c) 55 °C and 2 mm; (d) 43 °C and 2 mm;

b) Spatial temperature maps reconstructed from the FBG array measurements

After reporting temperatures of the one-point temporal profile (Fig. 2.1.3) and the spatial profile evolution (Fig. 2.1.4), it is important to show two-dimensional spatial maps (distance along the sensor *vs.* distance between the FBG arrays). Fig. 2.1.5 shows such maps (at the time moment of the highest temperature) with imposed circles defined by the set radius r_s . The temperature maps show that the “zone-control” logic approach prevents temperatures higher than T_s . Nevertheless, it is worth mentioning that oscillations also affect spatial distribution - temperatures higher than T_s can be observed for a short time even out of the set radii.

Fig. 2.1.5 reports photos of the thermal damage of the ablated tissues, which is clearly visible for both tests with $T_s = 55\text{ }^\circ\text{C}$, while thermal damage for $T_s = 43\text{ }^\circ\text{C}$, is distinguishable only for a 6 mm set radius. The uncontrolled case, as expected from spatial thermal maps that reach $>150\text{ }^\circ\text{C}$, experienced the largest thermal damage, coagulation, and carbonization.

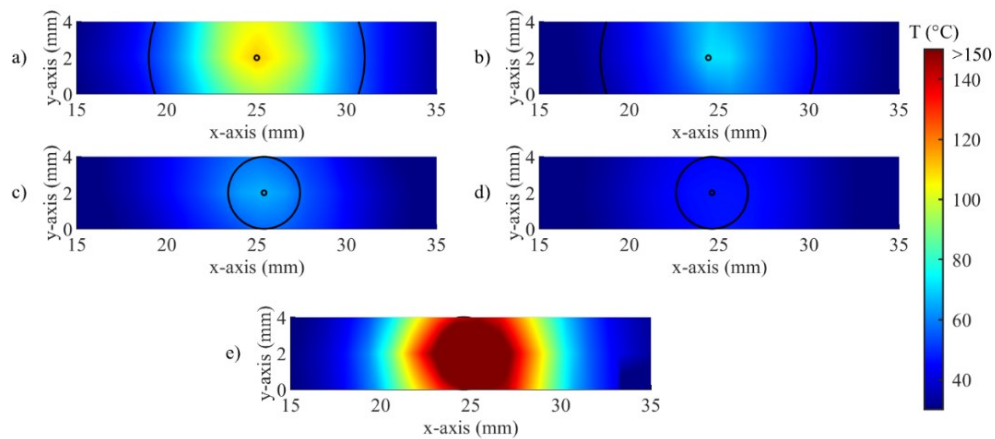


Fig. 2.1.5. Two-dimensional spatial temperature maps (distance along the sensor *vs.* distance between the FBG arrays) for controlled (a - d) and uncontrolled tests (e), where (a) $55\text{ }^\circ\text{C}$ and 6 mm; (b) $43\text{ }^\circ\text{C}$ and 6 mm; (c) $55\text{ }^\circ\text{C}$ and 2 mm; (d) $43\text{ }^\circ\text{C}$ and 2 mm;

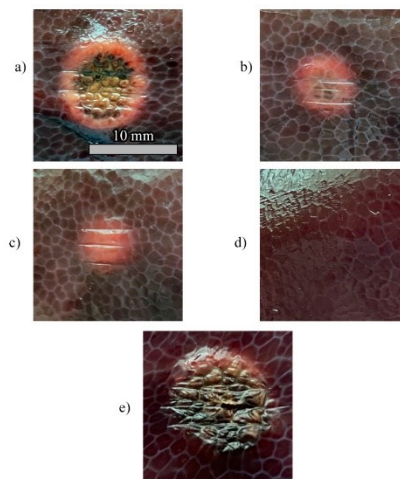


Fig. 2.1.6. Photos of the thermal damage after the ablation tests: (a) $55\text{ }^\circ\text{C}$ and 6 mm; (b) $43\text{ }^\circ\text{C}$ and 6 mm; (c) $55\text{ }^\circ\text{C}$ and 2 mm; (d) $43\text{ }^\circ\text{C}$ and 2 mm; and (e) uncontrolled ablation.

Discussions:

The results show that the main aspect that limits the effective and accurate LA ON-OFF control is the presence of temperature oscillations. As a result, the thermal dose distribution is not fully contained in the region of interest. Therefore, it is clear that the main future works should be focused on the improvement of the LA controlling strategy.

Moreover, since the thermal effect on biological tissues is based on temperature and its duration (thermal dose), it can be more interesting to control not the temperature map, but the thermal dose. Possible methods to measure thermal dose can be applications of the Arrhenius equation or the cumulative thermal dose (CEM43) estimation, which have been already used to assess the severity of thermal damage for different types of tissue in [104]. Indeed, later the experiments done in Paper A were post-processed and modeled in COMSOL to obtain thermal damage simulation of the tests [105]. The obtained results are shown in Fig. 2.1.7. Such modeling in real-time during the procedure would significantly improve thermal dose control and treatment efficacy in the future.

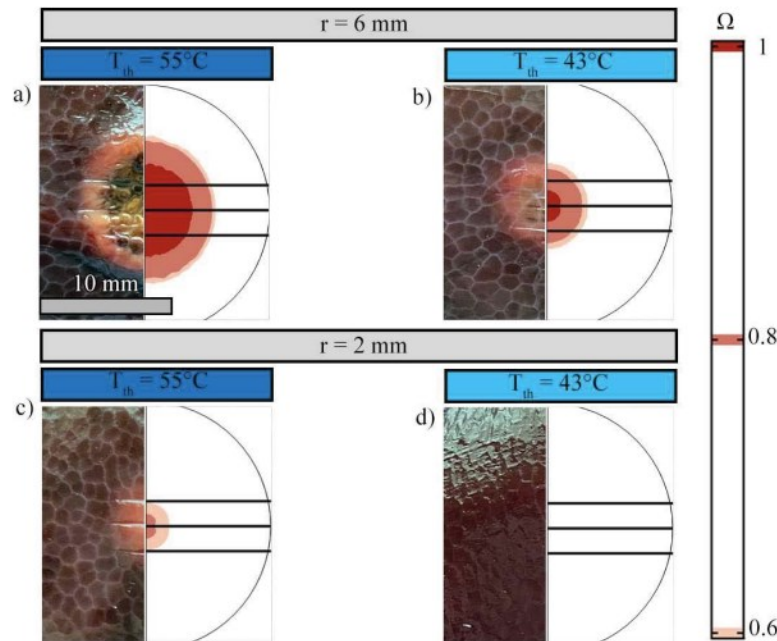


Fig. 2.1.7. Photos of the thermal damage after the ablation tests and modeling of corresponded thermal damage for different set temperature T_{th} and set radii r .

Most of the previous investigations of real-time LA control employed single-point measurements [89], [97], [106], or multi-point contactless thermometry [91]. The application of FBG arrays for superficial ablation can be an effective tool for LA control and an alternative to contactless imaging techniques, which can not be used in environments with high electromagnetic interference. In this regard, the matrix of fiber optic sensing points (in this case 40 x 3 matrix) can provide accurate temperature maps for LA regulation.

It is important to mention, that several works already utilized more dense matrices for strain and temperature which provided better spatial resolution of

measurements [107], [108]. Moreover, it is also possible to incorporate/weave fiber sensors in a special material to provide a portable sensing structure for better use in different environments. In addition, several machine learning techniques were developed to improve the spatial resolution of such measurements [109], [110].

See Paper A in the Appendix for more details of this work.

2.2. Paper B: ON-OFF interstitial LA control

Paper Title: “Quasi-distributed fiber optic sensor-based control system for interstitial laser ablation of tissue: theoretical and experimental investigations” [2].

Paper Objective:

After the implementation of the ON-OFF control strategy for superficial ablation control (Paper A), it was important to evaluate the effect of oscillations in an interstitial case. Indeed, since both the sensors and the laser-guiding fiber are inside the *ex vivo* tissue, laser-tissue interaction and heat distribution will significantly differ from the setup of Paper A (superficial ablation assisted by a collimator and sensors positioned on the tissue surface). To facilitate pre-planning of the interstitial LA procedure, the COMSOL model was developed and used to simulate ON-OFF control logic and its effect on temperature maps and tissue thermal damage.

Therefore, the investigation was focused on the development and testing of LA regulation for interstitial ablation. Four parallel highly dense FBG arrays were positioned parallel to the laser fiber inside *ex vivo* porcine liver tissue. My part of the work was the sensors calibration, development of a custom-made LabVIEW program, experimental setup development, conduction of the experiments, and paper writing. The COMSOL model was developed and described in the paper by my colleagues.

Methods:

The setup consists of four parallel FBG arrays inserted in the liver phantom parallel to the laser fiber (Fig. 2.1.1). The custom-made plexiglass box was used to guarantee accurate positioning of the laser fiber and the sensors. The placement of the fibers was performed using medical needles: they were inserted into the tissue, then FBG arrays were placed inside of the needles, after the needles were pulled out and the sensing fibers remained in the tissue.

Two main input parameters were: set temperature T_s (40 °C for all controlled tests) and controlled distance d . The controlled distance is the distance (in the axis of the laser applicator) between the maximum measured temperature during LA and the controlled plane z_d , at which temperature is controlled using ON-OFF logic. The main concept of the developed LabVIEW program is similar to the three stages used in Paper A for the zone-control.

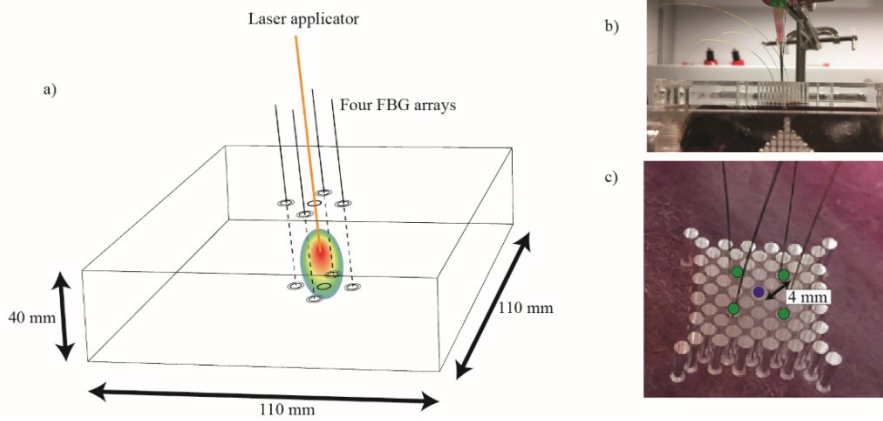


Fig. 2.2.1. Experimental setup for interstitial LA control: (a) schematics; (b) photo of the custom-made box used to guarantee accurate positioning of the sensors and the fiber in the tissue; (c) photo of the top of the box: fiber sensors were positioned in the green-labeled holes, the laser fiber – at the central hole.

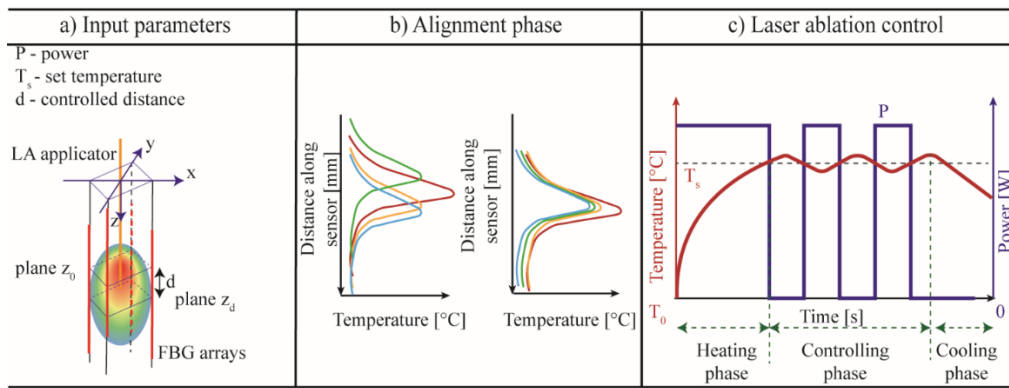


Fig. 2.2.2. Temperature control for interstitial LA: (a) input parameters: set temperature and controlled distance d . FBG sensing regions (red lines) are not spatially aligned; (b) alignment of measured profiles; (c) control logic.

Numerical Simulation

Before the actual experiments, the finite element method (FEM) solver using COMSOL was used to model the experimental setup had been developed (Fig. 2.1.3). The geometry and the mesh of the model are reported in Fig. 2.1.3. The model includes the laser applicator, porcine liver tissue and fiber sensors (with the corresponding dimensions, absorption coefficients, thermal conductivity, density, and heat capacity coefficients).

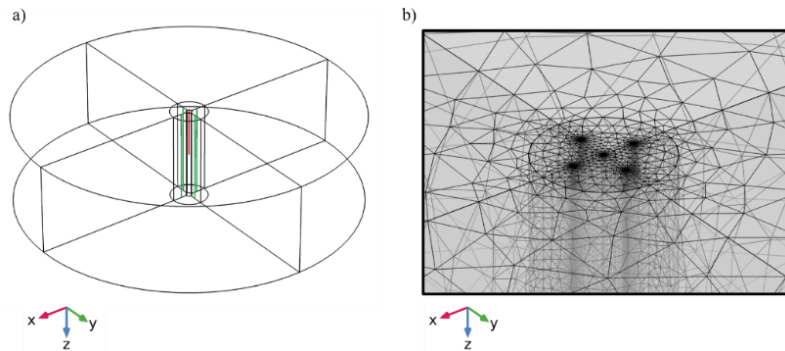


Fig. 2.2.3. COMSOL model of experimental setup: (a) geometry model consisting of laser fiber, FBG arrays, and cylinder of porcine liver tissue; (b) Zoom-in of the central part of used mesh (minimum mesh size is 0.01 mm)

The temperature-related laser-tissue interaction was modeled using the heat diffusion equation:

$$\rho \cdot c \cdot \frac{\partial T}{\partial t} + \nabla(-k\nabla T) = Q_{laser} \quad (\text{Eq. 2.2.1})$$

where ρ is density ($\text{kg}\cdot\text{m}^{-3}$), c is specific heat ($\text{J}\cdot\text{kg}^{-1}\cdot\text{K}^{-1}$), k is thermal conductivity ($\text{W}\cdot\text{m}^{-1}\cdot\text{K}^{-1}$), T is temperature of tissue (K), and Q_{laser} is related to heat generated by a laser ($\text{W}\cdot\text{m}^{-3}$) [111].

The optical related interaction between tissue and laser: light penetration and related energy absorption by tissue was modeled based on the Beer-Lambert law:

$$Q_{laser} = \alpha_a \cdot I_r \cdot e^{-\alpha_a \cdot d_t} \quad (\text{Eq. 2.2.2})$$

where α_a is the absorption coefficient (m^{-1}), d_t is axial depth in tissue (m), and I_r is laser irradiance ($\text{W}\cdot\text{m}^{-2}$) [45].

To measure thermal damage induced by laser irradiation (degree of tissue injury $\theta(r,t)$) in the model, the Arrhenius equation [111] was used:

$$\theta(r,t) = \theta_0 + A_f \cdot \int_0^{\tau_{irr}} (1-\theta)^{n_p} \cdot \exp\left(-\frac{E_a}{R \cdot T}\right) dt \quad (\text{Eq. 2.2.3})$$

where A_f is the frequency factor (s^{-1}), τ_{irr} (s) is total irradiation time, n_p is the polynomial order, E_a ($\text{J}\cdot\text{mol}^{-1}$) is the denaturation activation energy, R ($\text{J}\cdot\text{mol}^{-1}\cdot\text{K}$) is the universal gas constant, and T (K) is the absolute temperature in tissue. The portion of damaged tissue, PDT , is therefore calculated based on the degree of tissue injury θ , according to [112]:

$$PDT = \min(\max(\theta, 0), 1) \quad (\text{Eq. 2.2.4})$$

Results:

The results of the pre-treatment stage (numerical modeling of LA control) are provided in Fig. 2.2.3, which reports maximum fractions of necrotic tissue for uncontrolled ablation and different variations of the controlled distance. The highest volume of the necrotic tissue corresponds to the uncontrolled case (53 mm^3), for controlled cases necrotic volumes are 34.4 mm^3 and 27.9 mm^3 for $d = -3 \text{ mm}$ and $+3 \text{ mm}$ correspondingly, 24.2 mm^3 and 23.0 mm^3 for $d = -2 \text{ mm}$ and $+2 \text{ mm}$. For $d = 0 \text{ mm}$, the size of the necrotic part is 21.1 mm^3 .

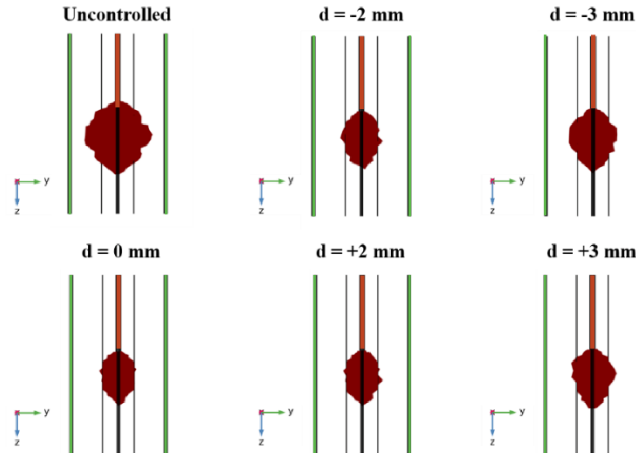


Fig. 2.2.4. Results of numerical simulation of LA control: necrotic tissues visualization for uncontrolled ablation and different controlled cases.

The temporal evolutions for maximum temperatures measured by each FBG array are provided in Fig. 2.2.5. The left column reports the temperature profiles of 4 sensing points positioned on the controlled plane z_d (LA control is based on only one of the sensing points), maximum temperatures measured by each FBG array are shown on the right column. Four FBG arrays do not provide similar temperature measurements for the same trials due to possible uncertainties in the fibers positioning and inhomogeneity of the tissue. Also for the interstitial case, the effect of oscillations is clearly seen, especially for bigger controlled distances.

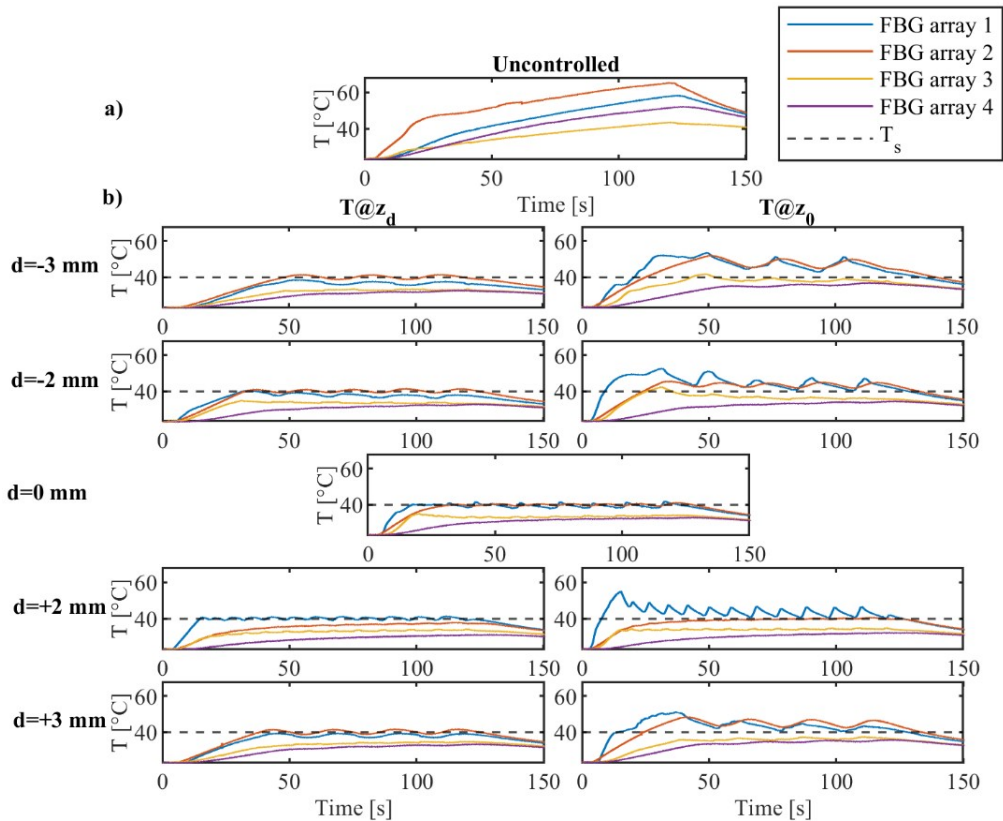


Fig.2.2.5. Temporal evolutions for maximum temperatures measured by FBG arrays. Left column: temperature measured at z_d plane, right column: maximum temperatures measured by each FBG array.

Fig. 2.2.6 reports spatial profile evolution (the distance along the sensor vs. time) for the FBG array used for LA control; the contour lines define the regions with temperature >40 °C. For uncontrolled ablation, the maximum temperature reaches ~ 65 °C and the heat is dissipated to the edges of the sensors during the whole ablation time.

Fig. 2.2.5-6 show that for the same distances the direction (+d or -d) affects the overshooting and related delay response:

- 1.4 °C and 6.6 s for -3 mm and 1.4 °C and 5.0 s for +3 mm;
- 1.0 °C and 4.2 s for -2 mm and 2.2 °C and 5.0 s for +2 mm;
- 0.6 °C and 3.5 s for 0 mm.

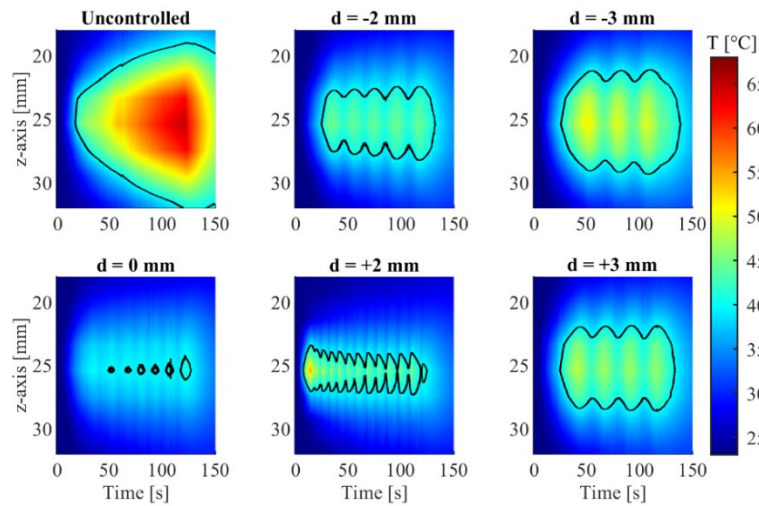


Fig. 2.2.6 Temperature profile evolutions (distance along the sensor vs. time) for controlled and uncontrolled tests.

The comparison between the simulated and the experimental results is presented in Fig. 2.2.7: the depicted maximum temperature profiles measured at the controlled z_d plane proves the feasibility of the simulation of ON-OFF control. As can be seen, most of the simulations accurately predict the heating phase of ablation and its cooling trend.

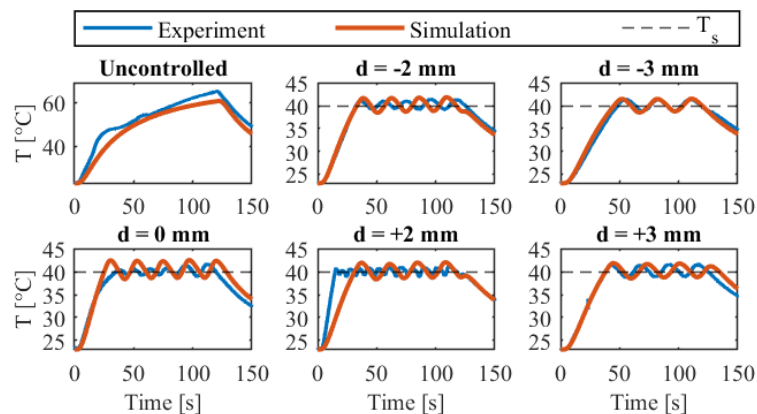


Fig. 2.2.7. Temporal evolutions for the controlled temperatures: comparison of experimental and simulation results.

Discussions:

According to the results, the developed numerical model can effectively simulate LA treatment and predict thermal maps and related thermal effects on the tissue. Moreover, it effectively deals with the lack of volumetric temperature information, which comes from the fact that FBG arrays are not able to provide accurate 3-dimensional temperature mapping.

Paper B confirms the main conclusions of Paper A that ON-OFF logic introduces oscillations (and related overshooting and undershooting) that affect controlling performance and related efficacy of the treatment. Moreover, as the results show, this disadvantage becomes more significant for the cases when the controlled distance (and the related thermal zone) needs to be bigger, or the tissue between the laser applicator and sensors has low thermal conductivity.

In addition, the results in this paper demonstrate that temperature response and overshooting are different for the same controlled distances in the forward and backward directions (+d and -d). This phenomenon can be explained by the fact that temperature rise behind the beam propagation direction is caused only by heat conduction and not by direct laser absorption. Therefore, it is clear that homogeneous laser irradiation in all directions from the applicator is needed. Moreover, it can reduce or avoid charring, carbonization, and valorization of the tissue near the bare tip of the applicator when high laser power is used.

Considering already discussed Papers A-B, it is clear that LA control is able to regulate the thermal damage for both cases: superficial and interstitial ablations. Moreover, the developed COMSOL model can be an effective tool to predict the laser-tissue interactions and to optimize input parameters before the actual procedure. Nevertheless, overshooting and undershooting of the control is still a significant disadvantage of the ON-OFF LA treatment.

Moreover, in case of a fast system response, which can happen in case of very close positioning of the laser applicator and the sensor, the laser will be switching on and off with a high frequency, which can be harmful to the equipment. The latter problem was solved in Papers A-B by introducing comparison frequency f_s (~ 2 Hz) at which measured temperature and set temperature were compared. Another solution that can be implemented can be the use of upper and lower set points for temperature control.

In general, an alternative controlling technique should be developed to reduce the over- and undershooting of the laser ablation of biological tissues. For instance, a few studies [90], [94] have been already investigating PID control for LA, but none of them considered quasi-distributed fiber sensors for PID-based control, which can be the future improvement of the proposed work for the optimal control of thermal effect during biological tissue LA.

2.3 Paper C: PID interstitial LA control

Paper Title: “PID Controlling Approach Based on FBG Array Measurements for Laser Ablation of Pancreatic Tissues” [3].

Paper Objective:

A further improvement of the control strategy to avoid ON-OFF-related oscillations can be based on PID control, which has been proven to be effective mostly for single-point measurement [90] and in adaptive control systems [113].

Considering the disadvantages of ON-OFF control mentioned in the previous sections, the need for a better controlling technique is clear to reduce collateral damage to healthy tissues and guarantee the proper treatment of the targeted region. Therefore, this work focused on the development of the setup and LabVIEW program for PID-based LA control based on one FBG array measurement. Again, COMSOL modeling was modified for PID pre-treatment optimization (P, I, and D gains, power, and the set temperature values).

The development of the COMSOL model was performed by my colleagues. My tasks were the creation of the LabVIEW program, experimental setup development, conduction of the experiments, and paper writing.

Methods:

The experimental setup shown in Fig.2.3.1 consists of one custom-made FBG array positioned parallel to the laser fiber inside the *ex vivo* pancreatic tissue. FBG array has 40 gratings, each grating has a 1.15 mm grating length, and an edge-to-edge distance of 0.05 mm.

The developed LabVIEW program has two main phases (Fig.2.3.3):

- (a) the input of preset parameters: set temperature T_{set} , PID gains, and d (distance between the grating with maximum temperature and the controlled grating);
- (b) start of ablation with constant power (3.3 W) until a threshold of 10 °C of temperature change is reached. Then, the position of the grating exposed to the maximum temperature (FBG_{max}) is saved and the position of the controlled grating (FBG_{con}) is calculated using d value. After, regulation of the controlled temperature (T_{con}) at the controlled grating (FBG_{con}) is performed using the PID approach. Finally, after 300 s of steady-state time (t_{ss}), the laser is switched off.

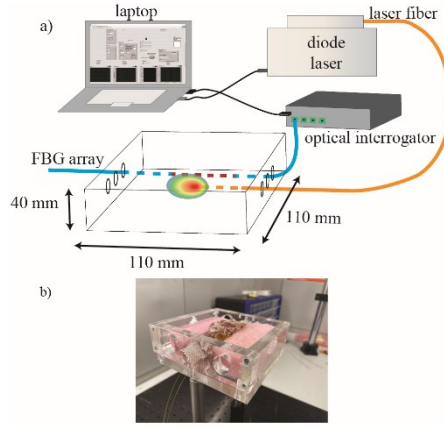


Fig. 2.3.1. Experimental setup of PID control of LA (a) Schematics: FBG array and laser fiber inserted in the pancreatic tissue positioned in custom-made plexiglass box; (b) photo of the setup

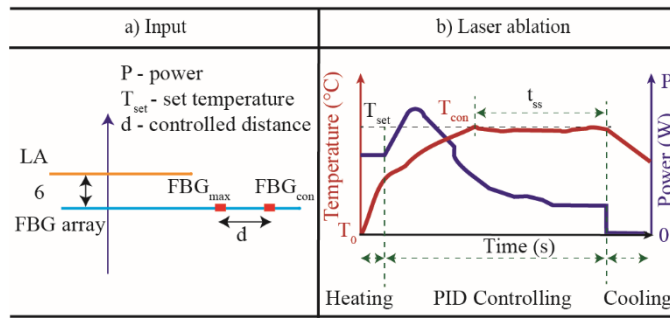


Fig. 2.3.2. PID-based temperature control: (a) input parameters: set temperature, controlled distance and power; (b) control logic consisting of three phases: heating, PID controlling, and cooling.

PID controller follows the equation:

$$C(t) = k_p \cdot (T_{set} - T_{con}) + k_i \cdot \int_0^t (T_{set} - T_{con}(\tau)) d\tau + k_d \cdot \frac{d(T_{set} - T_{con}(t))}{dt} \quad (2.3.1)$$

The PID controller maintains the temperature T_{con} (K) at the same value of the setpoint temperature T_{set} (K), upon a proper selection of the proportional k_p ($A \cdot K^{-1}$), integral k_i ($A \cdot K^{-1} \cdot s^{-1}$) and derivative k_d ($A \cdot s \cdot K^{-1}$) gain coefficients.

Results:

Numerical results

Initially, the COMSOL model was used to find optimal PID gains for each test using an iterative approach by testing different sets of gains. For example, Fig. 2.3.3. reports the results of PID optimization (5 sets of different gain values) for the set temperature of 43 °C, and the controlled distance of 10.8 mm. As can be seen, sets 1-3 experience abrupt changes in power (mainly maximum and minimum power are utilized) when the controlled temperature approaches the setpoint value (Fig. 2.3.3 b). Thus, some overshooting and very lethargic setpoint tracking can be observed with these gains. For set 5 (light blue curve in Fig. 2.3.3 a), when the integral gain is zero, as expected, the steady-state response is not able to reach the setpoint temperature.

Conversely, the gain parameters of set 4 ($k_p = 0.7 \text{ A}\cdot\text{K}^{-1}$, $k_i = 0.006 \text{ A}\cdot\text{K}^{-1}\cdot\text{s}^{-1}$ and $k_d = 0 \text{ A}\cdot\text{s}\cdot\text{K}^{-1}$) showed a smoother power profile and a thermal response characterized by a rise time of $\sim 350 \text{ s}$ and a smaller temperature overshoot of $\sim 1.8 \text{ }^\circ\text{C}$ (Fig. 2.3.3, green line). Therefore, these gains were used for the PID experiments.

Moreover, the COMSOL model was used to evaluate volumetric temperature distribution. Fig. 2.3.3. right reports two semicircles for the controlled distances equal to 10.8 mm and 7.2 mm. The ranges of the color bar correspond to (i) sublethal damage around $T \sim 43 \text{ }^\circ\text{C}$, (ii) instantaneous thermal damage for $T \geq 60 \text{ }^\circ\text{C}$, (iii) vapor diffusion and tissue desiccation at $T \geq 100 \text{ }^\circ\text{C}$, (iv) removal of tissue mass for $T \geq 300 \text{ }^\circ\text{C}$ [103]. As expected, an increase in the controlled distance leads to a bigger distribution of heat around the laser applicator.

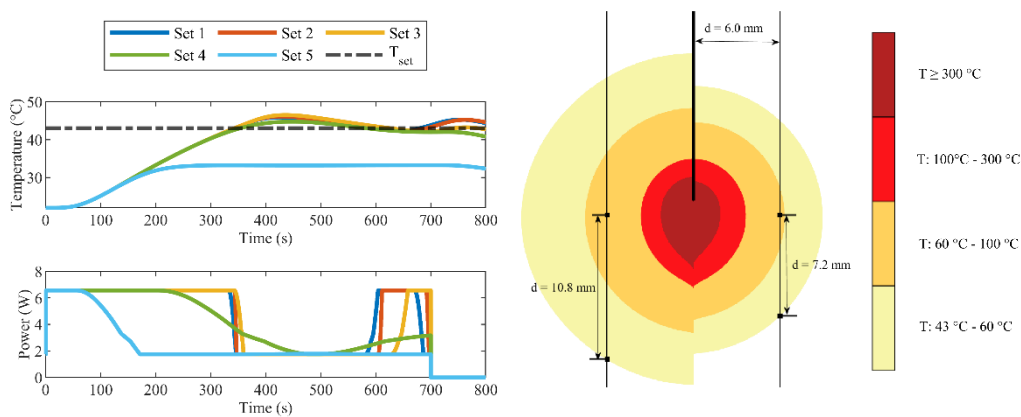


Fig. 2.3.3. (left) Simulated temperature and laser power profiles for the different sets of PID gain values. (right) simulated temperature distributions for controlled distance equal to $d = 10.8 \text{ mm}$ (left) and $d = 7.2 \text{ mm}$ (right).

Experimental results

The controlled temperature and related power during different sets of the experiments are shown in Fig. 2.3.4. For all cases, the developed LA regulation reaches the set temperature T_{set} after about 350 s of irradiation, and then maintained for $t_{\text{ss}} = 300 \text{ s}$. The abrupt increase of power can be seen at the stage transition: between the constant heating phase and PID control. The repeatability of the control logic can be seen in Fig. 2.3.4 (right): temperature reached T_{set} after approximately the same amount of time for all trials and maintained it for 300 s.

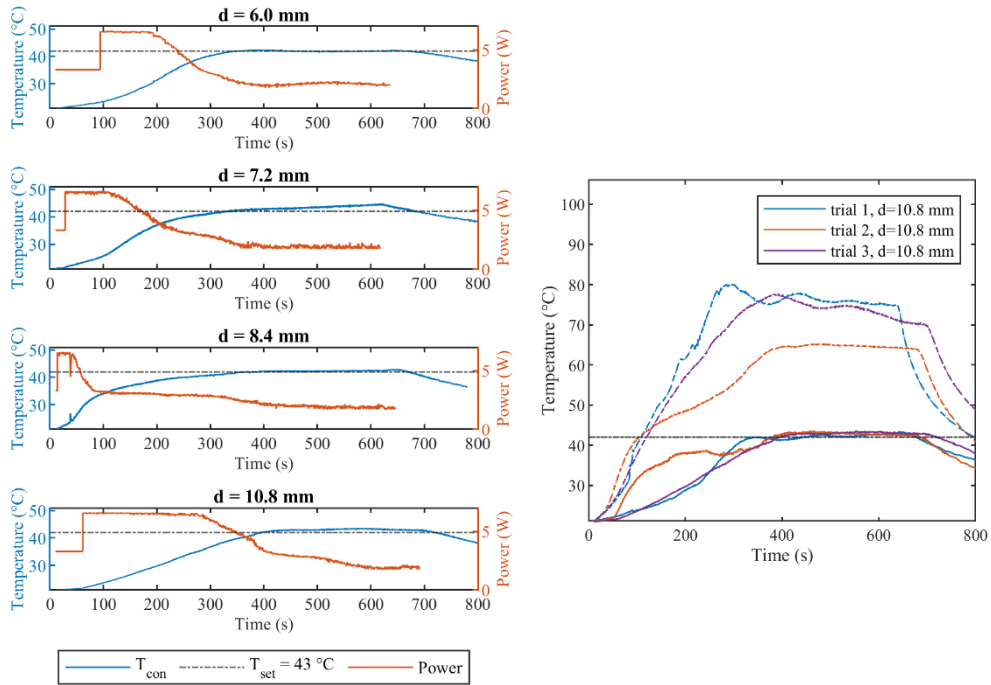


Fig. 2.3.4. (left) measured controlled temperature, set temperature (43 °C) and laser power profiles for different controlled distances; (right) measured maximum temperature profile and profiles measured by adjacent gratings for controlled distance of 10.8 mm.

The effect of LA control on the ablated region dimensions and irradiated energy is summarised in Table 2.3.1. The energy calculation was done by analyzing the laser power profile and the total duration of the ablation. As can be seen, the size of ablation was effectively controlled by changing the controlled distance, d .

TABLE 2.3.1. LA REGULATION RESULTS FOR DIFFERENT CONTROLLED DISTANCES

d (mm)	Time of PID regulation (s)	Energy (J)	Ablated dimensions (mm x mm)
6.0	541.7	1844	7.57×6.71
7.2	588.6	1943	12.07×8.03
8.4	631.8	1729	14.15×10.76
10.8	629.8	2695	17.39×14.11

2.4 Discussions

Discussions of Paper A-C:

The results validate the use of PID-control logic for LA regulation and prove that the FEM solver can be effectively used for pre-treatment optimization of the procedure parameters (power and PID gain values).

It is worth noting that according to Fig. 2.3.4 (left), power was close to the minimum power of the used laser diode (~ 1.0 W) when temperatures were maintained near the set temperature (steady-state zone). Therefore, if the set temperature used would be lower, it would be more difficult to maintain it and guarantee proper LA control. As a result, the main challenge of the current setup is the limited power range of the used laser. One of the possible solutions can be the use of a power attenuator. However, in this case, the maximum power possible for the whole system would be limited by the safe power margin of the attenuator.

Nevertheless, PID regulation can be considered as an optimal choice for LA control, which avoids the temperature oscillations effect inherent to ON-OFF control logic. Moreover, the laser switching at ON-OFF can lead to thermal relaxation of the tissue and have a completely different biological effect than continuous-wave ablation. Therefore, for future works PID control for LA regulation is preferable.

In general, fiber optic sensing for LA control provides main advantages such as immunity to electromagnetic interference, small laser energy absorption by the sensors, and small size. The conventional sensors can not provide such unique features needed for LA. For example, PID regulation using thermocouple was recently applied for LA regulation [90], but due to the laser energy absorption of thermocouple (and related overestimation) forced the authors to position a plastic plate between the laser fiber and the sensor. Obviously, the high invasiveness of a such setup makes it difficult to implement in a clinical scenario. Another example is work performed by Paiella *et al.* – clinical testing of interstitial laser thermotherapy with feedback-control based on thermistors measurements, that provide unsatisfactory results in terms of device handling, safety, and feasibility [96].

Thus, the limitations of convenient sensors observed in the literature encouraged the works performed in Papers A- C to investigate the use of fiber optic sensors for LA control. In parallel to these works, research on PID control based on FBG monitoring was performed for a laser-heated needle for biopsy tract ablation and showed promising results [114], [115]. Therefore, it is clear that fiber sensing can be an optimal tool well suited for LA purposes.

Nevertheless, one of the current limitations of fiber sensing use for thermal treatments is the temperature-strain cross-sensitivity that can lead to measurement artifacts. In Papers A-C these artifacts were minimized by using higher diameter needle for sensors placing (0.819 mm for needle vs. 145 μm for sensors). As a result, the sensors and tissue had slightly looser adhesion between each other, thus decreasing the strain effect [116], [117].

In order to significantly decrease the strain effect, a capillary made of glass or plastic needs to be used to encapsulate FBG arrays. On the other hand, the capillary can affect sensor dynamic response and absorb the part of the laser light during LA. Therefore, more research has to be performed to define the optimal trade-off between encapsulation of the array and the metrological properties of the sensor.

The results of Paper A-C show the need for homogeneous laser irradiation for proper temperature regulation and better heat distribution. In this regard, more investigation on the use of applicators with different irradiation profiles (bare fiber, diffuser, tapered tip) has to be performed. Other possible ways to improve LA control, can be the use of different nanoparticles to change the absorption properties of the region of ablation, and additional research on laser wavelength-tissue interaction with a possible introduction of multi-wavelength ablation or the use of several applicators in parallel for better treatment of cancer tissues.

Chapter 3. Measurements of intra-tissue parameters during LA

3.1 Paper D: TFBG RI sensitivity increase

Paper Title: “Optimization of cladding diameter for refractive index sensing in tilted fiber Bragg gratings” [4].

Paper Objective: During my studies, several works on fiber optics RI sensing and related biosensing were performed [118]–[121]. In this regard, it is clear that these investigations can find possible applications also for laser cancer treatment, such as a RI sensor to measure tissue changes (stemmed from the presence of the malignant tissues or tissue coagulation/carbonization) or cancer-related biosensing. One of the possible ways to improve sensitivity can be a chemical etching of the fiber. In this context, this work was focused on an experimental investigation of TFBG sensitivity increase due to chemical etching with an aim to define a trade-off between the wavelength and amplitude sensitivity of the cladding mode resonances and TFBG parameters: wavelength separation, sensor linearity, intensity level, and fiber thickness. In this work, two RI ranges were analyzed using step-wise etching and calibration in different sucrose solutions. The lower range corresponded to 1.34722 RIU - 1.34873 RIU (more suitable for possible biosensing) and the high RI range - 1.33679 RIU to 1.37078 RIU (for general RI sensing).

My tasks were experimental setup development, LUNA OBR 4600 measurements during RI calibration, data analysis, and paper writing. The fabrication of TFBG sensors, chemical etching of the fibers, and preparation of different sucrose concentrations were performed by my colleagues.

Methods:

The experimental setup consists of optical backscatter reflectometer LUNA OBR 4600 and a connected TFBG sensor with a gold reflector connected to the second end of the TFBG fiber. As a result of a such connection, the transmission spectrum of TFBG was reflected from the gold reflector, and the final "transmission-reflection" spectrum was measured by the reflectometer. Thus, it was possible to measure the TFBG cladding mode resonances and the core mode.

The etching procedure was following the technique discussed in the previous work [118]. The closed compartment (cylinder) fixed with rubber plugs at each end was used to perform etching (Hydrofluoric (HF) solution inside the container) and RI calibration (different sucrose solutions in the container). After each step, the sensor was rinsed in distilled water. The experimental setup is shown in Fig.3.1.1.

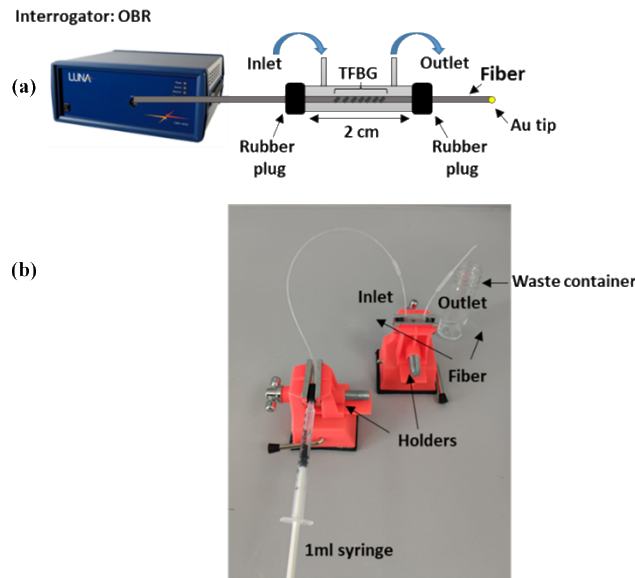


Fig. 3.1.1. Experimental setup for TFBG etching and RI calibration: the sensor was immersed in a closed container with different sucrose concentrations (during RI calibration) and HF solution (during etching). (a) schematics of the setup; (b) photo of the setup: a 1 ml syringe was used to inject the sample to the container.

Results:

The TFBG spectrum changes after each etching step are reported in Fig. 3.1.2 (with an offset for clarity of the image). The fiber diameter was reduced by etching from 125 μm to 13 μm . More etching leads to a decrease in the number of cladding mode resonances due to the mode escaping to the surrounding medium. For diameters less than 40 μm , most of the cladding mode resonances are no longer distinguishable, and only a few modes in the range of 1590 nm – 1605 nm can be seen.

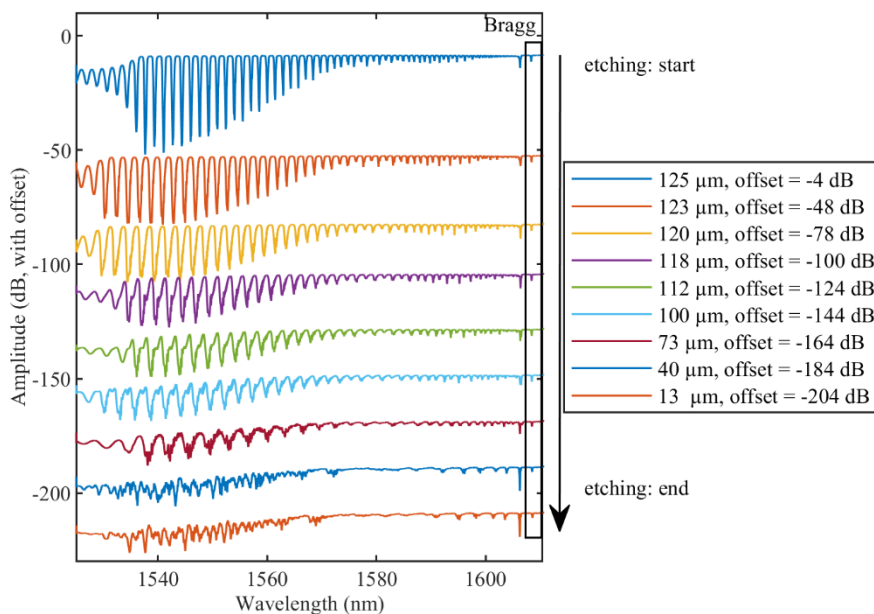


Fig. 3.1.2. TFBG spectra changes during chemical etching of the fiber. Rectangle highlight the core mode of the TFBG. Offset has been introduced for clarity of spectra plotting on one graph.

Etching leads to changes in the spectral amplitude of the cladding mode

resonances (Fig. 3.1.3 left): the minimum amplitude decreases from -53.3 dB to -22 dB for a 73 μm diameter. When fiber diameters of 40 μm and 13 μm are reached, just a few modes close to the Bragg wavelength can be measured and their intensity is roughly -8 dB.

Also, etching leads to an increase in the wavelength span between adjacent dips (Fig. 3.1.3 right); this effect of etching is in accordance with [122]. The wavelength spans between the dips increase from 1 nm to 3 nm for unetched TFBGs and fiber diameters of 73 μm , respectively.

Also, the spectral quality significantly deteriorates: cladding mode resonances become poorly defined (especially high-order modes - at shorter wavelengths), which can be possibly explained by the increase of the surface roughness after etching [122].

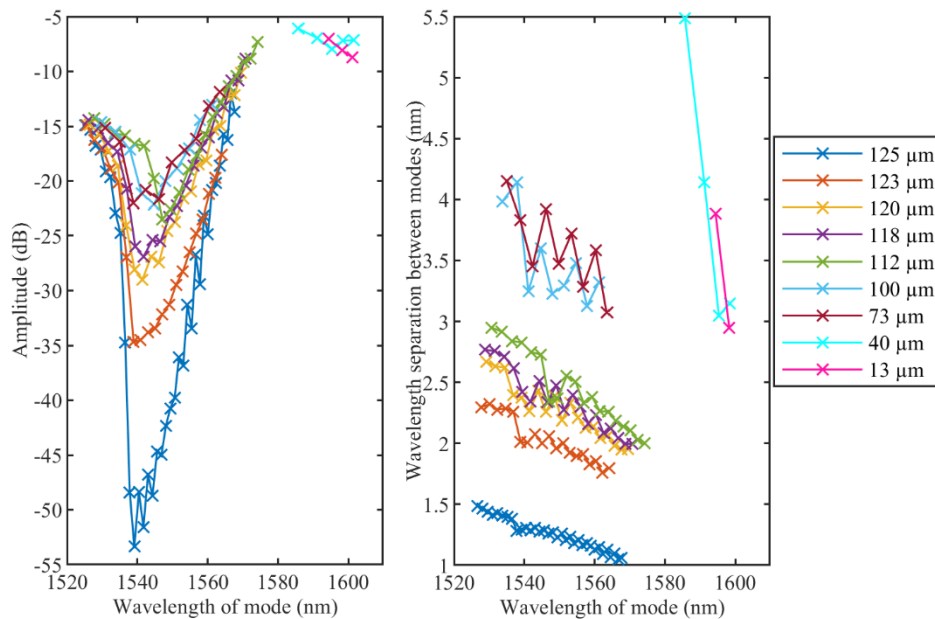


Fig. 3.1.3. Evolution of amplitude levels (left figure) and wavelength spans (right figure) of cladding modes during etching process. Only modes that are distinguishable for both RI variation ranges are illustrated.

The effect of etching on amplitude and wavelength sensitivity of the cladding mode resonances is reported in Fig. 3.1.4 (high RI range) and Fig. 3.1.5 (low RI range). The cladding mode resonances that have sensitivity with linearity higher than 0.9 ($R^2 > 0.9$) are labeled by dot markers. The maximum amplitude sensitivities were 1008 dB/RIU (high RI range) and 8160 dB/RIU (low RI range) for unetched TFBG. With more etching, the amplitude sensitivity of the cladding mode resonances decreases.

It is important to highlight the specificity of sensing: for the high RI range, only several cladding mode resonances (1543 nm and 1547 nm) have high sensitivity and good linearity, while only one cladding mode resonance at 1543 nm has high amplitude sensitivity for low the RI range. It can be explained by the fact that resonances with the effective refractive index closer to the surrounding refractive

index are the most sensitive. Regarding wavelength sensitivity of the cladding mode resonances, for the high RI range – the maximum sensitivity is 38.8 nm/RIU (at a 100 μm diameter), and for the low RI range - 156 nm/RIU (at a 40 μm diameter).

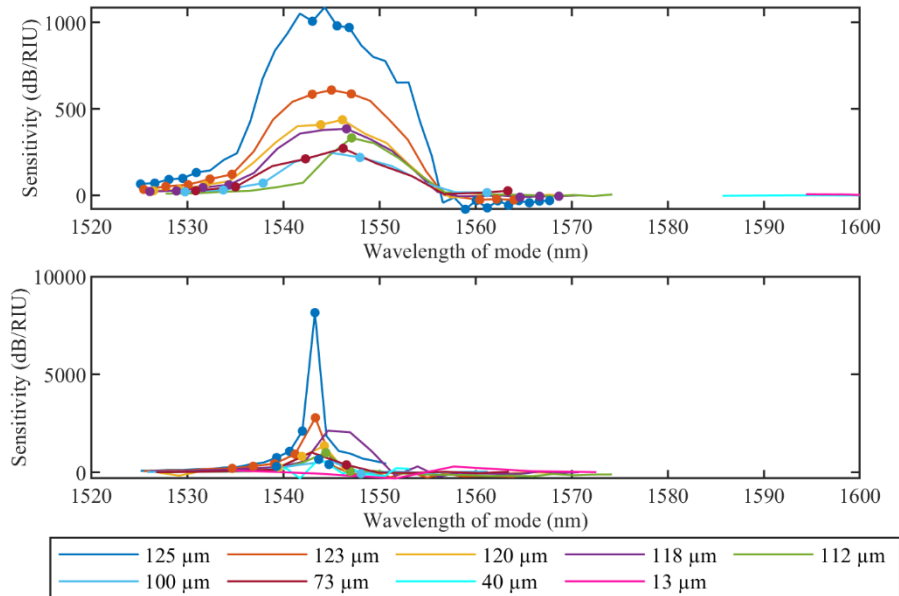


Fig. 3.1.4. Effect of chemical etching on TFBG amplitude sensitivity for: (a) high RI range (1.33679 RIU to 1.37078 RIU); and (b) low RI range (1.34722 RIU to 1.34873 RIU). Dot markers show the modes with sensitivity higher than 0.9 ($R_2 > 0.9$).

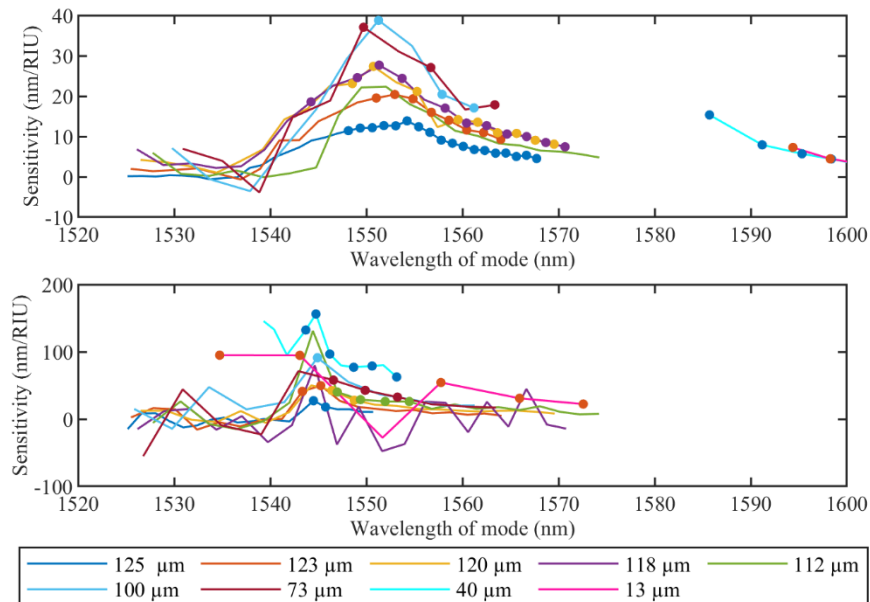


Fig. 3.1.5. Effect of chemical etching on TFBG wavelength sensitivity for: (a) high RI range (1.33679 RIU to 1.37078 RIU); and (b) low RI range (1.34722 RIU to 1.34873 RIU). Dot markers show the modes with sensitivity higher than 0.9 ($R_2 > 0.9$).

Discussion:

The experimental investigation results demonstrate that etching is not effective to increase the amplitude sensitivity of TFBG. However, it can increase the wavelength sensitivity if the optimal etching diameter will be reached (100 μm and 40 μm for the low and high RI ranges used in Paper D). The performed experimental optimization is not universal for all RI ranges: different RI ranges will correspond to different optimal diameters and sensitivities.

Several methods for RI sensing can be utilized. In this work, the cladding mode resonances tracking (also called peak tracking in this paper) was applied. Other works report the envelope-tracking method based on the measurement of the cladding mode resonances comb (the area between upper and lower envelopes) [123][124]. However, this method is more suitable for high RI range variation (which, by the way, will be observed in Paper E) and not effective for small RI ranges (as in Paper D) since for small RI variations only several cladding mode resonances are exposed to amplitude changes and the total envelope area is not changed significantly. In addition, this phenomenon is more clear for etched TFBGs due to the amplitude sensitivity decrease (reported in Fig. 3.1.4). Considering that biosensing is gaining more popularity and it is usually associated with small RI ranges [118], [125], [126], an efficient method suitable for small RI range variations has high importance (peak tracking in Paper D).

Another conventional method for RI measurements with TFBG relies on tracking cladding mode resonances close to the cut-off region, where the mode effective index is close to the RI value of the surrounding medium. However, this approach also proved to be ineffective for etched TFBGs due to the wavelength span increase with etching and related decrease of the amount the resonances (shown in Fig. 3.1.3). As a result, it becomes more challenging to find a mode near the cut-off for a wide range of SRI values. Therefore, the cladding mode resonances tracking is an optimal tool for the setup and applications of Paper D.

The results show that the high RI range has a smaller wavelength and amplitude sensitivity. It can be explained by the fact that for higher RI values, more and more high-order cladding modes become lossy (not distinguishable on the spectrum). Therefore, only low-order modes (positioned closer to the core mode) are visible for all values in the high RI range. The analysis of such modes results in low sensitivities because low-order modes are positioned far from the cut-off and have lower sensitivities.

In this work, wavelength sensitivity can be considered more important than amplitude sensitivity. The main reasons for it are the robustness of this wavelength detection approach. Indeed, amplitude detection can be affected by fluctuations of the light source, fiber bendings, and different attenuation effects.

In this regard, the etching of TFBG allowed approximately 4 times wavelength sensitivity increase for a quite large fiber diameter ($\sim 100 \mu\text{m}$), which does not compromise significantly the mechanical properties of the sensor. With the help

of the figures and outcome of this work, an optimal fiber diameter can be chosen as a function of the desired sensitivity, so the sensor design can be adapted accordingly to the project specifications.

3.2 Paper E: TFBG measurements during laser ablation

Paper Title: “Tilted fiber Bragg grating measurements during laser ablation of hepatic tissues: quasi-distributed temperature reconstruction and cladding mode resonances analysis” [5].

Paper Objective: Considering works focused on fiber sensing during thermal treatments performed during the Ph.D. study and analysis done in Paper D, the idea of TFBG application for laser ablation worth to be investigated. In addition, recent works investigated TFBG applications as a laser guiding device and the point sensor at the same time [6]. In this regard, the objectives of Paper E were the investigation of other sensing modalities of TFBG: RI sensing, different techniques for the core mode tracking and quasi-distributed temperature measurements [5].

For this reason, TFBG temperature and RI calibration (in different sucrose concentrations) were performed. For temperature measurements during LA three methods for the core mode tracking (maximum tracking, X-dB Bandwidth, and centroid methods) were utilized. In addition, an innovative method for temperature profile measurement along TFBG (quasi-distributed measurements) was proposed.

For this investigation, my work was focused on the development of the LabVIEW program for fiber sensing and laser diode regulation, experimental setup development, conduction of the experiments, the development of the TFBG temperature profile reconstruction algorithm, and paper writing.

Methods:

The developed system consists of the laser diode and the Micron Optics interrogator, both connected to a computer where a custom-made LabVIEW program was used to start laser ablation of healthy porcine liver tissue and perform monitoring of the FBG array and TFBG spectra.

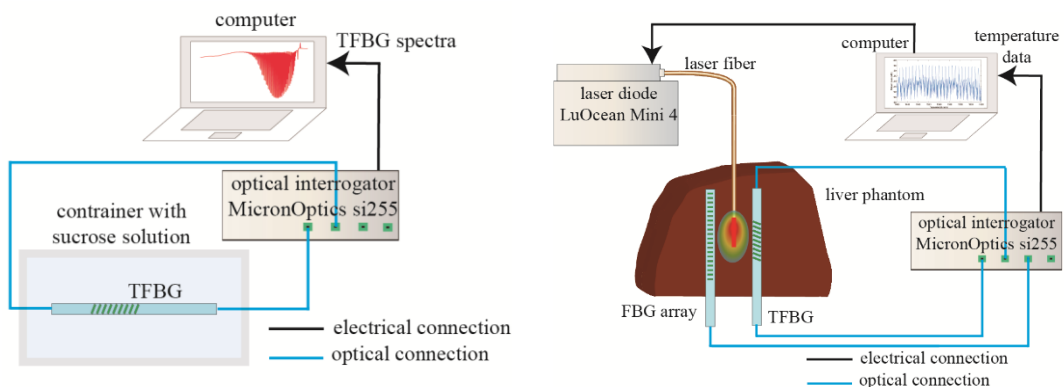


Fig. 3.2.1. (left) Schematics of setup for TFBG calibration in the container with different sucrose solutions (12 % - 60 %); (right) Schematics of setup for LA ablation: TFBG sensor and FBG array were positioned at a 2 mm distance from the applicator on the half of the ex vivo liver; the second half of liver covers sensors and applicator in a “sandwich” approach.

Commercially available TFBG (Technica Optical Components, Atlanta, USA) with an 8° tilt angle, a 10 mm grating length, and the custom-made FBG array of 40 gratings (grating length is 1.15 mm, edge-to-edge distance is 0.05 mm) were used. The TFBG core-to-core Bragg resonance was calibrated in the range from 34 °C - 50 °C, the resulting sensitivity is $(7.05 \pm 0.01) \times 10^{-6} \text{ } ^\circ\text{C}^{-1}$. RI calibration was performed in different sucrose concentrations: 0 % to 60 % with a step of 6 % that corresponds to the 1.333 RIU - 1.4419 RIU range, which is typical for biological tissues [127], [128]. For this RI calibration, due to the high RI range, the envelope method was applied. An example of the envelope areas in different sucrose concentrations is given in Fig 3.2.3: envelope areas of $A=1$ and $A=0.1657$ correspond to 0 % to 60 % concentrations.

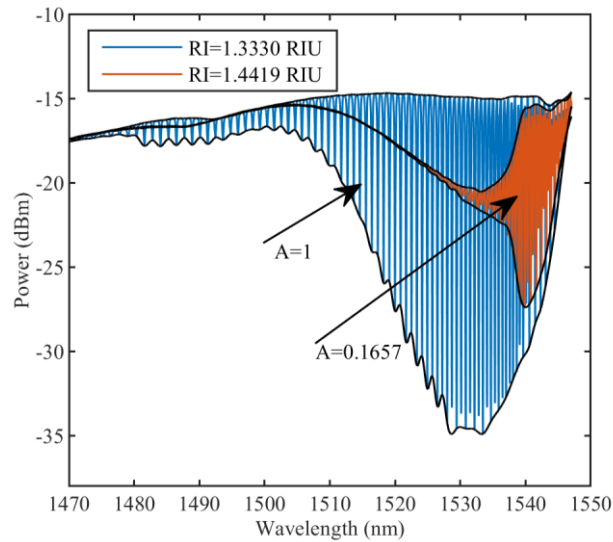


Fig. 3.2.3. TFBG cladding mode resonances combs for water (blue line, RI = 1.333 RIU) and a 60 % sucrose solution (red line, RI = 1.4419 RIU); related normalized area A decreases from 1.00 (reference value, RI = 1.333 RIU) to 0.1657 (RI=1.4419 RIU).

Core mode: conventional peak tracking methods

Temperature measurements by TFBG core mode tracking utilized 3 techniques: maximum tracking, X-dB Bandwidth, and centroid [129]. The maximum tracking technique tracks the maximum amplitude value of the core-to-core Bragg resonance. X-dB Bandwidth tracks the center of the inner bandwidth, which is defined as X dB below the maximum value.

For the centroid method, the Bragg wavelength is estimated as the center of the mass of the FBG reflection spectrum:

$$\lambda_{B,e} = \frac{\sum_n \lambda_n \times R(\lambda_n)}{\sum_n R(\lambda_n)} \quad (\text{Eq. 3.2.1})$$

where index n sweeps the main portion of the core mode spectrum.

Core mode: reconstruction algorithm

Since the core-to-core Bragg resonance tracking measurements provide only point temperature information (at the TFBG center), a need to obtain spatial temperature information is important for effective LA monitoring. In this regard, we propose to use the algorithm based on CFBG reconstruction devised in our

previous works [130], [131]

The main principle is the following: the spectrum (for this work it is the core-to-core Bragg resonance of TFBG) is modeled as an array of FBGs, where each FBG is modeled using coupled mode theory [79]. Then, iterative optimization is used to minimize the difference between the real measured TFBG spectrum and the TFBG modeled spectra perturbed by a set of different Gaussian temperature profiles. Afterward, the temperature profile, which corresponds to the smallest mismatch, is defined as temperature along the TFBG.

Results:

Calibration of TFBG sensor for different RI

Fig. 3.2.4 reports the results of RI calibration of TFBG for the RI range of 1.333 RIU - 1.4419 RIU (sucrose concentration range 0 % - 60 %). The comb of cladding mode resonances (envelope area) decreases significantly for higher RI values, and for 60 % concentration, the cut-off region starts near 1530 nm due to the lossy behavior of the high-order modes at this concentration. The analysis of envelopes measured between 1470 nm and 1547 nm for different concentrations is reported in Fig. 3.2.4 right and is similar to the calibration results of [123].

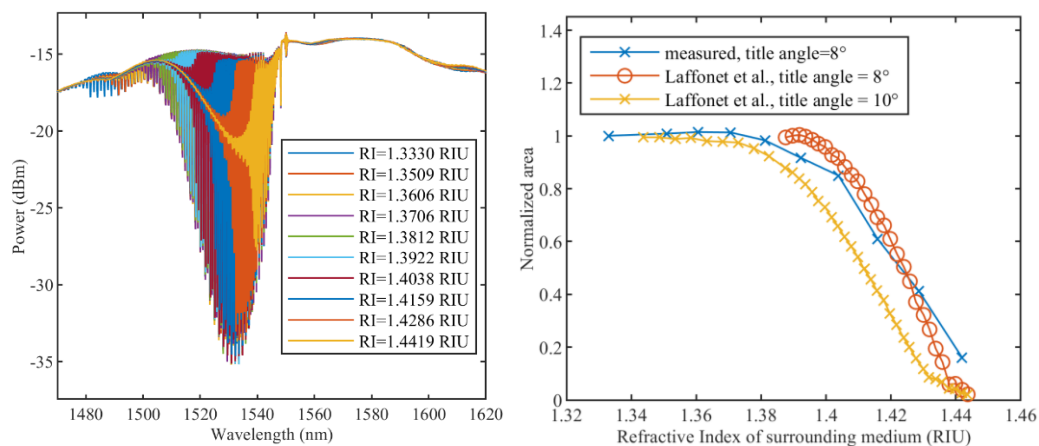


Fig. 3.2.4. (left) TFBG spectra measured in different sucrose concentrations; (right) comparison of the obtained results and the data presented in the work of Laffonet *et al.* [123]

Analysis of the cladding mode resonances during LA

The changes in envelope areas of the TFBG spectra during LA are presented in Fig. 3.2.5 for different time moments: at the start of ablation ($t=0$ s), after 90 s, and at the moment when the laser was switched off ($t=180$ s). The normalized area between two envelopes (left y-axis) and related temperature changes measured by the FBG array (right y-axis) are given in Fig. 3.2.5 bottom. As can be seen, the trend of temperature evolution can be approximately correlated with the changes in the normalized area.

Thus, ideally, we expect to obtain information about the maximum temperature from the minimum value of the normalized area. Moreover, after complete

cooling, the normalized area is expected to be correlated with the RI change of the ablated tissue.

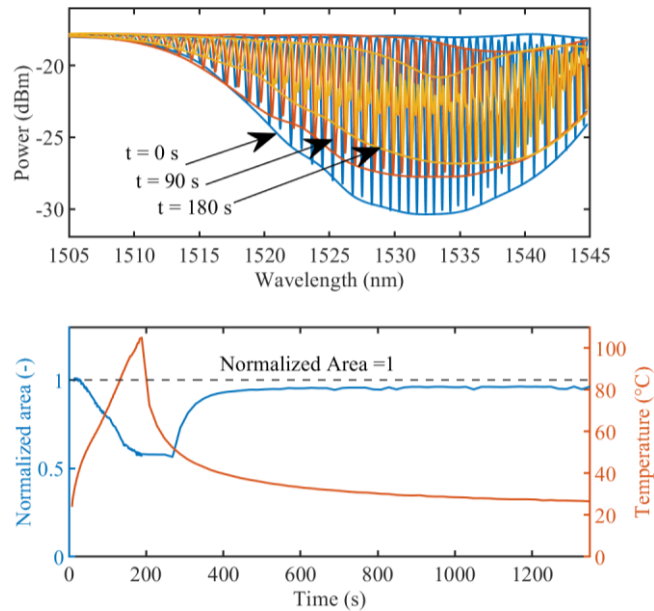


Fig. 3.2.5. (top) TFBG spectra at different time instances: before the laser ablation at $t=0$ s (blue color); at $t=90$ s (red color), and when laser was switched off $t=180$ s; (bottom) Normalized area evolution (left y-axis) and temperature measured by FBG array (right y-axis) during LA experiment.

In this regard, 25 trials of LA with FBG and TFBG measurements were performed to assess this hypothesis. Fig. 3.2.6 show the relation between maximum temperature measured by TFBG core-to-core mode resonance (using maximum peak tracking) and the related minimum value of the normalized area for each trial.

As expected, higher temperature leads to a smaller area between envelopes. Indeed, for the low maximum temperatures (~ 26 °C) the related normalized area is very close to 1 because there is no significant wavelength shift and no amplitudes decrease of the cladding mode resonances. However, due to the high value or RMSE between the fitting and the measured data (RMSE = 0.148), results show that the repeatability of the experimental trials is low and the temperature cannot be accurately correlated with the normalized area. Moreover, due to the high effect of temperature on the cladding comb, RI changes of the tissues after LA are challenging to measure too. The possible reasons for the low efficacy of cladding comb analysis during LA are provided in the discussion section. As a result, it is very challenging to obtain useful information about temperature and RI changes from the cladding comb analysis.

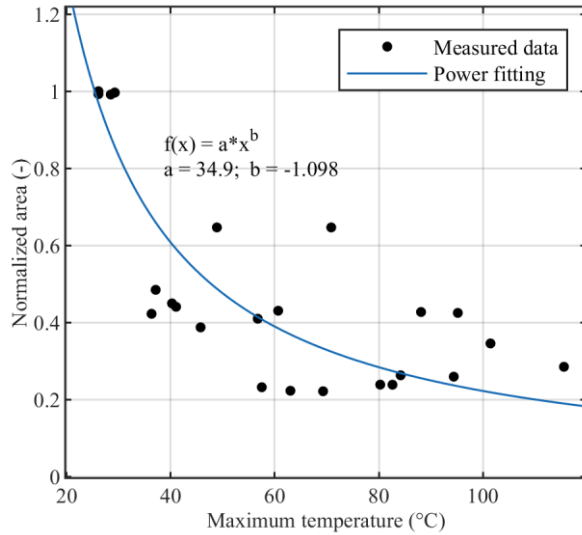


Fig. 3.2.6. Relation between maximum temperature measured by TFBG core-to-core mode analysis (using maximum peak tracking) and related minimum value of normalized area for each of 25 experimental trials. RMSE between data and fitting is 0.148.

Analysis of the core mode during LA

Fig. 3.2.7 top shows FBG array temperature measurements during one LA trial. After 180 s, the maximum temperature reaches 105.2 °C (measured by FBG array), while the TFBG core mode analysis provides: 80.9 °C measured by maximum peak tracking, 69.5 °C by X-dB Bandwidth, and 64.3 °C by the centroid method. The RMSE between maximum temperatures measured by FBG array and TFBG (maximum peak tracking) is 18.31 °C.

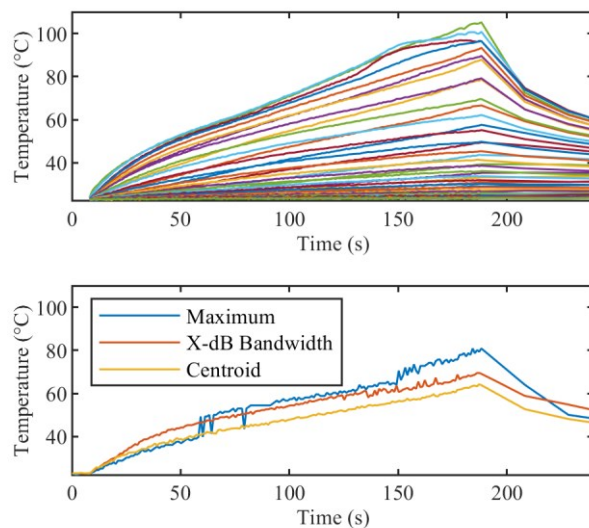


Fig. 3.2.7. (top) Temperature profiles measured by array of 40 FBGs during LA; (bottom) temperature reconstructed using analysis of core mode with direct peak-tracking techniques: maximum, X-dB Bandwidth (where X is -5 dB), centroid.

Fig. 3.2.8 and Fig. 3.2.9 report the results of the temperature profile along the TFBG using the proposed algorithm. Fig. 3.2.8 shows the temperature measured by the FBG array (dashed line) and temperature reconstructed along the TFBG (solid line) at different time moments. For this figure, to clearly illustrate the

algorithm's ability to reconstruct profile trends, TFBG temperature was normalized to the maximum temperature measured by the FBG array. Fig. 3.2.9 reports temperature evolution for both sensors during laser ablation of the tissue. The RMSE between the FBG array and TFBG measurements for three experiments is 7.8 ± 1.7 °C.

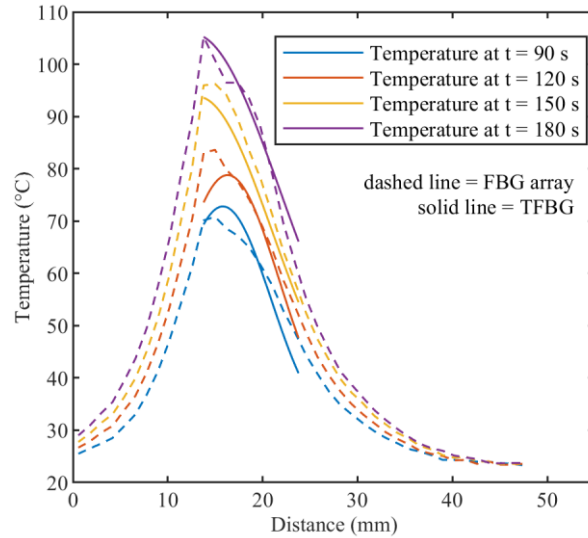


Fig. 3.2.8. Temperature measurements during LA at different time instances: dashed lines – FBG array measurements, solid lines – reconstructed TFBG temperature profiles (normalized).

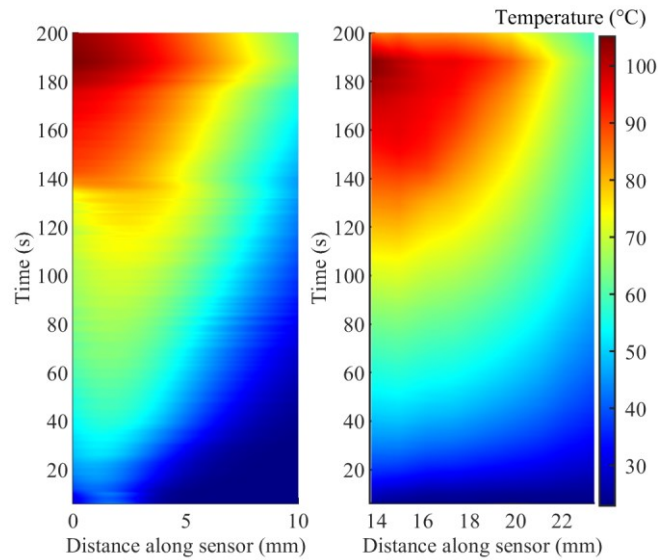


Fig. 3.2.9. Temperature measurements during LA: (a) FBG array; (b) TFBG temperature obtained by the proposed reconstruction algorithm. The RMSE between FBG array and TFBG profile measurements for three experiments is 7.8 ± 1.7 °C.

3.3 Discussion

As can be seen from the objective of the paper, the initial hypothesis of the investigation was to measure the RI change of the ablated tissue with the TFBG sensor. The planned approach was to track the cladding mode resonance (as in Paper D) and the core mode (using the peak tracking, X-dB, and centroid methods). Therefore, the idea was to compensate temperature effect on the cladding mode resonances by the value measured by the core mode tracking.

The experiments showed that during LA TFBG is exposed to high wavelength shifts and the appearance of leaky modes, which lead to significant changes in the cladding comb. Thus, the cladding mode resonances tracking was not possible. Indeed, it is in agreement with [123]: distinct temperature sensitivity of cladding modes leads not only to the shift of the cladding mode resonances but to the change of the shape of the TFBG spectrum under temperature elevation. Thus, the envelope method was utilized to measure the area between the upper and lower envelopes of the TFBG cladding resonances comb during LA.

However, the results show that temperature and RI information is not possible to accurately measure by the cladding comb analysis. The possible reasons can be inhomogeneity and structure of the tissue that does not allow ideal contact between the sensor surface and the tissue, the change of the TFBG surface after each experiment (even considering that TFBG was cleaned after each trial). Moreover, bending, strain, and humidity also have a cross-sensitivity effect on the shape of the TFBG spectrum [81], which makes RI measurements using the envelope method even more challenging.

As a result, we conclude that the main sensing modality of TFBG is temperature measurements based on the core mode analysis. The resulting RMSE of 7.8 ± 1.7 °C between TFBG profile reconstruction and FBG reference measurements can be mostly explained by the positioning of the sensors on the opposite sides of the diffuser and the high thermal gradients associated with LA. For future characterization of TFBG temperature measurements, the reference sensor and FBG should have the same exact placing, preferably in capillary or tubing to eliminate cross-sensitivity effects from other intra-tissue parameters.

The TFBG temperature sensor analyzed by conventional methods has several disadvantages over Rayleigh-based distributed sensing and FBG measurements: one-point measurement, averaging over the TFBG length (~ 1 cm), fragility (TFBG usually does not have a coating to allow coupling with leaky modes). However, a TFBG can be used as a sensor and a heat source, as proposed in a recent study [6]. In this regard, sensing modalities and capabilities of TFBG during LA need to be analyzed in detail, and this work can be considered a step toward such analysis.

Chapter 4. Discussion and future outlooks

Currently, the traditional treatments of cancer are surgical removal, chemotherapy, and radiation therapy [132]. However, some disadvantages limit the clinical applications of these approaches. For instance, surgical resection is associated with high invasiveness, long recovery time in hospital and rehabilitation, important associated costs, and the usual requirement of general anesthesia during the procedure [133]. Chemotherapy and radiation therapies have significant toxic side effects on the whole organism of the patient. As a result, different approaches have been proposed as alternatives to traditional tumor treatment methods.

One of them is the application of laser ablation - minimally-invasive photothermal therapy that utilizes a small flexible optical fiber to transport laser light into the targeted tissue. The main advantages of using optical fiber as a minimally-invasive applicator are flexibility and immunity of the applicator to electromagnetic interference. However, LA has a smaller volume of ablation region in comparison with other minimal-invasive ablation techniques [52].

As a result, the main clinical interest is in MRI/CT compatibility and the small size and flexibility of the applicator. However, the high cost of MRI/CT equipment and not widespread use of them as assistive tools for thermal treatments lead to a smaller commercial interest in LA development. Therefore, it is crucial to focus on the optimization of LA in its niche where minimal invasiveness of LA plays a crucial role (brain, prostate, pancreas). One of the possible optimization methods is the use of optical fibers not only to guide laser light but also to measure intra-tissue parameters during the treatment.

In this context, this thesis describes the possible use of fiber optic sensing for monitoring and controlling of LA. The main sensing technique for the developed LA control is FBG arrays – cheap and effective tool for temperature monitoring. Indeed, it has been already used for real-time monitoring [134], [135] or in combination with data-assimilation models to improve thermal mapping or prediction of temperature evolution [136]. In Chapter 2 custom-made highly dense FBG arrays optimized for LA are used for ON-OFF and PID temperature regulation.

One of the main limitations of FBG sensing is the temperature-strain cross-sensitivity that can lead to measurement artifacts. The possible solution can be the use of capillary to encapsulate fiber sensors and avoid strain and bending effect on it. However, the effect on sensor dynamic response and laser light absorption of capillary, and increase of invasiveness should be investigated in future works.

Another disadvantage of fiber sensing is the need to insert FBG sensors near the ablated region and the related increase of invasiveness of the treatment. In this regard, several techniques can be investigated in detail to use a fiber optic probe

able to both deliver the laser light and measure temperature. Several approaches are possible: (1) sensing and the laser fiber are separate devices bundled in the capillary (the strain cross-sensitivity is avoided too due to capillary), (2) the sensor is glued outside the capillary with the laser fiber. However, the bundling of two devices in one capillary leads to a bigger size and higher fragility of the applicator.

Therefore, a more sophisticated option can be the use of self-monitored and laser-guided features in one optical device based on: (3) double-cladding fibers (FBGs are inscribed in the core, and the laser is guided in the inner cladding), or (4) application of TFBG with an absorptive coating as a miniature heat source with sensing capabilities proposed by Alqarni *et al.* [6]. In this case, the tilt angle of the grating leads to the light coupling to cladding modes and absorption of it by coating. Thus, this technique is not based on laser absorption by the tissue, but on heat transfer from the absorptive coating surface of TFBG. As a result, a very controlled localized heat increase can be achieved [6]. In this context, Papers D-E propose a good approach to measure point temperature (based on different peak tracking methods) or quasi-distributed profile (based on the proposed algorithm).

In general, the main future works should be focused on LA control using a “smart applicator” – the device incorporating the laser fiber and the sensor. Moreover, since Papers A – C showed that for proper thermal regulation homogeneous laser irradiation is preferable, more investigations on the use of laser fiber with different irradiation profiles (bare fiber, diffuser, tapered tip) have to be performed.

Considering general future outlooks, it is important to highlight the need of standardization for thermal therapies in general, phototherapies, and specifically laser ablation to avoid misunderstanding of terminology and main concepts in the fields. Especially this problem become more essential for communication between clinicians, researchers, engineers, and technicians. A good example and reference guidance can be the work done for the standardization of image-guided tumor ablation [55], [137], and the most recent one in 2014 summarizing a 10-year update [138], where aspects of the field were standardized from the clinical point of view.

Bibliography

- [1] S. Korganbayev *et al.*, “Closed-loop temperature control based on fiber bragg grating sensors for laser ablation of hepatic tissue,” *Sensors (Switzerland)*, vol. 20, no. 22, pp. 1–16, Nov. 2020, doi: 10.3390/s20226496.
- [2] L. Bianchi, S. Korganbayev, A. Orrico, M. De Landro, and P. Saccomandi, “Quasi-distributed fiber optic sensor-based control system for interstitial laser ablation of tissue: theoretical and experimental investigations,” *Biomed. Opt. Express*, vol. 12, no. 5, p. 2841, May 2021, doi: 10.1364/BOE.419541.
- [3] S. Korganbayev *et al.*, “PID Controlling Approach Based on FBG Array Measurements for Laser Ablation of Pancreatic Tissues,” *IEEE Trans. Instrum. Meas.*, vol. 70, pp. 1–9, 2021, doi: 10.1109/TIM.2021.3112790.
- [4] S. Korganbayev *et al.*, “Optimization of Cladding Diameter for Refractive Index Sensing in Tilted Fiber Bragg Gratings,” *Sensors*, vol. 22, no. 6, p. 2259, Mar. 2022, doi: 10.3390/s22062259.
- [5] S. Korganbayev, M. De Landro, A. Wolf, D. Tosi, and P. Saccomandi, “Tilted fiber Bragg grating measurements during laser ablation of hepatic tissues: quasi-distributed temperature reconstruction and cladding mode resonances analysis,” *IEEE Sens. J.*, vol. 22, no. 16, pp. 15999–16007, 2022.
- [6] S. A. Alqarni, W. G. Willmore, J. Albert, and C. W. Smelser, “Self-monitored and optically powered fiber-optic device for localized hyperthermia and controlled cell death in vitro,” *Appl. Opt.*, vol. 60, no. 8, pp. 2400–2411, 2021.
- [7] M. R. Hamblin and Y. Huang, *Handbook of photomedicine*. Taylor & Francis, 2013.
- [8] T. P. Pivetta, C. E. A. Botteon, P. A. Ribeiro, P. D. Marcato, and M. Raposo, “Nanoparticle systems for cancer phototherapy: an overview,” *Nanomaterials*, vol. 11, no. 11, p. 3132, 2021.
- [9] F. Zhou, R. E. Nordquist, and W. R. Chen, “Photonics immunotherapy—a novel strategy for cancer treatment,” *J. Innov. Opt. Health Sci.*, vol. 9, no. 01, p. 1630001, 2016.
- [10] K. Plaetzer, B. Krammer, J. Berlanda, F. Berr, and T. Kiesslich, “Photophysics and photochemistry of photodynamic therapy: fundamental aspects,” *Lasers Med. Sci.*, vol. 24, no. 2, pp. 259–268, 2009.
- [11] H. S. Hwang, H. Shin, J. Han, and K. Na, “Combination of photodynamic therapy (PDT) and anti-tumor immunity in cancer therapy,” *J. Pharm. Investig.*, vol. 48, no. 2, pp. 143–151, 2018.
- [12] S. O. Gollnick, B. Owczarczak, and P. Maier, “Photodynamic therapy and anti-tumor immunity,” *Lasers Surg. Med. Off. J. Am. Soc. Laser Med. Surg.*, vol. 38, no. 5, pp. 509–515, 2006.
- [13] P. Agostinis *et al.*, “Photodynamic therapy of cancer: an update,” *CA. Cancer J. Clin.*, vol. 61, no. 4, pp. 250–281, 2011.
- [14] J. S. Dysart and M. S. Patterson, “Characterization of Photofrin photobleaching

for singlet oxygen dose estimation during photodynamic therapy of MLL cells in vitro,” *Phys. Med. Biol.*, vol. 50, no. 11, p. 2597, 2005.

- [15] C. M. Pacella and G. Mauri, *Image-guided laser ablation*. Springer, 2020.
- [16] E. Schena, P. Saccomandi, and Y. Fong, “Laser Ablation for Cancer: Past, Present and Future,” *J. Funct. Biomater.*, vol. 8, no. 2, p. 19, 2017, doi: 10.3390/jfb8020019.
- [17] A. Mukhopadhyaya *et al.*, “Localized hyperthermia combined with intratumoral dendritic cells induces systemic antitumor immunity,” *Cancer Res.*, vol. 67, no. 16, pp. 7798–7806, 2007.
- [18] R. W. Y. Habash, R. Bansal, D. Krewski, and H. T. Alhafid, “Thermal therapy, part 1: an introduction to thermal therapy,” *Crit. Rev. Biomed. Eng.*, vol. 34, no. 6, 2006.
- [19] M. M. Paulides *et al.*, “The clinical feasibility of deep hyperthermia treatment in the head and neck: new challenges for positioning and temperature measurement,” *Phys. Med. Biol.*, vol. 55, no. 9, p. 2465, 2010.
- [20] A. V. Suvernev, G. V. Ivanov, A. V. Efremov, and R. Tchervov, “Whole body hypothermia at 43.5–44 C,” in *Hyperthermia in Cancer Treatment: A Primer*, Springer, 2006, pp. 227–236.
- [21] M. Ahmed, C. L. Brace, F. T. Lee, and S. N. Goldberg, “Principles of and advances in percutaneous ablation,” *Radiology*, vol. 258, no. 2, pp. 351–369, Feb. 2011, doi: 10.1148/radiol.10081634.
- [22] P. Saccomandi, E. Schena, M. Diana, J. Marescaux, and G. Costamagna, “Thermal treatments of tumors: Principles and methods,” in *Biomedical Engineering Challenges: A Chemical Engineering Insight*, 2018, pp. 199–228.
- [23] T. W. I. Clark, “Chemical Ablation of Liver Cancer,” *Tech. Vasc. Interv. Radiol.*, vol. 10, no. 1, pp. 58–63, 2007, doi: 10.1053/j.tvir.2007.08.004.
- [24] J. J. Wendler *et al.*, “Irreversible electroporation (Ire): Standardization of terminology and reporting criteria for analysis and comparison,” *Polish J. Radiol.*, vol. 81, pp. 54–64, 2016, doi: 10.12659/PJR.896034.
- [25] C.-Y. Hsiao and K.-W. Huang, “Irreversible electroporation: a novel ultrasound-guided modality for non-thermal tumor ablation,” *J. Med. Ultrasound*, vol. 25, no. 4, pp. 195–200, 2017.
- [26] C. L. Brace, “Radiofrequency and Microwave Ablation of the Liver, Lung, Kidney, and Bone: What Are the Differences?,” *Curr. Probl. Diagn. Radiol.*, vol. 38, no. 3, pp. 135–143, 2009, doi: 10.1067/j.cpradiol.2007.10.001.
- [27] S. N. Goldberg, “Radiofrequency Tumor Ablation: Principles and Techniques,” in *Multi-Treatment Modalities of Liver Tumours*, Boston, MA: Springer US, 2002, pp. 87–118.
- [28] M. G. Lubner, C. L. Brace, J. L. Hinshaw, and F. T. Lee, “Microwave tumor ablation: Mechanism of action, clinical results, and devices,” *J. Vasc. Interv. Radiol.*, vol. 21, no. SUPPL. 8, pp. S192–S203, 2010, doi: 10.1016/j.jvir.2010.04.007.
- [29] R. J. Stafford, D. Fuentes, A. A. Elliott, J. S. Weinberg, and K. Ahrar, “Laser-Induced Thermal Therapy for Tumor Ablation,” *Crit. Rev. Biomed. Eng.*, vol. 38, no. 1,

pp. 79–100, 2010, doi: 10.1615/CritRevBiomedEng.v38.i1.70.

[30] J. G. Baust, A. A. Gage, T. E. Bjerklund Johansen, and J. M. Baust, “Mechanisms of cryoablation: Clinical consequences on malignant tumors,” *Cryobiology*, vol. 68, no. 1, pp. 1–11, 2014, doi: 10.1016/j.cryobiol.2013.11.001.

[31] Y.-F. Zhou, “High intensity focused ultrasound in clinical tumor ablation,” *World J. Clin. Oncol.*, vol. 2, no. 1, p. 8, 2011, doi: 10.5306/wjco.v2.i1.8.

[32] A. Mohammadi, L. Bianchi, S. Korganbayev, M. De Landro, and P. Saccomandi, “Thermomechanical Modeling of Laser Ablation Therapy of Tumors: Sensitivity Analysis and Optimization of Influential Variables,” *IEEE Trans. Biomed. Eng.*, vol. 69, no. 1, pp. 1–1, Jan. 2022, doi: 10.1109/TBME.2021.3092889.

[33] N. D. Schulmann, M. Soltani-Sarvestani, M. De Landro, S. Korganbayev, S. Cotin, and P. Saccomandi, “Model-Based Thermometry for Laser Ablation Procedure Using Kalman Filters and Sparse Temperature Measurements,” *IEEE Trans. Biomed. Eng.*, pp. 1–1, 2022, doi: 10.1109/TBME.2022.3155574.

[34] F. Morra *et al.*, “Spatially resolved thermometry during laser ablation in tissues: Distributed and quasi-distributed fiber optic-based sensing,” *Opt. Fiber Technol.*, vol. 58, p. 102295, Sep. 2020, doi: 10.1016/j.yofte.2020.102295.

[35] S. Korganbayev, M. De Landro, F. Morra, A. Cigada, and P. Saccomandi, “Fiber Optic Sensors for Distributed and Quasi-distributed Temperature Measurement,” in *Proceedings of IEEE Sensors*, Oct. 2020, vol. 2020-October, pp. 1–4, doi: 10.1109/SENSOR47125.2020.9278937.

[36] M. de Landro *et al.*, “Magnetic resonance-based measurement system: comparison of 2D and 3D echo-planar imaging sequences for thermometry application,” in *2021 IEEE International Instrumentation and Measurement Technology Conference (I2MTC)*, May 2021, vol. 2021-May, pp. 1–6, doi: 10.1109/I2MTC50364.2021.9460088.

[37] S. Korganbayev *et al.*, “Highly dense FBG arrays for millimeter-scale thermal monitoring during nanocomposite-enhanced laser ablation,” in *Optical Sensing and Detection VI*, Apr. 2020, vol. 11354, p. 19, doi: 10.1117/12.2555436.

[38] S. Korganbayev *et al.*, “Measurement of Enhanced Photothermal Effects of CuO-encapsulated Polymeric Nanospheres,” in *2021 IEEE International Symposium on Medical Measurements and Applications (MeMeA)*, Jun. 2021, pp. 1–5, doi: 10.1109/MeMeA52024.2021.9478675.

[39] I. Maor *et al.*, “Laser-induced thermal response and controlled release of copper oxide nanoparticles from multifunctional polymeric nanocarriers,” *Sci. Technol. Adv. Mater.*, vol. 22, no. 1, pp. 218–233, Dec. 2021, doi: 10.1080/14686996.2021.1883406.

[40] S. Asadi *et al.*, “Experimental Evaluation of Radiation Response and Thermal Properties of NPs-Loaded Tissues-Mimicking Phantoms,” *Nanomaterials*, vol. 12, no. 6, p. 945, Mar. 2022, doi: 10.3390/nano12060945.

[41] A. Gangi, H. Alizadeh, L. Wong, X. Buy, J. L. Dietemann, and C. Roy, “Osteoid osteoma: Percutaneous laser ablation and follow-up in 114 patients,” *Radiology*, vol. 242, no. 1, pp. 293–301, 2007, doi: 10.1148/radiol.2421041404.

[42] C. M. Pacella *et al.*, “Thyroid tissue: US-guided percutaneous interstitial laser

ablation - A feasibility study," *Radiology*, vol. 217, no. 3, pp. 673–677, 2000, doi: 10.1148/radiology.217.3.r00dc09673.

[43] T. J. Vogl, R. Straub, K. Eichler, O. Söllner, and M. G. Mack, "Colorectal Carcinoma Metastases in Liver: Laser-induced Interstitial Thermotherapy - Local Tumor Control Rate and Survival Data," *Radiology*, vol. 230, no. 2, pp. 450–458, Feb. 2004, doi: 10.1148/radiol.2302020646.

[44] F. Di Matteo *et al.*, "EUS-guided Nd:YAG laser ablation of normal pancreatic tissue: A pilot study in a pig model," *Gastrointest. Endosc.*, vol. 72, no. 2, pp. 358–363, 2010, doi: 10.1016/j.gie.2010.02.027.

[45] P. Saccomandi *et al.*, "Theoretical analysis and experimental evaluation of laser-induced interstitial thermotherapy in ex vivo porcine pancreas," *IEEE Trans. Biomed. Eng.*, vol. 59, no. 10, pp. 2958–2964, Oct. 2012, doi: 10.1109/TBME.2012.2210895.

[46] P. Saccomandi, A. Lapergola, F. Longo, E. Schena, and G. Quero, "Thermal ablation of pancreatic cancer: A systematic literature review of clinical practice and pre-clinical studies," *Int. J. Hyperth.*, vol. 35, no. 1, pp. 398–418, Dec. 2018, doi: 10.1080/02656736.2018.1506165.

[47] H. J. Schwarzmaier *et al.*, "MR-guided laser-induced interstitial thermotherapy of recurrent glioblastoma multiforme: Preliminary results in 16 patients," *Eur. J. Radiol.*, vol. 59, no. 2, pp. 208–215, 2006, doi: 10.1016/j.ejrad.2006.05.010.

[48] L. K. Swartz, K. G. Holste, M. M. Kim, A. Morikawa, and J. Heth, "Outcomes in Patients Treated with Laser Interstitial Thermal Therapy for Primary Brain Cancer and Brain Metastases," *Oncologist*, vol. 24, no. 12, pp. e1467–e1470, Dec. 2019, doi: 10.1634/theoncologist.2019-0213.

[49] R. Muschter, "<title>Laser-induced interstitial thermotherapy of benign prostatic hyperplasia and prostate cancer</title>," in *Medical Applications of Lasers II*, Dec. 1994, vol. 2327, pp. 287–292, doi: 10.1117/12.197575.

[50] J. A. S. Brookes, W. R. Lees, and S. G. Bown, "Interstitial laser photocoagulation for the treatment of lung cancer," *Am. J. Roentgenol.*, vol. 168, no. 2, pp. 357–358, Feb. 1997, doi: 10.2214/ajr.168.2.9016205.

[51] Y. Kerbage *et al.*, "Laser interstitial thermotherapy application for breast surgery: Current situation and new trends," *Breast*, vol. 33, pp. 145–152, Jun. 2017, doi: 10.1016/j.breast.2017.03.016.

[52] R. W. Y. Habash, R. Bansal, D. Krewski, and H. T. Alhafid, "Thermal therapy, Part III: ablation techniques," *Crit. Rev. Biomed. Eng.*, vol. 35, no. 1–2, 2007.

[53] E. Schena, D. Tosi, P. Saccomandi, E. Lewis, and T. Kim, "Fiber optic sensors for temperature monitoring during thermal treatments: An overview," *Sensors (Switzerland)*, vol. 16, no. 7, p. 1144, Jul. 2016, doi: 10.3390/s16071144.

[54] S. B. Solomon and S. G. Silverman, "Imaging in interventional oncology," *Radiology*, vol. 257, no. 3, pp. 624–640, 2010, doi: 10.1148/radiol.10081490.

[55] S. N. Goldberg *et al.*, "Image-guided tumor ablation: Standardization of terminology and reporting criteria," *Radiology*, vol. 235, no. 3, pp. 728–739, 2005, doi: 10.1148/radiol.2353042205.

[56] P. Saccomandi, E. Schena, and S. Silvestri, "Techniques for temperature

monitoring during laser-induced thermotherapy: An overview,” *Int. J. Hyperth.*, vol. 29, no. 7, pp. 609–619, Nov. 2013, doi: 10.3109/02656736.2013.832411.

[57] F. Fani, E. Schena, P. Saccomandi, and S. Silvestri, “CT-based thermometry: An overview,” *International Journal of Hyperthermia*, vol. 30, no. 4, pp. 219–227, 2014, doi: 10.3109/02656736.2014.922221.

[58] M. A. Lewis, R. M. Staruch, and R. Chopra, “Thermometry and ablation monitoring with ultrasound,” *International Journal of Hyperthermia*, vol. 31, no. 2, pp. 163–181, 2015, doi: 10.3109/02656736.2015.1009180.

[59] V. Rieke and K. B. Pauly, “MR thermometry,” *J. Magn. Reson. Imaging*, vol. 27, no. 2, pp. 376–390, 2008, doi: 10.1002/jmri.21265.

[60] B. Arnal, M. Pernot, and M. Tanter, “Monitoring of thermal ablation therapy based on shear modulus changes: Shear wave thermometry and shear wave lesion imaging,” *Proc. - IEEE Ultrason. Symp.*, vol. 58, no. 2, pp. 1522–1525, 2010, doi: 10.1109/ULTSYM.2010.5935503.

[61] N. Weiss *et al.*, “Temperature-density hysteresis in X-ray CT during HIFU thermal ablation: Heating and cooling phantom study,” *Int. J. Hyperth.*, vol. 30, no. 1, pp. 27–35, 2014, doi: 10.3109/02656736.2013.860241.

[62] N. Weiss, J. Sosna, S. N. Goldberg, and H. Azhari, “Non-invasive temperature monitoring and hyperthermic injury onset detection using X-ray CT during HIFU thermal treatment in ex vivo fatty tissue,” *Int. J. Hyperth.*, vol. 30, no. 2, pp. 119–125, 2014, doi: 10.3109/02656736.2014.883466.

[63] G. D. Pandeya *et al.*, “Feasibility of computed tomography based thermometry during interstitial laser heating in bovine liver,” *Eur. Radiol.*, vol. 21, no. 8, pp. 1733–1738, 2011, doi: 10.1007/s00330-011-2106-6.

[64] A. C. Steger, P. Shorvon, K. Walmsley, R. Chisholm, S. G. Bown, and W. R. Lees, “Ultrasound features of low power interstitial laser hyperthermia,” *Clin. Radiol.*, vol. 46, no. 2, pp. 88–93, Aug. 1992, doi: 10.1016/S0009-9260(05)80309-5.

[65] Z. Amin *et al.*, “Hepatic metastases: interstitial laser photocoagulation with real-time US monitoring and dynamic CT evaluation of treatment,” *Radiology*, vol. 187, no. 2, pp. 339–347, May 1993, doi: 10.1148/radiology.187.2.8475270.

[66] U. Techavipoo, T. Varghese, Q. Chen, T. A. Stiles, J. A. Zagzebski, and G. R. Frank, “Temperature dependence of ultrasonic propagation speed and attenuation in excised canine liver tissue measured using transmitted and reflected pulses,” *J. Acoust. Soc. Am.*, vol. 115, no. 6, pp. 2859–2865, Jun. 2004, doi: 10.1121/1.1738453.

[67] M. A. Lewis, R. M. Staruch, and R. Chopra, “Thermometry and ablation monitoring with ultrasound,” *Int. J. Hyperth.*, vol. 31, no. 2, pp. 163–181, 2015, doi: 10.3109/02656736.2015.1009180.

[68] P. Bruners *et al.*, “CT-based temperature monitoring during hepatic RF ablation: Feasibility in an animal model,” *Int. J. Hyperth.*, vol. 28, no. 1, pp. 55–61, 2012, doi: 10.3109/02656736.2011.619155.

[69] A. H. Mahnken and P. Bruners, “CT thermometry: will it ever become ready for use?,” *Int. J. Clin. Pract. Suppl.*, no. 171, pp. 1–2, Apr. 2011, doi: 10.1111/j.1742-1241.2011.02651.x.

- [70] S. Asadi, L. Bianchi, M. De Landro, S. Korganbayev, E. Schena, and P. Saccomandi, "Laser-Induced Optothermal Response of Gold Nanoparticles: from a Physical Viewpoint to Cancer Treatment Application," *J. Biophotonics*, vol. 14, no. 2, p. e202000161, Aug. 2021, doi: 10.1002/jbio.202000161.
- [71] B. F. Jones and P. Plassmann, "Digital infrared thermal imaging of human skin.," *IEEE Eng. Med. Biol. Mag. Q. Mag. Eng. Med. Biol. Soc.*, vol. 21, no. 6, pp. 41–48, 2002, doi: 10.1109/memb.2002.1175137.
- [72] H. Odéen and D. L. Parker, "Magnetic resonance thermometry and its biological applications – Physical principles and practical considerations," *Prog. Nucl. Magn. Reson. Spectrosc.*, vol. 110, pp. 34–61, 2019, doi: <https://doi.org/10.1016/j.pnmrs.2019.01.003>.
- [73] M. Viallon, S. Terraz, J. Roland, E. Dumont, C. D. Becker, and R. Salomir, "Observation and correction of transient cavitation-induced PRFS thermometry artifacts during radiofrequency ablation, using simultaneous Ultrasound/MR imaging," *Med. Phys.*, vol. 37, no. 4, pp. 1491–1506, 2010, doi: 10.1118/1.3309439.
- [74] U. Salem *et al.*, "Neurosurgical applications of MRI guided laser interstitial thermal therapy (LITT)," *Cancer Imaging*, vol. 19, no. 1, p. 65, 2019, doi: 10.1186/s40644-019-0250-4.
- [75] E. Walser *et al.*, "Focal Laser Ablation of Prostate Cancer: Results in 120 Patients with Low- to Intermediate-Risk Disease," *J. Vasc. Interv. Radiol.*, vol. 30, no. 3, pp. 401-409.e2, 2019, doi: 10.1016/j.jvir.2018.09.016.
- [76] J. Blackwell *et al.*, "Proton Resonance Frequency Shift Thermometry: A Review of Modern Clinical Practices," *J. Magn. Reson. Imaging*, vol. n/a, no. n/a, Nov. 2020, doi: <https://doi.org/10.1002/jmri.27446>.
- [77] F. Manns, P. J. Milne, X. Gonzalez-Cirre, D. B. Denham, J. M. Parel, and D. S. Robinson, "In situ temperature measurements with thermocouple probes during laser interstitial thermotherapy (LITT): Quantification and correction of a measurement artifact," *Lasers Surg. Med.*, vol. 23, no. 2, pp. 94–103, 1998, doi: 10.1002/(SICI)1096-9101(1998)23:2<94::AID-LSM7>3.0.CO;2-Q.
- [78] E. G. Macchi *et al.*, "Optical fiber sensors-based temperature distribution measurement in ex vivo radiofrequency ablation with submillimeter resolution," *J. Biomed. Opt.*, vol. 19, no. 11, p. 117004, Nov. 2014, doi: 10.1117/1.jbo.19.11.117004.
- [79] T. Erdogan, "Fiber grating spectra," *J. Light. Technol.*, vol. 15, no. 8, pp. 1277–1294, 1997, doi: 10.1109/50.618322.
- [80] T. Guo, F. Liu, and L. Y. Shao, "Tilted Fiber Bragg Grating Sensors," *Yingyong Kexue Xuebao/Journal Appl. Sci.*, vol. 36, no. 1, pp. 75–103, 2018, doi: 10.3969/j.issn.0255-8297.2018.01.005.
- [81] J. Albert, L. Shao, and C. Caucheteur, "Tilted fiber Bragg grating sensors," *Laser Photon. Rev.*, vol. 7, no. 1, pp. 83–108, 2013.
- [82] T. Guo, F. Liu, B. O. Guan, and J. Albert, "Tilted fiber grating mechanical and biochemical sensors," *Opt. Laser Technol.*, vol. 78, pp. 19–33, 2016, doi: 10.1016/j.optlastec.2015.10.007.
- [83] C. Leitao *et al.*, "Cortisol in-fiber ultrasensitive plasmonic immunosensing," *IEEE Sens. J.*, vol. 21, no. 3, pp. 1–1, 2020, doi: 10.1109/JSEN.2020.3025456.

- [84] T. Zhu, M. Loyez, K. Chah, and C. Caucheteur, "Partially gold-coated tilted FBGs for enhanced surface biosensing," *Opt. Express*, vol. 30, no. 10, p. 16518, May 2022, doi: 10.1364/OE.458548.
- [85] P. H. Möller *et al.*, "Temperature control and light penetration in a feedback interstitial laser thermotherapy system," *Int. J. Hyperthermia*, vol. 12, no. 1, pp. 49–63, Jan. 1996, doi: 10.3109/02656739609023689.
- [86] K. Orth, D. Russ, J. Duerr, R. Hibst, R. Steiner, and H. G. Beger, "Thermo-controlled device for inducing deep coagulation in the liver with the ND:YAG laser," *Lasers Surg. Med.*, vol. 20, no. 2, pp. 149–156, 1997, doi: 10.1002/(SICI)1096-9101(1997)20:2<149::AID-LSM5>3.0.CO;2-Q.
- [87] K. Ivarsson, J. Olsrud, C. Sturesson, P. H. Möller, B. R. Persson, and K. G. Tranberg, "Feedback interstitial diode laser (805 nm) thermotherapy system: Ex vivo evaluation and mathematical modeling with one and four-fibers," *Lasers Surg. Med.*, vol. 22, no. 2, pp. 86–96, 1998, doi: 10.1002/(SICI)1096-9101(1998)22:2<86::AID-LSM4>3.0.CO;2-S.
- [88] N. Daikuzono, S. Suzuki, H. Tajiri, H. Tsunekawa, M. Ohyama, and S. N. Joffe, "Laserthermia: A new computer-controlled contact Nd:YAG system for interstitial local hyperthermia," *Lasers Surg. Med.*, vol. 8, no. 3, pp. 254–258, Jan. 1988, doi: 10.1002/lsm.1900080306.
- [89] J. T. Lin, Y. S. Chiang, G. H. Lin, H. Lee, and H. W. Liu, "In vitro photothermal destruction of cancer cells using gold nanorods and pulsed-train near-infrared laser," *J. Nanomater.*, vol. 2012, 2012, doi: 10.1155/2012/861385.
- [90] T. H. Nguyen, S. Park, K. K. Hlaing, and H. W. Kang, "Temperature feedback-controlled photothermal treatment with diffusing applicator: theoretical and experimental evaluations," *Biomed. Opt. Express*, vol. 7, no. 5, p. 1932, May 2016, doi: 10.1364/boe.7.001932.
- [91] S. Nomura *et al.*, "Thermal Sensor Circuit Using Thermography for Temperature-Controlled Laser Hyperthermia," *J. Sensors*, vol. 2017, pp. 1–7, 2017, doi: 10.1155/2017/3738046.
- [92] J. N. Mehrabi, K. M. Kelly, J. D. Holmes, and C. B. Zachary, "Assessing the Outcomes of Focused Heating of the Skin by a Long-Pulsed 1064 nm Laser with an Integrated Scanner, Infrared Thermal Guidance, and Optical Coherence Tomography," *Lasers Surg. Med.*, vol. 53, no. 6, pp. 806–814, Aug. 2021, doi: 10.1002/lsm.23377.
- [93] W. A. Wohlgemuth *et al.*, "In vivo laser-induced interstitial thermotherapy of pig liver with a temperature-controlled Diode laser and MRI correlation," *Lasers Surg. Med.*, vol. 29, no. 4, pp. 374–378, 2001, doi: 10.1002/lsm.1131.
- [94] X. Feng, F. Gao, C. Xu, L. Gaoming, and Y. Zheng, "Self temperature regulation of photothermal therapy by laser-shared photoacoustic feedback," *Opt. Lett.*, vol. 40, no. 19, pp. 4492–4495, 2015, doi: 10.1364/ol.40.004492.
- [95] H. Assi *et al.*, "Real-time control of nanoparticle-mediated thermal therapy using photoacoustic imaging," *IEEE Trans. Biomed. Eng.*, vol. 68, no. 7, pp. 2188–2194, 2021, doi: 10.1109/TBME.2020.3037991.
- [96] S. Paiella *et al.*, "Laser Treatment (imILT) of Pancreatic Cancer: Safety and Feasibility Results From Two Phase 2a Studies," *J. Surg. Res.*, vol. 259, pp. 1–7, 2021,

doi: 10.1016/j.jss.2020.10.027.

- [97] S. Korganbayev, R. Pini, A. Orrico, A. Wolf, A. Dostovalov, and P. Saccomandi, "Towards temperature-controlled laser ablation based on fiber Bragg grating array temperature measurements," in *2020 IEEE International Workshop on Metrology for Industry 4.0 and IoT, MetroInd 4.0 and IoT 2020 - Proceedings*, Jun. 2020, pp. 268–272, doi: 10.1109/MetroInd4.0IoT48571.2020.9138171.
- [98] A. V. Dostovalov, A. A. Wolf, A. V. Parygin, V. E. Zyubin, and S. A. Babin, "Femtosecond point-by-point inscription of Bragg gratings by drawing a coated fiber through ferrule," *Opt. Express*, vol. 24, no. 15, p. 16232, 2016, doi: 10.1364/oe.24.016232.
- [99] T. G. Giallorenzi and A. Dandridge, *Optical Fiber Sensor Technology.*, vol. 3. Boston, MA: Springer US, 1987.
- [100] L. Huang, R. S. Dyer, R. J. Lago, A. A. Stolov, and J. Li, "Mechanical properties of polyimide coated optical fibers at elevated temperatures," in *Optical Fibers and Sensors for Medical Diagnostics and Treatment Applications XVI*, Mar. 2016, vol. 9702, p. 97020Y, doi: 10.1117/12.2210957.
- [101] D. Polito *et al.*, "A needlelike probe for temperature monitoring during laser ablation based on fiber Bragg grating: Manufacturing and characterization," *J. Med. Devices, Trans. ASME*, vol. 9, no. 4, p. 041006, 2015, doi: 10.1115/1.4030624.
- [102] P. Saccomandi *et al.*, "Estimation of optical properties of neuroendocrine pancreas tumor with double-integrating-sphere system and inverse Monte Carlo model," *Lasers Med. Sci.*, vol. 31, no. 6, pp. 1041–1050, 2016, doi: 10.1007/s10103-016-1948-1.
- [103] A. J. Welch and M. J. C. C. Van Gemert, *Optical-Thermal Response of Laser-Irradiated Tissue*, vol. 2. Dordrecht: Springer Netherlands, 2011.
- [104] P. S. Yarmolenko *et al.*, "Thresholds for thermal damage to normal tissues: An update," *Int. J. Hyperth.*, vol. 27, no. 4, pp. 320–343, Jun. 2011, doi: 10.3109/02656736.2010.534527.
- [105] L. Bianchi, A. Orrico, S. Korganbayev, M. De Landro, and P. Saccomandi, "Two-dimensional temperature feedback control strategy for thermal ablation of biological tissue," in *2021 IEEE International Workshop on Metrology for Industry 4.0 and IoT, MetroInd 4.0 and IoT 2021 - Proceedings*, Jun. 2021, pp. 301–306, doi: 10.1109/MetroInd4.0IoT51437.2021.9488457.
- [106] K. Ivarsson, J. Olsrud, and C. Sturesson, "Feedback Interstitial Diode Laser (805 nm) Thermo-therapy System : Ex Vivo Evaluation and Mathematical Modeling With One and Four-Fibers," vol. 96, no. September 1997, pp. 86–96, 1998.
- [107] P. Saccomandi *et al.*, "Feedforward neural network for force coding of an MRI-compatible tactile sensor array based on fiber Bragg grating," *J. Sensors*, vol. 2015, 2015.
- [108] P. Saccomandi *et al.*, "Medical smart textiles based on fiber optic technology: an overview," *J. Sensors*, vol. 2015, no. 2, pp. 204–221, 2015.
- [109] A. Wolf, N. Shabalov, V. Kamynin, and A. Kokhanovskiy, "2D temperature field reconstruction using optical frequency domain reflectometry and machine-learning algorithms," *Available SSRN 4091309*.
- [110] A. Kokhanovskiy *et al.*, "Highly dense fbg temperature sensor assisted with deep

- learning algorithms,” *Sensors*, vol. 21, no. 18, p. 6188, 2021.
- [111] M. H. Niemz, *Laser-Tissue Interactions*. Berlin, Heidelberg: Springer Berlin Heidelberg, 2007.
- [112] M. COMSOL, “Heat Transfer Module,” *Manual*, pp. 1–222, 2015.
- [113] L. Sun, C. M. Collins, J. L. Schiano, M. B. Smith, and N. B. Smith, “Adaptive real-time closed-loop temperature control for ultrasound hyperthermia using magnetic resonance thermometry,” *Concepts Magn. Reson. Part B Magn. Reson. Eng.*, vol. 27, no. 1, pp. 51–63, Oct. 2005, doi: 10.1002/cmr.b.20046.
- [114] H. H. Abd Raziff *et al.*, “A Temperature-Controlled Laser Hot Needle with Grating Sensor for Liver Tissue Tract Ablation,” *IEEE Trans. Instrum. Meas.*, vol. 69, no. 9, pp. 7119–7124, 2020, doi: 10.1109/TIM.2020.2978920.
- [115] H. H. A. Raziff *et al.*, “Laser-heated needle for biopsy tract ablation: In vivo study of rabbit liver biopsy,” *Phys. Medica*, vol. 82, no. February, pp. 40–45, 2021, doi: 10.1016/j.ejmp.2021.01.067.
- [116] L. Bianchi *et al.*, “Fiber Bragg Grating Sensors-Based Thermometry of Gold Nanorod-Enhanced Photothermal Therapy in Tumor Model,” *IEEE Sens. J.*, vol. 22, no. 12, pp. 11297–11306, Jun. 2022, doi: 10.1109/JSEN.2021.3082042.
- [117] B. A. Patterson, D. D. Sampson, P. A. Krug, and S. K. Jones, “In vivo quasi-distributed temperature sensing with fibre Bragg gratings,” in *Conference on Lasers and Electro-Optics Europe - Technical Digest*, 2001, pp. 402–403, doi: 10.1109/cleo.2001.947973.
- [118] M. Sypabekova *et al.*, “Functionalized etched tilted fiber Bragg grating aptasensor for label-free protein detection,” *Biosens. Bioelectron.*, vol. 146, p. 111765, Dec. 2019, doi: 10.1016/j.bios.2019.111765.
- [119] M. Sypabekova *et al.*, “Fiber optic refractive index sensors through spectral detection of Rayleigh backscattering in a chemically etched MgO-based nanoparticle-doped fiber,” *Opt. Lett.*, vol. 43, no. 24, p. 5945, Dec. 2018, doi: 10.1364/ol.43.005945.
- [120] S. Korganbayev *et al.*, “Refractive Index Sensor by Interrogation of Etched MgO Nanoparticle-Doped Optical Fiber Signature,” *IEEE Photonics Technol. Lett.*, vol. 31, no. 15, pp. 1253–1256, Aug. 2019, doi: 10.1109/LPT.2019.2924652.
- [121] S. Korganbayev *et al.*, “Partially etched chirped fiber Bragg grating (pECFBG) for joint temperature, thermal profile, and refractive index detection,” *Opt. Express*, vol. 26, no. 14, p. 18708, Jul. 2018, doi: 10.1364/oe.26.018708.
- [122] C. Chen, C. Caucheteur, P. Mégret, and J. Albert, “The sensitivity characteristics of tilted fibre Bragg grating sensors with different cladding thicknesses,” *Meas. Sci. Technol.*, vol. 18, no. 10, p. 3117, 2007.
- [123] G. Laffon and P. Ferdinand, “Tilted short-period fibre-Bragg-grating-induced coupling to cladding modes for accurate refractometry,” *Meas. Sci. Technol.*, vol. 12, no. 7, pp. 765–770, 2001, doi: 10.1088/0957-0233/12/7/302.
- [124] C. Caucheteur *et al.*, “Enhancement of cladding modes couplings in tilted Bragg gratings owing to cladding etching,” in *Proceedings of WFOPC2005 - 4th IEEE/LEOS Workshop on Fibres and Optical Passive Components*, 2005, vol. 2005, pp. 234–239, doi: 10.1109/WFOPC.2005.1462132.

- [125] F. Chiavaioli, F. Baldini, S. Tombelli, C. Trono, and A. Giannetti, "Biosensing with optical fiber gratings," *Nanophotonics*, vol. 6, no. 4. Walter de Gruyter GmbH, pp. 663–679, 2017, doi: 10.1515/nanoph-2016-0178.
- [126] M. Loyez, J. Albert, C. Caucheteur, and R. Wattiez, "Cytokeratins biosensing using tilted fiber gratings," *Biosensors*, vol. 8, no. 3, p. 74, 2018, doi: 10.3390/bios8030074.
- [127] R. Khan, B. Gul, S. Khan, H. Nisar, and I. Ahmad, "Refractive index of biological tissues: Review, measurement techniques, and applications," *Photodiagnosis Photodyn. Ther.*, vol. 33, p. 102192, 2021.
- [128] "Refractometer." <http://www.refractometer.pl/refraction-datasheet-sucrose>.
- [129] D. Tosi, "Review and analysis of peak tracking techniques for fiber Bragg grating sensors," *Sensors*, vol. 17, no. 10, p. 2368, 2017.
- [130] S. Korganbayev *et al.*, "Detection of thermal gradients through fiber-optic Chirped Fiber Bragg Grating (CFBG): Medical thermal ablation scenario," *Opt. Fiber Technol.*, vol. 41, no. December 2017, pp. 48–55, Mar. 2018, doi: 10.1016/j.yofte.2017.12.017.
- [131] R. Min *et al.*, "Largely tunable dispersion chirped polymer FBG," *Opt. Lett.*, vol. 43, no. 20, p. 5106, Oct. 2018, doi: 10.1364/OL.43.005106.
- [132] S. Sartori, F. Di Vece, F. Ermili, and P. Tombesi, "Laser ablation of liver tumors: An ancillary technique, or an alternative to radiofrequency and microwave?," *World J. Radiol.*, vol. 9, no. 3, p. 91, 2017, doi: 10.4329/wjr.v9.i3.91.
- [133] C. Brace, "Thermal tumor ablation in clinical use," *IEEE Pulse*, vol. 2, no. 5, pp. 28–38, Sep. 2011, doi: 10.1109/MPUL.2011.942603.
- [134] W. Chen *et al.*, "Performance assessment of FBG temperature sensors for laser ablation of tumors," in *2015 IEEE International Symposium on Medical Measurements and Applications (MeMeA) Proceedings*, 2015, pp. 324–328.
- [135] E. De Vita *et al.*, "Fiber Optic Sensors-Based Thermal Analysis of Perfusion-Mediated Tissue Cooling in Liver Undergoing Laser Ablation," *IEEE Trans. Biomed. Eng.*, vol. 68, no. 3, pp. 1066–1073, 2021, doi: 10.1109/TBME.2020.3004983.
- [136] S. Roujol, B. D. de Senneville, S. Hey, C. Moonen, and M. Ries, "Robust adaptive extended Kalman filtering for real time MR-thermometry guided HIFU interventions.," *IEEE Trans. Med. Imaging*, vol. 31, no. 3, pp. 533–542, Mar. 2012, doi: 10.1109/TMI.2011.2171772.
- [137] S. N. Goldberg *et al.*, "Image-guided Tumor Ablation: Standardization of Terminology and Reporting Criteria," *J. Vasc. Interv. Radiol.*, vol. 20, no. 7 SUPPL., pp. 728–739, 2009, doi: 10.1016/j.jvir.2009.04.011.
- [138] M. Ahmed *et al.*, "Image-guided tumor ablation: standardization of terminology and reporting criteria—a 10-year update," *J. Vasc. Interv. Radiol.*, vol. 25, no. 11, pp. 1691–1705, 2014.

Journal Publications:

- [1] S. Korganbayev et al., "Optimization of Cladding Diameter for Refractive Index Sensing in Tilted Fiber Bragg Gratings," *Sensors*, vol. 22, no. 6, p. 2259, Mar. 2022, doi: 10.3390/s22062259.
- [2] S. Asadi et al., "Experimental Evaluation of Radiation Response and Thermal Properties of NPs-Loaded Tissues-Mimicking Phantoms," *Nanomaterials*, vol. 12, no. 6, p. 945, Mar. 2022, doi: 10.3390/nano12060945.
- [3] A. Mohammadi, L. Bianchi, S. Korganbayev, M. De Landro, and P. Saccomandi, "Thermomechanical Modeling of Laser Ablation Therapy of Tumors: Sensitivity Analysis and Optimization of Influential Variables," *IEEE Trans. Biomed. Eng.*, vol. 69, no. 1, pp. 302–313, Jan. 2022, doi: 10.1109/TBME.2021.3092889.
- [4] N. D. Schulmann, M. Soltani-Sarvestani, M. De Landro, S. Korganbayev, S. Cotin, and P. Saccomandi, "Model-Based Thermometry for Laser Ablation Procedure Using Kalman Filters and Sparse Temperature Measurements," *IEEE Trans. Biomed. Eng.*, pp. 1–1, 2022, doi: 10.1109/TBME.2022.3155574.
- [5] D. Paloschi, K. A. Bronnikov, S. Korganbayev, A. Wolf, A. Dostovalov, and P. Saccomandi, "3D Shape Sensing with Multicore Optical Fibers: Transformation Matrices Versus Frenet-Serret Equations for Real-Time Application," *IEEE Sens. J.*, vol. 21, no. 4, pp. 4599–4609, Feb. 2021, doi: 10.1109/JSEN.2020.3032480.
- [6] I. Maor et al., "Laser-induced thermal response and controlled release of copper oxide nanoparticles from multifunctional polymeric nanocarriers," *Sci. Technol. Adv. Mater.*, vol. 22, no. 1, pp. 218–233, Dec. 2021, doi: 10.1080/14686996.2021.1883406.
- [7] A. Mohammadi, L. Bianchi, S. Korganbayev, M. De Landro, and P. Saccomandi, "Thermomechanical Modeling of Laser Ablation Therapy of Tumors: Sensitivity Analysis and Optimization of Influential Variables," *IEEE Trans. Biomed. Eng.*, pp. 1–1, 2021, doi: 10.1109/TBME.2021.3092889.
- [8] S. Korganbayev et al., "PID Controlling Approach Based on FBG Array Measurements for Laser Ablation of Pancreatic Tissues," *IEEE Trans. Instrum. Meas.*, vol. 70, pp. 1–9, 2021, doi: 10.1109/TIM.2021.3112790.
- [9] S. Asadi, L. Bianchi, M. De Landro, S. Korganbayev, E. Schena, and P. Saccomandi, "Laser-Induced Optothermal Response of Gold Nanoparticles: from a Physical Viewpoint to Cancer Treatment Application," *J. Biophotonics*, vol. 14, no. 2, p. e202000161, Aug. 2021, doi: 10.1002/jbio.202000161.
- [10] L. Bianchi, S. Korganbayev, A. Orrico, M. De Landro, and P. Saccomandi, "Quasi-distributed fiber optic sensor-based control system for interstitial laser ablation of tissue: theoretical and experimental investigations," *Biomed. Opt. Express*, vol. 12, no. 5, p. 2841, May 2021, doi: 10.1364/BOE.419541.
- [11] T. Ayupova et al., "Fiber Optic Refractive Index Distributed Multi-Sensors by Scattering-Level Multiplexing with MgO Nanoparticle-Doped Fibers," *IEEE Sens. J.*, vol. 20, no. 5, pp. 2504–2510, Mar. 2020, doi: 10.1109/JSEN.2019.2953231.

- [12] S. Korganbayev et al., “Closed-loop temperature control based on fiber bragg grating sensors for laser ablation of hepatic tissue,” *Sensors (Switzerland)*, vol. 20, no. 22, pp. 1–16, Nov. 2020, doi: 10.3390/s20226496.
- [13] F. Morra et al., “Spatially resolved thermometry during laser ablation in tissues: Distributed and quasi-distributed fiber optic-based sensing,” *Opt. Fiber Technol.*, vol. 58, p. 102295, Sep. 2020, doi: 10.1016/j.yofte.2020.102295.
- [14] A. Beisenova et al., “Multi-fiber distributed thermal profiling of minimally invasive thermal ablation with scattering-level multiplexing in MgO-doped fibers,” *Biomed. Opt. Express*, vol. 10, no. 3, pp. 1282–1296, Mar. 2019, doi: 10.1364/BOE.10.001282.
- [15] A. Beisenova, A. Issatayeva, S. Korganbayev, C. Molardi, W. Blanc, and D. Tosi, “Simultaneous Distributed Sensing on Multiple MgO-Doped High Scattering Fibers by Means of Scattering-Level Multiplexing,” *J. Light. Technol.*, vol. 37, no. 13, pp. 3413–3421, Jul. 2019, doi: 10.1109/JLT.2019.2916991.
- [16] M. Sypabekova et al., “Functionalized etched tilted fiber Bragg grating aptasensor for label-free protein detection,” *Biosens. Bioelectron.*, vol. 146, p. 111765, Dec. 2019, doi: 10.1016/j.bios.2019.111765.
- [17] D. Tosi, E. Schena, C. Molardi, and S. Korganbayev, “Fiber optic sensors for sub-centimeter spatially resolved measurements: Review and biomedical applications,” *Opt. Fiber Technol.*, vol. 43, no. March, pp. 6–19, Jul. 2018, doi: 10.1016/j.yofte.2018.03.007.
- [18] M. Jelbuldina, A. Korobeinyk, S. Korganbayev, D. Tosi, K. Dukenbayev, and V. J. Inglezakis, “Real-Time Temperature Monitoring in Liver during Magnetite Nanoparticle-Enhanced Microwave Ablation with Fiber Bragg Grating Sensors: Ex Vivo Analysis,” *IEEE Sens. J.*, vol. 18, no. 19, pp. 8005–8011, Oct. 2018, doi: 10.1109/JSEN.2018.2865100.
- [19] S. Korganbayev et al., “Thermal Profile Detection Through High-Sensitivity Fiber Optic Chirped Bragg Grating on Microstructured PMMA Fiber,” *J. Light. Technol.*, vol. 36, no. 20, pp. 4723–4729, Oct. 2018, doi: 10.1109/JLT.2018.2864113.
- [20] S. Korganbayev et al., “Detection of thermal gradients through fiber-optic Chirped Fiber Bragg Grating (CFBG): Medical thermal ablation scenario,” *Opt. Fiber Technol.*, vol. 41, no. December 2017, pp. 48–55, Mar. 2018, doi: 10.1016/j.yofte.2017.12.017.
- [21] M. Jelbuldina, A. V. Korobeinyk, S. Korganbayev, V. J. Inglezakis, and D. Tosi, “Fiber Bragg grating based temperature profiling in ferromagnetic nanoparticles-enhanced radiofrequency ablation,” *Opt. Fiber Technol.*, vol. 43, no. May, pp. 145–152, Jul. 2018, doi: 10.1016/j.yofte.2018.05.004.
- [22] S. Korganbayev et al., “Partially etched chirped fiber Bragg grating (pECFBG) for joint temperature, thermal profile, and refractive index detection,” *Opt. Express*, vol. 26, no. 14, p. 18708, Jul. 2018, doi: 10.1364/oe.26.018708.
- [23] P. Saccomandi et al., “Linearly chirped fiber Bragg grating response to thermal gradient: from bench tests to the real-time assessment during in vivo laser ablations of biological tissue,” *J. Biomed. Opt.*, vol. 22, no. 09, p. 1, Sep. 2017, doi: 10.1117/1.jbo.22.9.097002.

[24] S. Korganbayev, M. De Landro, A. Wolf, D. Tosi, and P. Saccomandi, "Tilted fiber Bragg grating measurements during laser ablation of hepatic tissues: quasi-distributed temperature reconstruction and cladding mode resonances analysis," *IEEE Sens. J.*, vol. 22, no. 16, pp. 15999–16007, 2022.

Letters:

[1] M. Jelbuldina, S. Korganbayev, Z. Seidagaliyeva, S. Sovetov, T. Tuganbekov, and D. Tosi, "Fiber Bragg Grating Sensor for Temperature Monitoring During HIFU Ablation of Ex Vivo Breast Fibroadenoma," *IEEE Sensors Lett.*, vol. 3, no. 8, pp. 1–4, Aug. 2019, doi: 10.1109/LSENS.2019.2932910.

[2] S. Korganbayev et al., "Refractive Index Sensor by Interrogation of Etched MgO Nanoparticle-Doped Optical Fiber Signature," *IEEE Photonics Technol. Lett.*, vol. 31, no. 15, pp. 1253–1256, Aug. 2019, doi: 10.1109/LPT.2019.2924652.

[3] M. Sypabekova et al., "Fiber optic refractive index sensors through spectral detection of Rayleigh backscattering in a chemically etched MgO-based nanoparticle-doped fiber," *Opt. Lett.*, vol. 43, no. 24, p. 5945, Dec. 2018, doi: 10.1364/OL.43.005945.

[4] R. Min et al., "Largely tunable dispersion chirped polymer FBG," *Opt. Lett.*, vol. 43, no. 20, p. 5106, Oct. 2018, doi: 10.1364/OL.43.005106.

Conference Proceedings:

[1] L. Bianchi, A. Orrico, S. Korganbayev, M. De Landro, and P. Saccomandi, "Two-dimensional temperature feedback control strategy for thermal ablation of biological tissue," in *2021 IEEE International Workshop on Metrology for Industry 4.0 and IoT, MetroInd 4.0 and IoT 2021 - Proceedings*, Jun. 2021, pp. 301–306, doi: 10.1109/MetroInd4.0IoT51437.2021.9488457.

[2] M. de Landro et al., "Magnetic resonance-based measurement system: comparison of 2D and 3D echo-planar imaging sequences for thermometry application," in *2021 IEEE International Instrumentation and Measurement Technology Conference (I2MTC)*, May 2021, vol. 2021-May, pp. 1–6, doi: 10.1109/I2MTC50364.2021.9460088.

[3] A. Orrico, L. Bianchi, S. Korganbayev, M. De Landro, and P. Saccomandi, "Controlled photothermal therapy based on temperature monitoring: theoretical and experimental analysis," in *2021 IEEE International Symposium on Medical Measurements and Applications (MeMeA)*, Jun. 2021, pp. 1–6, doi: 10.1109/MeMeA52024.2021.9478671.

[4] S. Korganbayev et al., "Feedback-controlled thermal therapy of tissues based on fiber Bragg grating thermometers," in *2021 IEEE International Symposium on Medical Measurements and Applications (MeMeA)*, Jun. 2021, pp. 1–6, doi: 10.1109/MeMeA52024.2021.9478749.

[5] S. Korganbayev et al., "Measurement of Enhanced Photothermal Effects of CuO-encapsulated Polymeric Nanospheres," in *2021 IEEE International Symposium on Medical Measurements and Applications (MeMeA)*, Jun. 2021, pp. 1–5, doi: 10.1109/MeMeA52024.2021.9478675.

- [6] S. Korganbayev, M. De Landro, F. Morra, A. Cigada, and P. Saccomandi, "Fiber Optic Sensors for Distributed and Quasi-distributed Temperature Measurement," in *Proceedings of IEEE Sensors*, Oct. 2020, vol. 2020-October, pp. 1–4, doi: 10.1109/SENSORS47125.2020.9278937.
- [7] D. Paloschi, S. Korganbayev, K. Bronnikov, A. Wolf, A. Dostovalov, and P. Saccomandi, "Transformation matrices for 3D shape sensing with polyimide-coated multicore optical fiber," in *2020 IEEE International Workshop on Metrology for Industry 4.0 and IoT, MetroInd 4.0 and IoT 2020 - Proceedings*, Jun. 2020, pp. 250–254, doi: 10.1109/MetroInd4.0IoT48571.2020.9138221.
- [8] S. Korganbayev, R. Pini, A. Orrico, A. Wolf, A. Dostovalov, and P. Saccomandi, "Towards temperature-controlled laser ablation based on fiber Bragg grating array temperature measurements," in *2020 IEEE International Workshop on Metrology for Industry 4.0 and IoT, MetroInd 4.0 and IoT 2020 - Proceedings*, Jun. 2020, pp. 268–272, doi: 10.1109/MetroInd4.0IoT48571.2020.9138171.
- [9] M. Shaimerdenova et al., "Spatial multiplexing of refractive index distributed sensors by means of high-scattering MgO nanoparticle doped optical fiber," in *Optical Fibers and Sensors for Medical Diagnostics and Treatment Applications XX*, Feb. 2020, vol. 11233, p. 29, doi: 10.1117/12.2545468.
- [10] A. Issatayeva et al., "2D temperature sensing obtained by multiplexing of optical backscattering reflectometry," in *Optical Fibers and Sensors for Medical Diagnostics and Treatment Applications XX*, Feb. 2020, vol. 11233, p. 28, doi: 10.1117/12.2545123.
- [11] M. Jelbuldina et al., "Multi-fiber distributed temperature profiling in ex vivo magnetite nanoparticle-mediated laser tissue ablation," in *Optical Interactions with Tissue and Cells XXXI*, Feb. 2020, vol. 11238, p. 16, doi: 10.1117/12.2546104.
- [12] S. Korganbayev et al., "Highly dense FBG arrays for millimeter-scale thermal monitoring during nanocomposite-enhanced laser ablation," in *Optical Sensing and Detection VI*, Apr. 2020, vol. 11354, p. 19, doi: 10.1117/12.2555436.
- [13] T. Ayupova et al., "Fiber Taper Refractive Index Sensor detection by Optical Backscatter Reflectometer," in *Photonics West (BIOS)*, 2020.
- [14] A. Issatayeva et al., "Multiplexing of distributed temperature sensing achieved by nanoparticle-doped fibers," in *Proceedings of SPIE - The International Society for Optical Engineering*, Nov. 2019, vol. 11190, p. 16, doi: 10.1117/12.2537186.
- [15] C. Molardi et al., "Parallel multiplexing in optical backscatter reflectometry by the use of nano-particles doped optical fiber," in *Progress in Biomedical Optics and Imaging - Proceedings of SPIE*, Feb. 2019, vol. 10872, p. 28, doi: 10.1117/12.2510100.
- [16] C. Molardi et al., "Emerging distributed sensing applications by means of MgO based nanoparticle doped optical fibers," 2019.
- [17] M. Jelbuldina, S. Korganbayev, A. V. Korobeinyk, V. J. Inglezakis, and D. Tosi, "Temperature Profiling of ex-vivo Organs during Ferromagnetic Nanoparticles-Enhanced Radiofrequency Ablation by Fiber Bragg Grating Arrays," in *Proceedings of the Annual International Conference of the IEEE Engineering in Medicine and Biology Society, EMBS*, Jul. 2018, vol. 2018-July, pp. 1–4, doi: 10.1109/EMBC.2018.8513227.
- [18] D. Tosi et al., "High Spatial Resolution Fiber Optic Sensors and Their Impact in Biomedical Measurements and Diagnostic," in *2018 Conference on Lasers and Electro-*

Optics Pacific Rim, CLEO-PR 2018, 2018, vol. Part F113-, p. Tu3K.2, doi: 10.1364/cleopr.2018.tu3k.2.

[19] M. Jelbuldina, S. Korganbayev, A. V. Korobeinyk, V. J. Inglezakis, and D. Tosi, "Fiber bragg grating sensors for temperature monitoring during nanoparticle-assisted microwave ablation," in Optics InfoBase Conference Papers, 2018, vol. Part F124-, p. WF3, doi: 10.1364/ofs.2018.wf3.

[20] M. Shaimerdenova et al., "Detection of various Thrombin concentrations using etched fiber Bragg gratings functionalized with DNA aptamer," in Proceedings of SPIE - The International Society for Optical Engineering, Oct. 2018, vol. 10820, p. 22, doi: 10.1117/12.2502457.

[21] M. Shaimerdenova et al., "An etched chirped fiber Bragg grating for measurement of refractive index and temperature pattern," in Proceedings of SPIE - The International Society for Optical Engineering, Oct. 2018, vol. 10820, p. 121, doi: 10.1117/12.2502471.

[22] S. Korganbayev et al., "Compact Fiber Optic Sensors for Dual Temperature and Refractive Index Profiling Based on Partially Etched Chirped Fiber Bragg Grating@nu.edu.kz," in Proceedings of IEEE Sensors, Oct. 2018, vol. 2018-October, pp. 1–4, doi: 10.1109/ICSENS.2018.8589819.

[23] C. Molardi, S. Korganbayev, W. Blanc, and D. Tosi, "Characterization of a nanoparticles-doped optical fiber by the use of optical backscatter reflectometry," in Proceedings of SPIE - The International Society for Optical Engineering, Oct. 2018, vol. 10821, p. 76, doi: 10.1117/12.2502600.

[24] S. Korganbayev et al., "Thermal gradient estimation with fiber-optic chirped FBG sensors: Experiments in biomedical applications," in Proceedings of IEEE Sensors, Oct. 2017, vol. 2017-December, pp. 1–3, doi: 10.1109/ICSENS.2017.8234119.

[25] S. Korganbayev et al., "Linearly chirped fiber-optic Bragg grating as distributed temperature sensor for laser ablation," in Proceedings of IEEE Sensors, Oct. 2017, pp. 1–3, doi: 10.1109/ICSENS.2016.7808610.

[26] D. Tosi, S. Korganbayev, N. Zhakin, R. Gassino, G. Perrone, and A. Vallan, "Towards inline spatially resolved temperature sensing in thermal ablation with chirped fiber Bragg grating," in 2016 IEEE International Symposium on Medical Measurements and Applications, MeMeA 2016 - Proceedings, May 2016, pp. 1–6, doi: 10.1109/MeMeA.2016.7533777.





Patent:

[1] D. Tosi, N. S. Zhakin, and S. B. Korganbayev, "Method of distributed temperature sensing during thermal tumour ablation using a fiber optic temperature sensor with a linearly chirped bragg grating," Apr. 18, 2019.

APPENDIX

Article

Closed-Loop Temperature Control Based on Fiber Bragg Grating Sensors for Laser Ablation of Hepatic Tissue

Sanzhar Korganbayev ^{1,*}, Annalisa Orrico ¹, Leonardo Bianchi ¹, Martina De Landro ¹, Alexey Wolf ², Alexander Dostovalov ² and Paola Saccomandi ¹

¹ Department of Mechanical Engineering, Politecnico di Milano Milan, 20133 Milano MI, Italy; annalisa.orrico@mail.polimi.it (A.O.); leonardo.bianchi@polimi.it (L.B.); martina.delandro@polimi.it (M.D.L.); paola.sacomandi@polimi.it (P.S.)

² Laboratory of Fiber Optics, Institute of Automation and Electrometry SB RAS, Novosibirsk 630090, Russia; wolf@iae.nsk.su (A.W.); dostovalov@iae.nsk.su (A.D.)

* Correspondence: sanzhar.korganbayev@polimi.it; Tel.: +39-348-776-1649

Received: 5 October 2020; Accepted: 11 November 2020; Published: 13 November 2020



Abstract: Laser ablation (LA) of cancer is a minimally invasive technique based on targeted heat release. Controlling tissue temperature during LA is crucial to achieve the desired therapeutic effect in the organs while preserving the healthy tissue around. Here, we report the design and implementation of a real-time monitoring system performing closed-loop temperature control, based on fiber Bragg grating (FBG) spatial measurements. Highly dense FBG arrays (1.19 mm length, 0.01 mm edge-to-edge distance) were inscribed in polyimide-coated fibers using the femtosecond point-by-point writing technology to obtain the spatial resolution needed for accurate reconstruction of high-gradient temperature profiles during LA. The zone control strategy was implemented such that the temperature in the laser-irradiated area was maintained at specific set values (43 and 55 °C), in correspondence to specific radii (2 and 6 mm) of the targeted zone. The developed control system was assessed in terms of measured temperature maps during an ex vivo liver LA. Results suggest that the temperature-feedback system provides several advantages, including controlling the margins of the ablated zone and keeping the maximum temperature below the critical values. Our strategy and resulting analysis go beyond the state-of-the-art LA regulation techniques, encouraging further investigation in the identification of the optimal control-loop.

Keywords: laser ablation; thermal ablation; temperature measurements; optical fiber; fiber Bragg grating sensors; feedback system; real-time monitoring; closed-loop temperature control

1. Introduction

Many thermal ablation (TA) therapies are being proposed as alternatives to the traditional cancer treatment methods, e.g., resectional surgery, chemotherapy, and radiation therapy, for the treatment of non-surgical patients [1]. All TA techniques are based on localized temperature change that is created to induce the malignant cell necrosis in the ablated tumor at cytotoxic temperatures (50–60 °C) [2]. The main advantage of TA treatment over conventional treatment techniques is TA's minimal invasiveness, as, for instance, small-size applicators can be used under percutaneous or endoscopic guidance to induce local temperature change [3–5]. Depending on the frequency of electromagnetic waves that induce tissue's temperature change, TA techniques are divided into high-intensity focused ultrasound [6], microwave [7], radiofrequency [8], and laser ablation (LA) [9].

Among all these techniques, LA holds good promises for clinical application, taking advantage of the small and flexible fiber optic applicators guiding laser energy into deep-lying tumors [10],

which makes the procedure also safe and compatible with magnetic resonance imaging (MRI) and computed tomography (CT) techniques. Besides, the laser can be used for the treatment of superficial tumors, also inside of hollow organs, such as the and gastrointestinal mucosa [11,12], and biliary tree [13], and in combination with selectively absorbing nanomaterials for photothermal therapy [14,15]. LA's efficacy has been already investigated for the treatment of tumors in several organs, including bones [16], brain [17], thyroid [18], liver [19], and pancreas [20–22].

However, the abovementioned advantages are not preponderating two main limitations of LA treatment. The first one is an inefficient ablation selectivity when healthy surrounding tissues can also be damaged. The second limitation is the use of an open-loop approach, i.e., laser parameters (power, position, and treated shape) are usually set before the procedure without modulation during the ablation [3]. One of the possible solutions to both problems is the development of an ablation controlling technique based on intra-tissue tumor parameters, such as temperature, strain, tissue's refractive index, and other biological markers. Due to the nature of TA treatments, the temperature during ablation is the most important parameter among them that significantly affects treatment efficacy [23].

The complex phenomenon of the laser–tissue interaction (absorption, reflection, and scattering) and a small diameter of the laser-guiding fiber leads to a high spatial thermal gradient [24]. As a result, the ablated area has several regions with different biological effects that depend on the duration of the ablation and the maximum temperature reached. In this context, the temperature range between 42 and 45 °C is considered to be optimal for hyperthermal treatment since it activates immune responses by promoting the migration and maturation of Langerhans cells [25]. At a temperature between 50 to 55 °C, coagulative necrosis starts in organs [3], and it has been observed that cellular death can occur instantaneously in cell culture [26]. A temperature of 60 °C is the threshold for rapid protein denaturation, which leads to a cytotoxic effect and coagulative necrosis. In order to evaluate the effect of the ablation duration and the maximum temperature reached, i.e., relative treatment effectiveness, different models are proposed. For instance, thermal dose can be expressed as equivalent minutes of exposure at 43 °C (Cumulative Equivalent Minutes at 43 °C, CEM43), which has been found to correlate with the severity of thermal damage for several tissue types [27]. Volumes of the regions with different thermal doses depend on complex combinations of different parameters, such as penetration depth of the laser light, shape of the applicator, absorption, mechanical and thermal properties of the tissue, etc. [23]. Hence, it is challenging to have effective pre-operative modeling of LA treatment and to obtain optimal settings of the laser parameters before the procedure. As a result, temperature monitoring in terms of both accuracy and spatial resolution plays a crucial role in effective LA treatment.

Most of the works on real-time power regulation during LA use temperature as a primary parameter to control the ablation procedure. Ivarsson et al. developed temperature-controlled stepwise power regulation for LA of ex vivo bovine muscle experiments; the temperature was monitored using thermistors (10 mm spatial resolution) [28]. Möller and collaborators used ablation control based on 5-point thermistor probe temperature measurements for in vivo LA in rats and compared them with in vitro temperature control and light penetration experiments [29]. In [30], regulation is based on photo-optic probe temperature measurements during in vivo pig liver LA; the tissue necroses were evaluated with MRI after the treatment. Lin et al. employed thermocouple-based temperature measurements to regulate ablation [31,32].

State-of-the-art works, to the best of our knowledge, utilize conventional thermistor probes and thermocouple sensors that impair the accurate thermometry during LA. These sensors allow single-point measurements, thus restricting the number of sensors that can be simultaneously employed to measure and control the ongoing treatment to guarantee reduced invasiveness. Additionally, the laser light and heat absorption by metallic material of the probes can cause measurement artifact above 20 °C when the relative distance between applicator and sensor is small (a few millimeters) [33,34]. In this setup, the closer the distance between the metallic sensor and the applicator, the higher the overestimation due to the direct light absorption. This property forces to locate sensors far from the

applicator tip (>1 cm), thus limiting the options for the control of the extension of the region under treatment. Both the mentioned problems lead to low spatial resolution thermometry, with potential sub-optimal and inefficient real-time LA regulation [33].

Fiber optic technology is a perspective alternative for traditional sensing methods. Indeed, fiber optic sensors have low heat conductivity, they are immune to electromagnetic interferences, and prone to the laser light absorption because of the fiber material (glass or polymer) [35]. The most popular fiber optic temperature measurements for TAs are divided into two types: distributed and quasi-distributed [36]. Distributed sensing relies on Rayleigh scattering phenomena and measures only the relative change of temperature profile since it analyzes the spectral shift between two states: measured and reference one (without temperature change) [37]. Currently, the main technique for thermal measurements is optical frequency-domain reflectometry (OFDR) based Luna OBR4600, which has sub-mm spatial accuracy [38]. Standard single-mode fiber is used as a cheap sensor for distributed sensing, but an expensive interrogator is needed for it. The high interrogator cost and low sampling rates make distributed sensing not well suited for real-time temperature monitoring needed for ablation regulation [35].

Quasi-distributed sensing relies on fiber Bragg grating (FBG) measurements. FBG is a structure with a periodic change of the refractive index along the fiber core. FBG acts as a wavelength-dependent reflector: incident broadband light is reflected at a specific wavelength, called the Bragg wavelength, λ_B [39]. The reflected wavelength depends on the grating period (the distance between two high-index regions), which is changed during external temperature perturbations. In addition, multi-point measurements are possible when a chain of FBGs, each with a different grating period, is inscribed along the fiber core. In this case, the set of different Bragg wavelengths is analyzed to monitor the spatial temperature profile along the fiber. FBG monitoring allows lower costs of the interrogators and high sampling rates (up to 10 kHz), which makes FBG sensing more suitable for LA regulation [40].

Several studies implemented fiber optic- [36,37,41] and quasi-distributed sensing [33,42–45] to monitor temperature during LA, and showed the capability of fiber optic sensors to provide spatial maps of the tissue temperature after the treatment completion. However, none of these studies investigate the performance of fiber optic sensors for temperature-based LA regulation, where also real-time monitoring is indispensable.

In these regards, this work focuses on the development of the first platform dedicated to real-time spatial temperature monitoring and related therapy regulation by introducing FBG-based strategy. To improve the accuracy and spatial resolution of the sensors, custom-made highly dense FBG arrays were inscribed in polyimide-coated single-mode fibers. With this sensing technique, the temperature was monitored simultaneously in 120 regions of an *ex vivo* liver undergoing LA. The developed closed-loop temperature control algorithm aimed at maintaining the temperature in the laser-irradiated liver area at specific set thresholds (43 and 55 °C), in correspondence to specific radii (2 and 6 mm) of the targeted zone. The obtained thermal maps and ablated tissue analysis prove the efficacy of the fabricated FBG arrays and the developed algorithm for LA controlling. Besides, thermal maps clearly show the importance of temperature threshold setting to control the spatial extension of the ablated zone and to keep the maximum temperature below critical values.

2. Materials and Methods

2.1. FBG-Based Sensing

For temperature measurements, custom-made arrays of 40 FBGs were inscribed in a single-mode optical fiber SM1500(9/125)P (Fibercore Ltd., Southampton, UK) using the femtosecond point-by-point writing technology [46]. Femtosecond pulses with a wavelength of 1026 nm, duration of 232 fs, pulse repetition rate of 1 kHz, and pulse energy of ~100 nJ were produced by Pharos 6W laser system (Light Conversion Ltd., Vilnius, Lithuania) and focused into the fiber core region with a microobjective (NA = 0.65). Precise fiber positioning in the process of FBG writing was provided by

ABL1000 air-bearing linear stage (Aerotech Inc., Pittsburgh, PA, USA). The design of the grating lengths has been performed to space the resulting Bragg wavelengths at each 4 nm, and to fit the spectral region (Figure 1a) of the Micron Optics si255 interrogation unit (Micron Optics, Atlanta, GA, USA), which ranges from 1460 to 1620 nm. The choice to coat the gratings with polyimide is motivated by the excellent thermal properties of this material over the standard acrylate coating, such as the high-temperature resistance up to 400 °C, and the low thermal conductivity [46–48]. The transparency of the polyimide coating for IR femtosecond radiation allowed us to inscribe FBG arrays through the protective coating, thus preserving temperature and mechanical performance of the fiber. The FBG arrays have grating lengths of 1.19 mm, and the edge-to-edge distances between gratings equal to 0.01 mm. The chosen length of an FBG provided a simultaneous high spatial resolution and a narrow spectral width of an individual resonance peak, which reduced the mutual influence of neighboring resonances during nonuniform heating of the array. Indeed, the maximum temperature near the laser applicator tip can overcome 300 °C and gradient can be up to 50 °C/mm [24], and the developed FBGs can measure such temperature without any interference between FBG peaks.

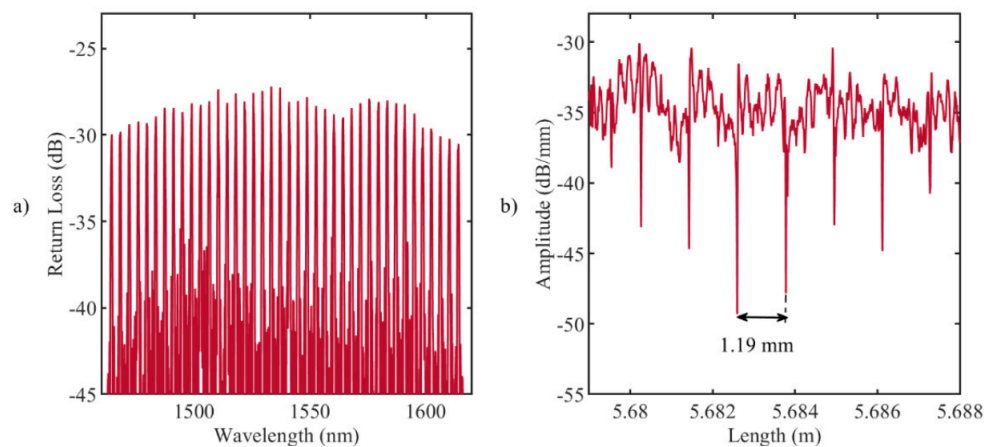


Figure 1. (a) Reflection spectrum of the fabricated fiber Bragg grating (FBG) array with the femtosecond point-by-point writing technology: 40 gratings, equidistant in 1464.5–1614.5 nm wavelength range; (b) LUNA OBR 4600 backscattering signal: the distance between the ends of the gratings (drops in amplitude) is 1.19 mm.

Figure 1b illustrates the backscattering signal measured by LUNA OBR 4600 reflectometer (9.607 μm spatial resolution): each drop in amplitude corresponds to the ends of the grating, and the distance between drops is approximately equal to 1.19 mm. The analysis of the reflected Bragg wavelength shifts, $\Delta\lambda_B$, provides information about the temperature along the grating, ΔT [49]:

$$\frac{\Delta\lambda_B}{\lambda_B} = \frac{\lambda_{B,\Delta T} - \lambda_{B,initial}}{\lambda_B} = \alpha\Delta T \quad (1)$$

where α (°C⁻¹) is the thermal sensitivity of the grating.

The thermal sensitivity of the FBGs is $(7.43 \pm 0.01) \times 10^{-6}$ °C⁻¹, as obtained after static calibration in a thermostatic dry-block calibrator in the temperature range 20 to 130 °C.

2.2. Experimental Setup

For ablation experiments, an 808 nm continuous wave diode laser (LuOcean Mini 4, Lumics, Berlin, Germany) emitting in the near-infrared range was used. Ablation was performed with a laser power of 5 W in a superficial manner: laser light was guided through a 440 μm diameter quartz optical fiber connected to a collimator (OZ Optics Ltd., Ottawa, ON, Canada) and positioned perpendicularly to the porcine liver surface at a 7 cm distance from it (Figure 2a). The laser beam spot diameter was 10 mm, and the ablation duration was 90 s.

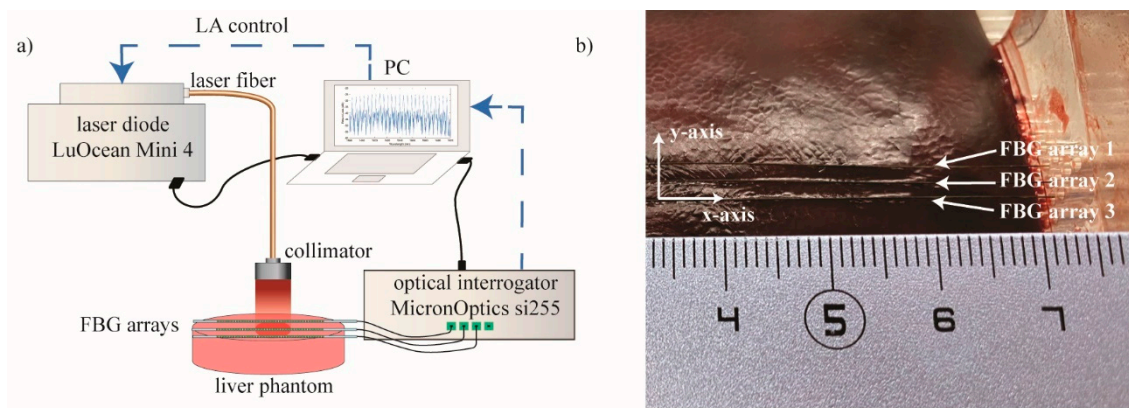


Figure 2. (a) Schematic representation of the experimental setup: superficial LA of ex vivo porcine liver. Laser control was based on FBG temperature measurements. (b) Picture of the plexiglass box containing the liver and allowing the 2 mm-distance arrangement of the three FBG arrays.

Experiments were performed on ex vivo porcine liver. The liver was obtained from a local butcher the same day of the experiment and stored at 4 °C until the experiment was carried out. Three highly dense FBG arrays, (FBG arrays 1, 2, and 3) were placed on the liver surface by means of a custom-made box. The plexiglass box was used to control the relative position between each fiber, equal to 2 mm (Figure 2b). The laser spot was focused on the center of the arrays, and Micron Optics si255 interrogation unit was used to measure the reflected Bragg wavelength spectra of the array, with a sampling frequency of 100 Hz.

2.3. Temperature-Feedback Control Strategy for the Zone Control Logic

The developed real-time closed-loop temperature control algorithm utilizes an ON–OFF logic based on spatial temperature information, and performs a strategy that the authors call *zone-control logic*. The implemented *zone-control logic* consists of three main sub-parts: (i) alignment, (ii) creation of the spatial temperature maps and definition of the radius, and (iii) laser ablation control (Figure 3).

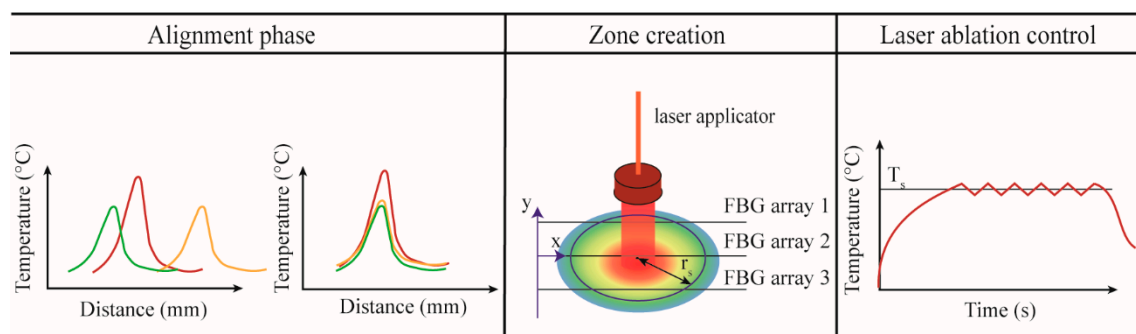


Figure 3. Main phases of the *zone-control logic* designed to regulate the laser ablation (LA) according to the quasi-distributed temperature measured with FBG arrays.

In the alignment phase, the tissue is heated up by the laser source until the maximum temperature reaches the pre-phase threshold temperature (about 33 °C). This threshold is usually reached within 4–5 s from the laser activation and has been chosen to avoid potential damage to the tissue. The profiles measured by the three arrays are aligned employing the centroid method, which finds the centers of the Gaussian distribution along y -axis measured by each array and shift one over the other in order to match the centers [36]. The alignment is a crucial step; indeed, when several FBG arrays are used, the alignment between the acquired temperature profiles is mandatory to correctly reconstruct the real-time temperature map.

It is important to highlight that the temperature measurements have higher spatial resolution along the x -axis (FBG array resolution is 1.2 mm) and lower resolution along y -axis (distance between FBG arrays is 2 mm). For better thermal mapping, the temperature profiles are linearly interpolated along and between the FBG arrays. Once the interpolation is performed, the thermal map is visualized in real-time during the ongoing LA procedure. From this map, the software defines the position in which the maximum temperature value is located, and, starting from this position, the user can select the radius (r_s) of the circumference corresponding to the zone that has to be controlled at the set temperature T_s .

In the case of uncontrolled ablation, the laser light is delivered in continuous modality. Ablation starts at room temperature T_0 , and the laser is ON until the moment when the laser system is switched off by the user. In the case of controlled ablation, the control logic works as follows: ablation starts at room temperature T_0 , and the laser is ON until the moment when the maximum temperature measured by the sensor placed at r_s exceeds the set temperature T_s . Then, the laser follows an ON–OFF logic to maintain a maximum temperature close to T_s . The comparison of T_s with the measured maximum temperature is executed each $\Delta\tau$ seconds. The comparing period should not be less than 1 ms to prevent pulsed-mode behavior of the laser, which may lead to other laser–tissue interaction effects, such as explosive evaporation and cavitation in the irradiated tissue [50]. The preliminary evaluation of the optimal $\Delta\tau$ carried out by the authors shows that $\Delta\tau = 1$ s leads to smooth temperature control and a spatially confined ablation region [51]; hence, this value for the comparison period was used for all experiments presented in this work.

The experiments were performed with the settings listed in Table 1:

Table 1. Settings used for the experiments: for the temperature-based controlled ablations (*zone-control logic*) set temperature T_s and radius (r_s) of the circumference of the zone under control are defined.

Setting	Test a	Test b	Test c	Test d	Test e
T_s (°C)	55	43	55	43	uncontrolled
r_s (mm)	6	6	2	2	

LA without feedback regulation (uncontrolled ablation) was considered as a reference. The *zone-control logic* was designed and implemented in LabVIEW; the program was developed to receive Bragg wavelengths data from the Micron Optics interrogation unit, reconstruct spatial temperature maps, define the values for r_s and T_s , and adjust the laser power based on these measurements using an ON–OFF logic in real time (Figure 3).

3. Results

3.1. Thermal Analyses on the Temperature Profiles Measured by FBG Array 2

The first analyses on the effect of the *zone-control logic* on the LA outcome are performed considering the temperature profiles measured by the 40 gratings of the FBG array 2 experiencing the highest temperature along the y -axis. The results of these analyses are illustrated in Figures 4–7.

Figure 4 reports tissue temperatures during LA measured in correspondence to the grating of FBG array 2 experiencing the highest temperature. The profiles obtained in the controlled cases (Figure 4, blue, red, yellow, and purple lines) are distinguishable from the uncontrolled experiment. (Figure 4, green line). In particular, the experiments performed with the temperature-feedback control show that the maximum temperatures follow the set thresholds; moreover, a characteristic sawtooth-like shape is observed, due to the effect of the laser that is switched ON and OFF according to the set T_s and r_s . In each experiment, these maximum temperatures oscillate around the correspondent T_s , and the magnitude of these oscillations depends on r_s . The table enclosed in Figure 4 lists the values of these

oscillations, ΔT_p , which are calculated by the difference between the temperature at the highest peak and the subsequent valley.

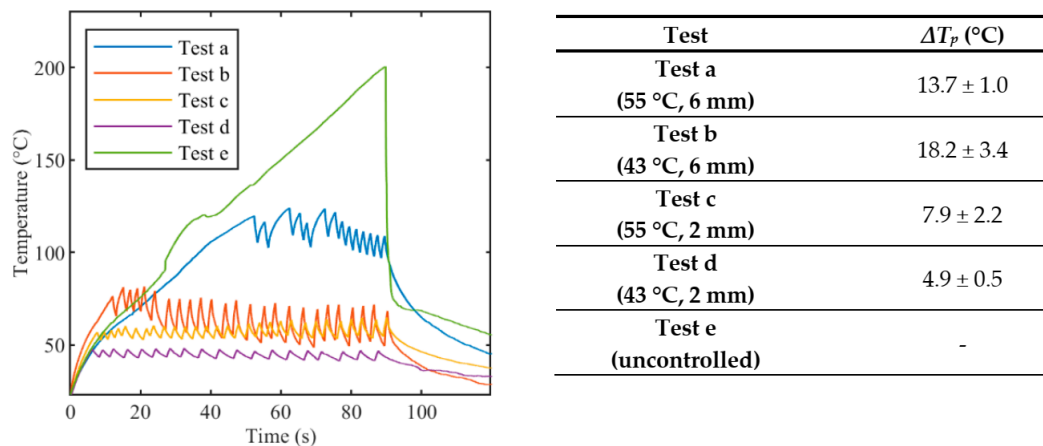


Figure 4. Peak temperature profiles recorded from array #2 during laser ablation: uncontrolled ablation and controlled ablation with different set temperature values T_s . In the Table, oscillations ΔT_p are expressed as mean value \pm standard deviation.

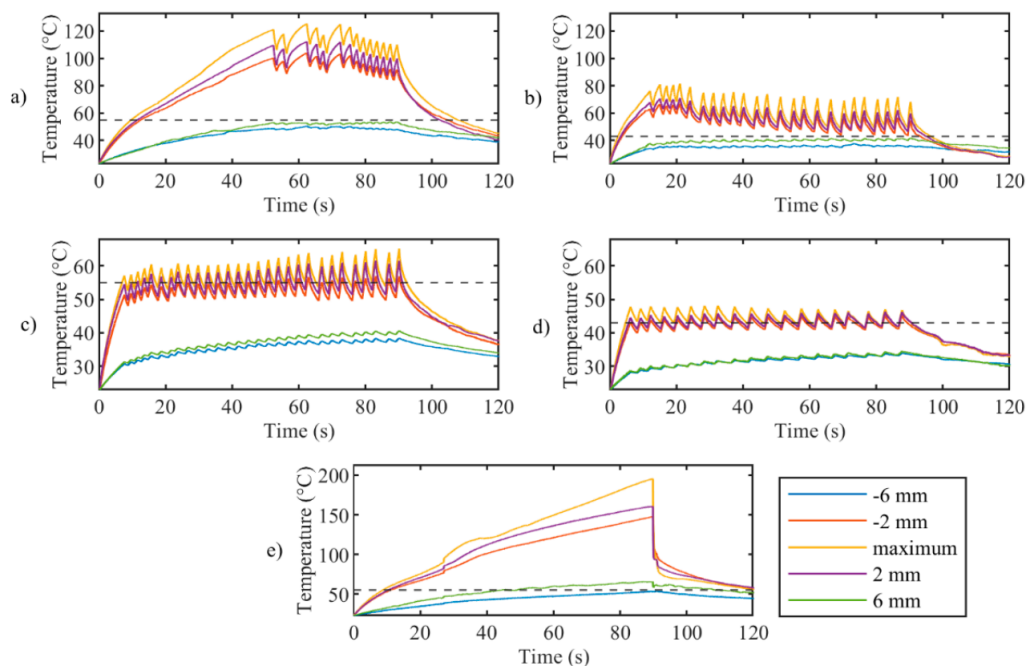


Figure 5. Trends in time of the maximum temperature (yellow curves) and the temperature measured at r_s distances from the center (other 115 profiles are not shown for clarity of the figures) for controlled ablation carried out in (a) Test a, 55 °C and 6 mm; (b) Test b, 43 °C and 6 mm; (c) Test c, 55 °C and 2 mm; (d) Test d, 43 °C and 2 mm; (e) uncontrolled ablation.

In the case of uncontrolled ablation, tissue temperature achieves 200 °C after 90 s of ablation, showing an irregular trend during the time and no oscillations.

Figure 5 presents the maximum temperature profile (yellow lines) and the profiles measured by the sensor placed at the set r_s on FBG array 2. It clearly illustrates that oscillations decrease with distance from the maximum temperature for controlled ablation cases; this happens because, at a certain distance from the laser spot, the temperature elevation due to heat conduction is predominant over the intermittent effect of the control logic. Figure 5 also confirms the proper placement of the FBG

arrays with respect to the laser beam, showing the symmetry of the temperature profiles measured at r_s of ± 6 mm (blue and green curves) and r_s of ± 2 mm (red and purple curves).

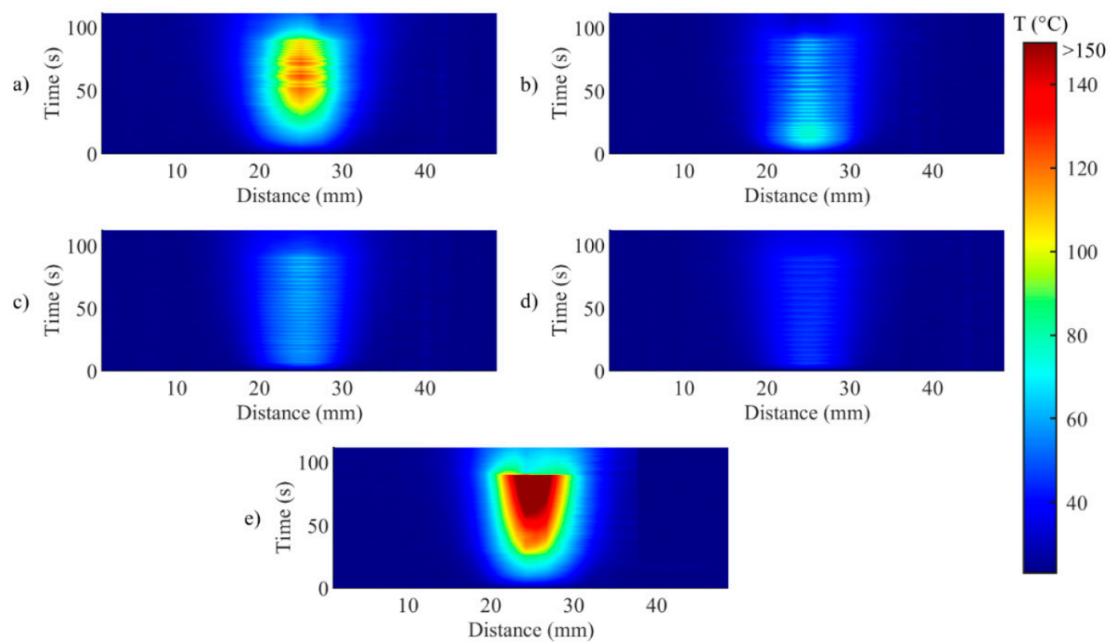


Figure 6. Two-dimensional thermal maps (distance along the sensor vs. time) during (a) Test a, 55 °C and 6 mm; (b) Test b, 43 °C and 6 mm; (c) Test c, 55 °C and 2 mm; (d) Test d, 43 °C and 2 mm; (e) uncontrolled ablation.

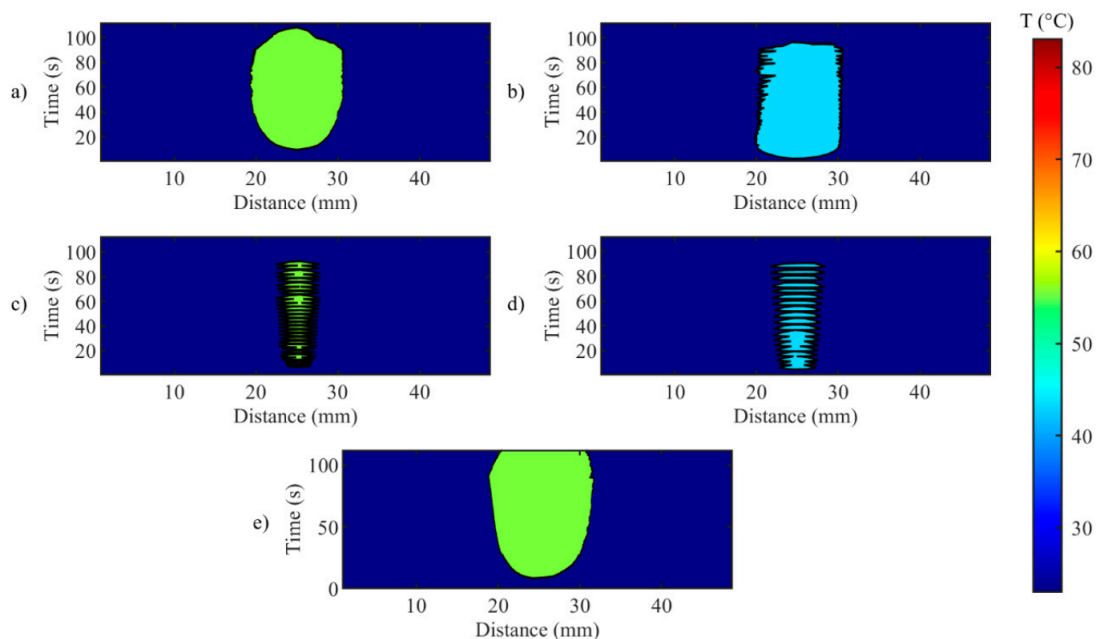


Figure 7. Evolution of the width of the hyperthermia zone (>43 °C) in time for during (a) Test a, 55 °C and 6 mm; (b) Test b, 43 °C and 6 mm; (c) Test c, 55 °C and 2 mm; (d) Test d, 43 °C and 2 mm; (e) uncontrolled ablation.

Figure 6 illustrates the temporal evolution of the temperature profile measured by the FBG array 2, for both controlled (Figure 6a–d) and uncontrolled ablations (Figure 6e). This representation highlights the effect of the control strategy on both the maximum temperature and on the unidimensional distribution of the temperature, in correspondence to the central axis of the ablated region.

For uncontrolled ablation, after the start, the temperature increase causes the heat distributing towards edges of the ablated area with less regular behavior than controlled cases; when ablation is over, the temperature starts to decrease, but the heat dissipation is continuing towards the edges.

Figure 6 anticipates that the edges of the ablated zones are not uniform, as further analyzed in Figure 7, which depicts the evolution of the width of the hyperthermia zone ($>43\text{ }^{\circ}\text{C}$) in time. It is worth mentioning that the zone is small and not continuous for the cases $T_s = 55\text{ }^{\circ}\text{C}$, $r_s = 2\text{ mm}$ and for the case $T_s = 43\text{ }^{\circ}\text{C}$, $r_s = 2\text{ mm}$ (Figure 7c,d). The discontinuities shown in the mentioned cases are due to temperature oscillations occurring around T_s . This phenomenon happens because r_s is chosen close to the center of the circumference, and when T_s was reached, the laser was set immediately OFF, not allowing broadening of the hyperthermia zone. These results highlight the relevance of the size of the zone to be controlled, and the effect of r_s on the temperature distribution experienced by the biological tissue.

3.2. Thermal Analyses on the Spatial Temperature Distribution

Detailed analyses on the effect of the *zone-control logic* on the LA outcome are performed considering the spatial temperature distributions measured by all the 120 gratings. The results of these analyses are illustrated in Figures 8–12.

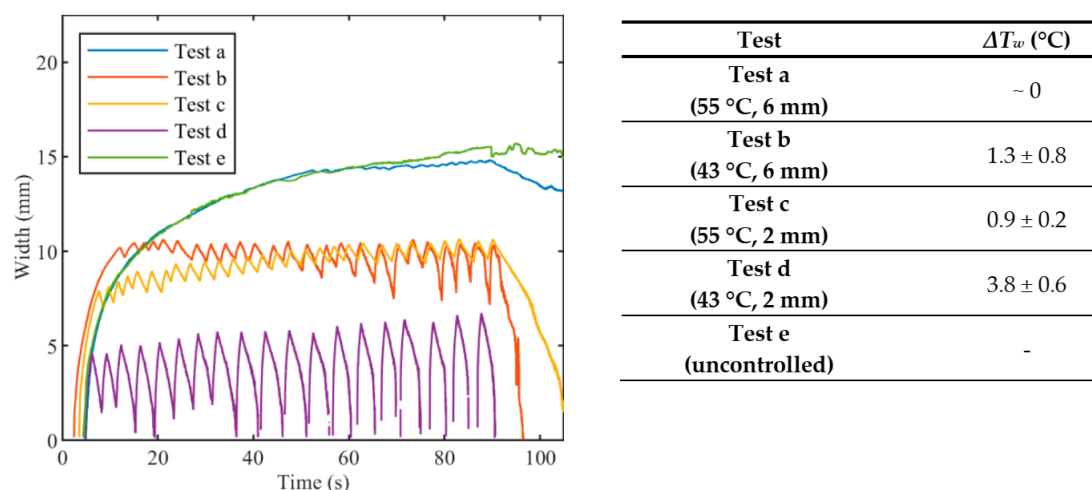


Figure 8. Width of hyperthermia zone ($>43\text{ }^{\circ}\text{C}$) vs. time for controlled ablations with different set temperatures T_s and radii r_s , and for uncontrolled ablation. In the table, oscillations are expressed as mean value \pm standard deviation.

The widths of the contours at $43\text{ }^{\circ}\text{C}$ are presented in Figure 8. Both T_s and r_s affect the width of the hyperthermia zone and the fluctuations of the width. Indeed, the width at $43\text{ }^{\circ}\text{C}$ observed in Test a ($T_s = 55\text{ }^{\circ}\text{C}$, $r_s = 6\text{ mm}$) is close to the width at $43\text{ }^{\circ}\text{C}$ observed in Test e (uncontrolled ablation), and both reach a value of about 15 mm at the end of the thermal procedure. Due to the effect of the heat conduction, after that the laser is switched OFF, the Test a and uncontrolled case show different behavior: the width at $43\text{ }^{\circ}\text{C}$ for the uncontrolled case remains almost constant whereas it starts to drop off immediately for Test a. The widths at $43\text{ }^{\circ}\text{C}$ achieved with Test c ($T_s = 55\text{ }^{\circ}\text{C}$, $r_s = 2\text{ mm}$) and Test b ($T_s = 43\text{ }^{\circ}\text{C}$, $r_s = 6\text{ mm}$) presents similar trends, with a maximum value of about 10 mm at the end of the ablation. For the Test d ($T_s = 43\text{ }^{\circ}\text{C}$, $r_s = 2\text{ mm}$), fluctuation of the width at $43\text{ }^{\circ}\text{C}$ reaches approximately 7 mm, corresponding also to the maximum value at the end of the procedure. The Table enclosed in Figure 8 lists the values of the oscillations of the width (ΔT_w), which are calculated by the difference between the temperature at the highest peak and the temperature at the subsequent lowest peak.

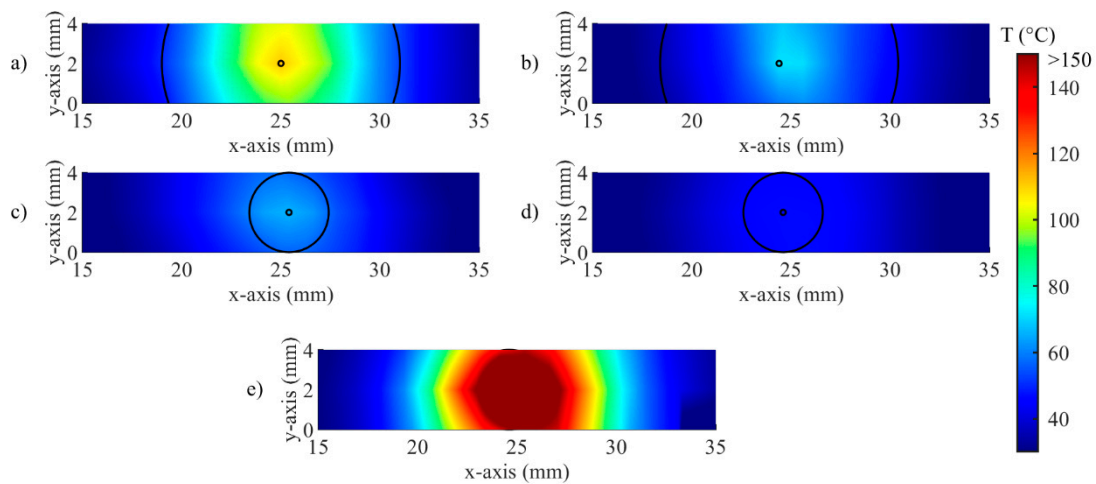


Figure 9. Visualization of the real-time temperature maps and zone control circumferences at $t = 90$ s for (a) Test a, 55 °C and 6 mm; (b) Test b, 43 °C and 6 mm; (c) Test c, 55 °C and 2 mm; (d) Test d, 43 °C and 2 mm; (e) uncontrolled ablation.

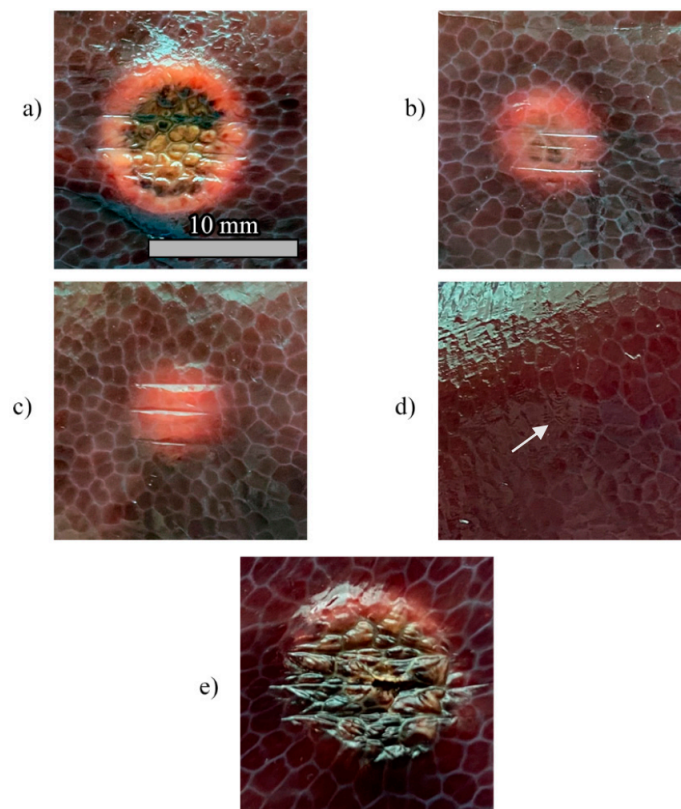


Figure 10. Pictures of the tissue damage produced by the different control strategies for (a) Test a, 55 °C and 6 mm; (b) Test b, 43 °C and 6 mm; (c) Test c, 55 °C and 2 mm; (d) Test d, 43 °C and 2 mm; (e) uncontrolled ablation.

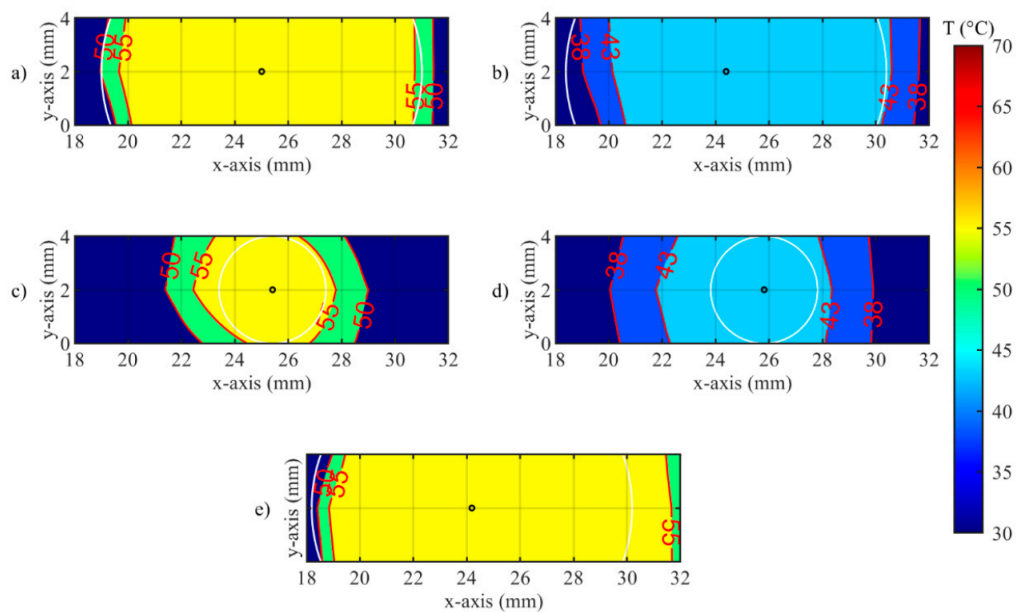


Figure 11. Isotherms of spatial distribution measured on the tissue when laser changes its state from ON to OFF, for (a) Test a, 55 °C and 6 mm; (b) Test b, 43 °C and 6 mm; (c) Test c, 55 °C and 2 mm; (d) Test d, 43 °C and 2 mm; (e) uncontrolled ablation.

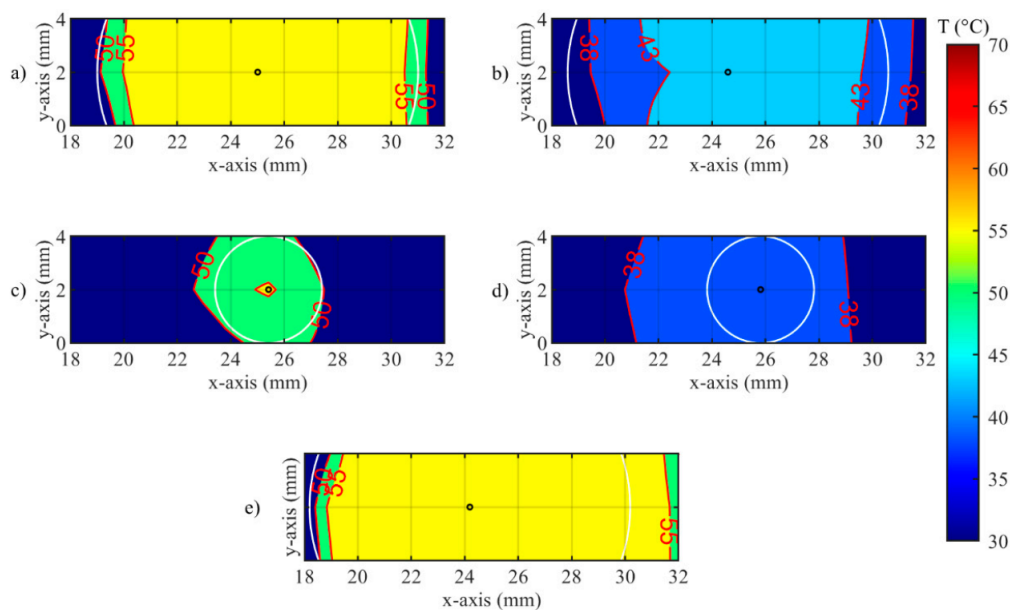


Figure 12. Isotherms of spatial distribution measured on the tissue when laser changes its state from OFF to ON, for (a) Test a, 55 °C and 6 mm; (b) Test b, 43 °C and 6 mm; (c) Test c, 55 °C and 2 mm; (d) Test d, 43 °C and 2 mm; (e) uncontrolled ablation.

An example of the real-time visualization provided by the developed software is given in Figure 9. Here, the spatial distribution of temperature measured by the FBGs is updated during the procedure, and the circumference defined according to r_s are overlapped. The entire circumference is represented for $r_s = 2$ mm (Figure 9c,d), because the distance between arrays is 2 mm; in the case of $r_s = 6$ mm (Figure 9a,b), only two arcs of the circumference can be traced. As expected, no circumference is illustrated for the uncontrolled case (Figure 9e).

Thermal damages obtained in the hepatic tissue with controlled and uncontrolled ablations are presented in Figure 10. The RGB images show that the damage is visible for $T_s = 55$ °C, regardless of the

value of r_s (Figure 10a,c), and that the damaged area increases with r_s . In the experiments carried out at $T_s = 43\text{ }^\circ\text{C}$, the thermal damage is distinguishable only for $r_s = 6\text{ mm}$ (Figure 10b), whereas a minor effect of tissue dehydration is slightly noticeable for $r_s = 2\text{ mm}$ (Figure 10d, white arrow). As expected, the high temperature (up to $200\text{ }^\circ\text{C}$) experienced by the tissue during uncontrolled ablation (Figure 10e) caused the largest damaged area as well as the more severe damage. It is worth highlighting that the uncontrolled ablation margins of the lesion are more irregular than the margins obtained with the *zone-control logic*.

A closer look at the effect of the developed *zone-control logic* is provided by Figures 11 and 12. In these illustrations, the effect of the oscillations previously presented for single fiber measurements is observable on the spatial temperature distribution. Figures 11 and 12 show two specific moments of the implemented temperature feedback regulation, i.e., when the control logic sets the laser from ON to OFF (Figure 11) and from OFF to ON (Figure 12). In the figures, the isothermal regions between the set T_s and $T_s - 5\text{ }^\circ\text{C}$ are shown for each test.

Figure 11 illustrates the isotherms in correspondence of the peak of overshooting (here, laser changes its state from ON to OFF). Indeed, the isotherms of set temperatures reach the set radii, and, in some points, exceeds it. The value of the radius affects the overshooting area: indeed, for $r_s = 2\text{ mm}$, the isotherms at both set T_s are larger than the set circumference.

In Figure 12 the undershooting situation is presented (laser state changes from OFF to ON). Here, the isotherms of set temperature are distant from the set radius, moreover for test d, no region at $43\text{ }^\circ\text{C}$ is detected.

The time evolutions of the spatial temperature maps (thermal and isothermal) for controlled and uncontrolled cases (Test b and e, correspondingly) are reported in the Supplementary Video. The video illustrates the effect of the set parameters on the heat distribution during the ablation procedure.

4. Discussion

This work originally presents a real-time closed-loop temperature control strategy, called *zone-control logic*, for controlling and tuning the laser ablation outcome in biological tissues. The temperature feedback control strategy is based on a custom-made software providing real-time monitoring of the spatial temperature distribution measured by a network of 120 FBGs. FBG arrays with high spatial resolution properties (1.2 mm distance between centers of consecutive gratings) and high-temperature resistance coating were fabricated with the femtosecond point-by-point writing technology [46]. LabVIEW software was used to design and implement the ON–OFF program that regulates the mode of operation of the laser source with the temperature measured in the hepatic tissue. The user interface of the software allows clinician to set two parameters of the procedure, i.e., the radius of the zone to be controlled and the specific temperature, that will be controlled automatically during the procedure. The choice of the parameter values should be based on individual patient's needs, i.e., the size of the tumor obtained from pre-operative images, or typical temperature settings known from the literature. In addition, the real-time temperature mapping is also provided on the user interface.

The results of this work show that the implemented strategy is suitable to achieve the desired control of the ablated area, by opportunely tuning the radius and the set temperature. The set temperature was contained within the proper range, corresponding to specific thermal states of biological tissues inside the low-temperature damage accumulation process [52,53]. Only a few previous studies presented the real-time control of the laser settings according to the tissue temperature, and most of them employed single-point measurements [28,31,51], or contactless thermometric systems [25]. Conversely, our *zone-control logic* allows for a multipoint control of the tissue temperature, which can be adapted according to the size of the desired tissue region to be treated. With the proposed unique approach, the choice of the radius and the temperature threshold can be adapted to the specific needs of the therapy. Our results demonstrated that the width at $43\text{ }^\circ\text{C}$ close to 15 mm can be reached by keeping the ablation zone with radius 6 mm at $55\text{ }^\circ\text{C}$ for 90 s, obtaining a spatial thermal effect similar to the one achieved

with uncontrolled ablation, but in safer conditions. Indeed, when continuous laser irradiation is used, tissue temperature rapidly increased to high values (200 °C) due to the constant supply of laser energy, with potential risks for the organ.

The Figures 6–8 confirm the effect of the control logic on the extension of the thermal margins of the zones, and the effectiveness of having real-time monitoring to observe the evolution of the treatment (Figure 9). Figure 10 further proves the relevance of the *zone-control logic* to contain the damage to the interested area and to achieve regular margins, clearly showing the different thermal outcome in RGB images obtained after uncontrolled and controlled ablations.

The multi-point temperature measurement is enabled thanks to highly dense FBG arrays. The main advantages over other temperature monitoring methods for LA control (thermocouples, thermistors, and photo-optic probes) [28–30] are the following: quasi-distributed sensing capability, minimal invasiveness, and no self-heating, that make them well suited for LA applications. The quasi-distributed monitoring property of FBGs allows for high-spatial-resolution temperature measurements along the fiber and accurate evaluation of the temperature distribution. These peculiarities make the FBGs the good candidates to scale the implemented strategy to control also interstitial laser applications [44].

It has been observed, and further confirmed by this work, that the ON–OFF strategy leads to oscillations of the maximum temperature values across the set threshold [51]. The oscillations contribute to the thermal history of the treatment, due to the heat that remains in the tissue after the laser is turned off and to the cooling occurring between consecutive irradiations [25]. Figure 5 shows that these oscillations are marked in correspondence of the center of the ablation zone, but their amplitudes significantly decrease with the radius of the zone under control, providing smoothly increasing temperature trends at 6 mm from the center of the ablation zone (Figure 5, blue and green curves). Indeed, since the irradiation is repeated before complete cooling of the medium, the elevations of the tissue temperature can be additive [25], but slower than the temperature increase produced by continuous laser (uncontrolled ablation). A further improvement of the control strategy towards the extinguishment of the oscillations can be based on proportional–integral–derivative (PID) control, which has been proved to be effective mostly for single-point measurement [54] and in adaptive control systems [55].

5. Conclusions

This work presents a novel *zone-control logic*, aimed at controlling the outcome of LA in biological tissues through the temperature measured by highly dense FBGs arrays. The implemented strategy and monitoring system provide laser thermal treatment with the ability to maintain a controlled temperature in the targeted area. The results of this study encourage further investigation of the optimal control-loop and laser system settings for improving LA effects. This study provides the foundation for the use of a control strategy for optimizing laser ablation and obtaining predictable outcomes in a clinical scenario, which still requires the support of the technology to provide a reliable endpoint for the treatment efficacy.

Supplementary Materials: The following are available online at <http://www.mdpi.com/1424-8220/20/22/6496/s1>, Video S1: Spatial thermal map (x- and y-axis) evolution during the laser ablation experiments. In the video, the controlled ablation experiment (Test b) is on the top; the uncontrolled experiment (Test e) is on the bottom. Two types of maps are provided: isothermal and thermal distributions. The 6 mm radii are marked with black circles for the controlled and uncontrolled cases.

Author Contributions: Conceptualization, S.K. and P.S.; methodology, S.K., L.B., M.D.L. and P.S.; software, A.O. and S.K.; investigation, S.K., A.O., L.B. and M.D.L.; resources, P.S.; FBG fabrication, A.W. and A.D.; data curation, S.K. and A.O.; writing—original draft preparation, S.K., P.S.; writing—review and editing, S.K., L.B., M.D.L., A.W. and P.S.; supervision, P.S.; funding acquisition, P.S. All authors have read and agreed to the published version of the manuscript.

Funding: This project has received funding from the European Research Council (ERC) under the European Union's Horizon 2020 research and innovation programme (Grant agreement No. 759159). The work of A.W. and A.D. is supported by the State Budget of the Russian Federation (IAE project No. AAAAA17-117062110026-3).

Conflicts of Interest: The authors declare no conflict of interest.

References

1. Sartori, S.; Di Vece, F.; Ermili, F.; Tombesi, P. Laser Ablation of Liver Tumors: An Ancillary Technique, or an Alternative to Radiofrequency and Microwave? *World J. Radiol.* **2017**, *9*, 91. [[CrossRef](#)] [[PubMed](#)]
2. Brace, C.L. Radiofrequency and Microwave Ablation of the Liver, Lung, Kidney, and Bone: What Are the Differences? *Curr. Probl. Diagn. Radiol.* **2009**, *38*, 135–143. [[CrossRef](#)] [[PubMed](#)]
3. Chu, K.F.; Dupuy, D.E. Thermal Ablation of Tumours: Biological Mechanisms and Advances in Therapy. *Nat. Rev. Cancer* **2014**, *14*, 199. [[CrossRef](#)] [[PubMed](#)]
4. Ahmed, M.; Brace, C.L.; Lee, F.T., Jr.; Goldberg, S.N. Principles of and Advances in Percutaneous Ablation. *Radiology* **2011**, *258*, 351–369. [[CrossRef](#)] [[PubMed](#)]
5. Di Matteo, F.M.; Saccomandi, P.; Martino, M.; Pandolfi, M.; Pizzicannella, M.; Balassone, V.; Schena, E.; Pacella, C.M.; Silvestri, S.; Costamagna, G. Feasibility of EUS-Guided Nd:YAG Laser Ablation of Unresectable Pancreatic Adenocarcinoma. *Gastrointest. Endosc.* **2018**, *88*, 168–174.e1. [[CrossRef](#)]
6. Zhou, Y.-F. High Intensity Focused Ultrasound in Clinical Tumor Ablation. *World J. Clin. Oncol.* **2011**, *2*, 8. [[CrossRef](#)]
7. Lubner, M.G.; Brace, C.L.; Hinshaw, J.L.; Lee, F.T., Jr. Microwave Tumor Ablation: Mechanism of Action, Clinical Results, and Devices. *J. Vasc. Interv. Radiol.* **2010**, *21*, S192–S203. [[CrossRef](#)]
8. Goldberg, S.N. Radiofrequency Tumor Ablation: Principles and Techniques. In *Multi-Treatment Modalities of Liver Tumours*; Springer: Boston, MA, USA, 2002; pp. 87–118.
9. Stafford, R.J.; Fuentes, D.; Elliott, A.A.; Weinberg, J.S.; Ahrar, K. Laser-Induced Thermal Therapy for Tumor Ablation. *Crit. Rev. Biomed. Eng.* **2010**, *38*, 79–100. [[CrossRef](#)]
10. Schena, E.; Saccomandi, P.; Fong, Y. Laser Ablation for Cancer: Past, Present and Future. *J. Funct. Biomater.* **2017**, *8*, 19. [[CrossRef](#)]
11. Tozburun, S. Superficial Photothermal Laser Ablation of Ex Vivo Sheep Esophagus Using a Cone-shaped Optical Fiber Tip. *J. Biophotonics* **2020**, *13*, e201960116. [[CrossRef](#)]
12. Quero, G.; Saccomandi, P.; Kwak, J.-M.; Dallemagne, B.; Costamagna, G.; Marescaux, J.; Mutter, D.; Diana, M. Modular Laser-Based Endoluminal Ablation of the Gastrointestinal Tract: In Vivo Dose–Effect Evaluation and Predictive Numerical Model. *Surg. Endosc.* **2019**, *33*, 3200–3208. [[CrossRef](#)] [[PubMed](#)]
13. Saccomandi, P.; Quero, G.; Gassino, R.; Lapergola, A.; Guerriero, L.; Diana, M.; Vallan, A.; Perrone, G.; Schena, E.; Costamagna, G.; et al. Laser Ablation of the Biliary Tree: In Vivo Proof of Concept as Potential Treatment of Unresectable Cholangiocarcinoma. *Int. J. Hyperth.* **2018**, *34*, 1372–1380. [[CrossRef](#)] [[PubMed](#)]
14. Yang, J.; Choi, J.; Bang, D.; Kim, E.; Lim, E.-K.; Park, H.; Suh, J.-S.; Lee, K.; Yoo, K.-H.; Kim, E.-K.; et al. Convertible Organic Nanoparticles for Near-Infrared Photothermal Ablation of Cancer Cells. *Angew. Chem. Int. Ed.* **2011**, *50*, 441–444. [[CrossRef](#)] [[PubMed](#)]
15. Asadi, S.; Bianchi, L.; De Landro, M.; Korganbayev, S.; Schena, E.; Saccomandi, P. Laser-Induced Optothermal Response of Gold Nanoparticles: From a Physical Viewpoint to Cancer Treatment Application. *J. Biophotonics* **2020**, e202000161. [[CrossRef](#)]
16. Gangi, A.; Alizadeh, H.; Wong, L.; Buy, X.; Dietemann, J.-L.; Roy, C. Osteoid Osteoma: Percutaneous Laser Ablation and Follow-up in 114 Patients. *Radiology* **2007**, *242*, 293–301. [[CrossRef](#)]
17. Schwarzmaier, H.-J.; Eickmeyer, F.; von Tempelhoff, W.; Fiedler, V.U.; Niehoff, H.; Ulrich, S.D.; Yang, Q.; Ulrich, F. MR-Guided Laser-Induced Interstitial Thermotherapy of Recurrent Glioblastoma Multiforme: Preliminary Results in 16 Patients. *Eur. J. Radiol.* **2006**, *59*, 208–215. [[CrossRef](#)]
18. Pacella, C.M.; Bizzarri, G.; Guglielmi, R.; Anelli, V.; Bianchini, A.; Crescenzi, A.; Pacella, S.; Papini, E. Thyroid Tissue: US-Guided Percutaneous Interstitial Laser Ablation—A Feasibility Study. *Radiology* **2000**, *217*, 673–677. [[CrossRef](#)]
19. Vogl, T.J.; Straub, R.; Eichler, K.; Söllner, O.; Mack, M.G. Colorectal Carcinoma Metastases in Liver: Laser-Induced Interstitial Thermotherapy—Local Tumor Control Rate and Survival Data. *Radiology* **2004**, *230*, 450–458. [[CrossRef](#)]
20. Di Matteo, F.; Martino, M.; Rea, R.; Pandolfi, M.; Rabitti, C.; Masselli, G.M.P.; Silvestri, S.; Pacella, C.M.; Papini, E.; Panzera, F. EUS-Guided Nd: YAG Laser Ablation of Normal Pancreatic Tissue: A Pilot Study in a Pig Model. *Gastrointest. Endosc.* **2010**, *72*, 358–363. [[CrossRef](#)]

21. Saccomandi, P.; Schena, E.; Caponero, M.A.; Di Matteo, F.M.; Martino, M.; Pandolfi, M.; Silvestri, S. Theoretical Analysis and Experimental Evaluation of Laser-Induced Interstitial Thermotherapy in Ex Vivo Porcine Pancreas. *IEEE Trans. Biomed. Eng.* **2012**, *59*, 2958–2964. [[CrossRef](#)]
22. Saccomandi, P.; Lapergola, A.; Longo, F.; Schena, E.; Quero, G. Thermal Ablation of Pancreatic Cancer: A Systematic Literature Review of Clinical Practice and Pre-Clinical Studies. *Int. J. Hyperth.* **2018**, *35*, 398–418. [[CrossRef](#)] [[PubMed](#)]
23. Welch, A.J.; Van Gemert, M.J.C. *Optical-Thermal Response of Laser-Irradiated Tissue*; Welch, A.J., Van Gemert, M.J.C., Eds.; Springer: Dordrecht, The Netherlands, 2011. [[CrossRef](#)]
24. Brace, C. Thermal Tumor Ablation in Clinical Use. *IEEE Pulse* **2011**, *2*, 28–38. [[CrossRef](#)] [[PubMed](#)]
25. Nomura, S.; Arake, M.; Morimoto, Y.; Tsujimoto, H.; Miyazaki, H.; Saitoh, D.; Shinomiya, N.; Hase, K.; Yamamoto, J.; Ueno, H. Thermal Sensor Circuit Using Thermography for Temperature-Controlled Laser Hyperthermia. *J. Sens.* **2017**, *2017*, 1–7. [[CrossRef](#)]
26. Wheatley, D.N.; Kerr, C.; Gregory, D.W. Heat-Induced Damage to HeLa-S3 Cells: Correlation of Viability, Permeability, Osmosensitivity, Phase-Contrast Light-, Scanning Electron- and Transmission Electron-Microscopical Findings. *Int. J. Hyperth.* **1989**, *5*, 145–162. [[CrossRef](#)] [[PubMed](#)]
27. Yarmolenko, P.S.; Moon, E.J.; Landon, C.; Manzoor, A.; Hochman, D.W.; Viglianti, B.L.; Dewhirst, M.W. Thresholds for Thermal Damage to Normal Tissues: An Update. *Int. J. Hyperth.* **2011**, *27*, 320–343. [[CrossRef](#)] [[PubMed](#)]
28. Ivarsson, K.; Olsrud, J.; Stuesson, C. Feedback Interstitial Diode Laser (805 Nm) Thermotherapy System: Ex Vivo Evaluation and Mathematical Modeling With One and Four-Fibers. *Lasers Surg. Med.* **1998**, *22*, 86–96. [[CrossRef](#)]
29. Möller, P.H.; Lindberg, L.; Henriksson, P.H.; Persson, B.R.; Tranberg, K.G. Temperature Control and Light Penetration in a Feedback Interstitial Laser Thermotherapy System. *Int. J. Hyperth.* **1996**, *12*, 49–63. [[CrossRef](#)]
30. Wohlgemuth, W.A.; Wamser, È.; Reiss, T.; Wagner, T. In Vivo Laser-Induced Interstitial Thermotherapy of Pig Liver With a Temperature-Controlled Diode Laser and MRI Correlation. *Lasers Surg. Med.* **2001**, *29*, 374–378. [[CrossRef](#)]
31. Lin, J.T.; Chiang, Y.S.; Lin, G.H.; Lee, H.; Liu, H.W. In Vitro Photothermal Destruction of Cancer Cells Using Gold Nanorods and Pulsed-Train near-Infrared Laser. *J. Nanomater.* **2012**, *2012*, 1385. [[CrossRef](#)]
32. Lin, J.; Hong, Y.; Chang, C. Selective Cancer Therapy via IR-Laser-Excited Gold Nanorods. In *Optical Interactions with Tissues and Cells XXI*; Jansen, E.D., Thomas, R.J., Eds.; International Society for Optics and Photonics: San Francisco, CA, USA, 2010; Volume 7562, p. 75620R. [[CrossRef](#)]
33. Saccomandi, P.; Schena, E.; Silvestri, S. Techniques for Temperature Monitoring during Laser-Induced Thermotherapy: An Overview. *Int. J. Hyperth.* **2013**, *29*, 609–619. [[CrossRef](#)]
34. Manns, F.; Milne, P.J.; Gonzalez-Cirre, X.; Denham, D.B.; Parel, J.; Robinson, D.S. In Situ Temperature Measurements with Thermocouple Probes during Laser Interstitial Thermotherapy (LITT): Quantification and Correction of a Measurement Artifact. *Lasers Surg. Med. Off. J. Am. Soc. Laser Med. Surg.* **1998**, *23*, 94–103. [[CrossRef](#)]
35. Schena, E.; Tosi, D.; Saccomandi, P.; Lewis, E.; Kim, T. Fiber Optic Sensors for Temperature Monitoring during Thermal Treatments: An Overview. *Sensors* **2016**, *16*, 1144. [[CrossRef](#)] [[PubMed](#)]
36. Morra, F.; De Landro, M.; Korganbayev, S.; Wolf, A.; Dostovalov, A.; Cigada, A.; Saccomandi, P. Spatially Resolved Thermometry during Laser Ablation in Tissues: Distributed and Quasi-Distributed Fiber Optic-Based Sensing. *Opt. Fiber Technol.* **2020**, *58*, 102295. [[CrossRef](#)]
37. Macchi, E.G.; Tosi, D.; Braschi, G.; Gallati, M.; Cigada, A.; Busca, G.; Lewis, E. Optical Fiber Sensors-Based Temperature Distribution Measurement in Ex Vivo Radiofrequency Ablation with Submillimeter Resolution. *J. Biomed. Opt.* **2014**, *19*, 117004. [[CrossRef](#)] [[PubMed](#)]
38. Beccaria, A.; Bellone, A.; Mirigaldi, A.; Serafini, V.; Olivero, M.; Vallan, A.; Perrone, G. Temperature Monitoring of Tumor Hyperthermal Treatments with Optical Fibers: Comparison of Distributed and Quasi-Distributed Techniques. *Opt. Fiber Technol.* **2020**, *60*, 102340. [[CrossRef](#)]
39. Erdogan, T. Fiber Grating Spectra. *J. Light. Technol.* **1997**, *15*, 1277–1294. [[CrossRef](#)]
40. Lee, K.K.C.; Mariampillai, A.; Haque, M.; Standish, B.A.; Yang, V.X.D.; Herman, P.R. Temperature-Compensated Fiber-Optic 3D Shape Sensor Based on Femtosecond Laser Direct-Written Bragg Grating Waveguides. *Opt. Express* **2013**, *21*, 24076–24086. [[CrossRef](#)]

41. Ashikbayeva, Z.; Aitkulov, A.; Jelbuldina, M.; Issatayeva, A.; Beisenova, A.; Molardi, C.; Saccomandi, P.; Blanc, W.; Inglezakis, V.J.; Tosi, D. Distributed 2D Temperature Sensing during Nanoparticles Assisted Laser Ablation by Means of High-Scattering Fiber Sensors. *Sci. Rep.* **2020**, *10*, 12593. [[CrossRef](#)]
42. Chen, W.; Gassino, R.; Liu, Y.; Carullo, A.; Perrone, G.; Vallan, A.; Tosi, D. Performance Assessment of FBG Temperature Sensors for Laser Ablation of Tumors. In Proceedings of the 2015 IEEE International Symposium on Medical Measurements and Applications (MeMeA) Proceedings, Turin, Italy, 7–9 May 2015; pp. 324–328.
43. Gassino, R.; Liu, Y.; Konstantaki, M.; Vallan, A.; Pissadakis, S.; Perrone, G. A Fiber Optic Probe for Tumor Laser Ablation With Integrated Temperature Measurement Capability. *J. Light. Technol.* **2017**, *35*, 3447–3454. [[CrossRef](#)]
44. Saccomandi, P.; Schena, E.; Di Matteo, F.M.; Pandolfi, M.; Martino, M.; Rea, R.; Silvestri, S. Laser Interstitial Thermotherapy for Pancreatic Tumor Ablation: Theoretical Model and Experimental Validation. In Proceedings of the Annual International Conference of the IEEE Engineering in Medicine and Biology Society, EMBS, Boston, MA, USA, 30 August–3 September 2011. [[CrossRef](#)]
45. De Vita, E.; De Landro, M.; Massaroni, C.; Iadicicco, A.; Saccomandi, P.; Schena, E.; Campopiano, S. Fiber Optic Sensors-Based Thermal Analysis of Perfusion-Mediated Tissue Cooling in Liver Undergoing Laser Ablation. *IEEE Trans. Biomed. Eng.* **2020**, *1*. [[CrossRef](#)]
46. Dostovalov, A.V.; Wolf, A.A.; Parygin, A.V.; Zyubin, V.E.; Babin, S.A. Femtosecond Point-by-Point Inscription of Bragg Gratings by Drawing a Coated Fiber through Ferrule. *Opt. Express* **2016**, *24*, 16232–16237. [[CrossRef](#)] [[PubMed](#)]
47. Gratten, K.T.V.; Meggitt, B.T. *Optical Fiber Sensor Technology: Volume 3: Applications and Systems*; Springer: Boston, MA, USA, 1999; Volume 3.
48. Huang, L.; Dyer, R.S.; Lago, R.J.; Stolov, A.A.; Li, J. Mechanical Properties of Polyimide Coated Optical Fibers at Elevated Temperatures. In *Optical Fibers and Sensors for Medical Diagnostics and Treatment Applications XVI*; Gannot, I., Ed.; International Society for Optics and Photonics: San Francisco, CA, USA, 2016; p. 97020Y. [[CrossRef](#)]
49. Othonos, A.; Kalli, K.; Kohnke, G.E. Fiber Bragg Gratings: Fundamentals and Applications in Telecommunications and Sensing. *Phys. Today* **2000**, *53*, 61. [[CrossRef](#)]
50. Brinkmann, R.; Hansen, C.; Mohrenstecher, D.; Scheu, M.; Birngruber, R. Analysis of Cavitation Dynamics during Pulsed Laser Tissue Ablation by Optical On-Line Monitoring. *IEEE J. Sel. Top. Quantum Electron.* **1996**, *2*, 826–835. [[CrossRef](#)]
51. Korganbayev, S.; Pini, R.; Orrico, A.; Wolf, A.; Dostovalov, A.; Saccomandi, P. Towards Temperature-Controlled Laser Ablation Based on Fiber Bragg Grating Array Temperature Measurements. In Proceedings of the 2020 IEEE International Workshop on Metrology for Industry 4.0 & IoT, Roma, Italy, 3–5 June 2020; pp. 268–272.
52. Thomsen, S. Pathologic Analysis of Photothermal and Photomechanical Effects of Laser-Tissue Interactions. *Photochem. Photobiol.* **1991**, *53*, 825–835. [[CrossRef](#)]
53. Nagarajan, V.K.; Ward, J.M.; Yu, B. Association of Liver Tissue Optical Properties and Thermal Damage. *Lasers Surg. Med.* **2020**, *52*, 779–787. [[CrossRef](#)]
54. Nguyen, T.H.; Park, S.; Hlaing, K.K.; Kang, H.W. Temperature Feedback-Controlled Photothermal Treatment with Diffusing Applicator: Theoretical and Experimental Evaluations. *Biomed. Opt. Express* **2016**, *7*, 1932. [[CrossRef](#)]
55. Sun, L.; Collins, C.M.; Schiano, J.L.; Smith, M.B.; Smith, N.B. Adaptive Real-Time Closed-Loop Temperature Control for Ultrasound Hyperthermia Using Magnetic Resonance Thermometry. *Concepts Magn. Reson. Part B Magn. Reson. Eng.* **2005**, *27B*, 51–63. [[CrossRef](#)]

Publisher's Note: MDPI stays neutral with regard to jurisdictional claims in published maps and institutional affiliations.



© 2020 by the authors. Licensee MDPI, Basel, Switzerland. This article is an open access article distributed under the terms and conditions of the Creative Commons Attribution (CC BY) license (<http://creativecommons.org/licenses/by/4.0/>).



Quasi-distributed fiber optic sensor-based control system for interstitial laser ablation of tissue: theoretical and experimental investigations

LEONARDO BIANCHI,  SANZHAR KORGANBAYEV,  ANNALISA ORRICO,  MARTINA DE LANDRO,  AND PAOLA SACCOMANDI* 

Department of Mechanical Engineering, Politecnico di Milano, Milan, Italy

**paola.saccomandi@polimi.it*

Abstract: This work proposes the quasi-distributed real-time monitoring and control of laser ablation (LA) of liver tissue. To confine the thermal damage, a pre-planning stage of the control strategy based on numerical simulations of the bioheat-transfer was developed to design the control parameters, then experimentally assessed. Fiber Bragg grating (FBG) sensors were employed to design the automatic thermometry system used for temperature feedback control for interstitial LA. The tissue temperature was maintained at a pre-set value, and the influence of different sensor locations (on the direction of the beam propagation and backward) on the thermal outcome was evaluated in comparison with the uncontrolled case. Results show that the implemented computational model was able to properly describe the temperature evolution of the irradiated tissue. Furthermore, the realized control strategy allowed for the accurate confinement of the laser-induced temperature increase, especially when the temperature control was actuated by sensors located in the direction of the beam propagation, as confirmed by the calculated fractions of necrotic tissues (e.g., 23 mm³ and 53 mm³ for the controlled and uncontrolled LA, respectively).

© 2021 Optical Society of America under the terms of the [OSA Open Access Publishing Agreement](#)

1. Introduction

Electromagnetic-based thermal techniques are currently widely investigated as minimally invasive treatments for solid tumor removal [1]. Among the diverse ablative procedures [2–4], laser ablation (LA) has raised considerable attention for clinical applications [5]. Typical advantages are the capability to deliver the therapeutic laser beam through small and flexible optical fibers able to target deep-seated organs [6], and the compatibility with diagnostic imaging techniques for therapy guidance [7]. Furthermore, the reduced invasiveness and pain, associated with this ablative procedure, could reduce the recovery time, and could represent an alternative to surgical resection [8]. In this concern, interstitial LA, based on the irreversible thermal damage of neoplasms due to photothermal conversion of near-infrared (NIR) light into heat, has shown promising results for the local treatment of liver [9], brain [10,11], prostate [12], lung [13], pancreas [14] and breast tissue [15].

However, LA still holds some downsides which prevent the inclusion of this technique into clinical practice, such as the charred tissue at the applicator tip due to high-temperature gradient (>50 °C/mm) and consequent overheating [16], and the potential risk of irreversible injury to the surrounding healthy structures. Indeed, the maintenance of thermal coagulation and necrosis within the selected tissue margins, surrounding the targeted tumor shape, is often challenging. This concern can be ascribed to the absence of a real-time temperature feedback control strategy and the lack of dedicated pre-treatment planning which are responsible for the inaccuracy of the overall thermal procedure [6,17]. The evaluation and control of the spatially resolved tissue temperature evolution are of paramount importance as the prime factors triggering the damage

to tumorous cells and allowing for a safety temperature margin around the lesion to prevent undesired damage. Temperatures of 60 °C are typically known to induce instantaneous and irreversible thermal damage, due to protein denaturation, collapses of the cellular membranes, and impairment of mitochondrial function. Conversely, temperatures comprised between 41–45 °C typically refer to the so-called sublethal damage as reversible injury occurs [18]. However, if these temperature values are kept for a sufficiently long time, the thermal effect can still be achieved in the tissue. In this regard, the synergistic role of temperature and time in the induction of thermal damage is described by well-known models such as Cumulative Equivalent Minutes at 43 °C (CEM43) and Arrhenius [19,20].

Different strategies have been implemented for the local monitoring of the biological tissue temperature and to confine the attained temperature values within specific ranges during thermal therapies. Most of the works in this field employ standard sensors, such as thermocouples and thermistors [21–23]. These works usually rely on the use of single-point measurement to perform the temperature control strategy, hence leading to increased invasiveness when more sensors are needed for performing both control and monitoring in the tissue. In other cases, thermometric approaches based on diagnostic imaging are also proposed for regulating heating, eliminating tissue carbonization, and protecting fiber optic applicators [24]. These techniques are interesting for the estimation of the thermal dose based on the spatially resolved measured temperature map, but they are still far to be considered as routinely and widely available approaches for all the thermal procedures in clinical settings. On the contrary, fiber optic technology is an advantageous alternative to conventional sensing methods. Thanks to the possible multipoint temperature measurements and low heat conductivity, fiber optic sensors are suitable for laser-assisted therapies [25]. Particularly, fiber Bragg grating (FBG) sensors embedded into biocompatible optical fibers are attractive for quasi-distributed sensing during thermal treatments due to also the multiplexing capability [26,27]. Recently, our group has developed an FBG-based closed-loop temperature control algorithm able to control tissue temperature during contactless irradiation in order to maintain the desired set temperature at the margins of the targeted zone [28]. In this preliminary experimental work, the use of FBG arrays allowed for quasi-distributed monitoring, able to also provide information about the spatial temperature distribution reached in the tissue. Although the results demonstrated the feasibility of FBGs control to confine the temperature in a specific area, this study was limited to a superficial treatment without any assessment of the pre-planning procedural settings parameters. Indeed, contactless LA was used as a first step to validate our strategy, but it remains far from clinical settings.

To move towards a real application of LA, an efficient control strategy should be investigated in a contact modality (i.e., interstitial) and supported by simulation-based pre-planning models [29]. These tools allow optimizing the control parameters, e.g., the appropriate laser dose, the sensor position, to attain the required pre-planning of the experiments. This approach has been adopted also in some excellent recent studies, which are still using some simplifications, such as the non-dependency of the tissue optical properties with coagulation [29], or the low sensing resolution of the temperature-based modulation technique [30].

In the present study, we combine the implementation of a pre-planning control stage with the use of FBGs for temperature feedback control of interstitial LA and for model validation. Therefore, a computational model of the bioheat transfer in biological tissue has been implemented for numerically assessing the volumetric heat distribution and the associated tissue changes. Highly dense FBG arrays have been utilized to spatially confine the thermal distribution at specific locations from the laser applicator, assuring the maintenance of pre-set margins of ablation. Additionally, the effects of the position of the controlling sensors on the final thermal outcome have been investigated from both theoretical and experimental viewpoints.

2. Materials and methods

2.1. Laser irradiation of the tissue phantom

To evaluate the efficacy of the developed interstitial LA control approach, experiments on *ex vivo* porcine liver tissue were performed. We selected the liver tissue since it is well characterized in terms of optical and thermal properties [31–33]. Hence, it can be a valuable model for studying the control strategy for interstitial LA, from both a theoretical and empirical viewpoint. The fresh swine liver tissue was obtained from a local butchery on the same day of the experiments, and it was kept at 4 °C before the tests. An 808 nm diode laser (LuOcean Mini 4, Lumics, Berlin, Germany) was used to irradiate the liver at room temperature. The initial tissue temperature, $T_0 = 23$ °C, was measured with a type K thermocouple. Laser light was conveyed by a flexible quartz optical fiber inserted into the liver tissue. The laser power of 2 W was delivered for 120 s during each ablation test. This choice is motivated by the use of the *ex vivo* liver, where the absence of heat-sink effect due to blood perfusion could lead to high temperatures close to the applicator tip, especially in uncontrolled experiments. Moreover, in all the controlled tests, the control logic resulted to be activated under these settings.

2.2. Fiber optic sensors

To provide temperature measurements for LA control, four custom-made FBG array fiber-optic sensors were employed. The polyimide coating of the utilized fibers provides a high-temperature resistance (up to 400 °C) and low thermal conductivity properties [34–36], important for accurate measurements near the laser applicator tip, where temperature gradient can reach 50 °C/mm [16]. Each FBG array has 40 gratings and the following properties: a grating length equal to 1.19 mm, and a 0.01 mm edge-to-edge distance between gratings. As a result, the arrays have a spatial resolution of 1.2 mm and the total sensing length equal to 48 mm. The thermal sensitivity of the sensors is $(7.43 \pm 0.01) \times 10^{-6}$ °C⁻¹. More details about sensors' fabrication, characteristics, and calibration are provided in the previous work of our group [28]. The principle of FBG temperature reconstruction is based on the phenomenon of Bragg wavelength shift induced by the applied temperature. As a result, peak tracking of FBG reflected spectrum allows measurements of temperature change along the FBG structure. To measure the reflection spectra of the FBG arrays, Micron Optics si255 interrogation unit (Micron Optics, Atlanta, USA) with 100 Hz sampling rate was utilized. The data from Micron Optics were analyzed in real-time on a computer by the custom LabVIEW program developed to obtain real-time temperature profiles along the connected FBG arrays and use temperature information for controlling the laser diode power settings.

2.3. Experimental arrangement

To guarantee accurate positioning of the laser applicator and the sensors inside the liver, a custom-made plexiglass box was used (Fig. 1(a) and Fig. 1(b)) [26]. The box with holes positioned at a 2 mm distance from each other on all sides of the box allows a wide range of different positionings of the sensors and the laser applicator. Figure 1 illustrates the experimental arrangement used for all tests: the central hole was used for the laser applicator (blue circle in Fig. 1(c)), and four holes positioned at 4 mm distances from the central hole were used to insert FBG arrays parallel to the applicator (green circles in Fig. 1(c)). The fibers were sequentially inserted into the tissue. A needle (18 gauge) was utilized to insert FBG array fibers into hepatic tissue and it was removed before proceeding with the laser irradiation. Each insertion was manually performed and needed approximately 2 min.

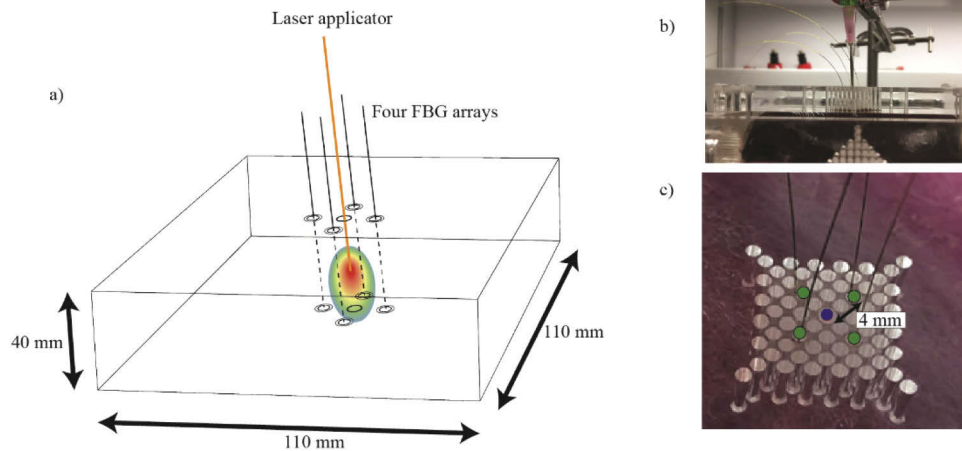


Fig. 1. Experimental setup: (a) schematics of the positioning of laser applicator and fiber Bragg grating (FBG) arrays in the liver placed in plexiglass box; (b) photo of the experimental box employed for maintaining the position of the fibers; (c) close-up of the box with labeled holes for the placement of the fiber optic sensors (green color, diameter of the hole equal to 1 mm) and the laser applicator (blue color, diameter of the hole equal to 1.5 mm) inside the *ex vivo* liver.

2.4. Control logic

The quasi-distributed sensing property of FBG arrays allows for different temperature control approaches depending on the arrangement of the applicator and the sensors, and the controlled parameter of the temperature (e.g., maximum temperature, the temperature at a specific position, overall temperature profile). The algorithm for interstitial ablation developed in this work aims to maintain the temperatures at the margins of the treated region below the pre-set value. The treated region is defined by 4 parallel FBG arrays and the plane z_d which is perpendicular to the laser applicator axis (that is the z -axis) and positioned at a distance d from the applicator tip (Fig. 2(a)). This approach allows controlling the temperature distribution at any distance from the applicator tip, which can be essential in case of the presence of affecting factors at specific positions, such as blood vessels, tumor's edge, or healthy tissue that should be preserved undamaged.

The algorithm consists of three main stages: (i) pre-setting: setting of the input parameters based on simulation outcome, before the start of LA; (ii) alignment phase; (iii) ON-OFF control of laser irradiation based on temperature measurements.

For the first stage, after positioning of the sensors and the laser applicator in the box, three parameters are needed to be set before the LA procedure: the laser power P , the set temperature T_S and the controlled distance d . T_S is the maximum tissue temperature maintained by the control algorithm on the selected zone. This zone is defined by the z_d plane perpendicular to the laser applicator and 4 point-measurements, from the 4 FBG arrays, located within the defined plane; the position of the z_d plane (which lies in the xy plane) is defined by the controlled distance d (Fig. 2(a)). The efficacy of the pre-set values for the aimed ablation is validated by the simulations before the LA procedure. Five different planes of interest z_d were considered at d equal to -3 mm, -2 mm, 0 mm, +2mm, and +3 mm, where the positive sign indicates that the same direction of the laser beam irradiation is considered.

Automatic spatial alignment of FBGs' temperature profiles is utilized in the second stage of the algorithm (Fig. 2(b)). The alignment employs the centroid method that adjusts the centers of temperature profiles measured by each FBG array along the z -direction [26]. Particularly,

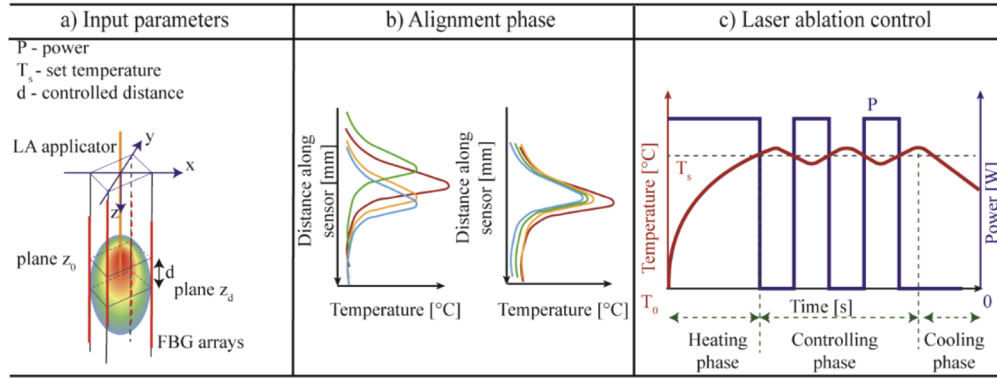


Fig. 2. Laser ablation (LA) control: (a) pre-set of input parameters: laser power P , set temperature T_s , and controlled distance d to define the controlled plane z_d . Red lines illustrate the sensing regions of fiber Bragg grating (FBG) arrays that are not spatially aligned; (b) alignment of measured temperature profiles for four FBG arrays. Peaks of measured temperatures correspond to plane z_0 ; (c) ON-OFF control of maximum temperature measured at the plane z_d : the graph depicts the power and temperature evolution. T_0 represents the room temperature.

the centroid method is automatically implemented at the moment when maximum temperatures measured by each FBG array reach 6°C when a clear Gaussian temperature profile can be observed. The alignment is performed in one LabVIEW iteration (~ 3 ms).

The developed algorithm implemented in LabVIEW utilizes an ON-OFF control logic: the laser power P is switched off if the measured peak temperature is equal to or higher than the set temperature T_s , and switched on if the measured peak temperature is less than T_s (Fig. 2(c)). Comparison of the 4 measured temperature values on the z_d plane and T_s is performed each $\Delta\tau$ seconds:

$$\begin{cases} P = 0W & \text{if } T - T_s \geq 0 \quad \wedge \quad t = n \cdot \Delta\tau \quad n \in \mathbb{N} \\ P = 2W & \text{if } T - T_s < 0 \quad \wedge \quad t = n \cdot \Delta\tau \quad n \in \mathbb{N} \end{cases} \quad (1)$$

The temperature comparison period $\Delta\tau$ was set to 0.5 s to avoid possible overloading of the laser diode equipment [37]. It is important to highlight that the system response is delayed due to $\Delta\tau$, and, to more extent, due to the delayed temperature response at a 4 mm distance from the applicator, due to the heat conduction in the treated tissue. T_s can be set by the user; in this study, for both simulations and experiments, it was set at 40°C to ensure, at the selected spatial location, the avoidance of a temperature value able to activate the tissue immune responses that typically occur in the range between 42°C and 45°C [38].

3. Computational model of temperature-controlled interstitial laser ablation

3.1. Theoretical model

The laser-induced thermal response of *ex vivo* biological tissue was modeled by the heat diffusion equation [39], expressed as

$$\rho \cdot c \cdot \frac{\partial T}{\partial t} + \nabla(-k\nabla T) = Q_{laser} \quad (2)$$

where ρ ($\text{kg}\cdot\text{m}^{-3}$), c ($\text{J}\cdot\text{kg}^{-1}\cdot\text{K}^{-1}$) and k ($\text{W}\cdot\text{m}^{-1}\cdot\text{K}^{-1}$) are the density, the specific heat, and the thermal conductivity of tissue, respectively; T (K) is the tissue temperature and Q_{laser} ($\text{W}\cdot\text{m}^{-3}$) is

the heat generation term due to laser-tissue interaction. The contribution of the metabolic heat source and the blood perfusion were placed equal to zero in the present model, for simulating the LA procedure on *ex vivo* tissue. The penetration of laser light in the tissue and the deposited thermal energy due to laser light absorption in the biological media can be addressed according to the Beer-Lambert law [14]:

$$Q_{laser} = \alpha_a \cdot I_r \cdot e^{-\alpha_a \cdot d_t} \quad (3)$$

where α_a (m^{-1}) is the absorption coefficient, d_t (m) is the axial depth in tissue, and I_r ($\text{W} \cdot \text{m}^{-2}$) is the laser irradiance, defined as a function of radial distance since the spatial beam profile is assumed to be a 2-D Gaussian distribution with a standard deviation of σ (m). The following equation reports the expression of I_r :

$$I_r = \frac{P}{2\pi\sigma^2} \exp\left(-\frac{r^2}{2\sigma^2}\right) \quad (4)$$

where P (W) is the power of the continuous-wave mode laser emitter and r (m) is the radial distance. In the present model, a laser radiation wavelength comprised within the so-called *therapeutic window*, i.e., 808 nm, was adopted. Hence, considering the interaction of NIR laser light with biological materials, typically defined as turbid media, the scattering cannot be neglected in comparison with the linear absorption phenomenon [14]. Thus, the effective attenuation coefficient, α_{eff} (m^{-1}), based upon diffusion approximation [40], was introduced to consider both the scattering and the absorption contributions:

$$\alpha_{eff} = \sqrt{3\alpha_a(\alpha_a + \alpha_s(1-g))} \quad (5)$$

where g and α_s (m^{-1}) are respectively the anisotropy and the scattering coefficient. Therefore, the absorption coefficient α_a in Eq. (3) was replaced with the effective attenuation coefficient α_{eff} of Eq. (5). The optical properties of the hepatic tissue were considered to change according to the portion of the damaged tissue (*PDT*) and were defined as follows:

$$\alpha_a = \alpha_{a,n} \cdot (1 - PDT) + \alpha_{a,c} \cdot PDT \quad (6)$$

$$\alpha_s = \alpha_{s,n} \cdot (1 - PDT) + \alpha_{s,c} \cdot PDT \quad (7)$$

$$g = g_n \cdot (1 - PDT) + g_c \cdot PDT \quad (8)$$

where $\alpha_{a,n}$ (m^{-1}), $\alpha_{s,n}$ (m^{-1}) and g_n are respectively the absorption, scattering, and anisotropy coefficients of native tissue, while $\alpha_{a,c}$ (m^{-1}), $\alpha_{s,c}$ (m^{-1}) and g_c are the absorption, scattering, and anisotropy coefficients of the coagulated tissue [22,41].

To assess the thermal damage during the laser irradiation procedure, the Arrhenius equation [39] was considered in the model. The degree of tissue injury $\theta(r,t)$, which is dependent on temperature and exposure time, was expressed as:

$$\theta(r,t) = \theta_0 + A_f \cdot \int_0^{\tau_{irr}} (1 - \theta)^{n_p} \cdot \exp\left(-\frac{E_a}{R \cdot T}\right) dt \quad (9)$$

where θ_0 is the initial degree of tissue injury, A_f (s^{-1}) is the frequency factor, τ_{irr} (s) is the total irradiation time, n_p is the polynomial order, E_a ($\text{J} \cdot \text{mol}^{-1}$) is the denaturation activation energy, R ($\text{J} \cdot \text{mol}^{-1} \cdot \text{K}$) is the universal gas constant, and T (K) is the absolute temperature in tissue. The portion of damaged tissue, *PDT*, is therefore calculated based on the degree of tissue injury θ , according to [42]:

$$PDT = \min(\max(\theta, 0), 1) \quad (10)$$

Table 1 reports the optical properties of native and coagulated liver tissue and the parameters utilized in the Arrhenius model.

Table 1. Optical properties of swine hepatic tissue (native and coagulated) and parameters utilized for the Arrhenius thermal damage model.

Optical properties of porcine liver tissue					
Absorption coefficient, α_a (m^{-1})		Scattering coefficient, α_s (m^{-1})		Anisotropy factor, g	
Native	Coagulated	Native	Coagulated	Native	Coagulated
0.73 [32]	0.88 [32]	55 [32]	380.3 [32]	0.93 [32]	0.9 [32]
Parameters for the Arrhenius thermal damage model					
Frequency factor, A_f (s^{-1})		Activation energy, E_a ($\text{J}\cdot\text{mol}^{-1}$)		Universal gas constant, R ($\text{J}\cdot\text{mol}^{-1}\cdot\text{K}$)	
$5.5\cdot 10^{41}$ [33]		$2.77\cdot 10^5$ [33]		8.314 [33]	

To accurately predict the temperature distribution of the target tissue, the density ρ , the heat capacity c , and the thermal conductivity k of the porcine liver tissue were considered temperature-dependent. The trend of heat capacity and thermal conductivity were attained from [31] and the dynamic changes of density were expressed according to the following equation:

$$\begin{cases} \rho(T) = 1000 \cdot (1.3 - 0.3 \cdot k_p \cdot m_w) \\ k_p = 1 - 4.98 \cdot 10^{-4} \cdot (T - 20) \end{cases} \quad (11)$$

in which m_w indicates the water mass percentage in hepatic tissue, i.e., ~69% [41].

3.2. Numerical simulation

The finite element method (FEM)-based solver, COMSOL Multiphysics (COMSOL, Inc., Burlington, MA, USA) was adopted for solving the numerical model of the temperature-controlled LA procedure, performed on *ex vivo* porcine tissue. The simulation geometry concerned the modeling of the porcine liver tissue phantom (a cylinder of 5.5 cm in radius and 3 cm in thickness), the laser applicator, which was positioned along the central z-axis of the cylinder, and 4 pass-through FBG arrays located according to the experimental setup (Fig. 3(a)). Table 2 shows the dimensions of the adopted laser fiber applicator and of the FBG sensors, which are constituted by an outer polyimide coating and a silica glass core. Moreover, it reports the physical properties adopted for the materials characterizing the FBG sensors [43].

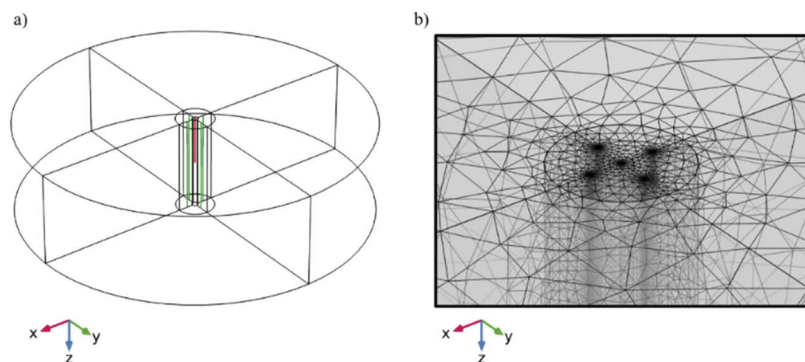


Fig. 3. (a) Geometry of the implemented model for feedback-controlled interstitial ablation simulation: laser applicator (red) and FBG array sensors (green) embedded in hepatic tissue are shown. (b) Close-up of the central part of the mesh utilized in the implemented model, with a minimum mesh size of 0.01 mm.

The COMSOL built-in free mesh generator was employed to generate free tetrahedral mesh elements for the physical domain discretization, with a minimum mesh size of 0.01 mm (Fig. 3(b)).

Table 2. Dimensions of laser fiber and fiber Bragg grating (FBG) sensors and physical properties of the materials constituting the FBG arrays.

Dimensions of laser fiber and FBG sensors		
	Size (radius)	
Laser fiber applicator	0.1500 mm	
Polyimide coating of the FBG sensor	0.0775 mm	
Silica glass of the FBG sensor	0.0625 mm	
Physical properties of FBG materials		
Property	Polyimide	Silica glass
Absorption coefficient	0 cm^{-1}	10^{-5} cm^{-1}
Thermal conductivity	$0.12 \text{ W}\cdot\text{m}^{-1}\cdot\text{K}^{-1}$	$1.1 \text{ W}\cdot\text{m}^{-1}\cdot\text{K}^{-1}$
Density	$1.42 \text{ g}\cdot\text{cm}^{-3}$	$2.17 \text{ g}\cdot\text{cm}^{-3}$
Heat capacity	$1.09 \text{ J}\cdot\text{g}^{-1}\cdot\text{K}^{-1}$	$680 \text{ J}\cdot\text{g}^{-1}\cdot\text{K}^{-1}$

The numerical resolution of all the implemented simulations has been performed on an Intel Core i7-9800X workstation (3.8 GHz clock speed and 64.0 GB RAM).

4. Results

4.1. Simulation results

Figure 4 shows the temperature distribution for the different case-studies, namely, the uncontrolled procedure, and the LA control based on the comparison between the setpoint temperature T_s and the temperature assessed at different z_d planes with d equal to -3 mm, -2 mm, 0 mm, +2 mm, and +3 mm. For each displayed figure, the left semi-figure depicts the thermal values comprised between T_s (40 °C) and the maximum temperature obtained in the biological tissue. In the right part of each image, the corresponding volumes of hepatic tissue characterized by temperatures ≥ 40 °C (volume in yellow) and ≥ 60 °C (volume in brown) are also shown. The latter temperature was displayed as typically identified as the threshold value at which instantaneous thermal damage occurs in biological tissues [44]. The displayed spatial temperature profiles concern the heat distribution immediately before the laser source was turned off for the first time, thus, in case of controlled ablations, when the control phases initiate. This choice aims at attaining comparable thermal results among the different LA controls, based on the different locations. For all the cases, the maximum temperature is reached close to the applicator tip, where temperatures above 300 °C are observed. The uncontrolled laser irradiation shows the highest temperature values compared to all control cases. Furthermore, in this case, temperatures equal to 40 °C extend up to 1.76 mm away from the cylindrical region of tissue comprised between the laser tip and the location of the FBG sensors. In Fig. 4, the aforementioned distance between the point corresponding to the maximum extent at which temperatures of 40 °C can be found and the closest FBG sensor is indicated as r_{ext} . In case of temperature feedback control based on the comparison with the temperature at d equal to -3 mm, -2 mm, i.e., backward to the delivered laser beam, r_{ext} results equal to 0.73 mm and 0.22 mm, for d equal to -3 mm, -2 mm, respectively. For the control performed at d equal to +3 mm, +2 mm, i.e., along the laser beam propagation, the values of r_{ext} correspond to 0.49 mm and 0.13 mm, accordingly. Conversely, concerning the temperature control based upon the comparison at $d = 0$ mm, temperatures of 40 °C remain confined to the volume comprised between the laser applicator and the modeled FBG optical fibers.

Among all the considered cases, the uncontrolled LA shows the maximum volume of liver tissue at temperatures ≥ 40 °C, i.e., 509.2 mm³. The control performed at $d = -3$ mm and

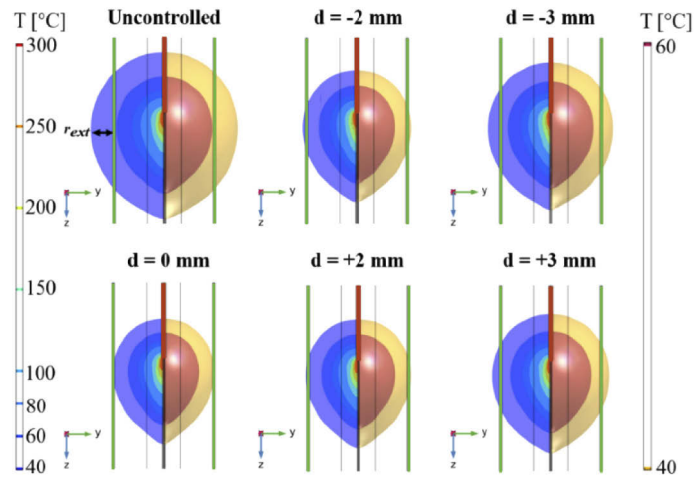


Fig. 4. Simulated temperature distribution for the different case-studies of interstitial thermal ablation, i.e., the uncontrolled procedure, and the control based on the comparison between the setpoint temperature T_s (40 °C) and the temperature assessed at the different d values, equal to -3 mm, -2 mm, 0 mm, +2 mm, and +3 mm. The heat distributions refer to the instant of time immediately before the laser source was turned off for the first time. For each figure, the left semi-figure depicts the thermal values comprised between T_s and the maximum attained temperature, whereas, in the right part, the corresponding volumes of tissue associated with temperatures ≥ 40 °C (yellow) and ≥ 60 °C (brown) are displayed.

$d = +3$ mm produced volumes of tissues at temperature ≥ 40 °C of 276.3 mm³ and 225.6 mm³, respectively. Smaller volumes of biological tissue heated up to temperatures equal to and over 40 °C refer to the control performed at 2 mm since for $d = -2$ mm and $d = +2$ mm, values of 192.8 mm³ and 175.7 mm³ are respectively shown. The smallest volume of tissue at 40 °C is attained in case of the temperature controlled based upon the comparison at $d = 0$ mm, i.e., 155.9 mm³. Similarly, the values of tissue volume characterized by temperatures ≥ 60 °C are lower for $d = 0$ mm, and progressively increase for $d = +2$ mm and $d = -2$ mm, $d = +3$ mm and $d = -3$ mm, up to the maximum value of 132.6 mm³, concerning the uncontrolled case. The previous analysis shows that, considering the same distances from the laser tip, temperatures remain more confined when the control is performed based on sensing locations in the forward direction of the beam propagation, compared to the corresponding locations set backward. Moreover, the closer the location of the controlling point to the laser applicator, the smaller the extent of temperatures over the setpoint value. Additionally, considering the temperature trend over time (Fig. 5), two relevant factors should be taken into account when evaluating the implemented control strategy. Firstly, since in the simulation the temperature values attained in the biological tissue undergoing LA and the setpoint temperatures are compared every $\Delta\tau = 0.5$ s, the time which elapses between when the setpoint temperature is exceeded and the laser source is turned off can cause a short delay in the control system (green circle of Fig. 5(b)). Secondly, the heat diffusion due to the tissue thermal properties once the laser is switched off can cause a response delay before the tissue temperature starts decreasing. Therefore, a consequent temperature overshoot can be observed (Fig. 5(b)).

Figure 6 depicts the temperature evolution over time for the different control cases. Considering the same distances from the laser tip, smaller overshoots are registered when the control is performed based on sensing locations placed backward to the beam propagation. Indeed, for the control performed upon the comparison of temperature at $d = -3$ mm and $d = -2$ mm, the overshoots (1.3 °C and 1.8 °C) are slightly lower than the values for the control performed based

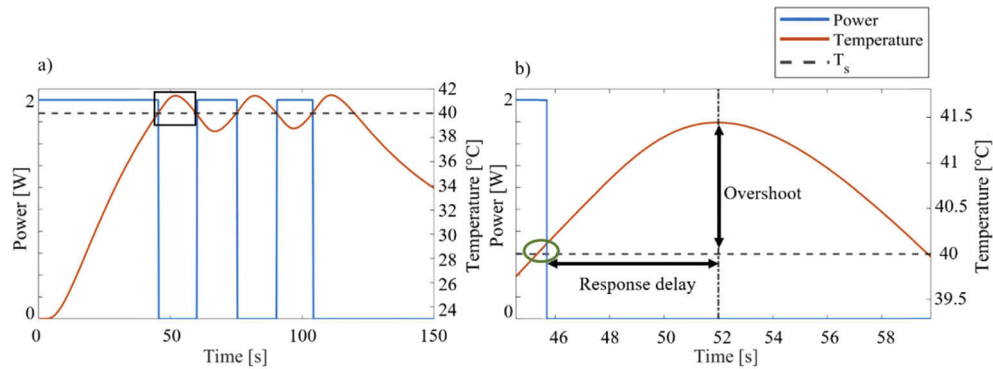


Fig. 5. (a) Power and temperature profiles attained by the simulation of temperature feedback-controlled interstitial laser irradiation of liver tissue. (b) Close-up on the simulated power and temperature evolution over time (corresponding to the black rectangle of figure a) to show an example of the small delay in the control system which can occur due to the time which elapses between when the setpoint temperature is exceeded and when the laser source is turned off (green circle), since the measured and the setpoint temperatures are compared every $\Delta\tau = 0.5$ s. The response delay after the simulated laser power is switched off and the associated temperature overshoot are also shown.

on the temperature at $d = +3$ mm and $d = +2$ mm (1.4 °C and 2.0 °C). Conversely, the response delay results higher when the control is performed based on sensing locations set behind the laser beam. That corresponds to 6.2 s and 5.8 s for $d = -3$ mm and $d = +3$ mm, respectively, and 5.1 s and 5.0 s for $d = -2$ mm and $d = +2$ mm, respectively. The lowest values of temperature overshoot and response delay concern the control implemented based upon the temperature assessed at d equal to 0 mm, i.e., 2.1 °C and 4.8 s.

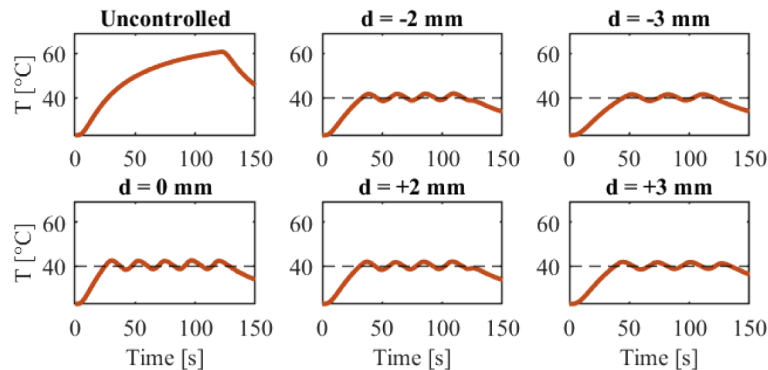


Fig. 6. Simulated temperature evolution obtained for the uncontrolled and the different temperature-controlled interstitial ablations in liver tissue. The dashed line indicates the set temperature T_S .

Figure 7 shows temperature distribution and the tissue volumes at 40 °C and 60 °C, for instance for LA controlled at $d = -3$ mm, and the associated maximum distances from the laser applicator axis at which temperatures corresponding to the setpoint and 60 °C extend, in case of overshoot. It can be noticed that, although temperatures of 40 °C can be found at larger distances ($r_{\text{ext}} = 0.91$ mm in case of overshoot, while $r_{\text{ext}} = 0.73$ mm when the laser is switched off), in case of overshoot (Fig. 7(a)) the inner tissue temperature results decreased compared to the heat

distribution immediately before the laser is turned off (Fig. 7(b)). Indeed, temperatures ≥ 60 °C result more confined to the region closer to the laser tip.

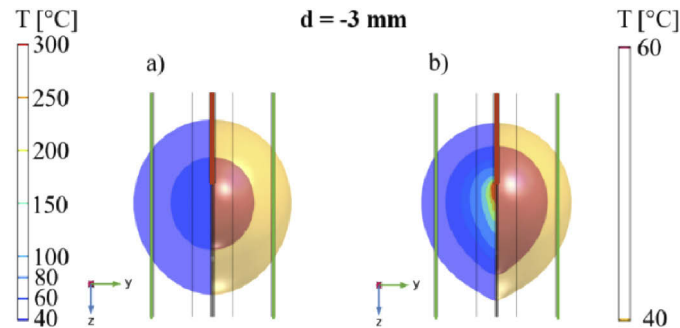


Fig. 7. Simulated temperature distribution and volumes of hepatic tissues at 40 °C and 60 °C concerning feedback-controlled LA at $d = -3$ mm, in case of (a) overshoot and (b) at the instant of time immediately before the laser source was turned off.

The thermal evolution during LA determines reversible and irreversible tissue changes, thus also irreversible tissue damage can occur. Figure 8 depicts the fraction of necrotic tissue attained in the different presented cases. The maximum fraction of necrotic tissue refers to the uncontrolled LA, i.e., 53 mm³. Then, considering the same distances from the laser tip, fractions of necrotic tissue result larger in case of control performed based upon sensing locations placed behind the beam, compared to the ones positioned along the laser beam propagation direction. Hence, for d equal to -3 mm and -2 mm, the fractions of necrotic tissue are 34.4 mm³ and 24.2 mm³, respectively, while for d equal to +3 and +2 mm, necrotic tissues equal to 27.9 mm³ and 23.0 mm³, respectively. The minimum value is shown by the control actuated at d equal to 0 mm (21.1 mm³). Table 3 reports the complete outlook of the results attained from the thermal analysis performed by means of the FEM-based simulation of laser-tissue interaction and the subsequent heat transfer in biological material.

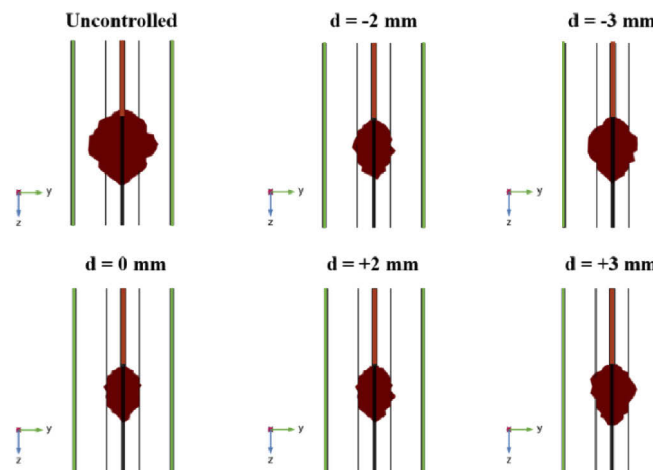


Fig. 8. Simulated fractions of necrotic tissue attained at the end of laser irradiation (laser exposure time of 120 s) for the different case-studies, i.e., uncontrolled treatment and temperature-controlled irradiation at different d values (see Visualization 1).

Table 3. Overview of the results attained for the feedback-controlled laser interstitial irradiation simulation: the volumes of hepatic tissue characterized by temperatures ≥ 40 °C and ≥ 60 °C, immediately before the laser source was turned off for the first time, the temperature overshoots, the response delays, and the fractions of necrotic tissues are reported for the uncontrolled irradiation and the diverse control cases, based on the temperature assessed at the different d values.

	Uncontrolled	$d = -3$ mm	$d = -2$ mm	$d = 0$ mm	$d = +2$ mm	$d = +3$ mm
Volume [mm ³] at $T \geq 40$ °C	509.2	276.3	192.8	155.9	175.7	225.6
Volume [mm ³] at $T \geq 60$ °C	132.6	82.1	59.7	49.3	54.9	69.1
Overshoot [°C]	-	1.3	1.8	2.1	2.0	1.4
Response delay [s]	-	6.2	5.1	4.8	5.0	5.8
Fraction of necrotic tissue [mm ³]	53.0	34.4	24.2	21.1	23.0	27.9

4.2. Experimental results

After assessment of the thermal outcome at the set temperature T_S and diverse controlling distances with the implemented simulation, we performed *ex vivo* liver LA experiments with the defined input parameters to demonstrate the feasibility of the proposed LA control algorithm. In accordance with the simulations, T_S was set to 40 °C, and the d values were chosen equal to -3 mm, -2 mm, 0 mm, +2 mm, and +3 mm. Figure 9(a) reports the maximum temperatures measured by each FBG array during uncontrolled ablation. The difference in measured temperature profiles can be explained by sensor positioning uncertainties and inhomogeneities of the tissue. The temperature profiles for controlled cases are depicted in Fig. 9(b): temperatures on controlled z_d planes in the first column, and maximum measured temperatures (aligned to be on the z_0 plane) in the second column; while for the case of $d = 0$ mm, only one graph is presented because the controlled plane z_d lies in the z_0 plane. As it can be seen, the maximum temperature at z_d follows the set temperature value with some differences related to the ON-OFF control technique. Overshoot and delay response values are: 1.4 °C, 1 °C, 0.6 °C, 0.6 °C, and 1.4 °C; and 6.6 s, 4.2 s, 3.5 s, 2.2 s and 5 s for d equal to -3 mm, -2 mm, 0 mm, +2 mm, and +3 mm, correspondingly. The difference between measured temperature responses for the same distances in the backward and forward direction of the laser irradiation obtained during experiments validates the simulation results discussed in Section 4.1. This behavior can be explained by the fact that temperature rise behind the beam propagation direction is caused only by heat conduction and not by direct laser absorption. This phenomenon also can be appreciated in Fig. 10 (temperature profile evolution and associated contour maps showing the setpoint temperature value) for temperature profiles for the z_d planes reported in Fig. 9(b) (left column). Indeed, the plane z_0 and the planes with positive d have smoother temperature control and more spatially confined ablation regions.

The comparison between the simulated and the experimental results is presented in Fig. 11: the depicted maximum temperature profiles measured at the controlled z_d plane prove the feasibility of the simulation of ON-OFF control. Most of the simulations accurately predict the heating phase of ablation and its cooling trend. The difference in the controlling phase is mainly due to a phase shift of controlling actions. Overshoot and delay response values follow the trends discussed in the experimental section: 1.4 °C, 2.0 °C, 1.3 °C, 1.8 °C, and 2.1 °C, and 6.2 s, 5.1 s, 4.8 s, 5.0 s, and 5.8 s, for d equal to -3 mm, -2 mm, 0 mm, +2 mm, and +3 mm, correspondingly. The discrepancy for $d = +2$ mm can be explained by the possible inaccurate positioning of the sensor, which is also related to rapid temperature increase at z_0 at the beginning of ablation, as shown in Fig. 9(b) (blue line in the subplot $d = +2$ mm, referring to $T@z_0$). The high overshoot difference between simulation and experiments for z_0 can be explained by a stronger effect of laser absorption than heat conduction aspects.

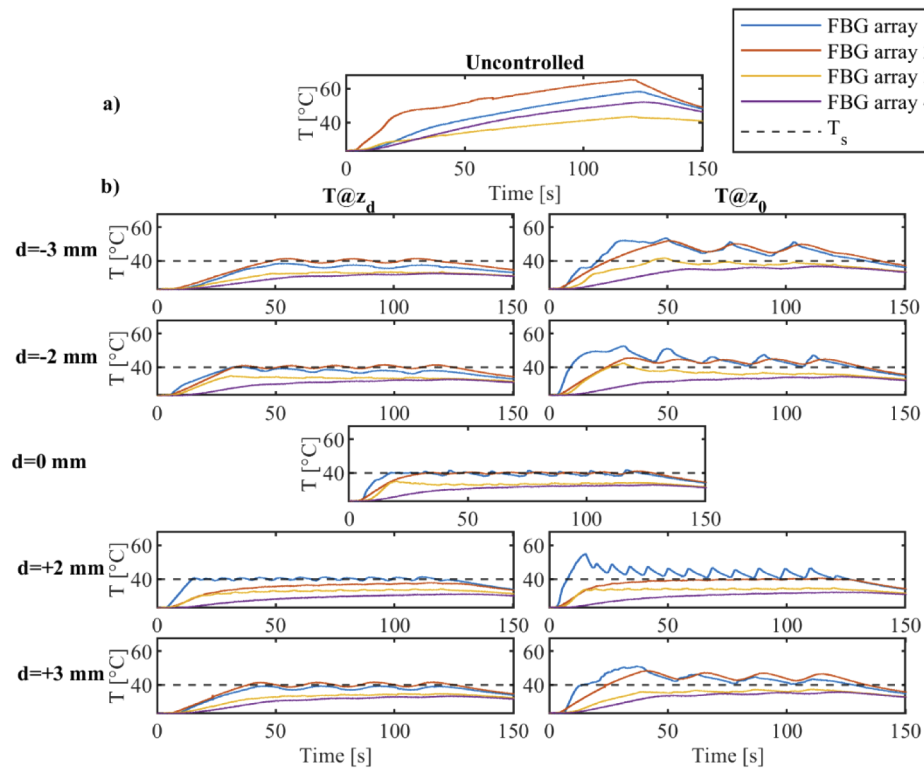


Fig. 9. Temperature profiles measured by four fiber Bragg grating (FBG) arrays during (a) uncontrolled ablation and (b) controlled ablation: the left column reports the temperature measured at z_d plane (controlled profiles), the right column depicts the temperature profiles at the z_0 plane (peak temperatures measured by FBG arrays) during the same experiment.

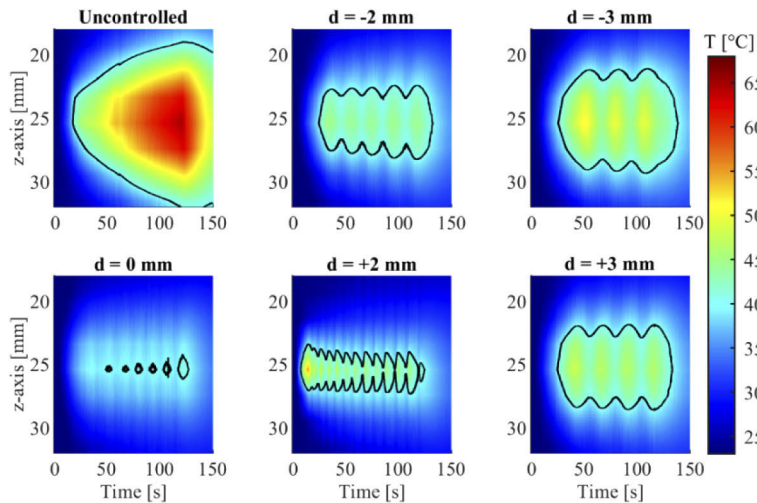


Fig. 10. Two-dimensional temperature map (time vs. distance along the controlled sensor positioned along the z -axis) attained through the FBG arrays measurements for the uncontrolled ablation treatment and the temperature feedback-controlled ablations: $T_s = 40$ °C, $d = -3, -2, 0, +2,$ and $+3$ mm. The black contour lines define the region of hepatic tissue at temperature ≥ 40 °C.

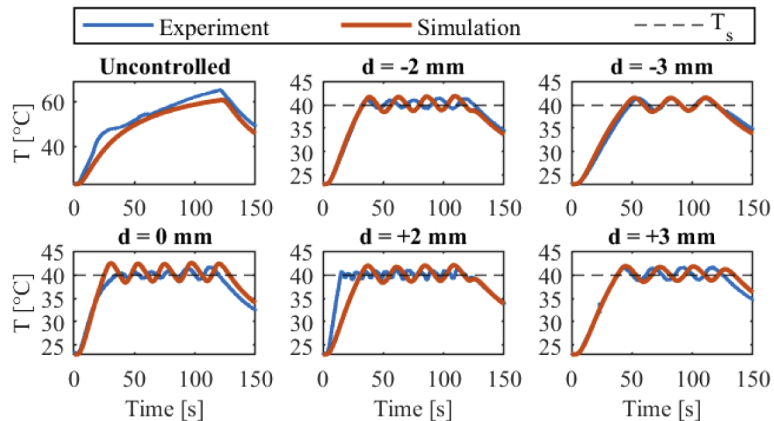


Fig. 11. Trends of uncontrolled LA and controlled temperature profiles obtained during LA experiments where the temperature was modulated based upon 40 gratings-highly dense FBG array measurements and comparison with temperature evolution attained with the FEM-based solver, adopted for solving the numerical model of the temperature-controlled interstitial LA procedure. The similarity of graphs validates the efficacy of the developed numerical model.

5. Discussion and conclusions

In this work, we theoretically and experimentally prove the feasibility of the use of highly dense FBG arrays for temperature-based control of interstitial LA. The interstitial approach leads to different possible fiber sensor arrangements in the ablated tissue and a variety of control methods for LA. We propose to use FBG arrays equidistant from the laser applicator to maintain stable temperatures at the margins of the treated region. A FEM-based simulation implemented in COMSOL Multiphysics is used to test pre-set parameters before the actual procedure and define the planned treatment in terms of peak temperature profiles, volumetric heat distribution, and fraction of the necrotic tissue. It is important to highlight that the volumetric and thermal damage evaluation is performed prior to treatment, while in real-time only temperature control at the specific plane is performed. The user interface of the developed LabVIEW program allows adjusting three input parameters (laser power, set temperature, and control distance) before the procedure, then LA control with real-time visualization of the measured temperature is performed. Simulation data were used to evaluate the overall ablation treatment and deal with a lack of volumetric temperature information stemmed from the inability to attain highly accurate 3D thermal maps with the utilized FBG arrays arrangement. According to numerical results, pre-set input parameters were chosen to contain the laser-induced thermal distribution (Figs. 4 and 6) in specific planes below the threshold values related to thermal damage process [45,46]. For the procedure with the tested input parameters, the fraction of necrotic tissue (Fig. 8) in the margins of the interested region was also calculated.

One of the main advantages of the proposed control approach is the use of highly dense FBG arrays. They provide several advantages over conventional measurement techniques for LA (i.e., thermistors, photo-optic probes, thermocouples, contactless thermometric systems) [23,47–49]: minimal invasiveness due to miniature dimensions of the fibers [26], low laser light absorption due to silica glass and polyimide material [34–36], reduced cost compared to other sensing techniques such as MRI-thermometry or fluoroptic sensors (e.g., approximately 50 \$ considering a 1 mm sensitive length [50]), good metrological characteristics (i.e., response time in the order of 0.1 s and accuracy of <1 °C), and multipoint measurements derived from wavelength-division capabilities of FBG arrays [51]. These characteristics make FBG arrays

well-suited for controlled interstitial ablation [14]. Indeed, previous studies employed mostly single-point metallic sensors for measuring and keeping the temperature at the desired threshold. Lin *et al.* used thermocouples to maintain the set temperature during *in vitro* experiments of photothermal therapy [49]. Moreover, an interstitial laser thermotherapy system constituted by an Nd:YAG laser and temperature feedback circuits embedding an automatic thermometry system based on single thermistor and thermocouple probes has been evaluated for *in vivo* LA in rats and on liver phantom [23]. Additionally, a temperature-controlled system based on thermocouple monitoring and a single low-power Nd:YAG laser for interstitial local hyperthermia has been implemented for the treatment of carcinoma [21]. The proposed sensors can suffer from self-heating once exposed to the NIR radiation due to the light absorption of metallic components [52,53]. Thus, leading to measurement errors that cannot be corrected during real-time temperature monitoring.

Regarding the capability of multipoint measurements of FBG arrays, Fig. 9 illustrates one of its main advantages for LA control, i.e., the ability to measure the temperature distribution and the position of its maximum that can change during the ablation procedure: the shift of the temperature maximum from one array to another during the LA procedure was properly detected for $z_d=z_0$ case. Moreover, the highly dense FBG arrays used in the experiments provide high spatial resolution that allows for accurate thermal map reconstruction (Fig. 10) during LA control. We observed that the sensor's position does not substantially affect the overshoot (1.4-1.6 °C) and the response delay (~2-7 s), but it influences the resulting temperature distribution. Experimental data also clearly show the efficacy of the control approach (Fig. 9), and the similarity with numerical results (Fig. 11).

The use of computational models for the simulation of the temperature-controlled ablation procedure has been already introduced by some authors. Ivarsson *et al.* report a temperature-controlled stepwise power regulation system for LA, based on thermistors with a spatial resolution of 10 mm. A numerical model based on the bioheat equation was also implemented to calculate the heat distribution, however, the thermal damage prediction was not included in the model [48]. Moreover, an auto-controlled laser on-off strategy was presented, combined with a theoretical model that numerically solved the heat diffusion equation, for retrieving the final volume heating, during photothermal therapy. In 2016, a feedback system based on a proportional-integrative-derivative (PID) control of thermocouple-assisted photothermal ablation performed with a 980 nm laser emitter was proposed [22]. In this work, the simulation model was implemented exploiting the Pennes' equation, solved by using a finite-element method. However, two different tuning approaches (manual and automatic, respectively) were utilized for computational modeling and the actual experimental treatment. Further studies proposed both the simulated and experimental assessment of temperature-controlled LA performed on *ex vivo* porcine liver by means of a thermographic measurement system. The heat distribution and the subsequent thermal injury were attained from the numerical simulation, however, the optical properties of untreated and coagulated tissue were not taken into consideration [29]. Moreover, a recently implemented work from the same research group referred to the maintenance of a set tissue temperature to induce the predetermined thermal coagulation on porcine liver tissue LA (1064 nm laser), using a thermocouple for real-time thermal monitoring [30].

Our analysis takes into account the change of tissue properties during LA according to the temperature and degree of tissue injury, and properly describes the thermal effects on the tissue, as witnessed by the comparable thermal outcomes attained in simulation and experimental frameworks (Fig. 11). This agreement validates the developed model and its use for preoperative optimization of LA parameters. In the future, this model could also be employed to perform an intraoperative control in combination with real-time measurement of the tissue changes. For instance, a potential technique that can monitor the transition state between native and coagulated tissue could also be applied [54]. The retrieved data might be used in the model

for the estimation of the thermal outcome and the subsequent adjustment of the control settings during the procedure.

The ON-OFF control strategy used in our work allows, indeed, to effectively control the tissue temperature according to the set temperature, as also reported in other studies employing different thermal ablation techniques [55,56].

On the other hand, numerical and experimental results (Figs. 5, 6, 7, 9, and 11 and Table 3) demonstrate that the ON-OFF approach has some disadvantages, such as overshoot and delay response, that could affect the overall treatment [28]. Therefore, further evaluations on the effect of the wavelength and tissue optical properties could be of interest for assessing if overshoots and delay response can be limited, and new control techniques need to be introduced to improve treatment efficacy. For instance, a few studies [22,57] have been already investigating PID control for LA, but none of them considered quasi-distributed fiber sensors for PID-based control, which can be the future improvement of the proposed work for the optimal control of thermal effect during biological tissue LA. Lastly, being our analysis focused on the assessment of the validity of the theoretical model for pre-planning the control, a simplified and controllable approach neglecting the convective heat loss caused by blood perfusion was chosen. Indeed, the heat-sink effect has a significant impact on the temperature distribution in the target [58], hence future studies should also consider this phenomenon in both the pre-planning control strategy model and experiments, to approach the final clinical application. In order to implement our strategy in the *in vivo* conditions, other factors shall be considered in the future: a longer treatment time should be set to account for the thermal losses due to the concurrent blood perfusion; diffusing laser applicators could be employed to enlarge the treatment volume; the cross-sensitivity of FBGs to strain due to the physiological movements should be considered and possibly mitigated by the use of needles [59]; the position of sensors used for control should be tailored according to the tumor size, to attain the desired thermal damage.

Funding. European Research Council under the European Union's Horizon 2020 research and innovation programme (GA 759159).

Acknowledgment. This project has received funding from the European Research Council (ERC) under the European Union's Horizon 2020 research and innovation programme (Grant agreement No. 759159). The authors would like to acknowledge Alexey Wolf and Alexander Dostovalov at the Institute of Automation and Electrometry of the SB RAS, Novosibirsk (Russia) for producing FBG arrays for the measurements.

Disclosures. The authors declare no conflicts of interest.

Supplemental document. See [Supplement 1](#) for supporting content.

References

1. H. P. Kok, E. N. K. Cressman, W. Ceelen, C. L. Brace, R. Ivkov, H. Grüll, G. ter Haar, P. Wust, and J. Crezee, "Heating technology for malignant tumors: a review," *Int. J. Hyperthermia* **37**(1), 711–741 (2020).
2. J. E. Kennedy, "High-intensity focused ultrasound in the treatment of solid tumours," *Nat. Rev. Cancer* **5**(4), 321–327 (2005).
3. R. Tateishi, S. Shiina, T. Teratani, S. Obi, S. Sato, Y. Koike, T. Fujishima, H. Yoshida, T. Kawabe, and M. Omata, "Percutaneous radiofrequency ablation for hepatocellular carcinoma," *Cancer* **103**(6), 1201–1209 (2005).
4. M. G. Lubner, C. L. Brace, J. L. Hinshaw, and F. T. Lee, "Microwave tumor ablation: mechanism of action, clinical results, and devices," *J. Vasc. Interv. Radiol.* **21**(8), S192–S203 (2010).
5. S. Natarajan, S. Raman, A. M. Priester, J. Garritano, D. J. A. Margolis, P. Lieu, M. L. Macairan, J. Huang, W. Grundfest, and L. S. Marks, "Focal Laser Ablation of Prostate Cancer: Phase I Clinical Trial," *J. Urol.* **196**(1), 68–75 (2016).
6. E. Schena, P. Saccomandi, and Y. Fong, "Laser ablation for cancer: past, present and future," *J. Funct. Biomater.* **8**(2), 19 (2017).
7. F. M. Di Matteo, P. Saccomandi, M. Martino, M. Pandolfi, M. Pizzicannella, V. Balassone, E. Schena, C. M. Pacella, S. Silvestri, and G. Costamagna, "Feasibility of EUS-guided Nd:YAG laser ablation of unresectable pancreatic adenocarcinoma," *Gastrointest. Endosc.* **88**(1), 168–174.e1 (2018).
8. R. J. Stafford, D. Fuentes, A. A. Elliott, J. S. Weinberg, and K. Ahrar, "Laser-induced thermal therapy for tumor ablation," *Crit. Rev. Biomed. Eng.* **38**(1), 79–100 (2010).
9. T. J. Vogl, R. Straub, K. Eichler, O. Söllner, and M. G. Mack, "Colorectal carcinoma metastases in liver: laser-induced interstitial thermotherapy—local tumor control rate and survival data," *Radiology* **230**(2), 450–458 (2004).

10. H.-J. Schwarzmaier, F. Eickmeyer, W. von Tempelhoff, V. U. Fiedler, H. Niehoff, S. D. Ulrich, Q. Yang, and F. Ulrich, "MR-guided laser-induced interstitial thermotherapy of recurrent glioblastoma multiforme: preliminary results in 16 patients," *Eur. J. Radiol.* **59**(2), 208–215 (2006).
11. L. K. Swartz, K. G. Holste, M. M. Kim, A. Morikawa, and J. Heth, "Outcomes in patients treated with laser interstitial thermal therapy for primary brain cancer and brain metastases," *Oncologist* **24**(12), e1467–e1470 (2019).
12. R. Muschter, "Laser-induced interstitial thermotherapy of benign prostatic hyperplasia and prostate cancer," in *Medical Applications of Lasers II*, S. G. Bown, J. Escourrou, F. Frank, H. J. Geschwind, G. Godlewski, F. Laffitte, and H. H. Scherer, eds. (SPIE, 1994), 2327, pp. 287–292.
13. J. A. S. Brookes, W. R. Lees, and S. G. Bown, "Interstitial laser photocoagulation for the treatment of lung cancer," *AJR, Am. J. Roentgenol.* **168**(2), 357–358 (1997).
14. P. Saccomandi, E. Schena, M. A. Caponero, F. M. Di Matteo, M. Martino, M. Pandolfi, and S. Silvestri, "Theoretical analysis and experimental evaluation of laser-induced interstitial thermotherapy in ex vivo porcine pancreas," *IEEE Trans. Biomed. Eng.* **59**(10), 2958–2964 (2012).
15. Y. Kerbage, N. Betrouni, P. Collinet, H. Azais, S. Mordon, A.-S. Dewalle-Vignion, and B. Merlot, "Laser interstitial thermotherapy application for breast surgery: Current situation and new trends," *The Breast* **33**, 145–152 (2017).
16. A. J. Welch and M. J. C. Van Gemert, *Optical-Thermal Response of Laser-Irradiated Tissue* (Springer, 2011).
17. P. Saccomandi, E. Schena, and C. M. Pacella, "New horizons for laser ablation: nanomedicine, thermometry, and hyperthermal treatment planning tools," in *Image-Guided Laser Ablation* (Springer International Publishing, 2020), pp. 145–151.
18. K. F. Chu and D. E. Dupuy, "Thermal ablation of tumours: biological mechanisms and advances in therapy," *Nat. Rev. Cancer* **14**(3), 199–208 (2014).
19. S. A. Sapareto and W. C. Dewey, "Thermal dose determination in cancer therapy," *Int. J. Radiat. Oncol., Biol., Phys.* **10**(6), 787–800 (1984).
20. J. Pearce, "Mathematical models of laser-induced tissue thermal damage," *Int. J. Hyperthermia* **27**(8), 741–750 (2011).
21. N. Daikuzono, S. Suzuki, H. Tajiri, H. Tsunekawa, M. Ohyama, and S. N. Joffe, "Laserthermia: a new computer-controlled contact Nd:YAG system for interstitial local hyperthermia," *Lasers Surg. Med.* **8**(3), 254–258 (1988).
22. T. H. Nguyen, S. Park, K. K. Hlaing, and H. W. Kang, "Temperature feedback-controlled photothermal treatment with diffusing applicator: theoretical and experimental evaluations," *Biomed. Opt. Express* **7**(5), 1932 (2016).
23. P. H. Mollert, L. Lindbergt, P. H. Henriksson, and K. Tranberg, "Temperature control and light penetration in a feedback interstitial laser thermotherapy system," *Int. J. Hyperthermia* **12**(1), 49–63 (1996).
24. R. J. McNichols, A. Gowda, M. Kangasniemi, J. A. Bankson, R. E. Price, and J. D. Hazle, "MR thermometry-based feedback control of laser interstitial thermal therapy at 980 nm," *Lasers Surg. Med.* **34**(1), 48–55 (2004).
25. E. Schena, D. Tosi, P. Saccomandi, E. Lewis, and T. Kim, "Fiber optic sensors for temperature monitoring during thermal treatments: an overview," *Sensors* **16**(7), 1144 (2016).
26. F. Morra, M. De Landro, S. Korganbayev, A. Wolf, A. Dostovalov, A. Cigada, and P. Saccomandi, "Spatially resolved thermometry during laser ablation in tissues: distributed and quasi-distributed fiber optic-based sensing," *Opt. Fiber Technol.* **58**, 102295 (2020).
27. L. Bianchi, R. Mooney, Y. R. Cornejo, C. Hyde, E. Schena, J. M. Berlin, K. S. Aboody, and P. Saccomandi, "Fiber Bragg grating sensors for thermometry during gold nanorods-mediated photothermal therapy in tumor model," in *2020 IEEE Sensors* (IEEE, 2020), pp. 1–4.
28. S. Korganbayev, A. Orrico, L. Bianchi, M. De Landro, A. Wolf, A. Dostovalov, and P. Saccomandi, "Closed-loop temperature control based on fiber Bragg grating sensors for laser ablation of hepatic tissue," *Sensors* **20**(22), 6496 (2020).
29. V. N. Tran, V. G. Truong, S. Jeong, and H. W. Kang, "Computational analysis of linear energy modulation for laser thermal coagulation," *Biomed. Opt. Express* **9**(6), 2575 (2018).
30. V. N. Tran, V. G. Truong, Y. W. Lee, and H. W. Kang, "Effect of optical energy modulation on the thermal response of biological tissue: computational and experimental validations," *Biomed. Opt. Express* **11**(12), 6905 (2020).
31. S. R. Guntur, K. Il Lee, D.-G. Paeng, A. J. Coleman, and M. J. Choi, "Temperature-dependent thermal properties of ex vivo liver undergoing thermal ablation," *Ultrasound Med. Biol.* **39**(10), 1771–1784 (2013).
32. J. P. Ritz, A. Roggan, C. Isbert, G. Miller, H. J. Buhr, and C. T. Germer, "Optical properties of native and coagulated porcine liver tissue between 400 and 2400 nm," *Lasers Surg. Med.* **29**(3), 205–212 (2001).
33. B. Cox, "Introduction to laser-tissue interactions," *PHAS* **4886**, 1–61 (2007).
34. K. Weir, "Optical fiber sensor technology," *J. Mod. Opt.* **42**(4), 938 (1995).
35. L. Huang, R. S. Dyer, R. J. Lago, A. A. Stolov, and J. Li, "Mechanical properties of polyimide coated optical fibers at elevated temperatures," *Proc. SPIE* **9702**, 97020Y (2016).
36. A. V. Dostovalov, A. A. Wolf, A. V. Parygin, V. E. Zyubin, and S. A. Babin, "Femtosecond point-by-point inscription of Bragg gratings by drawing a coated fiber through ferrule," *Opt. Express* **24**(15), 16232–16237 (2016).
37. S. Korganbayev, R. Pini, A. Orrico, A. Wolf, A. Dostovalov, and P. Saccomandi, "Towards temperature-controlled laser ablation based on fiber Bragg grating array temperature measurements," in *2020 IEEE International Workshop on Metrology for Industry 4.0 and IoT, MetroInd 4.0 and IoT 2020 - Proceedings* (2020).

38. S. Nomura, M. Arake, Y. Morimoto, H. Tsujimoto, H. Miyazaki, D. Saitoh, N. Shinomiya, K. Hase, J. Yamamoto, and H. Ueno, "Thermal sensor circuit using thermography for temperature-controlled laser hyperthermia," *J. Sensors* **2017**, 1–7 (2017).
39. M. H. Niemz, *Laser-Tissue Interactions*, Biological and Medical Physics, Biomedical Engineering (Springer, 2007).
40. A. Ishimaru, "Diffusion of light in turbid material," *Appl. Opt.* **28**(12), 2210 (1989).
41. Y. Mohammed and J. F. Verhey, "A finite element method model to simulate laser interstitial thermo therapy in anatomical inhomogeneous regions," *Biomed. Eng. Online* **4**(1), 2 (2005).
42. C. Multiphysics, "Heat Transfer Module," Manual 1–222 (2015).
43. D. K. Sardar, A. Sayka, and R. M. Yow, "Characterization of optical properties of polyimide precursors," *Semicond Manuf (Web Excl.)* **8**, 1–5 (2007).
44. S. N. Goldberg, G. S. Gazelle, and P. R. Mueller, "Thermal ablation therapy for focal malignancy," *Am. J. Roentgenol.* **174**(2), 323–331 (2000).
45. S. Thomsen, "Pathologic analysis of photothermal and photomechanical effects of laser-tissue interactions," *Photochem. Photobiol.* **53**(6), 825–835 (1991).
46. V. K. Nagarajan, J. M. Ward, and B. Yu, "Association of liver tissue optical properties and thermal damage," *Lasers Surg. Med.* **52**(8), 779–787 (2020).
47. W. A. Wohlgemuth, E. Wamser, T. Reiss, and T. Wagner, "In vivo laser-induced interstitial thermotherapy of pig liver with a temperature-controlled diode laser and MRI correlation," *Lasers Surg. Med.* **29**(4), 374–378 (2001).
48. K. Ivarsson, J. Olsrud, and C. Stureson, "Feedback interstitial diode laser (805 nm) thermotherapy system: ex vivo evaluation and mathematical modeling with one and four-fibers," *Lasers Surg. Med.* **22**(2), 86–96 (1998).
49. J.-T. Lin, Y.-S. Chiang, G.-H. Lin, H. Lee, and H.-W. Liu, "In vitro photothermal destruction of cancer cells using gold nanorods and pulsed-train near-infrared laser," *J. Nanomater.* **2012**, 1–6 (2012).
50. D. Polito, M. Arturo Caponero, A. Polimadei, P. Saccomandi, C. Massaroni, S. Silvestri, and E. Schena, "A needlelike probe for temperature monitoring during laser ablation based on fiber bragg grating: manufacturing and characterization," *J. Med. Devices* **9**(4), 041006 (2015).
51. T. Erdogan, "Fiber grating spectra," *J. Lightwave Technol.* **15**(8), 1277–1294 (1997).
52. P. Saccomandi, E. Schena, and S. Silvestri, "Techniques for temperature monitoring during laser-induced thermotherapy: An overview," *Int. J. Hyperthermia* **29**(7), 609–619 (2013).
53. F. Manns, P. J. Milne, X. Gonzalez-Cirre, D. B. Denham, J. Parel, and D. S. Robinson, "In situ temperature measurements with thermocouple probes during laser interstitial thermotherapy (LITT): quantification and correction of a measurement artifact," *Lasers Surg. Med.* **23**(2), 94–103 (1998).
54. P. Lanka, F. Kalloor Joseph, H. Kruit, S. Konugolu Venkata Sekar, A. Farina, R. Cubeddu, S. Manohar, and A. Pifferi, "Monitoring radiofrequency ablation of biological tissue using broadband time-resolved diffuse optical spectroscopy," in *Diffuse Optical Spectroscopy and Imaging VII*, H. Dehghani and H. Wabnitz, eds. (SPIE, 2019), p. 94.
55. M. Li, X. Yu, P. Liang, F. Liu, B. Dong, and P. Zhou, "Percutaneous microwave ablation for liver cancer adjacent to the diaphragm," *Int. J. Hyperthermia* **28**(3), 218–226 (2012).
56. M. Trujillo, J. Bon, M. José Rivera, F. Burdío, and E. Berjano, "Computer modelling of an impedance-controlled pulsing protocol for RF tumour ablation with a cooled electrode," *Int. J. Hyperthermia* **32**(8), 931–939 (2016).
57. X. Feng, F. Gao, C. Xu, L. Gaoming, and Y. Zheng, "Self temperature regulation of photothermal therapy by laser-shared photoacoustic feedback," *Opt. Lett.* **40**(19), 4492–4495 (2015).
58. E. De Vita, M. De Landro, C. Massaroni, A. Iadicicco, P. Saccomandi, E. Schena, and S. Campopiano, "Fiber optic sensors-based thermal analysis of perfusion-mediated tissue cooling in liver undergoing laser ablation," *IEEE Trans. Biomed. Eng.* **68**(3), 1066–1073 (2021).
59. C. Cavaiola, P. Saccomandi, C. Massaroni, D. Tosi, F. Giurazza, G. Frauenfelder, B. Beomonte Zobel, F. M. Di Matteo, M. A. Caponero, A. Polimadei, and E. Schena, "Error of a temperature probe for cancer ablation monitoring caused by respiratory movements: ex vivo and in vivo analysis," *IEEE Sens. J.* **16**(15), 5934–5941 (2016).

PID Controlling Approach Based on FBG Array Measurements for Laser Ablation of Pancreatic Tissues

Sanzhar Korganbayev¹, Graduate Student Member, IEEE, Annalisa Orrico², Graduate Student Member, IEEE, Leonardo Bianchi², Graduate Student Member, IEEE, Davide Paloschi², Graduate Student Member, IEEE, Alexey Wolf³, Alexander Dostovalov³, and Paola Saccomandi², Senior Member, IEEE

Abstract—In this article, we propose a temperature-based proportional–integral–derivative (PID) controlling algorithm using highly dense fiber Bragg grating (FBG) arrays for laser ablation (LA) of *ex vivo* pancreatic tissues. Custom-made highly dense FBG arrays with a spatial resolution of 1.2 mm were fabricated with the femtosecond point-by-point writing technology and optimized for LA applications. In order to obtain proper PID gain values, finite element method-based iterative simulation of different PID gains was performed. Then, the proposed algorithm, with numerically derived PID gains, was experimentally validated. In the experiments, the point temperature was controlled at different distances from the laser fiber tip (6.0, 7.2, 8.4, and 10.8 mm). The obtained results report robust controlling and correlation between controlled distance and the resulting area of ablation. The results of the work encourage further investigation of FBG array application for LA control.

Index Terms—Closed-loop temperature control, feedback system, fiber Bragg grating (FBG) sensors, optical fiber, pancreas, proportional–integral–derivative (PID) control, temperature monitoring, thermal ablation (TA).

I. INTRODUCTION

PANCREATIC ductal adenocarcinoma (PDAC) is the fourth cause of cancer deaths in the world, with about 57 600 new cases and 47 050 deaths in 2020 in the U.S. only [1]. This number is estimated to increase, and by 2030, PDAC will become the second leading cause of cancer-related deaths [2]. The main reasons for such statistics are difficulty in early diagnosis, high biological aggressiveness, and inefficiency of

traditional approaches. Recently, thermal ablation (TA) techniques have received increasing interest in PDAC treatment due to their minimal invasiveness [3]. The main principle of these techniques is based on inducing local temperature change that leads to tumor necrosis. Depending on the source of temperature change, different ablation types exist—radio frequency, microwave, ultrasound, and laser ablation (LA) [4].

Among all ablation techniques, LA has unique advantages, such as flexibility and electromagnetic immunity of the fiber optic applicator, which allow the treatment of deep-lying organs under image guidance [5]. LA is based on the laser light absorption and scattering inside ablated tissue, which leads to temperature elevation and, consequently, to thermal damage of the treated tumor. For deep tumors, laser wavelengths in the so-called “therapeutic window” (940–1100 nm) are mostly utilized due to a good tradeoff between penetration depth and absorption of laser light by the tissue that entails the possibility to ablate large areas (tens of millimeters) [6].

However, the main limitation of LA, and other ablation techniques, is an uncertainty of the treatment results due to the complexity of the ablation phenomenon and the heat-tissue interactions [7], [8].

One of the possible solutions is a minimization of the uncertainty of the procedure by introducing a closed-loop approach based on measurements of intratissue parameters in the ablated region. One of the most important parameters to evaluate the efficacy of TA is temperature. Different ranges of temperatures have different effects on biological tissues. Temperatures from 42 °C to 45 °C correspond to hyperthermia and related activation of an immune response. At temperatures from 50 °C to 55 °C, coagulative necrosis of organs and instantaneous death in cell culture can be observed [7], whereas 60 °C is the starting temperature for rapid denaturation. As a result, accurate control of the desired temperature range is an important factor to ensure efficient cancer treatment.

It is worth noting that not only the tissue temperature value but also the time the tissue is exposed to this value are important to properly evaluate the thermal effect [8]. Thus, different models have been proposed to assess the thermal damage of TA techniques considering both these aspects. One of the models is the cumulative equivalent minutes at 43 °C (CEM43), which has been used to assess the severity of

Manuscript received August 11, 2021; accepted September 5, 2021. Date of publication September 20, 2021; date of current version September 29, 2021. This work was supported by the European Research Council through the European Union’s Horizon 2020 Research and Innovation Program under Grant 759159. The work of Alexey Wolf and Alexander Dostovalov was supported by the Russian Ministry of Science and Higher Education under Grant 14.Y26.31.0017. The Associate Editor coordinating the review process was Yuya Koyama. (Corresponding author: Paola Saccomandi.)

Sanzhar Korganbayev, Annalisa Orrico, Leonardo Bianchi, Davide Paloschi, and Paola Saccomandi are with the Department of Mechanical Engineering, Politecnico di Milano, 20156 Milan, Italy (e-mail: sanzhar.korganbayev@polimi.it; annalisa.orrico@polimi.it; leonardo.bianchi@polimi.it; davide.paloschi@polimi.it; paola.saccomandi@polimi.it).

Alexey Wolf and Alexander Dostovalov are with the Department of Physics, Novosibirsk State University, 630090 Novosibirsk, Russia, and also with the Institute of Automation and Electrometry, Siberian Branch of the Russian Academy of Sciences, 630090 Novosibirsk, Russia (e-mail: wolf@iae.nsk.su; dostovalov@iae.nsk.su).

Digital Object Identifier 10.1109/TIM.2021.3112790

thermal damage for several tissue types [9]. In this regard, as will be discussed later in this article, the proposed LA regulation maintains controlling temperature at 43 °C during LA experiments.

The state-of-the-art works on temperature-based LA control mostly utilize traditional types of sensors: thermocouples [10], [11], and thermistor probes [12], [13]. The main disadvantages of these methods are the metallic material of the sensors and their low spatial resolution. Metallic material absorbs laser light and heat; thus leading to overestimation of temperature that can reach above 20 °C [14], [15]. The low spatial resolution of conventional sensors does not allow proper temperature reconstruction due to high thermal gradients, especially in the proximity of the applicator tip [8].

One of the possible alternatives to thermocouples and thermistors is the use of fiber Bragg grating (FBG) sensors. FBGs, as most optical sensors, are immune to electromagnetic interference, are small in size, and biocompatible. These advantages have led to increasing interest in FBG applications in LA treatments [16], [17].

Recently, our group has been working on FBG array applications for LA regulation using the ON–OFF controlling approach. The aim was the regulation of maximum temperature [18] and zone control [19] during contactless LA, and temperature control at different distances from the laser fiber tip during interstitial LA [20] of liver tissues. In order to improve controlling performance, in this article, we propose and experimentally validate a proportional–integral–derivative (PID)-based approach applied to the interstitial ablation of pancreatic tissue. In addition, the model of the heat transfer inside the tissue undergoing LA has been used for optimizing the choice of the PID parameters to be used in the experiments.

II. MATERIALS AND METHODS

A. FBG Array Sensors

FBG is a periodic modulation of refractive index in the fiber core that behaves as a wavelength-dependent reflector, transmitting all wavelengths except the characteristic Bragg wavelength λ_B . The Bragg wavelength is proportional to the periodicity of modulation Λ

$$\lambda_{B=2} = 2n_{\text{eff}}\Lambda \quad (1)$$

where n_{eff} is the effective refractive index of the core mode field.

The working principle of FBG relies on the fact that a temperature change ΔT alters Λ and n_{eff} , and, as a result, λ_B [21]

$$\frac{\Delta\lambda_B}{\lambda_B} = \alpha \cdot \Delta T \quad (2)$$

where α (°C⁻¹) is the thermal sensitivity of the grating and $\Delta\lambda_B$ is the variation of λ_B .

Therefore, it is possible to reconstruct temperature changes along the FBG by measuring the $\Delta\lambda_B$ values. In addition, an array of FBGs along with the fiber (each FBG with different Λ and λ_B) can provide quasi-distributed temperature measurements, where each FBG acts as a sensing point.

A custom-made highly dense FBG array used in the experiments was fabricated with femtosecond point-by-point writing technology. The FBG array was inscribed in polyimide-coated single-mode fiber SM1500(9/125)P (Fibercore, Ltd., Southampton, U.K.) with a reduced coating diameter (~ 145 μm). For femtosecond point-by-point inscription, Pharos 6W (Light Conversion, Vilnius, Lithuania) femtosecond laser system producing pulses with a wavelength of 1026 nm and duration of 232 fs was utilized. ABL1000 (Aerotech, Inc., Pittsburgh, PA, USA) air-bearing linear stage was used for high-precision pulling of the fiber through the glass ferrule to set the position and individual resonant wavelength for each FBG in the array.

Pulling of the fiber with the predefined velocity ($v_i \sim 1$ mm/s) and simultaneous femtosecond irradiation with laser pulse sequence ($f = 1$ kHz) results in FBG inscription. The obtained Bragg wavelength is defined by $\lambda_{B,i} = 2n_{\text{eff}}\Lambda_i = 2n_{\text{eff}}v_i/mf$, where $m = 2$ is an order of FBG.

All 40 FBGs in the array were uniformly distributed in the spectral range of the used interrogator (1460–1620 nm) in order to reduce mutual interference of the neighboring gratings. Each of the gratings had a length of 1.15 mm, an edge-to-edge distance of 0.05 mm (the total length of the FBG array is 48 mm), and a uniform refractive index modulation profile, which gave us an FWHM spectral width of the grating of ~ 700 pm. The reflection coefficient of an FBG in the range of 10%–20% allowed us to record the array reflection spectrum with a high dynamic range (> 30 dB).

These FBG properties were optimized to have a narrow Bragg spectral width and at the same time to ensure accurate measurements of high-gradient temperature profiles that can reach up to 50 °C/mm near the applicator during LA procedures [8]. Moreover, the polyimide coating of the array provides the high thermal resistance (up to 400 °C) needed for accurate quasi-distributed measurements in this application [22]–[24]. The temperature sensitivity of the arrays is $(7.43 \pm 0.01) \times 10^{-6}$ °C⁻¹. More information about the fabrication and the metrological characterization of the sensors can be found in the previous works of the group [19], [24].

The Micron Optics si255 optical interrogator (Micron Optics, Atlanta, USA, 1-pm accuracy, and wavelength range 1460–1620 nm) was utilized to measure the reflected spectra from the FBG arrays with a 100 Hz sampling rate.

B. Laser Ablation Equipment

Interstitial LA experiments were performed on *ex vivo* healthy porcine pancreatic tissue, which was obtained from a local farm. After the removal, the organs have been immediately placed in a sealed bag and stored in the fridge (4 °C). For the experiments, each specimen was prepared with a size suitable for placing in the custom-made box, which was used for accurate positioning of the sensor and laser fiber. The tissue temperature before the start of experiments was maintained at room temperature equal to 22 °C.

The diode laser (LuOcean Mini 4, Lumics, Berlin, Germany) working in continuous-wave mode at a 1064-nm

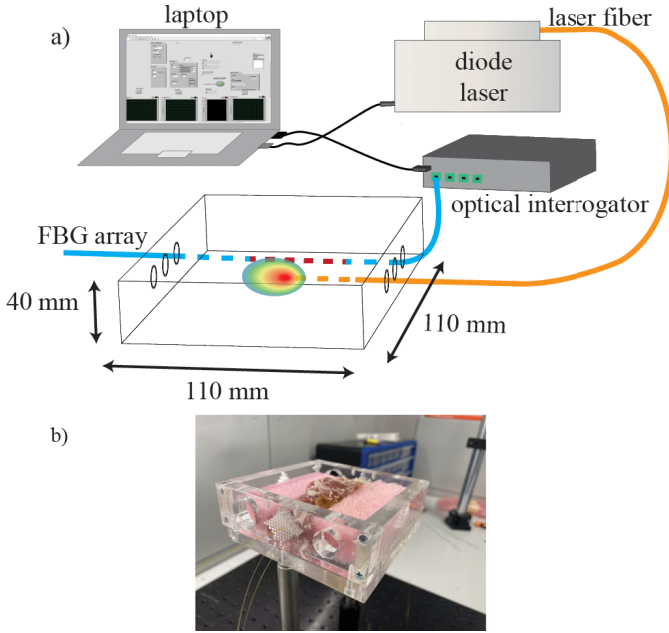


Fig. 1. (a) Schematics of the experimental setup: laser fiber and FBG array inserted in pancreatic tissue positioned in custom-made box; LA regulation setup consists of optical interrogator, diode laser, and laptop. (b) Photograph of sensors and laser fiber positioned in pancreatic tissue.

wavelength was used for ablation. This wavelength belongs to the “therapeutic window” largely used for assuring the overall absorption of the laser light by the biological tissues, thus, to entail the temperature increase necessary for the thermal therapy. It is worth noticing that 1064 nm is the wavelength that has been used for the first human trial on pancreatic tumors [25]. The flexible quartz optical fiber (300- μm diameter) was used to guide laser light inside the tissue.

The laser diode driver allows changing the output optical power via electrical current modulation during laser irradiation. For PID controlling, an electrical current range of 3000 (minimal current of the laser diode) to 8000 mA was chosen. In order to obtain corresponding power values, power was measured with a Newport 843-R-USB power meter (Newport Corporation, Irvine, CA, USA) for the current range selected. As a result, the obtained power range used for the PID temperature regulation experiments was 1.8–6.6 W.

C. Experimental Arrangement

The developed system consists of the laser diode and the interrogation system, both connected to a computer where a custom-made LabVIEW program was used to regulate LA.

A custom-made plexiglass box was employed to guarantee the accurate positioning of the laser fiber and sensors. The holes located on all sides of the box allow for different sensor and applicator arrangements in the tissue (Fig. 1).

The fibers were placed with the help of medical needles to prevent their damage during insertion into the pancreatic tissue. Initially, an 18-gauge needle (5-cm length) was inserted in the central hole of the lateral face of the box, and a 21-gauge needle (11-cm length) was inserted in a different hole at a

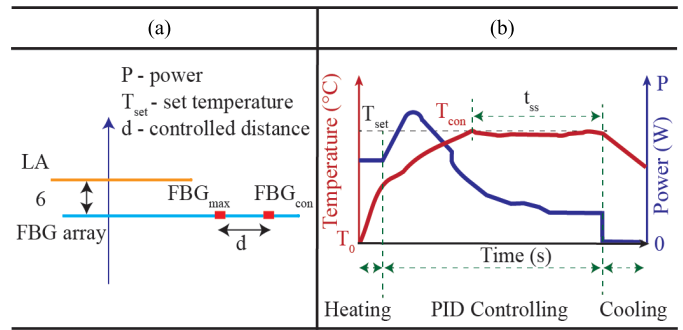


Fig. 2. Schematics of laser ablation algorithm. (a) Set of input parameters. (b) Schematics of controlled temperature evolution and related power during LA.

6-mm distance from the central one. Subsequently, the laser fiber and the FBG array fibers were inserted into the needles. The needles were then pulled out so that only the fibers remained inside the tissue.

The initial temperature of the pancreas, corresponding to 22.0 ± 0.5 °C, was measured with a thermocouple before each experiment. After experiments, the ablated volume was cut in the middle, and the axes of the ablated region were measured.

D. Controlling Algorithm

The developed LabVIEW program has two main phases (Fig. 2).

- 1) The input of preset parameters: set temperature T_{set} , PID gains, and d (distance between the grating with maximum temperature and the controlled grating).
- 2) Start of ablation with constant power (3.3 W) until a threshold of 10 °C of temperature change is reached. Then, the position of the grating exposed to the maximum temperature (FBG_{max}) is saved and position of the controlled grating (FBG_{con}) is calculated using the d value. After, regulation of the controlled temperature (T_{con}) at the controlled grating (FBG_{con}) is performed using the PID approach. Finally, after 300 s of steady-state time (t_{ss}), the laser is switched OFF.

E. Preplanning Model

In order to have an initial estimation of the gain coefficients of the PID controller, the heat-transfer phenomenon caused by the interaction between laser and the pancreas was simulated, along with the effects of the PID control.

The temperature distribution of an *ex vivo* biological tissue subjected to laser-induced thermal treatment is governed by the bio-heat transfer equation [26], expressed as

$$\rho \cdot c \cdot \frac{\partial T(t, r, z)}{\partial t} + \nabla(-k \nabla T(t, r, z)) = Q_{\text{source}} \quad (3)$$

where $T(t, r, z)(K)$ is the tissue temperature, while the density, the specific heat, and the thermal conductivity of the biological tissue are represented with $\rho(\text{kg} \cdot \text{m}^{-3})$, $c(\text{J} \cdot \text{kg}^{-1} \text{K}^{-1})$, and $k(\text{W} \cdot \text{m}^{-1} \text{K}^{-1})$ respectively; the term $Q_{\text{source}}(\text{W} \cdot \text{m}^{-3})$ represents the deposited thermal energy

TABLE I
PID GAINS FOR DIFFERENT SIMULATION SETS

	$k_p (A \cdot K^{-1})$	$k_i (A \cdot K^{-1} \cdot s^{-1})$	$k_d (A \cdot s \cdot K^{-1})$
Set 1	10	1	0
Set 2	1	10	5
Set 3	0.1	0.6	0
Set 4	0.7	0.006	0
Set 5	0.7	0	20

delivered by the laser source. Since the latter term is strongly affected by the light propagation in the tissue, a simple diffusion approximation method was employed to correctly predict the deposited thermal energy. The Beer–Lambert law [27] was used to predict the light propagation inside the tissue

$$\frac{\partial I(t, r, z)}{\partial z} = -\alpha_{\text{eff}} \cdot I(t, r, z). \quad (4)$$

The resulting deposited thermal energy [28] can be expressed as

$$Q_{\text{laser}} = \alpha_{\text{eff}} \cdot I_0(t, r) \cdot e^{-\alpha_{\text{eff}} \cdot z} \quad (5)$$

where $z(m)$ is the axial depth in tissue and $\alpha_{\text{eff}}(m^{-1})$ is the effective attenuation coefficient that was calculated based upon diffusion approximation [29] to consider both the absorption and the scattering phenomena. Lastly, $I_0(W \cdot m^{-2})$ represents the laser irradiance and is expressed as

$$I_0(t, r) = \frac{P(t)}{2\pi\sigma^2} \cdot e^{-\frac{r^2}{2\sigma^2}} \quad (6)$$

where $\sigma(m)$ is the standard deviation related to the beam profile, $r(m)$ is the radial distance, and $P(W)$ is the laser power that is linearly dependent on the laser current $C(A)$. This last parameter is set by a PID controller as follows:

$$C(t) = k_p \cdot (T_{\text{set}} - T_{\text{con}}) + k_i \cdot \int_0^t (T_{\text{set}} - T_{\text{con}}(\tau)) d\tau + k_d \cdot \frac{d(T_{\text{set}} - T_{\text{con}}(t))}{dt}. \quad (7)$$

The PID controller maintains the temperature $T_{\text{con}}(K)$ at the same value of the setpoint temperature $T_{\text{set}}(K)$, upon a proper selection of the proportional $k_p(A \cdot K^{-1})$, integral $k_i(A \cdot K^{-1} \cdot s^{-1})$ and derivative $k_d(A \cdot s \cdot K^{-1})$ gain coefficients.

III. RESULTS AND DISCUSSION

A. Preplanning of PID Gains

The numerical model of the interstitial LA was solved using the finite element method (FEM)-based solver: COMSOL Multiphysics (COMSOL, Inc., Burlington, MA, USA). Several simulations were run to assess the best set of parameters for the PID controller based on the tissue thermal response. The tested gain coefficients are reported in Table I, and corresponding temperature profiles are reported in Fig. 3(a).

Fig. 3 shows the simulated thermal responses and the related output power profiles needed to achieve the setpoint temperature of 43 °C under five different PID settings at $d = 10.8$ mm. The output power profiles of Set 1, Set 2,

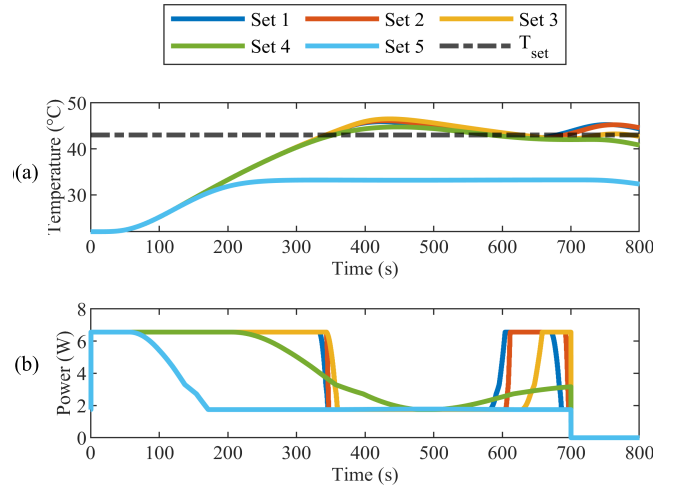


Fig. 3. Simulated temperature (a) and laser power (b) profiles for the different sets of PID gain values.

and Set 3 experience abrupt changes when the controlled temperature approaches the setpoint value [Fig. 3(b)]. These PID sets do not possess control moderation and use mainly the minimum and maximum power available; consequently, they are not able to react in advance to the heat diffusion generated by a thermal gradient. As a result, they experience temperature overshoots and very lethargic setpoint tracking due to the suboptimal choice of the gains [Fig. 3(a)].

The light blue curve denotes the thermal response of the tissue temperature in the absence of the integral term in the PID system. Since k_i is responsible for enforcing zero steady-state error [30], the steady-state response of Set 5 is not able to reach the setpoint temperature. Conversely, the gain parameters selected in Set 4, i.e., $k_p = 0.7 A \cdot K^{-1}$, $k_i = 0.006 A \cdot K^{-1} \cdot s^{-1}$ and $k_d = 0 A \cdot s \cdot K^{-1}$ showed a smoother power profile and a thermal response characterized by a rise time of ~ 350 s and a smaller temperature overshoot of ~ 1.8 °C (Fig. 3, green line). These last PID gain parameters were used for the experiments.

Robustness of selected PID gains for different controlled distances was checked by changing the position of the controlled point from $d = 10.8$ mm to $d = 7.2$ mm. Fig. 4 reports that the selected gains allow having a good controlling performance (i.e., rising time of ~ 350 s and a temperature overshoot of ~ 0.5 °C) also for $d = 7.2$ mm.

Fig. 5 shows the temperature distributions resulting from the LA regulation shown in Fig. 4 for $d = 10.8$ mm (Fig. 5 left-hand side) and $d = 7.2$ mm (right-hand side). Different thresholds were selected to display the volumes of pancreatic tissue subjected to specific temperatures, relevant for laser-assisted treatment purposes, in particular: 1) sublethal damage around $T \sim 43$ °C; 2) instantaneous thermal damage for $T \geq 60$ °C; 3) vapor diffusion and tissue desiccation at $T \geq 100$ °C; and 4) removal of tissue mass for $T \geq 300$ °C [31]. As can be seen from Fig. 5, the controlled distance d affects the temperature distribution and, therefore, the extension of the thermal damage.

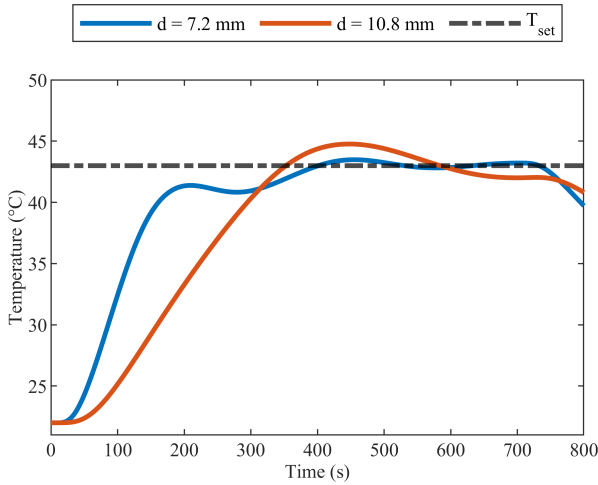


Fig. 4. Simulated controlled temperature profiles for different controlled distances.

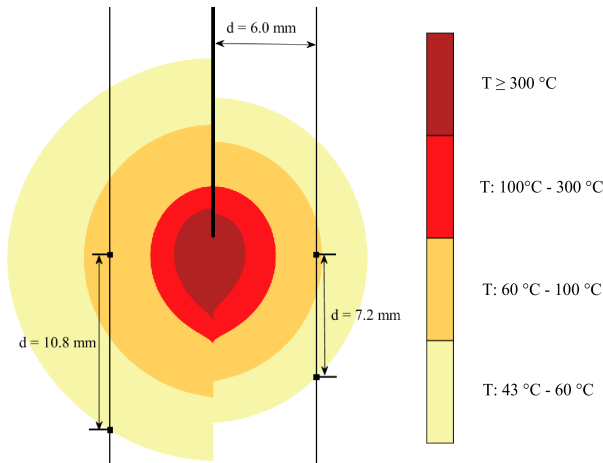


Fig. 5. Simulated temperature distributions for controlled distance equal to $d = 10.8$ mm (left) and $d = 7.2$ mm (right).

B. Experimental Results

After preplanning the PID controller and obtainment of the gain values, we used them for the experimental tests. In particular, experiments with different d values ($d = 6.0, 7.2, 8.4,$ and 10.8 mm) were performed to further assess the robustness of the control strategy toward different distances and to validate the proposed LA regulation approach.

Fig. 6 reports the evolution of the controlled temperature and the laser power during LA of the pancreas. As it can be seen, the controlling algorithm allows for the proper regulation of the set temperature T_{set} , which was reached approximately after 350 s in all cases and maintained for $t_{ss} = 300$ s. Concerning the laser power, it is maintained constant for the first seconds of the procedure. Then, it suddenly changes to 5 W. For $d = 6.0$ and 7.2 mm, 5 W are maintained for ~ 100 s, whereas for $d = 10.8$ mm it is maintained for ~ 200 s. After this constant phase, the power decreases until it reaches another plateau at approximately 2 W. This plateau corresponds to the constant and desired temperature profile

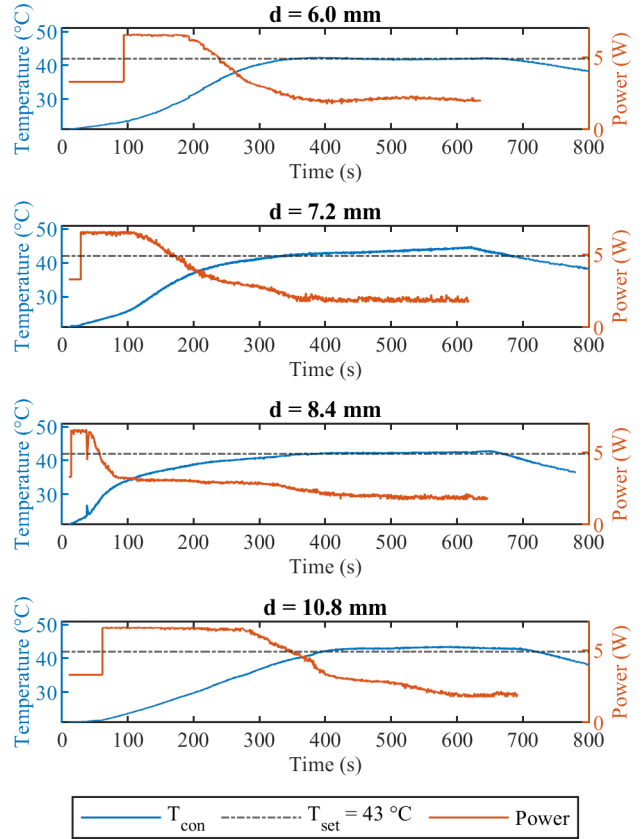


Fig. 6. Measured controlled temperature, set temperature (43 °C), and laser power profiles for different controlled distances.

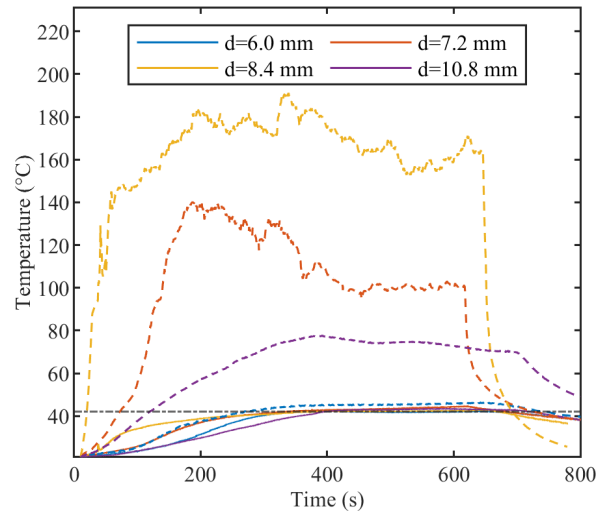


Fig. 7. Measured controlled temperature profiles (solid lines) and maximum measured temperature profiles (dashed lines) for different controlled distances.

measured in the tissue and achieved with the implemented control strategy.

Fig. 7 shows controlled temperatures for different d values and related maximum measured temperatures (dashed lines). Despite the high differences between controlled and maximum temperatures (up to 140 °C), the control has an overdamped behavior for all tests. The results shown in Fig. 7 further highlight the key role of the implemented control strategy for the

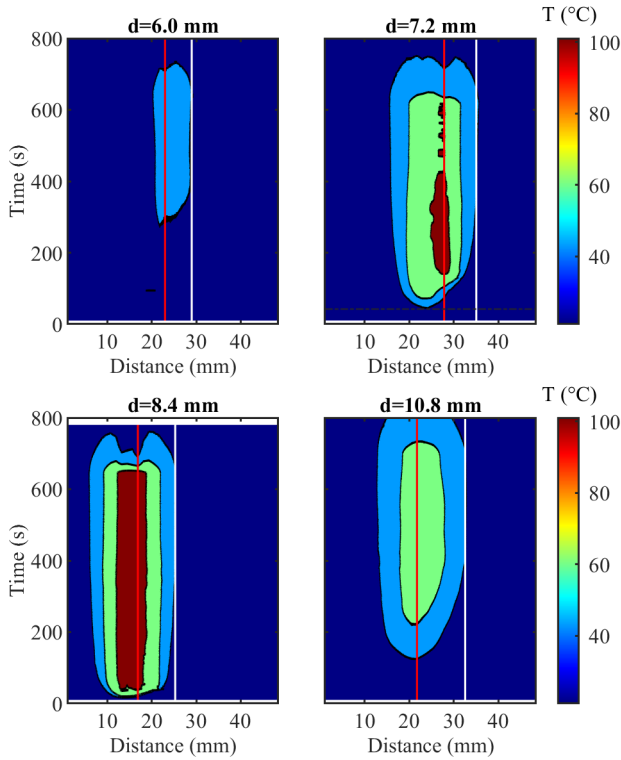


Fig. 8. Measured contour maps during laser ablation with different controlled distances for temperatures: 10 °C, 43 °C, 60 °C, and 100 °C. The red line shows the position of the FBG measuring the maximum temperature, and the white line depicts the position of the controlled grating.

application. Indeed, the complexity of the pancreas structure from the biological, optical, and thermal points of view causes irregular heat transfer in the organs, as demonstrated by the high and irregular maximum temperature profile measured on the FBGs of the array. Thus, the absence of a suitable control strategy can worsen the performance of the LA procedure.

The high spatial resolution of the highly dense FBG arrays allows for reconstructing temperature evolution maps (distance along with the array versus time) from the measured values, as shown in Fig. 8. The contour maps measured by the FBG array during laser ablation are depicted considering relevant temperatures for the LA biological outcome, i.e., 43 °C, 60 °C, and 100 °C. The red line shows the position of the FBG measuring the maximum temperature, and the white line depicts the position of the controlled grating. As can be seen from Fig. 9, the set temperature (43 °C contour) does not exceed the defined controlled distance (white line) for all tests. In addition, temperature contours can be used for the evaluation of instantaneous thermal damage ($T \geq 60$ °C) and vapor diffusion and tissue desiccation ($T \geq 100$ °C). We observe that for $d = 6.0$ mm, the FBG array experiences a temperature evolution which is maintained below 60 °C. This result is expected since the short control distance (with a set temperature of 43 °C) does not allow proper heat transfer in the tissue. For $d = 7.2$ mm, $d = 8.4$ mm, and $d = 10.8$ mm, the temperature is higher than the case of $d = 6.0$ mm, and at $d = 10.8$ mm, no contour at 100 °C is present. This result is also acceptable because the aim of the developed algorithm

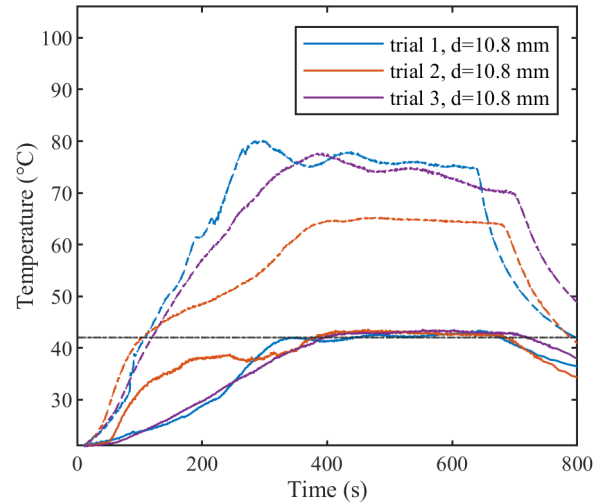


Fig. 9. Measured set temperature profiles (solid lines) and maximum temperature profiles (dashed lines) for the controlled distance of 10.8 mm.

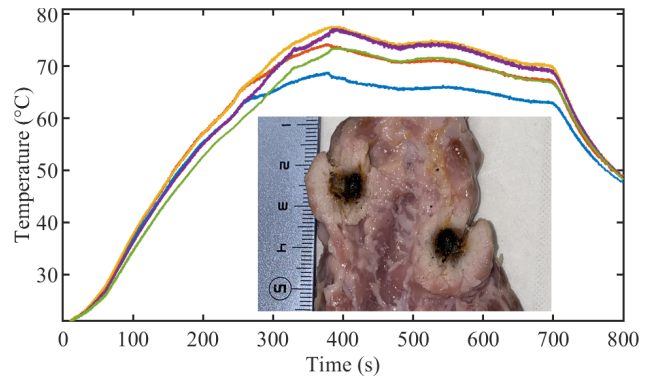


Fig. 10. Measured maximum temperature profile and profiles measured by adjacent gratings for controlled distance of 10.8 mm. Inset: Resulted ablated region of pancreatic tissue.

is to maintain the stable temperature at the controlled grating (white line in Fig. 8), while the maximum temperature can reach any value depending on laser-tissue interaction (as also shown in Fig. 7).

Fig. 9 shows the repeatability of the temperature control achievable with our approach. In this case, we report the maximum temperature profiles measured by the FBGs (dashed lines) and the controlled temperature measured by the FBG placed at $d = 10.8$ mm (continuous line). Three trials on different parts of *ex vivo* pancreatic tissue have been repeated, avoiding any overlap of the damaged zone between consecutive tests. As it can be seen, the control algorithm is able to maintain stable temperature during t_{ss} for all trials. The slight differences can be due to the inhomogeneity of the tissue.

Moreover, the high spatial resolution of the sensors can provide information about the thermal gradient. For instance, we observed that across an intragrating distance of about 2.4 mm, a temperature difference of ~ 10 °C can be measured (Fig. 10), which proves the need for high-resolution sensors for such measurements.

The final results of LA control are presented in Table II. The energy of the treatment was calculated by using the laser power values used for PID control and the duration of the controlled

TABLE II
LA REGULATION RESULTS FOR DIFFERENT CONTROLLED DISTANCES

d (mm)	Time of PID regulation (s)	Energy (J)	Ablated dimensions (mm x mm)
6.0	541.7	1844	7.57×6.71
7.2	588.6	1943	12.07×8.03
8.4	631.8	1729	14.15×10.76
10.8	629.8	2695	17.39×14.11

ablation. Table II reports that the size of the ablated area mostly depends on controlled distance d and is less correlated with energy or time of ablation. As a result, the proposed LA regulation approach allows controlling the size of the ablated region by changing the controlled distance parameter.

The obtained experimental results validate the proposed PID approach for LA regulation and show the efficacy of FEM-based pre-experiment simulations to obtain effective PID gain values. However, limitations regarding the reliability of the simulations in the prediction of the final clinical outcome are represented by the lack of literature about the behavior of the thermo-optical pancreatic properties with respect to temperatures and by the complexity of photothermal-induced heat transfer in biological tissue. Thus, thermo-optical tissue properties need to be investigated in detail to improve TA simulations and their applications in tumor treatment.

In the proposed approach, temperature measurements performed by custom-made highly dense FBG arrays allow for efficient controlling of temperature at different distances and ablation volumes. The high spatial resolution and electromagnetic immunity of the used sensors provide unique advantages in comparison with traditional measurement techniques. Indeed, in the recent work focused on the PID regulation of LA based on thermocouple measurements, a 0.5-mm plastic plate was positioned between the laser applicator and the thermocouple to prevent laser light artifacts along with self-heating [30]. This approach significantly limits possible clinical applications of all of the standard temperature sensors for LA. For instance, the recent work of Paiella *et al.* [32] on clinical testing of immune-stimulating interstitial laser thermotherapy of the pancreas using a feedback mode with conventional sensors (thermistors) reports unsatisfactory results in terms of device handling, safety, and feasibility.

Thus, the limitations of convenient sensors observed in the literature encourage further investigation of fiber optic use for LA control. Indeed, recent investigations of single-FBG-based measurements for PID-based control were performed for a laser-heated needle for biopsy tract ablation and showed promising results [33], [34]. In addition, the use of highly dense FBG arrays for LA regulation has been discussed in the recent works of our group [18]–[20], where an ON–OFF control law yielded undesirable overshoots and delayed responses in the temperature regulation.

Nevertheless, one of the limitations of FBG array use for TA is the temperature-strain cross-sensitivity that can lead to measurement artifacts during temperature monitoring. In our

experimental setup, this artifact was minimized using the difference between diameters of the needle utilized for FBG placing ($21 \text{ G} = 0.819 \text{ mm}$) and the FBG array diameter ($145 \text{ }\mu\text{m}$). This difference results in slightly looser adhesion between tissue and the sensor, thus decreasing strain effect [35], [36].

In order to significantly reduce strain artifacts stemming from the axial strain and bending, a suitable embodiment [glass or polytetrafluoroethylene (PTFE) capillary] to encapsulate FBG needs to be developed. However, it can affect sensor dynamic response and absorb the part of the laser light during LA. As a result, more investigations need to be performed in the encapsulation development to completely avoid strain artifacts during FBG temperature measurements.

IV. CONCLUSION

In conclusion, a temperature-based feedback approach for LA regulation was investigated. For temperature measurements, custom-made highly dense FBG arrays were inscribed in single-core fiber using point-by-point writing technology. The high spatial resolution (1.2 mm) and temperature resistance above the typical maximum temperatures of LA provide unique advantages for thermometry. Moreover, FEM-based iterative simulations were developed to optimize the choice of PID gains. In order to validate the closed-loop approach, the point temperature was controlled at different distances from the laser fiber tip (6, 7.2, 8.4, and 10.8 mm). The approach here proposed is an innovative feature for the specific application of laser ablation for tumor treatment, where usually no control at all is performed, but the procedure relies only on the experience of the doctor. The results show effective temperature control for all distances and for all experimental trials. The results of the work encourage further investigation of FBG array applications for LA regulation.

REFERENCES

- [1] R. L. Siegel, K. D. Miller, and A. Jemal, "Cancer statistics, 2020," *CA: A Cancer J. Clinicians*, vol. 70, no. 1, pp. 7–30, Jan. 2020, doi: [10.3322/caac.21590](https://doi.org/10.3322/caac.21590).
- [2] L. Rahib, B. D. Smith, R. Aizenberg, A. B. Rosenzweig, J. M. Fleshman, and L. M. Matrisian, "Projecting cancer incidence and deaths to 2030: The unexpected burden of thyroid, liver, and pancreas cancers in the united states," *Cancer Res.*, vol. 74, no. 11, pp. 2913–2921, Jun. 2014.
- [3] J. Han and K. J. Chang, "Endoscopic ultrasound-guided direct intervention for solid pancreatic tumors," *Clin. Endoscopy*, vol. 50, no. 2, pp. 126–137, Mar. 2017, doi: [10.5946/ce.2017.034](https://doi.org/10.5946/ce.2017.034).
- [4] A. Ruarus, L. Vroomen, R. Puijk, H. Scheffer, and M. Meijerink, "Locally advanced pancreatic cancer: A review of local ablative therapies," *Cancers*, vol. 10, no. 1, p. 16, Jan. 2018.
- [5] E. Schena, P. Saccomandi, and Y. Fong, "Laser ablation for cancer: Past, present and future," *J. Funct. Biomater.*, vol. 8, no. 2, p. 19, Jun. 2017, doi: [10.3390/jfb8020019](https://doi.org/10.3390/jfb8020019).
- [6] L. Bianchi *et al.*, "Thermal analysis of laser irradiation-gold nanorod combinations at 808 nm, 940 nm, 975 nm and 1064 nm wavelengths in breast cancer model," *Int. J. Hyperthermia*, vol. 38, no. 1, pp. 1099–1110, Jan. 2021.
- [7] K. F. Chu and D. E. Dupuy, "Thermal ablation of tumours: Biological mechanisms and advances in therapy," *Nat. Rev. Cancer*, vol. 14, no. 3, pp. 199–208, 2014.
- [8] A. J. Welch and M. J. C. Van Gemert, *Optical-Thermal Response of Laser-Irradiated Tissue*. Dordrecht, The Netherlands: Springer, 2011.
- [9] P. S. Yarmolenko *et al.*, "Thresholds for thermal damage to normal tissues: An update," *Int. J. Hyperthermia*, vol. 27, no. 4, pp. 320–343, Jun. 2011, doi: [10.3109/02656736.2010.534527](https://doi.org/10.3109/02656736.2010.534527).

- [10] J.-T. Lin, Y.-S. Chiang, G.-H. Lin, H. Lee, and H.-W. Liu, "In vitro photothermal destruction of cancer cells using gold nanorods and pulsed-train near-infrared laser," *J. Nanomater.*, vol. 2012, pp. 1–6, Jul. 2012, doi: [10.1155/2012/861385](https://doi.org/10.1155/2012/861385).
- [11] J. T. Lin, "Selective cancer therapy using IR-laser-excited gold nanorods," *SPIE Newsroom*, vol. 2, no. 4, p. 2507, Feb. 2010, doi: [10.1117/12.841348](https://doi.org/10.1117/12.841348).
- [12] K. Ivarsson, J. Olsrud, C. Stureson, P. H. Möller, B. R. Persson, and K.-G. Tranberg, "Feedback interstitial diode laser (805 nm) thermotherapy system: *Ex vivo* evaluation and mathematical modeling with one and four-fibers," *Lasers Surgery Med.*, vol. 22, no. 2, pp. 86–96, 1998.
- [13] P. H. Möller, L. Lindberg, P. H. Henriksson, B. R. R. Persson, and K.-G. Tranberg, "Temperature control and light penetration in a feedback interstitial laser thermotherapy system," *Int. J. Hyperthermia*, vol. 12, no. 1, pp. 49–63, Jan. 1996, doi: [10.3109/02656739609023689](https://doi.org/10.3109/02656739609023689).
- [14] P. Saccomandi, E. Schena, and S. Silvestri, "Techniques for temperature monitoring during laser-induced thermotherapy: An overview," *Int. J. Hyperthermia*, vol. 29, no. 7, pp. 609–619, Nov. 2013, doi: [10.3109/02656736.2013.832411](https://doi.org/10.3109/02656736.2013.832411).
- [15] F. Manns, P. J. Milne, X. Gonzalez-Cirre, D. B. Denham, J.-M. Parel, and D. S. Robinson, "In situ temperature measurements with thermocouple probes during laser interstitial thermotherapy (LITT): Quantification and correction of a measurement artifact," *Lasers Surgery Med.*, vol. 23, no. 2, pp. 94–103, 1998.
- [16] A. Othonos, K. Kalli, and G. E. Kohnke, "Fiber Bragg gratings: Fundamentals and applications in telecommunications and sensing," *Phys. Today*, vol. 53, no. 5, p. 61, 2000.
- [17] E. Udd and W. B. Spillman, Jr., *Fiber Optic Sensors: An Introduction for Engineers and Scientists*. Hoboken, NJ, USA: Wiley, 2011.
- [18] S. Korganbayev, R. Pini, A. Orrico, A. Wolf, A. Dostovalov, and P. Saccomandi, "Towards temperature-controlled laser ablation based on fiber Bragg grating array temperature measurements," in *Proc. IEEE Int. Workshop Metrol. Ind. 4.0 (IoT)*, Jun. 2020, pp. 268–272.
- [19] S. Korganbayev *et al.*, "Closed-loop temperature control based on fiber Bragg grating sensors for laser ablation of hepatic tissue," *Sensors*, vol. 20, no. 22, p. 6496, Nov. 2020.
- [20] L. Bianchi, S. Korganbayev, A. Orrico, M. De Landro, and P. Saccomandi, "Quasi-distributed fiber optic sensor-based control system for interstitial laser ablation of tissue: Theoretical and experimental investigations," *Biomed. Opt. Exp.*, vol. 12, no. 5, p. 2841, May 2021, doi: [10.1364/BOE.419541](https://doi.org/10.1364/BOE.419541).
- [21] T. Erdogan, "Fiber grating spectra," *J. Lightw. Technol.*, vol. 15, no. 8, pp. 1277–1294, Aug. 15, 1997.
- [22] K. T. V. Gratten and B. T. Meggitt, *Optical Fiber Sensor Technology*, vol. 3. Boston, MA, USA: Springer, 1998.
- [23] L. Huang, R. S. Dyer, R. J. Lago, A. A. Stolov, and J. Li, "Mechanical properties of polyimide coated optical fibers at elevated temperatures," *Proc. SPIE*, vol. 9702, Mar. 2016, Art. no. 97020Y, doi: [10.1117/12.2210957](https://doi.org/10.1117/12.2210957).
- [24] A. V. Dostovalov, A. A. Wolf, A. V. Parygin, V. E. Zyubin, and S. A. Babin, "Femtosecond point-by-point inscription of Bragg gratings by drawing a coated fiber through ferrule," *Opt. Exp.*, vol. 24, no. 15, pp. 16232–16237, 2016.
- [25] P. Saccomandi, A. Lapergola, F. Longo, E. Schena, and G. Quero, "Thermal ablation of pancreatic cancer: A systematic literature review of clinical practice and pre-clinical studies," *Int. J. Hyperthermia*, vol. 35, no. 1, pp. 398–418, Dec. 2018, doi: [10.1080/02656736.2018.1506165](https://doi.org/10.1080/02656736.2018.1506165).
- [26] M. H. Niemz, *Laser-Tissue Interactions*, 3rd ed. Berlin, Germany: Springer, 2007.
- [27] P. Saccomandi *et al.*, "Theoretical analysis and experimental evaluation of laser-induced interstitial thermotherapy in *ex vivo* porcine pancreas," *IEEE Trans. Biomed. Eng.*, vol. 59, no. 10, pp. 2958–2964, Oct. 2012, doi: [10.1109/TBME.2012.2210895](https://doi.org/10.1109/TBME.2012.2210895).
- [28] T. H. Nguyen, Y. H. Rhee, J. C. Ahn, and H. W. Kang, "Circumferential irradiation for interstitial coagulation of urethral stricture," *Opt. Exp.*, vol. 23, no. 16, pp. 20829–20840, Aug. 2015.
- [29] A. Ishimaru, "Diffusion of light in turbid material," *Appl. Opt.*, vol. 28, no. 12, pp. 2210–2215, 1989, doi: [10.1364/AO.28.002210](https://doi.org/10.1364/AO.28.002210).
- [30] T. H. Nguyen, S. Park, K. K. Hlaing, and H. W. Kang, "Temperature feedback-controlled photothermal treatment with diffusing applicator: Theoretical and experimental evaluations," *Biomed. Opt. Exp.*, vol. 7, no. 5, p. 1932, May 2016, doi: [10.1364/BOE.7.001932](https://doi.org/10.1364/BOE.7.001932).
- [31] A. J. Welch and M. J. C. Van Gemert, *Optical-Thermal Response of Laser-Irradiated Tissue*, vol. 2. Dordrecht, The Netherlands: Springer, 2011.
- [32] S. Paiella *et al.*, "Laser treatment of pancreatic cancer with immunostimulating interstitial laser thermotherapy protocol: Safety and feasibility results from two phase 2a studies," *J. Surgical Res.*, vol. 259, pp. 1–7, Mar. 2021.
- [33] H. H. Abd Raziff *et al.*, "A temperature-controlled laser hot needle with grating sensor for liver tissue tract ablation," *IEEE Trans. Instrum. Meas.*, vol. 69, pp. 7119–7124, 2020, doi: [10.1109/TIM.2020.2978920](https://doi.org/10.1109/TIM.2020.2978920).
- [34] H. H. A. Raziff *et al.*, "Laser-heated needle for biopsy tract ablation: In vivo study of rabbit liver biopsy," *Phys. Medica*, vol. 82, pp. 40–45, Feb. 2021, doi: [10.1016/j.ejomp.2021.01.067](https://doi.org/10.1016/j.ejomp.2021.01.067).
- [35] L. Bianchi *et al.*, "Fiber Bragg grating sensors-based thermometry of gold nanorod-enhanced photothermal therapy in tumor model," *IEEE Sensors J.*, early access, May 19, 2021, doi: [10.1109/JSEN.2021.3082042](https://doi.org/10.1109/JSEN.2021.3082042).
- [36] B. A. Patterson, D. D. Sampson, P. A. Krug, and S. K. Jones, "In vivo quasi-distributed temperature sensing with fibre Bragg gratings," in *Tech. Dig. Summaries papers Presented Conf. Lasers Electro-Opt. Postconf. Tech. Dig.*, May 2001, pp. 402–403.

Sanzhar Korganbayev (Graduate Student Member, IEEE) received the B.S. and M.S. degrees in electrical and electronics engineering from Nazarbayev University, Nur-Sultan, Kazakhstan, in 2016 and 2018, respectively. He is currently pursuing the Ph.D. degree with the Department of Mechanical Engineering, Politecnico di Milano, Milan, Italy.

He is currently involved in the LASER OPTIMAL Project (European Research Council Grant) for the development of software for real-time temperature monitoring and intraoperative adjustment of the laser ablation settings during tumor treatment. His research interests include fiber optic sensors and their applications for thermal and mechanical measurements.

Annalisa Orrico (Graduate Student Member, IEEE) received the B.S. and M.S. degrees in mechanical engineering from the Politecnico di Milano, Milan, Italy, in 2017 and 2020, respectively, where she is currently pursuing the Ph.D. degree with the Department of Mechanical Engineering.

She is currently involved in the HyperSIGHT project for the development of spectral imaging-based tools for the monitoring and prediction of thermal effects on tissues. Her research interest is the applications of imaging and fiber optic sensors for thermal measurements.

Leonardo Bianchi (Graduate Student Member, IEEE) received the M.Sc. degree (*cum laude*) in biomedical engineering from the Politecnico di Milano, Milan, Italy, in 2019, where he is currently pursuing the Ph.D. degree with the Department of Mechanical Engineering.

He is working in the framework of the LASER OPTIMAL project (European Research Council Grant) at the Politecnico di Milano. His research interests include the optimization of tumor laser ablation, from the numerical modeling and experimental assessment, nanoparticle-assisted photothermal therapies, and the related sensing techniques for temperature monitoring during treatments.

Davide Paloschi (Graduate Student Member, IEEE) received the B.S. and M.S. degrees in automation and control engineering from the Politecnico di Milano, Milan, Italy, in 2016 and 2018, respectively, where he is currently pursuing the Ph.D. degree with the Department of Mechanical Engineering.

From 2019 to 2020, he was a Research Fellow with the Department of Mechanical Engineering, Politecnico di Milano. His research interests include the monitoring of physiological parameters, model prediction, data analysis, and noise filtering.

Alexey Wolf received the M.Sc. degree in physics from Novosibirsk State University (NSU), Novosibirsk, Russia, and the Ph.D. degree in optics from the Institute of Automation and Electrometry, Siberian Branch of the Russian Academy of Sciences (IAE SB RAS), Novosibirsk, in 2013 and 2020, respectively.

He is currently a Researcher with the Laboratory of Nonlinear Waveguide Systems, NSU, and the Laboratory of Fiber Optics, IAE SB RAS, where he is involved in developing new types of fiber lasers and sensors based on specialty optical fibers. His scientific interests include femtosecond laser micromachining, fiber Bragg gratings, and new optical materials.

Alexander Dostovalov received the M.Sc. degree in physics from Novosibirsk State University (NSU), Novosibirsk, Russia, and the Ph.D. degree in optics from the Institute of Automation and Electrometry (IAE), Siberian Branch of the Russian Academy of Sciences, in 2009 and 2015, respectively.





Since 2018, he has been a Senior Research Fellow with IAE and the Laboratory of Nonlinear Waveguide Systems, NSU. He has authored more than 35 articles and five inventions. His research interests include femtosecond laser micromachining, fiber Bragg gratings inscription, fiber lasers, and sensors.

Paola Saccomandi (Senior Member, IEEE) received the Ph.D. degree in biomedical engineering from the Università Campus Bio-Medico di Roma, Rome, Italy, in 2014.

From 2016 to 2018, she was a Post-Doctoral Researcher with the IHU Strasbourg—Institute of Image-Guided Surgery of Strasbourg, Strasbourg, France. Since 2018, she has been an Associate Professor with the Department of Mechanical Engineering, Politecnico di Milano, Milan, Italy. She is a Principal Investigator of the European Research Council grant LASER OPTIMAL. Her main research interests include fiber optic sensors, biomedical imaging, and the development of light-based approaches for hyperthermal tumor treatment and monitoring.

Article

Optimization of Cladding Diameter for Refractive Index Sensing in Tilted Fiber Bragg Gratings

Sanzhar Korganbayev ¹, Marzhan Sypabekova ^{2,3,4}, Aida Amantayeva ³, Álvaro González-Vila ⁵,
Christophe Caucheteur ⁵, Paola Saccomandi ¹ and Daniele Tosi ^{3,6,*}

¹ Politecnico di Milano, 20156 Milan, Italy; sanzhar.korganbayev@polimi.it (S.K.);
paola.sacomandi@polimi.it (P.S.)

² School of Medicine, Nazarbayev University, Nur-Sultan 020000, Kazakhstan;
marzhan_sypabekova@baylor.edu

³ School of Engineering and Digital Sciences, Nazarbayev University, Nur-Sultan 010000, Kazakhstan;
aida.amantayeva@alumni.nu.edu.kz

⁴ Baylor Research and Innovative Collaborative, Baylor University, Waco, TX 76704, USA

⁵ Electromagnetism and Telecommunication Department, University of Mons, 7000 Mons, Belgium;
alvaro.gonzalezvila@umons.ac.be (Á.G.-V.); christophe.caucheteur@umons.ac.be (C.C.)

⁶ Biosensors and Bioinstrumentation Laboratory—National Laboratory Astana, Nur-Sultan 010000, Kazakhstan

* Correspondence: daniele.tosi@nu.edu.kz

Abstract: This work presents an experimental investigation of the effect of chemical etching on the refractive index (RI) sensitivity of tilted fiber Bragg gratings (TFBGs). Hydrofluoric acid (HF) was used stepwise in order to reduce the optical fiber diameter from 125 μm to 13 μm . After each etching step, TFBGs were calibrated using two ranges of RI solutions: the first one with high RI variation (from 1.33679 RIU to 1.37078 RIU) and the second with low RI variation (from 1.34722 RIU to 1.34873 RIU). RI sensitivity was analyzed in terms of wavelength shift and intensity change of the grating resonances. The highest amplitude sensitivities obtained are 1008 dB/RIU for the high RI range and 8160 dB/RIU for the low RI range, corresponding to the unetched TFBG. The highest wavelength sensitivities are 38.8 nm/RIU for a fiber diameter of 100 μm for the high RI range, and 156 nm/RIU for a diameter of 40 μm for the small RI range. In addition, the effect of the etching process on the spectral intensity of the cladding modes, their wavelength separation and sensor linearity (R^2) were studied as well. As a result, an optimization of the etching process is provided, so that the best trade-off between sensitivity, intensity level, and fiber thickness can be obtained.

Keywords: optical fiber sensors; refractive index sensing; tilted fiber Bragg grating; chemical etching; etching optimization



Citation: Korganbayev, S.; Sypabekova, M.; Amantayeva, A.; González-Vila, Á.; Caucheteur, C.; Saccomandi, P.; Tosi, D. Optimization of Cladding Diameter for Refractive Index Sensing in Tilted Fiber Bragg Gratings. *Sensors* **2022**, *22*, 2259. <https://doi.org/10.3390/s22062259>

Academic Editor: Min Yong Jeon

Received: 18 February 2022

Accepted: 14 March 2022

Published: 15 March 2022

Publisher's Note: MDPI stays neutral with regard to jurisdictional claims in published maps and institutional affiliations.



Copyright: © 2022 by the authors. Licensee MDPI, Basel, Switzerland. This article is an open access article distributed under the terms and conditions of the Creative Commons Attribution (CC BY) license (<https://creativecommons.org/licenses/by/4.0/>).

1. Introduction

Tilted Fiber Bragg Grating (TFBG) is a periodic modulation of the refractive index of the core of an optical fiber, photo-inscribed at a certain angle with respect to the fiber radial axis [1]. While a standard fiber Bragg grating (FBG) behaves as an optical narrow-band notch filter [2], the transmission spectrum of a TFBG reveals a collection of backward-propagating cladding mode resonances. In addition to the typical temperature and strain sensitivities, these structures are able to detect variations in the refractive index (RI) of the medium surrounding the optical fiber [3]. TFBGs have seen a substantial development as a sensing technology in the last few years, thanks to their association with different coating materials and their ability to measure and quantify multiple parameters [4–8].

Examples of applications in mechanical sensing include optical fiber accelerometers [9], cantilever-based micro-displacement sensors [10], and even three-dimensional shape sensors based on orthogonal TFBGs [4]. However, optical fiber biosensing is the field where TFBGs showcase their highest potential [11]. The biofunctionalization process consists

of immobilizing bioreceptors on the outer surface of a TFBG (using, for example, a thin metallic film coating or a silanization process) and performing a specific measurement of a biological analyte. In this configuration, TFBGs encode the RI information entirely in the cladding modes, as these resonances shrink or enlarge as the RI increases or decreases. Several research works have documented TFBG-based biosensors for the detection of cancer biomarkers [12,13], cardiac biomarkers [14], or protein-based analytes [15], among other immunosensing applications [16].

Typical TFBGs used for biosensing operate at infrared wavelengths on standard single-mode fibers (SMF) and with a tilt angle between 5° and 15° . In this way, their optical spectrum can be demodulated using commercial FBG interrogators or optical spectrum analyzers operating in the third optical transmission window. Additionally, a metallic thin film can be deposited on the TFBG surface to exploit plasmonic effects that occur when the P-polarized cladding modes are excited within the grating. On a surface plasmon resonance (SPR) biosensor [17], this film has the dual purpose of hosting bioreceptors and propagates the corresponding plasmon wave [16]. Plasmonic TFBGs provide higher sensitivity and a lower detection limit [18] when compared to bare TFBGs.

Another method to improve the performance of a TFBG is the use of chemical etching of the fiber cladding, forming an etched TFBG (eTFBG). This structure was previously reported for protein sensing [15] and showed a significant sensitivity improvement over a standard TFBG. The spectral properties of an eTFBG are similar to the properties of the original grating, but the wavelength spacing between cladding modes tends to change as the etching process progresses and the fiber cladding becomes thinner. Among their advantages, eTFBGs are based on standard TFBGs, so the same photo-inscription setup can be used for their fabrication. The optical spectrum of an eTFBG is polarization-independent and, unlike other TFBG configurations, does not require any additional polarizer or polarization controller [15]. Additionally, the cladding modes of an eTFBG span just a few tens of nanometers, and their interrogation can be carried out using standard equipment. eTFBGs encode the RI information in the cladding modes rather than in a core mode as for an etched FBG [19], so it is possible to obtain significant sensitivity ratings without completely depleting the cladding, hence maintaining most of the mechanical stability of the original fiber. Finally, by independently analyzing the Bragg mode, which is RI-insensitive, it is possible to compensate for temperature fluctuations.

In this work, the properties of eTFBGs targeting RI-sensing applications are experimentally investigated. Since the eTFBG behavior depends on the etching process itself, the sensitivity of the grating (both in terms of wavelength shift and intensity change), as well as the spectral intensity levels of the cladding modes, which are studied in every step of the process. The results allow the etching levels for eTFBGs to be optimized, hence providing the best trade-off between sensitivity, intensity level and fiber thickness.

2. Materials and Methods

2.1. Chemicals

Hydrofluoric acid (HF) was purchased from Sigma Aldrich (Darmstadt, Germany). D-Sucrose was purchased from Thermo Fisher Scientific (Runcorn, UK). Absolute ethanol was purchased from Aidabul Distillery (Kokshetau, Kazakhstan). Etching and calibration processes were conducted in a chemical fume hood at room temperature ($\pm 1^\circ\text{C}$).

2.2. TFBG Photo-Inscription

The photo-inscription of the TFBGs was carried out using the well-known phase-mask technique [20]. An excimer ArF laser emitting at 193 nm, the desired phase-mask and all the necessary optics were integrated in a Noria FBG Manufacturing System from NorthLab Photonics. A hydrogen-loaded photo-sensitive single-mode optical fiber (PS-1250 from Fibercore UK) was appropriately placed in the system and the photo-inscription parameters were set to a pulse energy of 5 mJ, a repetition rate of 50 Hz and a set of 3 bursts of 7500 pulses per TFBG. A custom phase-mask with a tilted holographic pattern

and a pitch of 1078 nm was chosen in order to obtain a TFBG operating at the third optical transmission window. As a result, a set of 1 cm-long TFBGs was produced, exhibiting a tilt angle of 10° . Once the photo-inscription process was finished, the gratings were thermally annealed at 100°C for 24 h to remove the residual hydrogen content still present in the optical fiber.

2.3. TFBG Interrogation

TFBG interrogation was carried out by a previously reported method [15] in which the optical spectrum is measured using an optical backscatter reflectometer (LUNA OBR 4600 from LunaInc, Blacksburg, VA, USA) with a resolution of 8 pm and a wavelength window between 1525 nm and 1610.5 nm. One end of the TFBG was connected to the OBR through a pigtail of SMF. The other end was spliced using a standard optical fiber splicer (Fujikura 12-S, SMF-SMF splicing mode) to another pigtail of SMF, which was connected to a gold reflector (LunaInc, Blacksburg, VA, USA). As a result, the transmission spectrum of the TFBG is reflected to the interrogator so that the overall “transmission-reflection” spectrum can be measured [21]. This setup allows the cladding modes from the TFBG to be analyzed, with the aim of obtaining information about the RI variation of the outer medium.

2.4. TFBG Chemical Etching

The etching process was adapted from the previous work [15] by implementing some modifications in the setup. The TFBG was etched by immersing the grating region in a solution of 48% HF in a container located inside a chemical fume hood (Waldner Secuflow airflow controller, ceiling-bench mounted) at room temperature. The etching was conducted in a closed compartment (cylinder) fixed with rubber plugs at each end. The container had two ports: an inlet where the sample was injected using a 1 mL syringe and an outlet, which was linked to the waste container. The container allowed the integrity of the etched TFBG to be maintained during the rinsing steps since the diameter of the fiber becomes thinner after every immersion in HF. Additionally, the container allowed HF vaporization to be avoided during the etching process. The TFBG region of the fiber was placed inside this cylinder, as shown in Figure 1. Before the etching process, the surface of the fiber inside the container was cleaned with ethanol and allowed to air dry. Then, the fiber was incubated in HF solution until the spectrum started to change. After each etching step, the fiber was rinsed thoroughly with dH_2O several times to remove remaining HF residues, and it was subsequently calibrated using sucrose control solutions with known RI.

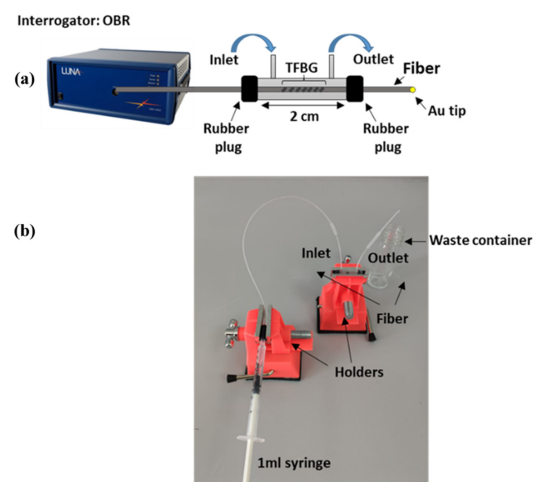


Figure 1. Experimental setup for fiber etching: (a) Schematic overview of the setup; and (b) Corresponding real image: TFBG was immersed in a closed compartment (cylinder) with 48% HF (during etching stage) or with different sucrose solutions (during RI calibration). The container had two ports: an inlet where the sample was injected using a 1 mL syringe and an outlet which was linked to the waste container.

Calculation of the fiber diameter after each etching step was based on a previously reported diameter estimation approach, where the final diameter was measured using a Leica DM4000 B Digital Microscope with $20\times/0.50$ objective, and a step-evolution of the diameter was estimated using quadratic fitting [15], as shown in Figure 2.

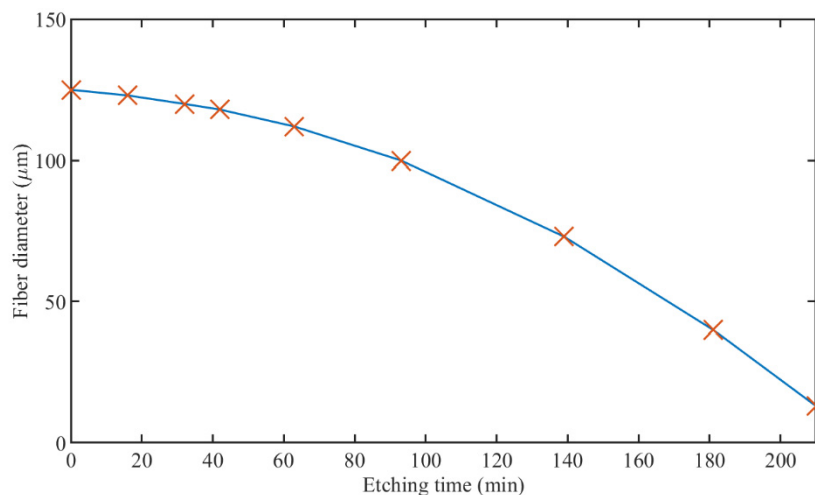


Figure 2. Evolution of TFBG diameter after etching in 48% HF solution. Markers show diameter values after each etching step; blue line—quadratic fitting of the curve.

2.5. RI Calibration and Spectral Analysis

Sucrose was used for the preparation of solutions in two RI ranges: the first one with high RI variation (from 1.33679 RIU to 1.37078 RIU; RIU: refractive index units), and the second with low RI variation (from 1.34722 RIU to 1.34873 RIU). The wider range extends for 3.4×10^{-2} RIU, which mimics the operation of most biosensors; the second range spans 1.5×10^{-3} RIU, which represents a sensor operating on a small-signal analysis, such as biosensors close to the limit of detection [22]. The RI of each solution was measured using an automatic digital refractometer (Anton Paar, Inc., USA, Abbemat 300). TFBG and eTFBG calibration with varying RI were performed by completely injecting the solution inside the container where the TFBG was placed using a 1 mL syringe. Calibration for both RI ranges was carried out after each step of the etching process to investigate the spectral properties and their relation to the etching levels.

Both wavelength and intensity of the cladding modes were tracked using a feature tracking method implemented in MATLAB[®] (Mathworks Inc., UK) and their variation with regard to the etching process was evaluated. Then, wavelength and intensity sensitivities for both RI ranges were calculated, as well as the coefficient of determination (R^2 value) of the fitted data.

3. Results

The response of the unetched TFBG to RI variations was studied, as can be seen in Figure 3. It should be noted that for the high-order cladding modes (which have lower wavelength values), amplitude changes are more significant than for the low-order modes. Indeed, the increase in RI leads to the gradual disappearance of the modes since they are no longer totally internally reflected by the cladding boundary and reach the cut-off condition [1]. The inset of Figure 3 shows a detailed view of one mode of the TFBG and how it changes due to the variation of the refractive index of the surrounding medium. For minor RI variations, in this case less than 0.0203 RIU, only wavelength shift is observable, while amplitude change corresponds to higher RI variations.

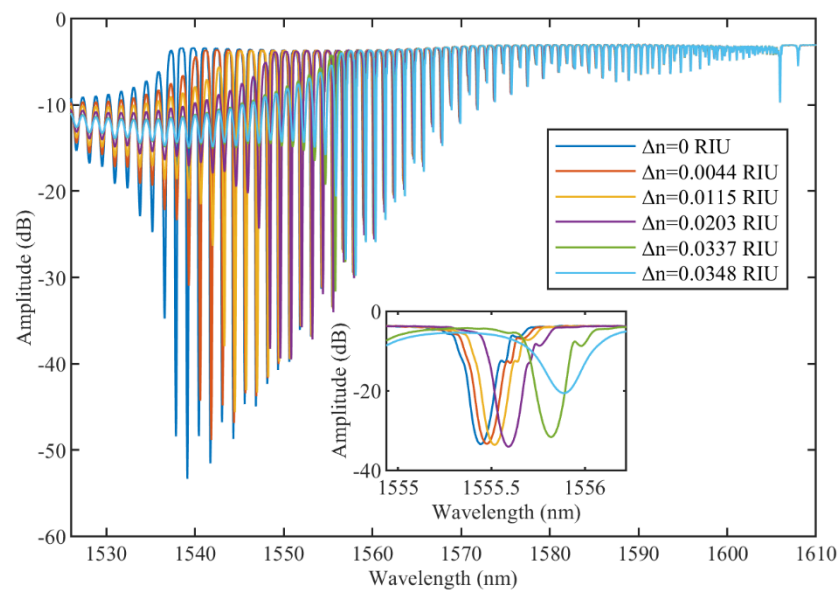


Figure 3. Spectral evolution of unetched TFBR subjected to surrounding RI variations. Inset reports effect on the cladding mode near 1555.5 nm.

Then, etching of the TFBR was performed stepwise to evaluate the sensing properties of TFBRs with different optical fiber diameter values. The spectral evolution as a function of the etching process is shown in Figure 4. The fiber diameter decreased due to etching steps from 125 μm to 13 μm . It worth noting that the spectra are provided with an offset for clarity of spectra plotting on one graph. Indeed, without considering an offset, the maximum amplitude value for the unetched TFBR is -5 dB and the minimum is -48 dB, while the etched TFBR (14 μm) has the maximum amplitude of -5 dB and the minimum of -22 dB. A smaller diameter leads to a decrease in the number of modes, due to the mode escaping to the surrounding medium. For a fiber diameter below 40 μm , most of the cladding modes are no longer distinguishable, and only few modes in the range of 1590–1605 nm can be used for interrogation in both RI ranges.

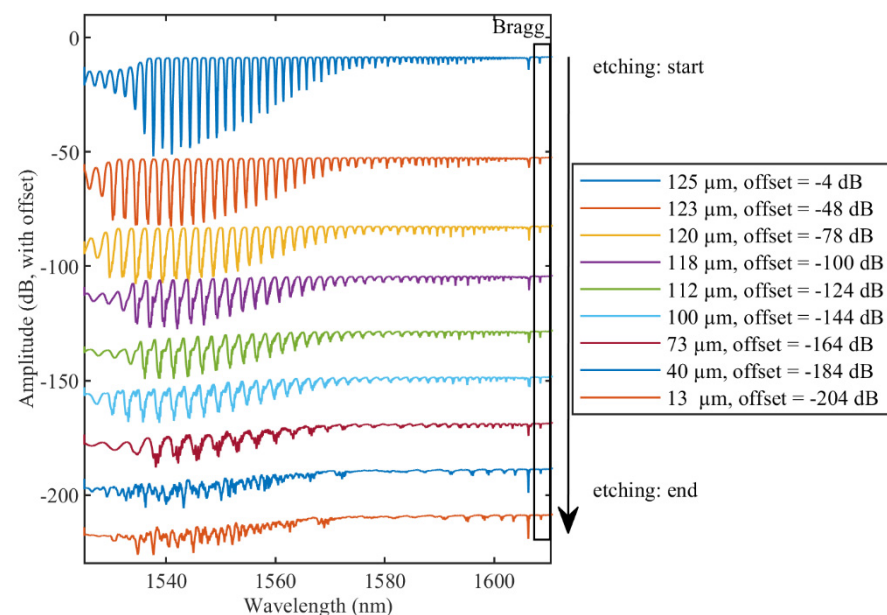


Figure 4. Evolution of TFBR transmission spectrum during the optical fiber etching. Rectangular area shows the Bragg mode of the TFBR. Offset has been introduced for clarity of spectra plotting on one graph.

The etching process changes the spectral amplitude of the cladding modes and the wavelength span between adjacent modes [23]. Figure 5 shows the dependence of both parameters on the wavelength of the modes themselves. As can be seen, the minimum amplitude of the unetched TFBG is equal to -53.3 dB, while an eTFBG with a fiber diameter of $73 \mu\text{m}$ reaches roughly -22 dB. When fiber diameters of $40 \mu\text{m}$ and $13 \mu\text{m}$ are reached, just a few modes close to the Bragg wavelength can be measured and their intensity is roughly -8 dB. Moreover, the spectral quality decreases significantly: modes become broader, poorly defined, especially high-order modes (at shorter wavelengths). One of the possible reasons for low spectral quality can be the surface roughness after the etching [23].

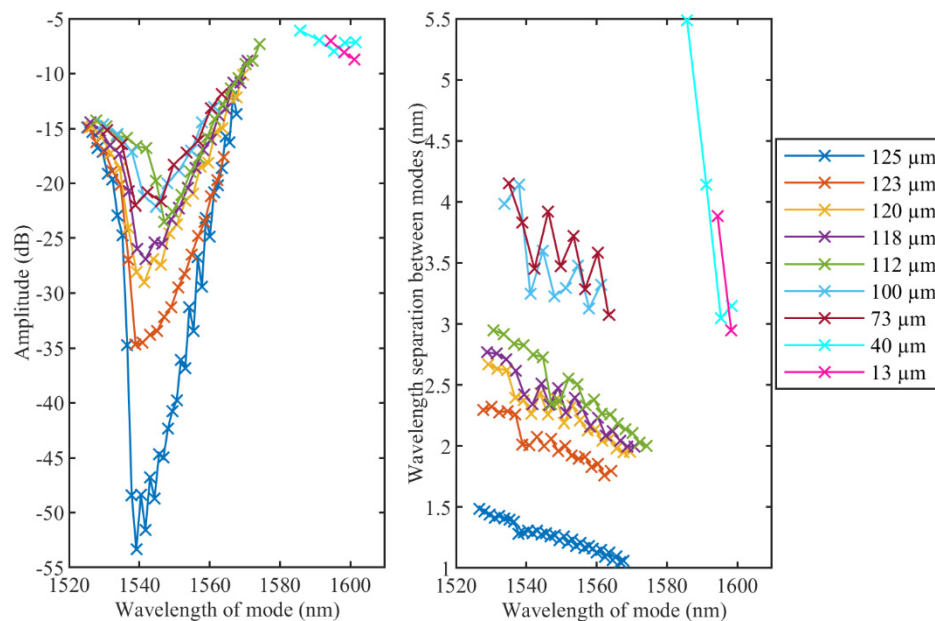


Figure 5. Evolution of amplitude levels (left) and wavelength spans (right) of cladding modes during etching process. Only modes which are distinguishable for both RI variation ranges are illustrated.

Additionally, Figure 5 illustrates the wavelength span evolution corresponding to different fiber diameters. The separation between modes increases from 1 nm to 3 nm for unetched TFBGs and fiber diameters of $73 \mu\text{m}$, respectively. The maximum wavelength span experimentally measured is 5.5 nm for the few distinguishable modes, corresponding to a fiber diameter of $40 \mu\text{m}$.

RI calibration has been performed for the high and low RI ranges for all cladding modes. For example, Figure 6 reports shifts of the wavelength and amplitude for both RI ranges and the related fitted linear regression for the most sensitive modes of the unetched TFBG. The same approach has been used for all modes to obtain the sensing information shown in Figures 7 and 8.

Amplitude and wavelength sensitivities of cladding modes after each etching step are illustrated in Figures 7 and 8. In both figures, dot markers show the modes with sensitivity linearity higher than 0.9 ($R^2 > 0.9$). As can be seen, maximum amplitude sensitivities for both ranges correspond to unetched TFBGs (1008 dB/RIU and 8160 dB/RIU) and the sensitivity decreases for smaller fiber diameters. It is worth noting that for the high RI variation range, only several modes between 1543 nm and 1547 nm have high sensitivity and good linearity ($R^2 > 0.9$), while for the small RI range, only one cladding mode at 1543 nm has high amplitude sensitivity. These results are in correspondence with the theory that the cladding modes with the effective refractive index closer to the surrounding refractive index are the most sensitive for RI variations.

For the wavelength sensitivity, the maximum value for the high RI range is 38.8 nm/RIU for a fiber diameter of $100 \mu\text{m}$ and 156 nm/RIU with $40 \mu\text{m}$ for the small range. It is important to highlight that for the small RI range, it was also possible to analyze the

“quasi-modes” in the range between 1530 nm and 1560 nm for diameters equal to 40 μm and 13 μm (in Figure 4, they correspond to the two last spectra). As a result, the highest wavelength sensitivity corresponds to 40 μm and is roughly 156 nm/RIU.

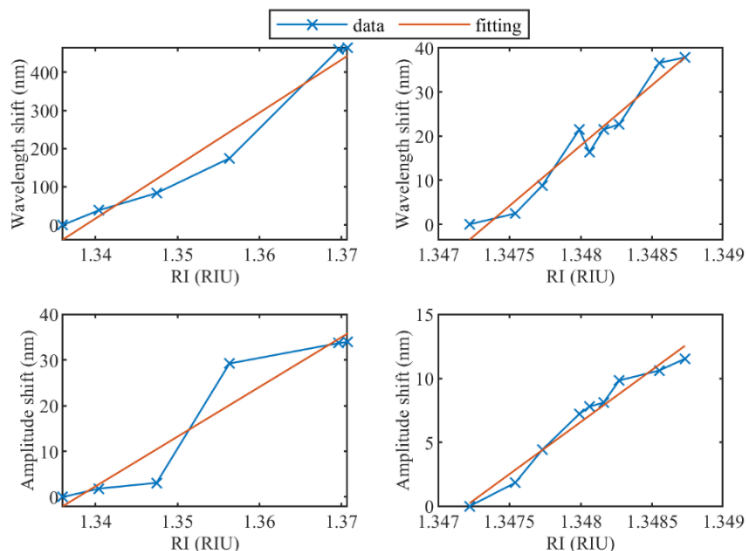


Figure 6. (left) Amplitude and wavelength shift for the high RI range from 1.33679 RIU to 1.37078 RIU of unetched TFBG; (right) Amplitude and wavelength shift for the small RI range from 1.34722 RIU to 1.34873 RIU of unetched TFBG.

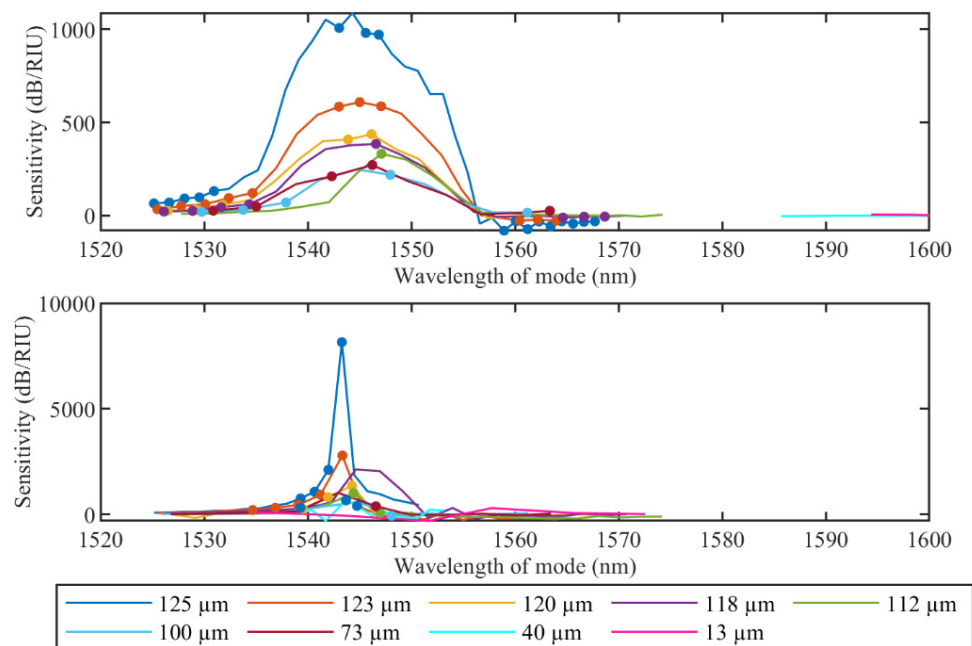


Figure 7. Evolution of the amplitude sensitivity for the high RI range from 1.33679 RIU to 1.37078 RIU (upper) and the small RI range from 1.34722 RIU to 1.34873 RIU (lower) of cladding modes during etching process. Dot markers show the modes with sensitivity higher than 0.9 ($R^2 > 0.9$).

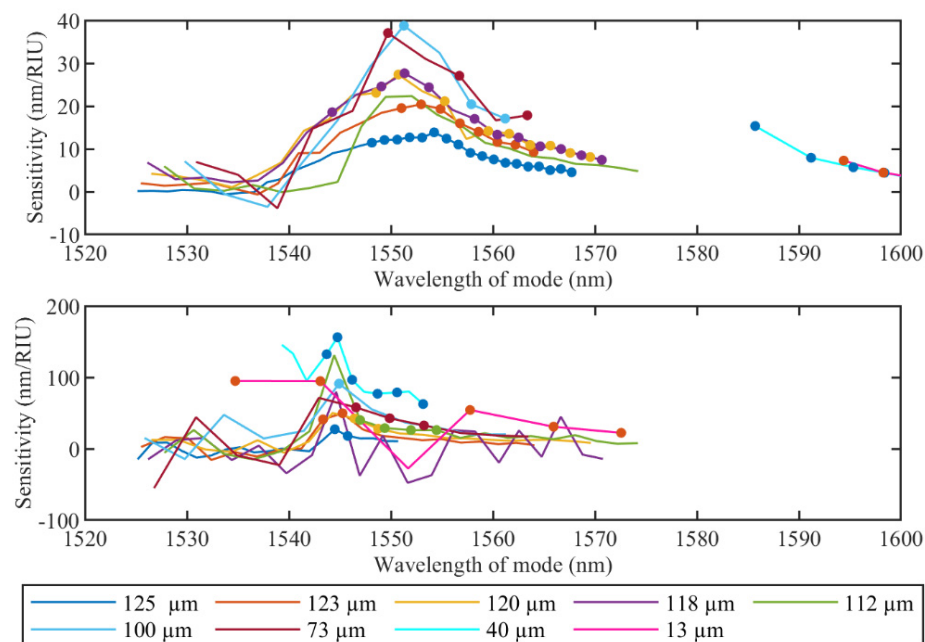


Figure 8. Evolution of the wavelength sensitivity for the high RI range from 1.33679 RIU to 1.37078 RIU (**upper**) and the small RI range from 1.34722 RIU to 1.34873 RIU (**lower**) of cladding modes during etching process. Dot markers show the modes with sensitivity linearity higher than 0.9 ($R^2 > 0.9$).

4. Discussion

The performed experimental investigation shows that the highest amplitude sensitivity corresponds to unetched TFBGs and decreases with etching. In contrast, in the case of the wavelength sensitivity, the highest values are reached for 100 μm and 40 μm fiber diameters. It is worth mentioning that the method used for tracking peaks of TFBG spectra differs from others reported in related research works. For instance, the envelope-tracking method, which evaluates the area between upper and lower envelopes of the TFBG spectrum [24,25] to assess the etching effect on RI sensitivity, is not suitable for small ranges of RI variations because amplitude changes are presented only in several modes and the area does not change significantly. Moreover, this effect is higher after etching due to the decrease in amplitude sensitivity. Considering the fact that small RI detection is gaining more popularity for biosensing applications [12,15,26], an efficient method suitable for small RI range variations has high importance. Another method, which follows individual resonances close to the cut-off region where mode effective index is equal to RI of the surrounding medium, is not effective for etched TFBGs. Indeed, in this case, wavelength separation increases, the dynamic range for each mode becomes bigger, but it becomes more difficult to find a mode near cut-off for a wide range of SRI values. As a result, it is preferable to analyze all modes and compare them for sensitivity values, as was carried out in the presented work.

It is worth discussing the reasons for smaller wavelength and amplitude sensitivities of TFBGs for the higher RI range in this work. With increase in RI of the surrounding medium, more and more high-order modes become no longer totally internally reflected by the cladding boundary (the modes become lossy). As a result, for high RI range analysis, the low-order mode has to be chosen to guarantee its presence for all RI values. However, since such mode is positioned far from the cut-off point, overall RI sensitivity will be low.

Additionally, it is important to mention that a step response of the TFBG sensor is present when the cutoff mode switches from one cladding mode to the adjacent one. This step jump can be considered as an uncertainty in the wavelength measurements. Moreover, high ambient temperature changes can also affect this step jump. However, due to high wavelength separation between the cladding modes (at least 1 nm in Figure 5 right)

and low temperature changes in laboratory conditions, this phenomenon was considered insignificant in this work.

Wavelength and intensity tracking play a significant role in optical fiber interrogation systems applied to sensing [27]. Intensity detection [28] is a common method particularly used with plasmonic gratings. However, from a system standpoint, where reliable long-term operation is required, the detection of the wavelength shift is preferable, as it is more robust with respect to the fluctuations of the light sources, fiber twists, and other attenuation effects. In this regard, the eTFBG achieves a significant improvement over the TFBG with the standard fiber diameter, as it allows an almost 4× sensitivity increase obtained with a quite large cladding (~100 μm), which does not compromise the mechanical strength of the fiber. With the help of the figures and outcome of this work, an optimal fiber diameter can be chosen as a function of the desired sensitivity, so the sensor design can be adapted accordingly to the project specifications.

5. Conclusions

An experimental investigation was carried out to evaluate the evolution of the TFBG properties after etching, aiming to improve RI sensitivity to the surrounding medium. TFBGs with an initial diameter of 125 μm were etched stepwise in the hydrofluoric acid solution until reaching a fiber diameter of 13 μm. RI calibration was performed after each etching step for different RI solutions in two ranges: the first one with high RI variation (from 1.33679 RIU to 1.37078 RIU), and the second with low RI variation (from 1.34722 RIU to 1.34873 RIU). Wavelength and amplitude sensitivities of all modes, spectral intensity levels of the cladding modes, their wavelength separation and linearity (R^2) were evaluated for each RI calibration. The highest amplitude sensitivities obtained are 1008 dB/RIU for the high RI range and 8160 dB/RIU for the low RI range, corresponding to the unetched TFBG. However, the highest wavelength sensitivities are 38.8 nm/RIU for a fiber diameter of 100 μm for the high RI range, and 156 nm/RIU for a diameter of 40 μm for the small RI range. The results allow the most suitable etching process to be selected in order to optimize RI sensitivity depending on the interrogation technique required by the application.

Author Contributions: Conceptualization, S.K., M.S., A.A., P.S. and D.T.; methodology, all authors.; investigation, S.K., M.S. and A.A.; data curation, S.K. and A.A.; software, S.K.; resources, Á.G.-V. and C.C.; visualization, S.K. and A.A.; writing—original draft, S.K., M.S., Á.G.-V. and A.A.; writing—review and editing, all authors; funding acquisition, P.S., D.T. and C.C. All authors have read and agreed to the published version of the manuscript.

Funding: This work has been funded by Fondazione Cariplo, grant No. 2017-2075. The research was funded by Nazarbayev University, under grants SMARTER (code: 091019CRP2117) and EPICGuide (code: 240919FD3908).

Institutional Review Board Statement: Not applicable.

Informed Consent Statement: Not applicable.

Data Availability Statement: Data underlying the results presented in this paper are not available to the public, but can be obtained from the authors upon reasonable request.

Conflicts of Interest: The authors declare no conflict of interest.

References

1. Guo, T.; Liu, F.; Shao, L.Y. Tilted Fiber Bragg Grating Sensors. *Yingyong Kexue Xuebao/J. Appl. Sci.* **2018**, *36*, 75–103. [[CrossRef](#)]
2. Erdogan, T. Fiber grating spectra. *J. Light. Technol.* **1997**, *15*, 1277–1294. [[CrossRef](#)]
3. Guo, T.; Liu, F.; Guan, B.O.; Albert, J. Tilted fiber grating mechanical and biochemical sensors. *Opt. Laser Technol.* **2016**, *78*, 19–33. [[CrossRef](#)]
4. Feng, D.; Zhou, W.; Qiao, X.; Albert, J. Compact optical fiber 3D shape sensor based on a pair of orthogonal tilted fiber bragg gratings. *Sci. Rep.* **2015**, *5*, 17415. [[CrossRef](#)] [[PubMed](#)]
5. Wang, T.; Liu, K.; Jiang, J.; Xue, M.; Chang, P.; Liu, T. Temperature-insensitive refractive index sensor based on tilted moiré FBG with high resolution. *Opt. Express* **2017**, *25*, 14900. [[CrossRef](#)]

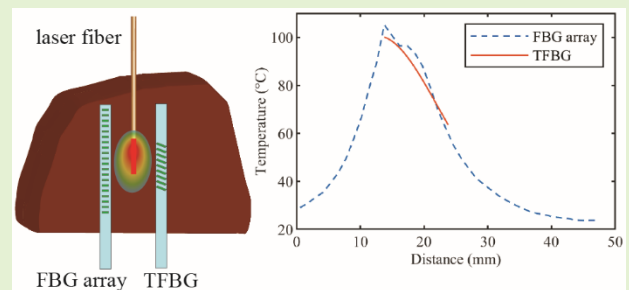
6. Huy, M.C.P.; Laffont, G.; Frignac, Y.; Dewynter-Marty, V.; Ferdinand, P.; Roy, P.; Blondy, J.-M.; Pagnoux, D.; Blanc, W.; Dussardier, B. Fibre Bragg grating photowriting in microstructured optical fibres for refractive index measurement. *Meas. Sci. Technol.* **2006**, *17*, 992–997. [[CrossRef](#)]
7. Alberto, N.J.; Marques, C.A.; Pinto, J.L.; Nogueira, R.N. Three-parameter optical fiber sensor based on a tilted fiber Bragg grating. *Appl. Opt.* **2010**, *49*, 6085–6091. [[CrossRef](#)]
8. Shao, L.Y.; Xiong, L.; Chen, C.; Laronche, A.; Albert, J. Directional bend sensor based on re-grown tilted fiber bragg grating. *J. Light. Technol.* **2010**, *28*, 2681–2687. [[CrossRef](#)]
9. Guo, T.; Shao, L.; Tam, H.-Y.; Krug, P.A.; Albert, J. Tilted fiber grating accelerometer incorporating an abrupt biconical taper for cladding to core recoupling. *Opt. Express* **2009**, *17*, 20651. [[CrossRef](#)]
10. Guo, T.; Chen, C.; Albert, J. Non-uniform-tilt-modulated fiber Bragg grating for temperature-immune micro-displacement measurement. *Meas. Sci. Technol.* **2009**, *20*, 34007. [[CrossRef](#)]
11. Sharma, A.K.; Marques, C. Design and performance perspectives on fiber optic sensors with plasmonic nanostructures and gratings: A review. *IEEE Sens. J.* **2019**, *19*, 7168–7178. [[CrossRef](#)]
12. Loyez, M.; Albert, J.; Caucheteur, C.; Wattiez, R. Cytokeratins biosensing using tilted fiber gratings. *Biosensors* **2018**, *8*, 74. [[CrossRef](#)] [[PubMed](#)]
13. Lobry, M.; Loyez, M.; Chah, K.; Hassan, E.M.; Goormaghtigh, E.; DeRosa, M.C.; Wattiez, R.; Caucheteur, C. HER2 biosensing through SPR-envelope tracking in plasmonic optical fiber gratings. *Biomed. Opt. Express* **2020**, *11*, 4862. [[CrossRef](#)] [[PubMed](#)]
14. Luo, B.; Wu, S.; Zhang, Z.; Zou, W.; Shi, S.; Zhao, M.; Zhong, N.; Liu, Y.; Zou, X.; Wang, L.; et al. Human heart failure biomarker immunosensor based on excessively tilted fiber gratings. *Biomed. Opt. Express* **2017**, *8*, 57. [[CrossRef](#)] [[PubMed](#)]
15. Sypabekova, M.; Korganbayev, S.; González-Vila, Á.; Caucheteur, C.; Shaimerdenova, M.; Ayupova, T.; Bekmurzayeva, A.; Vangelista, L.; Tosi, D. Functionalized etched tilted fiber Bragg grating aptasensor for label-free protein detection. *Biosens. Bioelectron.* **2019**, *146*, 111765. [[CrossRef](#)] [[PubMed](#)]
16. Guo, T.; González-Vila, Á.; Loyez, M.; Caucheteur, C. Plasmonic optical fiber-grating immunosensing: A review. *Sensors* **2017**, *17*, 2732. [[CrossRef](#)] [[PubMed](#)]
17. Caucheteur, C.; Guo, T.; Albert, J. Polarization-Assisted Fiber Bragg Grating Sensors: Tutorial and Review. *J. Light. Technol.* **2017**, *35*, 3311–3322. [[CrossRef](#)]
18. Chen, X.; Nan, Y.; Ma, X.; Liu, H.; Liu, W.; Shi, L.; Guo, T. In-situ detection of small biomolecule interactions using a plasmonic tilted fiber grating sensor. *J. Light. Technol.* **2019**, *37*, 2792–2799. [[CrossRef](#)]
19. Bekmurzayeva, A.; Dukenbayev, K.; Shaimerdenova, M.; Bekniyazov, I.; Ayupova, T.; Sypabekova, M.; Molardi, C.; Tosi, D. Etched fiber bragg grating biosensor functionalized with aptamers for detection of thrombin. *Sensors* **2018**, *18*, 4298. [[CrossRef](#)]
20. Hill, K.O.; Malo, B.; Bilodeau, F.; Johnson, D.C.; Albert, J. Bragg gratings fabricated in monomode photosensitive optical fiber by UV exposure through a phase mask. *Appl. Phys. Lett.* **1993**, *62*, 1035–1037. [[CrossRef](#)]
21. Chen, C.; Yu, Y.-S.; Yang, R.; Wang, C.; Guo, J.-C.; Xue, Y.; Chen, Q.-D.; Sun, H.-B. Reflective optical fiber sensors based on tilted fiber Bragg gratings fabricated with femtosecond laser. *J. Light. Technol.* **2012**, *31*, 455–460. [[CrossRef](#)]
22. Chiavaioli, F.; Gouveia, C.A.J.; Jorge, P.A.S.; Baldini, F. Towards a uniform metrological assessment of grating-based optical fiber sensors: From refractometers to biosensors. *Biosensors* **2017**, *7*, 23. [[CrossRef](#)] [[PubMed](#)]
23. Chen, C.; Caucheteur, C.; Mégret, P.; Albert, J. The sensitivity characteristics of tilted fibre Bragg grating sensors with different cladding thicknesses. *Meas. Sci. Technol.* **2007**, *18*, 3117. [[CrossRef](#)]
24. Laffon, G.; Ferdinand, P. Tilted short-period fibre-Bragg-grating-induced coupling to cladding modes for accurate refractometry. *Meas. Sci. Technol.* **2001**, *12*, 765–770. [[CrossRef](#)]
25. Caucheteur, C.; Chah, K.; Lhommé, F.; Debliquy, M.; Lahem, D.; Blondel, M.; Megret, P. Enhancement of cladding modes couplings in tilted Bragg gratings owing to cladding etching. In Proceedings of the WFOPC2005—4th IEEE/LEOS Workshop on Fibres and Optical Passive Components, Palermo, Italy, 22–24 June 2005; Volume 2005, pp. 234–239. [[CrossRef](#)]
26. Chiavaioli, F.; Baldini, F.; Tombelli, S.; Trono, C.; Giannetti, A. Biosensing with optical fiber gratings. *Nanophotonics* **2017**, *6*, 663–679. [[CrossRef](#)]
27. González-Vila, Á.; Kinet, D.; Mégret, P.; Caucheteur, C. Narrowband interrogation of plasmonic optical fiber biosensors based on spectral combs. *Opt. Laser Technol.* **2017**, *96*, 141–146. [[CrossRef](#)]
28. Caucheteur, C.; Loyez, M.; González-Vila, Á.; Wattiez, R. Evaluation of gold layer configuration for plasmonic fiber grating biosensors. *Opt. Express* **2018**, *26*, 24154. [[CrossRef](#)] [[PubMed](#)]

Tilted fiber Bragg grating measurements during laser ablation of hepatic tissues: quasi-distributed temperature reconstruction and cladding mode resonances analysis

Sanzhar Korganbayev, *Member, IEEE*, Martina De Landro, *Member, IEEE*, Alexey Wolf, Daniele Tosi, Paola Saccomandi, *Senior Member, IEEE*

Abstract—In this work, we investigate the application of tilted fiber Bragg grating (TFBG) sensors during *ex vivo* laser ablation of porcine hepatic tissues. Initially, TFBG's ability to measure the surrounding refractive index (RI) for different sucrose concentrations and the possibility to measure the RI of the targeted tissue during laser ablation (LA) is analyzed. After, the temperature sensing modality of TFBG is investigated in detail. We have implemented an algorithm for quasi-distributed spatial temperature profile reconstruction along TFBG. The algorithm models the TFBG core mode spectrum as a chain of Bragg gratings (each Bragg grating is modeled *via* coupled mode theory), where each grating is sensitive to local temperature changes. After, the Gaussian-shape temperature profile along the TFBG is reconstructed using the iterative optimization technique. Temperature measurements have been compared with highly-dense FBG array measurements and with conventional TFBG point temperature measurements based on the core mode tracking techniques (maximum tracking, X-dB Bandwidth, centroid methods). Overall, the proposed reconstruction algorithm is able to provide a quasi-distributed temperature profile along TFBG, which is not possible to obtain using conventional point temperature measurements based on the TFBG's core mode tracking. The resulted root-mean-square error in comparison to FBG array reference measurements is 7.8 ± 1.7 °C. In general, the results show that the main reliable sensing modality of TFBG during LA is temperature monitoring, which can be significantly improved by the proposed algorithm.

Index Terms—laser ablation, optical fiber sensors, refractive index sensing, temperature monitoring, thermal treatment, tilted fiber Bragg grating



I. Introduction

HYPERTHERMAL techniques can be considered as one of the main alternatives to traditional methods (surgical resection, chemotherapy, and radiation therapy) for cancer treatment [1], [2]. During such techniques, the tissue temperature increase is induced to destroy cancer cells, or sensitize tumors for radiotherapy and chemotherapy, or as complementary to cancer immune therapy [3]. Hyperthermia can be divided into several types according to the value of

temperature elevation: fever-range (39.5 °C – 41.5 °C), traditional (41.5 °C – 54 °C), and ablation (more than 60 °C) [4]. Moreover, hyperthermia can be categorized according to the way of treatment (invasive or non-invasive), and by the source of energy: microwave [5], radiofrequency [6], high-intensity focused ultrasound [7], and laser ablation (LA), and others [8].

Among all invasive hyperthermal techniques, laser ablation possesses unique features such as immunity to electromagnetic interference and the ability to reach deep-lying organs. These

Manuscript received xx, 2022; revised xx, 2022; accepted xx, 2022. Date of publication xx, 2022; date of current version xx, 2022. This project has received funding from the European Research Council (ERC) under the European Union's Horizon 2020 research and innovation programme (Grant agreement No. 759159). This work has been funded by Fondazione Cariplo, grant No. 2017-2075. Work of A. Wolf was supported by the state budget of the Russian Federation (IA&E SB RAS project №121030500067-5). Work of D. Tosi was funded through Nazarbayev University, under grants SMARTER (code: 091019CRP2117) and EPICGuide (code: 240919FD3908). (Corresponding authors: Sanzhar Korganbayev and Paola Saccomandi).

Sanzhar Korganbayev, Martina De Landro and Paola Saccomandi are with the Department of Mechanical Engineering, Politecnico di Milano, 20156 Milan, Italy (e-mail: sanzhar.korganbayev@polimi.it; martina.delandro@polimi.it; paola.saccomandi@polimi.it).

Alexey A. Wolf, is with Department of Physics, Novosibirsk State University, 630090 Novosibirsk, Russia, and also with the Institute of Automation and Electrometry, Siberian Branch of the Russian Academy of Sciences (SB RAS), 630090 Novosibirsk, Russia (e-mail: wolf@iae.nsk.su).

Daniele Tosi is with Nazarbayev University School of Engineering and Digital Sciences, Nur-Sultan, Kazakhstan, and with Biosensors and Bioinstrumentation Laboratory - National Laboratory Astana, Nur-Sultan, Kazakhstan (email: daniele.tosi@nu.edu.kz)

advantages stem from the fact that the energy is guided by flexible optical fiber made of glass or polymer [9]. As a result, an effective treatment that is compatible with magnetic resonance and computed tomography guidance is possible. Different research works have been performed to validate the efficiency of LA treatment for thyroid [10], brain [11], pancreas [12], bones [13], and liver [14].

Nevertheless, for the effective result of LA treatment without recurrences, irreversible damage to the whole cancer tissue has to be performed. Therefore, accurate monitoring of temperature and related tissue changes of the targeting tumor is of paramount importance [15]. In this regard, conventional invasive temperature monitoring methods, such as thermocouples [16], and thermistor probes [17], have two main limitations: the low spatial resolution and the metallic material of the devices. The low resolution of the sensors can not provide accurate temperature information due to high thermal gradients associated with LA, especially near the applicator [18]. The metallic material significantly absorbs the laser light, which leads to a change of heat distribution near the applicator and significant temperature overestimation (error can reach more than 20 °C) [9], [19].

Fiber optic sensing is one of the possible alternatives to conventional sensors for LA monitoring, due to their flexibility, sub-millimetric size, biocompatibility and immunity to electromagnetic interferences [18]. Moreover, fiber sensing is able to provide distributed (the whole fiber is a sensor) or quasi-distributed (fiber has several sensing points along its length) temperature measurements [20].

The most popular technique for distributed sensing during LA relies on Rayleigh scattering phenomena: temperature profile reconstruction is based on the analysis of spectral shift on each segment of the fiber between the measured and reference (no temperature change) states [21]. Rayleigh-based distributed sensing provides high sensing length, but its low spatial resolution, high interrogator cost, and low sampling rate limit its application for real-time monitoring during LA [20]–[22].

Quasi-distributed sensing is mainly based on fiber Bragg grating (FBG) temperature sensors. An FBG is a periodic modulation (with a specific grating period) of the refractive index along the fiber core. FBG acts as an optical narrowband notch filter: it transmits the whole input spectrum except the specific part of it. This portion is reflected from the FBG and centered at the Bragg wavelength [23]. Since the Bragg wavelength depends on temperature perturbations on the grating, monitoring of FBG peak can be used to measure temperature change at the grating [23].

Moreover, several FBGs with different grating periods can be inscribed along the fiber to obtain a spectrum with several different reflected Bragg wavelengths. The peak tracking of such spectra allows multi-point measurements (thus, the quasi-distributed sensing) along the chain of FBGs, called an FBG array.

The ability to provide multi-point measurements and immunity to electromagnetic interference pave the way for FBG sensing applications for laser hyperthermia [24]–[27].

Moreover, our group has recently demonstrated the efficacy of FBGs to regulate LA in real-time for maximum temperature control [28], zone control [29] during contactless LA, and temperature control during interstitial LA [30], [31] of *ex vivo* tissues.

A particular type of FBG is the tilted FBG (TFBG), in which the Bragg grating planes are tilted to the optical fiber axis. Due to the tilt of the grating and the related coupling between the core and cladding modes, TFBG is sensitive to fiber-related parameters (temperature, axial strain, pressure, bending, among others) and outside medium parameters, such as surrounding refractive index (RI) [32]–[35]. TFBGs have also been proposed for the simultaneous measurement of different quantities, benefiting from the difference in responses of cladding modes and core mode in the TFBG spectrum [36].

Recently, Alqarni *et al.* have used a TFBG structure to manufacture a self-monitored laser-irradiating device based on the application of TFBG with an absorptive coating as a miniature heat source with sensing capabilities [4]. In this case, the tilt angle of the grating leads to the light coupling to cladding modes and absorption of it by coating. Thus, this technique is not based on laser absorption by the tissue, but on heat transfer from the absorptive coating surface of TFBG. Temperature monitoring in [4] is based on conventional TFBG core mode tracking, in which TFBG acts as a sensing point and allows only a single-point measurement.

Considering the multi-sensing capabilities of the TFBG and its potential application in LA, it is useful to explore the possibility to use different TFBG sensing modalities for thermal treatment monitoring and improve TFBG temperature measurement capabilities.

In this regard, we investigate TFBG's ability to measure surrounding RI, which can be an important parameter to obtain information about the composition of tissues with which the TFBG sensor comes into contact. Indeed, the light propagation within tissue is sensitive to changes in medium microstructure, hence optical parameters could be used to directly quantify the tissue damage [37], [38]. It is known that the RI values of biological tissues are primarily mapped by their water content: the higher the content of water in the tissue, the closer its RI value to that of water (RI=1.33) and vice versa [39]. Thus, we perform TFBG calibration in the RI range for biological tissues and analyze the cladding mode resonances behavior during LA.

Moreover, we propose the reconstruction algorithm based on coupled-mode theory for measuring a quasi-distributed temperature profile along the TFBG during LA. The initial version of the algorithm has been already validated by our group for linearly chirped FBG (CFBG). CFBG is a fiber structure with the grating period linearly increased along the grating length, which results in a broad reflection spectrum that can be from a few to tens of nanometers in full-width half-maximum (FWHM) bandwidth [23]. The algorithm has been validated for measurements during LA using commercial CFBGs [40], [41], and using a custom-made plastic CFBG [42]. A detailed description of the CFBG spectrum model and related temperature profile reconstruction is provided in [43].

It is important to note that this algorithm is challenging to use

for TFBG due to the small amplitude and narrow bandwidth of the TFBG's core mode. Thus, in this work, we modify the algorithm and validate it by comparing its results with the conventional core mode tracking techniques and the FBG array measurements.

II. MATERIALS AND METHODS

A. Fiber optic interrogation system

The Micron Optics si255 optical interrogator (*Micron Optics*, Atlanta, USA) was utilized to measure the spectra of the FBG array and the TFBG with a 10 Hz sampling rate, with a synchronized approach. Both ends of TFBG were connected to two different channels of the interrogator and the overall "transmission-reflection" spectrum was measured.

B. Tilted fiber Bragg grating

For this work, we utilized commercially available TFBG (*Technica Optical Components*, Atlanta, USA) with an 8° tilt angle, a 10 mm grating length, apodized FBG profile, and core mode at 1550 nm with FWHM less than 0.5 nm. Fig. 1 reports the overall "transmission-reflection" spectrum of the TFBG sensor: the core mode centered at 1550 nm, the ghost mode at 1548 nm, and the cladding mode resonances comb is approximately in the range of 1509 nm – 1547 nm.

Moreover, separate calibrations specific for each sensing modality were performed: the core-to-core Bragg resonance calibration for temperature sensing, and RI calibration of the cladding mode resonances comb for RI sensing.

The core-to-core Bragg resonance of the TFBG was calibrated in the temperature range from 34 °C to 50 °C, where a T-type thermocouple was used as a reference temperature sensor. As a result, the core mode's temperature sensitivity of the TFBG is $(7.05 \pm 0.01) \times 10^{-6} \text{ } ^\circ\text{C}^{-1}$.

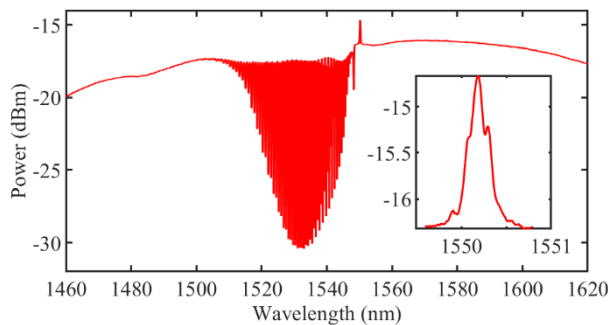


Fig. 1. The spectrum of a 10 mm – long TFBG with an 8° tilt angle; inset reports the core mode of TFBG (centered at 1550 nm).

C. Fiber Bragg grating array

For reference temperature measurements, the custom-made highly dense FBG array was fabricated with femtosecond point-by-point writing technique in polyimide-coated single-mode fiber SM1500(9/125)P with a reduced coating diameter of 145 μm (Fibercore Ltd., Southampton, UK). The array consists of 40 FBGs uniformly positioned along the sensing length of 48 mm (grating length is 1.15 mm, edge-to-edge distance is 0.05 mm), the reflection coefficients of FBGs are about 10-20 %, which allows a high dynamic range (> 30 dB). Fig. 2 reports the reflected spectrum of the FBG array.

FBG properties were optimized to provide high spatial

resolution and a high-quality spectrum for accurate temperature measurements of high-gradient temperature profiles possible during LA [18]. In addition, polyimide coating allows high-temperature measurements (> 400 °C for a short duration) [44]–[46]. The temperature sensitivity of the array is $(7.43 \pm 0.01) \times 10^{-6} \text{ } ^\circ\text{C}^{-1}$. Detailed information about the fabrication and metrological aspects of the FBG array is provided in the previous works of the group [29], [46].

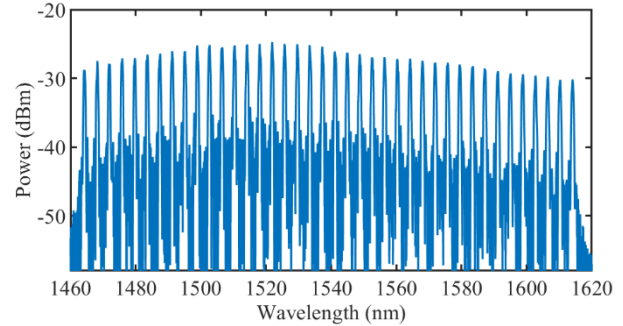


Fig. 2. Custom-made FBG array reflection spectrum: 40 FBG peaks at the range of 1460-1620 nm.

D. RI calibration of TFBG sensor

In order to analyze the effect of different RI on TFBG spectra, calibration of TFBG in different sucrose concentrations was performed. The sucrose solutions were used with a concentration range from 0 % to 60 % with a step of 6 % and corresponding to the RI range from 1.333 RIU to 1.4419 RIU (refractive index units), which is the typical range of RI for biological tissues [47], [48]. The different solutions were injected inside the container where the TFBG was placed. After each sucrose concentration, the TFBG and the container were rinsed with distilled water. Three calibration tests were performed. Fig. 3 illustrates the schematics of the experimental setup used for RI calibration.

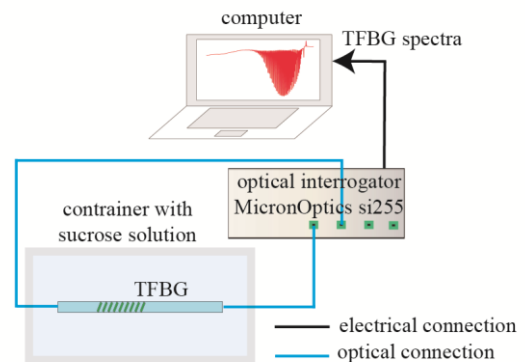


Fig. 3. Experimental setup for TFBG calibration using sucrose solutions with different concentrations in the range of 12 % - 60 % (1.333 RIU - 1.4419 RIU, referenced at 589 nm).

E. Laser ablation

Interstitial LA experiments were performed on *ex vivo* healthy porcine liver tissue, which was obtained from a local farm. The initial temperature of the liver, corresponding to $22.0 \pm 0.5 \text{ } ^\circ\text{C}$, was measured with a thermocouple before each experiment.

The developed system consists of the laser diode and the Micron Optics interrogator, both connected to a computer where a custom-made LabVIEW program was used to start

laser ablation and perform monitoring of the FBG array and TFBG spectra.

The diode laser (LuOcean Mini 4, Lumics, Berlin, Germany) working in continuous-wave mode at a 1064 nm wavelength and 2.6 W power was used for the thermal treatment. This wavelength belongs to the "therapeutic window" largely used for assuring the overall absorption of the laser light by the biological tissues, thus, entailing the temperature increase necessary for the thermal therapy [31]. Moreover, the program automatically switched off the laser after the preset time or if the temperature measured by the FBG array exceeded 300 °C. This operation is done for preserving the sensing fibers from thermal damage.

The 400 μm laser guiding fiber with the commercial diffuser (Molex, Lisle, USA) at the tip was utilized to obtain uniform tissue damage around it. The diffuser has a low OH core, a diameter of 400 μm, and a length of 10 mm. It is worth noting that the diffuser leads to a decrease of spatial thermal gradients exposed to the TFBG with respect to a standard bare fiber applicator [30]. Thus, TFBG's core mode shape changes are smaller and the possibility of the error in temperature reconstruction is minimized.

Liver tissue was cut into two halves, then the applicator and the sensors were positioned on the surface of one half (Fig. 4); after they were covered with another half in a "sandwich" approach. This approach is largely used to accurately control the relative positions of the applicator and sensors within the biological tissues [24]. The TFBG sensor and the FBG array were placed parallel to the applicator at different sides; the distance from the sensors to the applicator was 2 mm. Indeed, being the liver tissue highly homogeneous, we assumed the spatial distribution of the laser-induced temperature to be symmetric on the application plane.

F. Data analysis

Cladding mode resonances analysis

It is important to note that the standard approach of peak tracking of the cladding mode resonances is not effective for a wide range of RI [49]. Indeed, each mode is resonant and more sensitive to the specific range of RI, and its sensitivity decreases significantly for a high RI range. For a high RI range, the cladding mode resonance has to be visible for all RI values, hence positioned at low-order modes, at a higher wavelength (at about 1535 nm in Fig. 5), so such mode resonance is positioned far from the cut-off point and the overall RI sensitivity is low.

Therefore, the envelope method, firstly proposed in [50], was utilized for the RI measurements. This method is based on the determination of the lower and upper envelope curves of the TFBG cladding mode resonances comb, and then evaluation of the normalized area A between the envelopes. As RI increases, more modes become lossy leading to cladding mode resonances decreasing and bringing together the lower and the upper envelopes. Thus, the normalized area decreases too. As a result, the normalized area evolution can be correlated to the RI changes [50]. Fig. 5 illustrates the main principle of this correlation: the cladding modes and the normalized area A are changed for RI increase from 1.3330 to 1.4416 RIU.

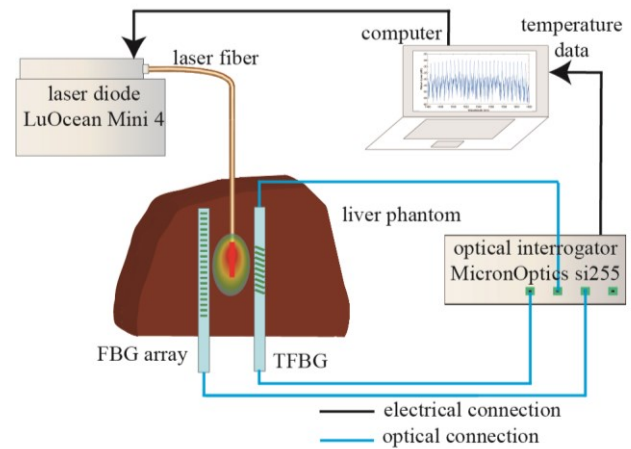


Fig. 4. Experimental setup for LA ablation: TFBG sensor and FBG array were placed at a 2 mm distance from the applicator on one half of *ex vivo* porcine liver. After, the second half of liver covers sensors and applicator in a "sandwich" approach.

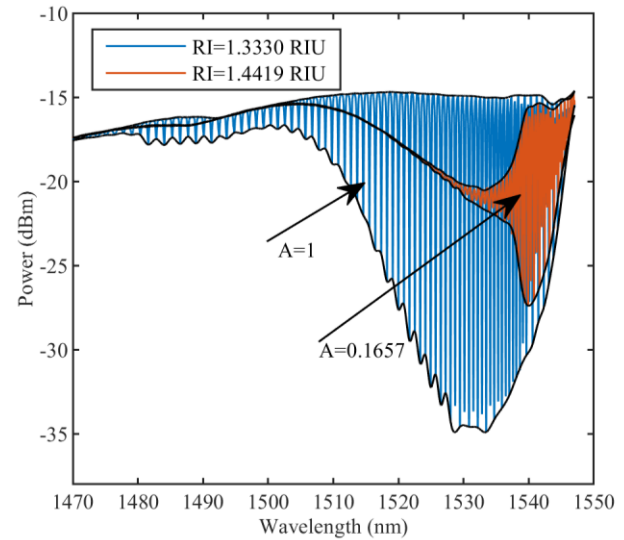


Fig. 5. The cladding mode resonances comb of TFBG positioned in water (blue line, RI = 1.333 RIU) and in a 60 % sucrose solution (red line, RI = 1.4419 RIU); related normalized area A decreases from 1.00 (reference value, RI = 1.333 RIU) to 0.1657 (RI=1.4419 RIU).

Core mode: conventional peak tracking

In our work, initially, the peak of the core mode is tracked with three conventional direct methods: maximum tracking, X-dB Bandwidth, and centroid [51].

For maximum tracking, the wavelength that corresponds to the maximum amplitude is detected as the core mode Bragg wavelength.

For X-dB Bandwidth, the inner bandwidth is defined as X dB below the maximum value; then, the center of the inner bandwidth is measured as the Bragg wavelength.

For the centroid method, the Bragg wavelength is estimated as the center of the mass of the FBG reflection spectrum according to the (1):

$$\lambda_{B,e} = \frac{\sum_n \lambda_n \times R(\lambda_n)}{\sum_n R(\lambda_n)} \quad (1)$$

where index n sweeps the main portion of the core mode spectrum.

Core mode: reconstruction algorithm

The algorithm used for TFBG temperature profile reconstruction is based on the CFBG reconstruction algorithm devised in our previous works [43], [52]. The main idea remains the same: the spectrum (of the TFBG, for this work) is modeled as a chain of FBGs using coupled mode theory [23], then the iterative approach is utilized to minimize the mismatch between the real measured TFBG spectrum and the TFBG model perturbed by Gaussian-shaped temperature profiles. Afterward, the temperature profile, which corresponds to the smallest mismatch, is defined as temperature along the TFBG.

However, it is important to notice that the CFBG spectra described in [43], [52] have higher amplitude and bandwidth than TFBG. Indeed, Fig.1 zoom-in reports that the measured core mode of TFBG (yellow line) has approximately 1 nm bandwidth and several dBm from the peak to the base. As a result, temperature reconstruction for TFBG is more challenging than for CFBG.

In this regard, we propose to optimize the method reported in [43] by iterative optimization of the bandwidth of the core mode for spectrum modeling. In other words, the edges of the modeled spectrum are not defined manually according to the measured spectrum but automatically adjusted, to minimize the difference between the measured spectrum and the modeled one. Fig. 6 illustrates the obtained results for spectrum modeling and related measured spectrum. After this bandwidth optimization, the remaining steps follow the same approach as in the CFBG reconstruction algorithm discussed in detail in [43]. The results of TFBG profile reconstruction were compared with FBG array data and TFBG core mode tracking using root-mean-square error (RMSE).

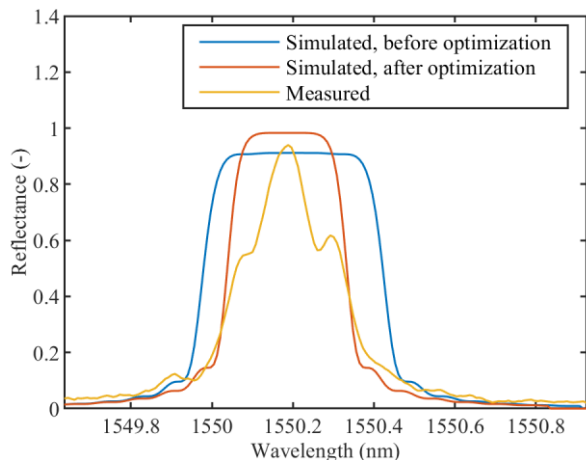


Fig. 6. TFBG core mode spectra: modeled before optimization (blue line), after optimization (red line), and normalized TFBG core mode measured with MicronOptics si255 (yellow line).

III. RESULTS

A. Calibration of TFBG sensor for different RI

The TFBG spectra for different sucrose concentrations from 0% to 60% (1.333 RIU to 1.4419 RIU) are reported in Fig. 7. As it can be clearly seen, the shape of the spectrum is significantly changed: the cut-off region starts approximately at 1530 nm for 60% sucrose concentration and the high-order modes become lossy. The obtained RI calibration results using

the envelope method (the normalized area was measured in the spectral region between 1470 nm and 1547 nm) are in accordance with the results in [50] (Fig. 8), in which TFBGs with different tilt angles were calibrated for surrounding RI sensing.

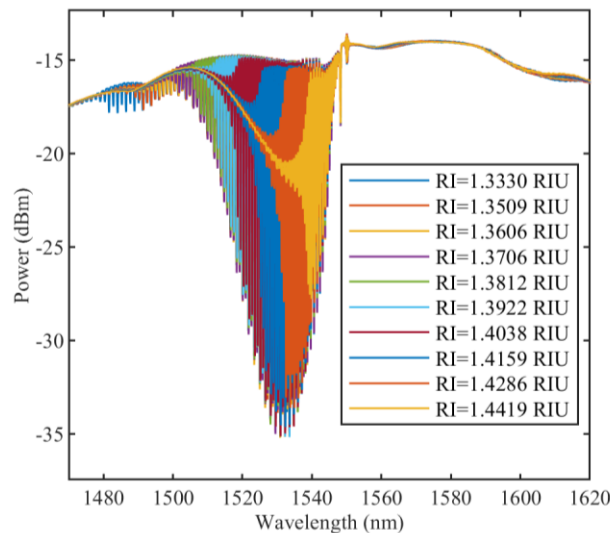


Fig. 7. TFBG spectra for different sucrose concentrations and related RI values (measured at room temperature).

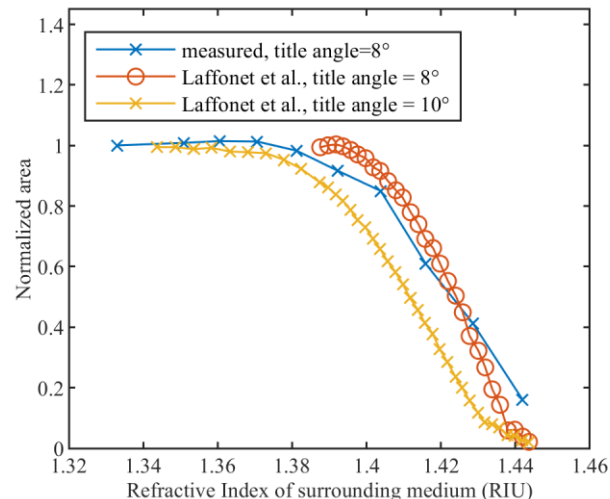


Fig. 8. Calibration of RI sensing with envelope method: average results of three calibration experiments (blue line with X marker). The obtained data is in accordance with Laffonet *et al.* [50], in which RI calibration of different TFBGs was performed.

B. Analysis of the cladding mode resonances during LA

Fig. 9 top illustrates TFBG spectra changes during LA of *ex vivo* liver at different time instants: before the start of ablation ($t=0$ s), after 90 s, and at the moment when the laser was switched off ($t=180$ s). Both the amplitude of the cladding mode resonances and the upper and lower envelopes of the spectra change during LA. The normalized area between two envelopes (left y-axis) and related temperature changes measured by the FBG array (right y-axis) are presented in Fig. 9 bottom. As can be seen, the trend of temperature evolution can be approximately correlated with the changes in the normalized area (Fig. 9 bottom). Thus, ideally, we expect to obtain information about the maximum temperature from the minimum value of the normalized area. Moreover, after

complete cooling, the normalized area is expected to be correlated with the RI change of the ablated tissue.

However, the results show that the repeatability of the experimental trials is low. As a result, it is very challenging to obtain useful information about temperature and RI changes from the cladding comb analysis. For instance, Fig. 10 reports the relation between maximum temperature measured by TFBG (using maximum peak tracking) and the related minimum value of the normalized area for each of 25 experimental trials. As expected, higher temperature leads to a smaller area between envelopes. Indeed, Fig. 10 shows that for the experiments with low maximum temperatures ($\sim 26^\circ\text{C}$) the related normalized area is very close to 1 because there is no significant shift and amplitudes decrease of the cladding mode resonances. However, due to the high value of RMSE between the fitting and the measured data (RMSE = 0.148), the temperature cannot be accurately correlated with the normalized area (Fig. 10).

Moreover, due to the high effect of temperature on the cladding comb, RI changes of the tissues after LA are challenging to measure too. The possible reasons for the low efficacy of cladding comb analysis during LA are provided in the discussion section.

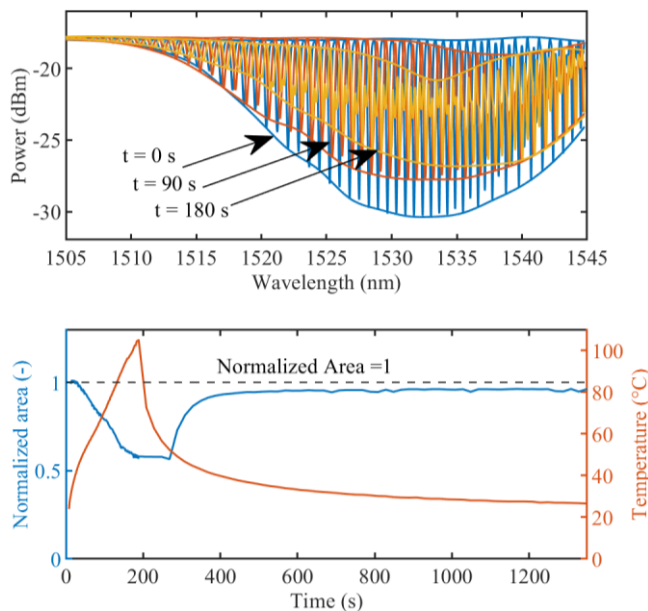


Fig. 9. (top) TFBG spectra measured during LA of *ex vivo* porcine liver at different time instances: before the laser ablation at $t=0\text{ s}$ (blue color); at $t = 90\text{ s}$ (red color), and when laser was switched off $t=180\text{ s}$. Amplitude changes of spectra, and related shape changes, can be seen. (bottom) Normalized area evolution (left y-axis) and temperature change measured by FBG array (right y-axis) during LA experiment.

C. Analysis of the core mode during LA

Fig. 11 top reports temperature evolution measured by the FBG array during one experiment. The maximum temperature reached after 180 s of ablation is 105.2°C . At the same moment, the TFBG core mode shows 80.9°C measured by maximum peak tracking, 69.5°C by X-dB Bandwidth, and 64.3°C by the centroid method. The RMSE between maximum temperatures measured by FBG array and TFBG (maximum peak tracking) is 18.31°C .

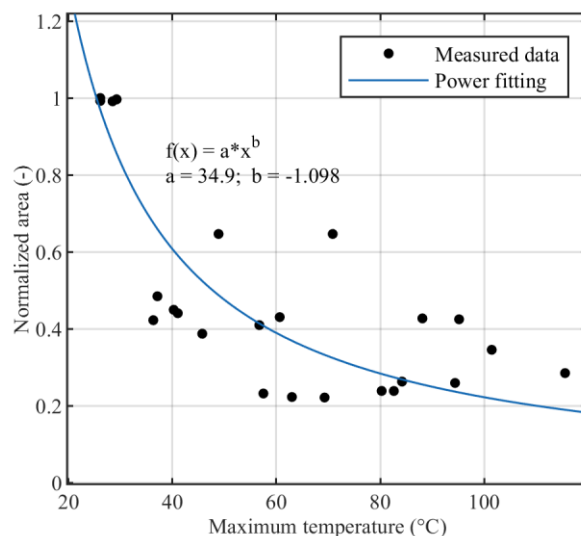


Fig. 10. Relation between maximum temperature measured by TFBG (using maximum peak tracking) and related minimum value of normalized area for each of 25 experimental trials. RMSE between data and fitting is 0.148.

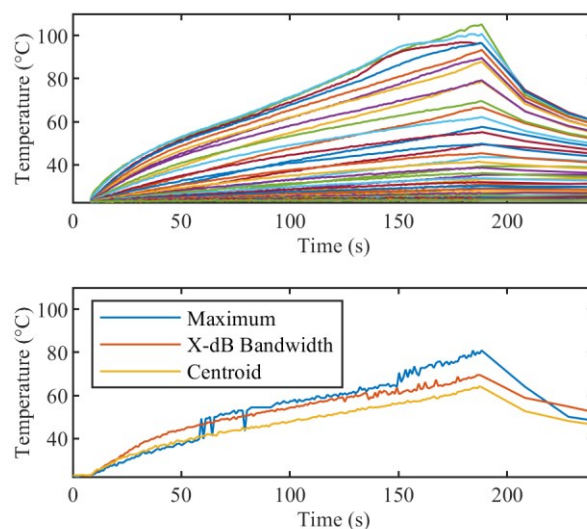


Fig. 11. (top) FBG array temperature for 40 gratings during laser ablation; (bottom) temperature reconstructed using analysis of core mode with direct peak-tracking techniques: maximum, X-dB Bandwidth (where X is -5 dB), centroid.

Fig. 12 and 13 report the results of the temperature profile along the TFBG using the proposed algorithm. Fig.12 shows the temperature measured by the FBG array (dashed line) and temperature reconstructed along the TFBG (solid line) at different time moments. For this figure, to clearly illustrate the algorithm's ability to reconstruct profile trends, TFBG temperature was normalized to the maximum temperature measured by the FBG array. Fig. 13 reports temperature evolution for both sensors during laser ablation of the tissue. The RMSE between the FBG array and TFBG measurements for three experiments is $7.8 \pm 1.7^\circ\text{C}$.

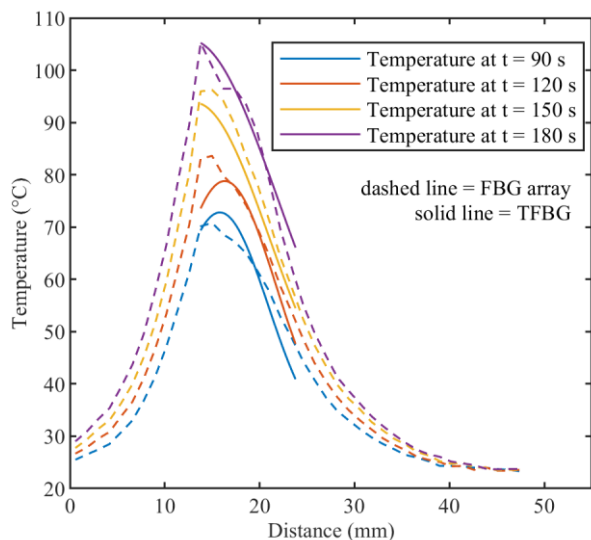


Fig. 12. Measurements during LA experiment at different time instants: dashed lines – FBG array temperature measurements, solid lines – reconstructed TFBG temperature profiles (normalized).

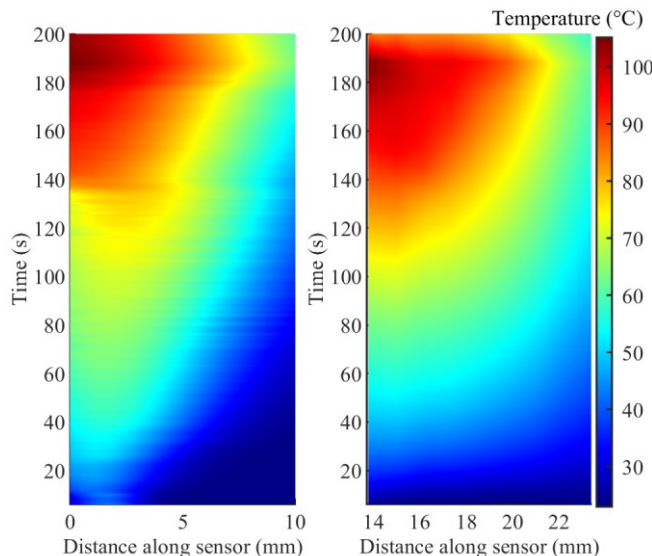


Fig. 13. Measurements during LA experiments: (a) FBG array; (b) TFBG temperature obtained by the proposed algorithm. The RMSE between FBG array and TFBG profile measurements for three experiments is 7.8 ± 1.7 °C.

IV. DISCUSSION

In general, the initial hypothesis was to obtain information about the RI of the ablated tissue using the cladding mode resonance tracking, while the temperature effect on the cladding mode resonances is compensated by temperature measured by the core mode tracking. However, the experiments showed that the cladding comb changed significantly during LA (high wavelength shift and appearance of leaky modes). Thus, the cladding resonances tracking was not possible. Indeed, it is in agreement with [50]: distinct temperature sensitivity of cladding modes leads not only to the shift of the cladding mode resonances, but to the change of the shape of the TFBG spectrum under temperature elevation. Thus, the envelope method was utilized to measure the area between upper and

lower envelopes of the TFBG cladding resonances comb during LA.

However, the results show that temperature and RI information is not possible to accurately measure by the cladding comb analysis. The possible reasons can be inhomogeneity and structure of the tissue that does not allow ideal contact between the sensor surface and the tissue, the change of the TFBG surface after each experiment (even considering that TFBG was cleaned after each trial). Moreover, bending, strain, and humidity also have a cross-sensitivity effect on the shape of the TFBG spectrum [32], which makes RI measurements using the envelope method even more challenging.

As a result, we conclude that the main sensing modality of TFBG is temperature measurements based on the core mode analysis. The resulted RMSE of 7.8 ± 1.7 °C between TFBG profile reconstruction and FBG reference measurements can be mostly explained by the positioning of the sensors on the opposite sides of the diffuser and the high thermal gradients associated with LA. For future characterization of TFBG temperature measurements, the reference sensor and FBG should have the same exact placing, preferably in capillary or tubing to eliminate cross-sensitivity effects from other intra-tissue parameters.

The TFBG temperature sensor analyzed by conventional methods has several disadvantages over Rayleigh-based distributed sensing and FBG measurements: one-point measurement, averaging over the TFBG length (~ 1 cm), fragility (TFBG usually does not have a coating to allow coupling with leaky modes). However, a TFBG can be used as a sensor and a heat source, as proposed in a recent study [4]. In this regard, sensing modalities and capabilities of TFBG during LA need to be analyzed in detail, and this work can be considered a step toward such analysis.

V. CONCLUSION

In this work, we have implemented a temperature profile reconstruction algorithm for TFBG and validated it during LA in *ex vivo* liver. The algorithm is based on modeling the TFBG core mode as a chain of FBGs, each sensitive to a local temperature shift. Afterward, the iterative optimization method is used to define the temperature profile along the TFBG. The obtained results were compared with direct peak-tracking techniques (maximum tracking, X-dB Bandwidth, centroid methods) used to measure the core mode shift of TFBG, and with FBG array measurements. In addition, the cladding mode resonances behavior for different sucrose concentrations, and then during LA was investigated. In general, the proposed reconstruction algorithm provides 7.8 ± 1.7 °C RMS error with respect to the FBG array temperature measurements and can be effective for real-time TFBG temperature profile measurements during LA ablation.

ACKNOWLEDGMENT

The authors would like to thank Annalisa Orrico, Giulia Saudelli and Leonardo Pascucci for the help provided during the experiments.

REFERENCES

[1] C. J. Diederich, "Thermal ablation and high-temperature thermal therapy: overview of technology and clinical implementation," *Int. J. Hyperth.*, vol. 21, no. 8, pp. 745–753, 2005.

[2] S. Sartori, F. Di Vece, F. Ermili, and P. Tombesi, "Laser ablation of liver tumors: An ancillary technique, or an alternative to radiofrequency and microwave?," *World J. Radiol.*, vol. 9, no. 3, p. 91, 2017, doi: 10.4329/wjr.v9.i3.91.

[3] D. Kalamida, I. V. Karagounis, A. Mitrakas, S. Kalamida, A. Giatromanolaki, and M. I. Koukourakis, "Fever-range hyperthermia vs. hypothermia effect on cancer cell viability, proliferation and HSP90 expression," *PLoS One*, vol. 10, no. 1, p. e0116021, 2015.

[4] S. A. Alqarni, W. G. Willmore, J. Albert, and C. W. Smelser, "Self-monitored and optically powered fiber-optic device for localized hyperthermia and controlled cell death in vitro," *Appl. Opt.*, vol. 60, no. 8, pp. 2400–2411, 2021.

[5] M. G. Lubner, C. L. Brace, J. L. Hinshaw, and F. T. Lee, "Microwave tumor ablation: Mechanism of action, clinical results, and devices," *J. Vasc. Interv. Radiol.*, vol. 21, no. SUPPL. 8, pp. S192–S203, 2010, doi: 10.1016/j.jvir.2010.04.007.

[6] S. N. Goldberg, "Radiofrequency Tumor Ablation: Principles and Techniques," in *Multi-Treatment Modalities of Liver Tumours*, Boston, MA: Springer US, 2002, pp. 87–118.

[7] Y.-F. Zhou, "High intensity focused ultrasound in clinical tumor ablation," *World J. Clin. Oncol.*, vol. 2, no. 1, p. 8, 2011, doi: 10.5306/wjco.v2.i1.8.

[8] R. J. Stafford, D. Fuentes, A. A. Elliott, J. S. Weinberg, and K. Ahrar, "Laser-Induced Thermal Therapy for Tumor Ablation," *Crit. Rev. Biomed. Eng.*, vol. 38, no. 1, pp. 79–100, 2010, doi: 10.1615/CritRevBiomedEng.v38.i1.70.

[9] F. Manns, P. J. Milne, X. Gonzalez-Cirre, D. B. Denham, J. M. Parel, and D. S. Robinson, "In situ temperature measurements with thermocouple probes during laser interstitial thermotherapy (LITT): Quantification and correction of a measurement artifact," *Lasers Surg. Med.*, vol. 23, no. 2, pp. 94–103, 1998, doi: 10.1002/(SICI)1096-9101(1998)23:2<94::AID-LSM7>3.0.CO;2-Q.

[10] C. M. Paccella *et al.*, "Thyroid tissue: US-guided percutaneous interstitial laser ablation - A feasibility study," *Radiology*, vol. 217, no. 3, pp. 673–677, 2000, doi: 10.1148/radiology.217.3.r00dc09673.

[11] H. J. Schwarzaier *et al.*, "MR-guided laser-induced interstitial thermotherapy of recurrent glioblastoma multiforme: Preliminary results in 16 patients," *Eur. J. Radiol.*, vol. 59, no. 2, pp. 208–215, 2006, doi: 10.1016/j.ejrad.2006.05.010.

[12] F. M. Di Matteo *et al.*, "Feasibility of EUS-guided Nd:YAG laser ablation of unresectable pancreatic adenocarcinoma," *Gastrointest. Endosc.*, vol. 88, no. 1, pp. 168-174.e1, Jul. 2018, doi: 10.1016/j.gie.2018.02.007.

[13] A. Gangi, H. Alizadeh, L. Wong, X. Buy, J. L. Dietemann, and C. Roy, "Osteoid osteoma: Percutaneous laser ablation and follow-up in 114 patients," *Radiology*, vol. 242, no. 1, pp. 293–301, 2007, doi: 10.1148/radiol.2421041404.

[14] T. J. Vogl, R. Straub, K. Eichler, O. Söllner, and M. G. Mack, "Colorectal Carcinoma Metastases in Liver: Laser-induced Interstitial Thermotherapy - Local Tumor Control Rate and Survival Data," *Radiology*, vol. 230, no. 2, pp. 450–458, Feb. 2004, doi: 10.1148/radiol.2302020646.

[15] K. F. Chu and D. E. Dupuy, "Thermal ablation of tumours: Biological mechanisms and advances in therapy," *Nat. Rev. Cancer*, vol. 14, no. 3, pp. 199–208, 2014, doi: 10.1038/nrc3672.

[16] J. T. Lin, Y. S. Chiang, G. H. Lin, H. Lee, and H. W. Liu, "In vitro photothermal destruction of cancer cells using gold nanorods and pulsed-train near-infrared laser," *J. Nanomater.*, vol. 2012, 2012, doi: 10.1155/2012/861385.

[17] K. Ivarsson, J. Olsrud, C. Sturesson, P. H. Möller, B. R. Persson, and K. G. Tranberg, "Feedback interstitial diode laser (805 nm) thermotherapy system: Ex vivo evaluation and mathematical modeling with one and four-fibers," *Lasers Surg. Med.*, vol. 22, no. 2, pp. 86–96, 1998, doi: 10.1002/(SICI)1096-9101(1998)22:2<86::AID-LSM4>3.0.CO;2-S.

[18] A. J. Welch and M. J. C. C. Van Gemert, *Optical-Thermal Response of Laser-Irradiated Tissue*, vol. 2. Dordrecht: Springer Netherlands, 2011.

[19] P. Saccomandi, E. Schena, and S. Silvestri, "Techniques for temperature monitoring during laser-induced thermotherapy: An overview," *Int. J. Hyperth.*, vol. 29, no. 7, pp. 609–619, Nov. 2013, doi: 10.3109/02656736.2013.832411.

[20] F. Morra *et al.*, "Spatially resolved thermometry during laser ablation in tissues: Distributed and quasi-distributed fiber optic-based sensing," *Opt. Fiber Technol.*, vol. 58, p. 102295, Sep. 2020, doi: 10.1016/j.yofte.2020.102295.

[21] E. G. Macchi *et al.*, "Optical fiber sensors-based temperature distribution measurement in ex vivo radiofrequency ablation with submillimeter resolution," *J. Biomed. Opt.*, vol. 19, no. 11, p. 117004, Nov. 2014, doi: 10.1117/1.jbo.19.11.117004.

[22] Z. Ashikbayeva *et al.*, "Distributed 2D temperature sensing during nanoparticles assisted laser ablation by means of high-scattering fiber sensors," *Sci. Rep.*, vol. 10, no. 1, p. 12593, Dec. 2020, doi: 10.1038/s41598-020-69384-2.

[23] T. Erdogan, "Fiber grating spectra," *J. Light. Technol.*, vol. 15, no. 8, pp. 1277–1294, 1997, doi: 10.1109/50.618322.

[24] R. Gassino, Y. Liu, M. Konstantaki, A. Vallan, S. Pissadakis, and G. Perrone, "A fiber optic probe for tumor laser ablation with integrated temperature measurement capability," *J. Light. Technol.*, vol. 35, no. 16, pp. 3447–3454, Aug. 2016, doi: 10.1109/JLT.2016.2618618.

[25] L. Bianchi *et al.*, "Fiber Bragg Grating Sensors-Based Thermometry of Gold Nanorod-Enhanced Photothermal Therapy in Tumor Model," *IEEE Sens. J.*, vol. 22, no. 12, pp. 11297–11306, Jun. 2022, doi: 10.1109/JSEN.2021.3082042.

[26] N. D. Schulmann, M. Soltani-Sarvestani, M. De Landro, S. Korganbayev, S. Cotin, and P. Saccomandi, "Model-Based Thermometry for Laser Ablation Procedure Using Kalman Filters and Sparse Temperature Measurements," *IEEE Trans. Biomed. Eng.*, pp. 1–1, 2022, doi: 10.1109/TBME.2022.3155574.

[27] Y. Liu, R. Gassino, A. Braglia, A. Vallan, and G. Perrone, "Fibre probe for tumour laser thermotherapy with integrated temperature measuring capabilities," *Electron. Lett.*, vol. 52, no. 10, pp. 798–800, 2016.

[28] S. Korganbayev, R. Pini, A. Orrico, A. Wolf, A. Dostovalov, and P. Saccomandi, "Towards temperature-controlled laser ablation based on fiber Bragg grating array temperature measurements," in *2020 IEEE International Workshop on Metrology for Industry 4.0 and IoT, MetroInd 4.0 and IoT 2020 - Proceedings*, Jun. 2020, pp. 268–272, doi: 10.1109/MetroInd4.0IoT48571.2020.9138171.

[29] S. Korganbayev *et al.*, "Closed-loop temperature control based on fiber bragg grating sensors for laser ablation of hepatic tissue," *Sensors (Switzerland)*, vol. 20, no. 22, pp. 1–16, Nov. 2020, doi: 10.3390/s20226496.

[30] L. Bianchi, S. Korganbayev, A. Orrico, M. De Landro, and P. Saccomandi, "Quasi-distributed fiber optic sensor-based control system for interstitial laser ablation of tissue: theoretical and experimental investigations," *Biomed. Opt. Express*, vol. 12, no. 5, p. 2841, May 2021, doi: 10.1364/BOE.419541.

[31] S. Korganbayev *et al.*, "PID Controlling Approach Based on FBG Array Measurements for Laser Ablation of Pancreatic Tissues," *IEEE Trans. Instrum. Meas.*, vol. 70, pp. 1–9, 2021, doi: 10.1109/TIM.2021.3112790.

[32] J. Albert, L. Shao, and C. Caucheteur, "Tilted fiber Bragg grating sensors," *Laser Photon. Rev.*, vol. 7, no. 1, pp. 83–108, 2013.

[33] T. Guo, F. Liu, B. O. Guan, and J. Albert, "Tilted fiber grating mechanical and biochemical sensors," *Opt. Laser Technol.*, vol. 78, pp. 19–33, 2016, doi: 10.1016/j.optlastec.2015.10.007.

[34] C. Leita *et al.*, "Cortisol in-fiber ultrasensitive plasmonic immunosensing," *IEEE Sens. J.*, vol. 21, no. 3, pp. 1–1, 2020, doi: 10.1109/JSEN.2020.3025456.

[35] T. Zhu, M. Loyez, K. Chah, and C. Caucheteur, "Partially gold-coated tilted FBGs for enhanced surface biosensing," *Opt. Express*, vol. 30, no. 10, p. 16518, May 2022, doi: 10.1364/OE.458548.

[36] T. Osuch, T. Jurek, K. Markowski, and K. Jedrzejewski, "Simultaneous measurement of liquid level and temperature using tilted fiber Bragg grating," *IEEE Sens. J.*, vol. 16, no. 5, pp. 1205–1209, 2015.

[37] R. Agah, A. H. Gandjbakhche, M. Motamedi, R. Nossal, and R. F. Bonner, "Dynamics of temperature dependent optical properties of tissue: dependence on thermally induced alteration," *IEEE Trans. Biomed. Eng.*, vol. 43, no. 8, pp. 839–846, 1996.

[38] M. De Landro *et al.*, "Prediction of In Vivo Laser-Induced Thermal Damage with Hyperspectral Imaging Using Deep Learning," *Sensors*, vol. 21, no. 20, p. 6934, 2021.

[39] M. E. Shvachkina, D. D. Yakovlev, A. B. Pravdin, and D. A.

- [40] Yakovlev, "Average refractive index of tendon as a function of water content," *J. Biomed. Photonics Eng.*, vol. 4, no. 1, pp. 13–21, 2018.
- [41] S. Korganbayev *et al.*, "Linearly chirped fiber-optic Bragg gratings as distributed temperature sensor for laser ablation," in *Proceedings of IEEE Sensors*, Oct. 2017, pp. 1–3, doi: 10.1109/ICSENS.2016.7808610.
- [42] P. Saccomandi *et al.*, "Linearly chirped fiber Bragg grating response to thermal gradient: from bench tests to the real-time assessment during in vivo laser ablations of biological tissue," *J. Biomed. Opt.*, vol. 22, no. 09, p. 1, Sep. 2017, doi: 10.1117/1.jbo.22.9.097002.
- [43] S. Korganbayev *et al.*, "Thermal Profile Detection Through High-Sensitivity Fiber Optic Chirped Bragg Grating on Microstructured PMMA Fiber," *J. Light. Technol.*, vol. 36, no. 20, pp. 4723–4729, Oct. 2018, doi: 10.1109/JLT.2018.2864113.
- [44] S. Korganbayev *et al.*, "Detection of thermal gradients through fiber-optic Chirped Fiber Bragg Grating (CFBG): Medical thermal ablation scenario," *Opt. Fiber Technol.*, vol. 41, no. December 2017, pp. 48–55, Mar. 2018, doi: 10.1016/j.yofte.2017.12.017.
- [45] T. G. Giallorenzi and A. Dandridge, *Optical Fiber Sensor Technology*, vol. 3. Boston, MA: Springer US, 1987.
- [46] L. Huang, R. S. Dyer, R. J. Lago, A. A. Stolov, and J. Li, "Mechanical properties of polyimide coated optical fibers at elevated temperatures," in *Optical Fibers and Sensors for Medical Diagnostics and Treatment Applications XVI*, Mar. 2016, vol. 9702, p. 97020Y, doi: 10.1117/12.2210957.
- [47] A. V. Dostovalov, A. A. Wolf, A. V. Parygin, V. E. Zyubin, and S. A. Babin, "Femtosecond point-by-point inscription of Bragg gratings by drawing a coated fiber through ferrule," *Opt. Express*, vol. 24, no. 15, p. 16232, 2016, doi: 10.1364/oe.24.016232.
- [48] R. Khan, B. Gul, S. Khan, H. Nisar, and I. Ahmad, "Refractive index of biological tissues: Review, measurement techniques, and applications," *Photodiagnosis Photodyn. Ther.*, vol. 33, p. 102192, 2021.
- [49] "Refractometer." <http://www.refractometer.pl/refraction-datasheet-sucrose>.
- [50] S. Korganbayev *et al.*, "Optimization of Cladding Diameter for Refractive Index Sensing in Tilted Fiber Bragg Gratings," *Sensors*, vol. 22, no. 6, p. 2259, Mar. 2022, doi: 10.3390/s22062259.
- [51] G. Laffon and P. Ferdinand, "Tilted short-period fibre-Bragg-grating-induced coupling to cladding modes for accurate refractometry," *Meas. Sci. Technol.*, vol. 12, no. 7, pp. 765–770, 2001, doi: 10.1088/0957-0233/12/7/302.
- [52] D. Tosi, "Review and analysis of peak tracking techniques for fiber Bragg grating sensors," *Sensors*, vol. 17, no. 10, p. 2368, 2017.
- [53] R. Min *et al.*, "Largely tunable dispersion chirped polymer FBG," *Opt. Lett.*, vol. 43, no. 20, p. 5106, Oct. 2018, doi: 10.1364/OL.43.005106.



Sanzhar Korganbayev (Member, IEEE) received the B.S. and M.S. degrees in electrical and electronics engineering from Nazarbayev University, Nur-Sultan, Kazakhstan, in 2016 and 2018, respectively. He is currently pursuing a Ph.D. degree with the Department of Mechanical Engineering, Politecnico di Milano. He is currently involved in the "LASER OPTIMAL" Project (European Research Council Grant GA 759159) for the development of software for real-time temperature

monitoring and intraoperative adjustment of the laser ablation settings during tumor treatment. His research interests include fiber optic sensors and their applications for thermal and mechanical measurements.



Martina De Landro is a PhD Student in Mechanical Engineering. She has received her MS degree in Biomedical Engineering from Università Campus Bio-Medico di Roma. She performed MS thesis at the IHU of Strasbourg, where she investigated the use of fiber optic sensors for catheters tracking. Her work focuses on the investigation of sensors and innovative images-based techniques for the monitoring of thermal outcome in tissues undergoing laser ablation.



Alexey Wolf received MSc degree in Physics from Novosibirsk State University (NSU) and PhD degree in Optics from the Institute of Automation and Electrometry of the SB RAS (IAE SB RAS) in 2013 and 2020, respectively. He currently works as a researcher in the Laboratory of Nonlinear Waveguide Systems at NSU and the Laboratory of Fiber Optics at IAE SB RAS, where he develops new types of fiber lasers and sensors based on specialty optical fibers. His scientific interests include femtosecond laser micromachining, fiber Bragg gratings, and new optical materials.



Daniele Tosi is an Associate Professor of Electrical and Computer Engineering at Nazarbayev University, and Head of Biosensors and Bioinstruments Laboratory at National Laboratory Astana. He is an Associate Editor of the IEEE Sensors Journal and the recipient of the IEEE Sensors Council Early Career Technical Award in 2018. He holds BSc (2004) and MSc (2006) in Telecommunication Engineering, and PhD (2010) in Electrical and Computer Engineering from Politecnico di



Torino. His research interests include optical fiber sensors, biomedical sensors, distributed sensing, and biosensors.

Paola Saccomandi (M 2011) received her PhD in Biomedical Engineering from Università Campus Bio-Medico di Roma in 2014. From 2016 to 2018 she was postdoctoral researcher at the IHU - Institute of Image-Guided Surgery of Strasbourg. Since 2018 she is Associate Professor at the Department of Mechanical Engineering of Politecnico di Milano. She is the Principal Investigator of the European Research Council grant "LASER OPTIMAL"- GA 759159. The main research interests of Prof. Saccomandi and her team include fiber optic sensors, biomedical imaging, and the development of light-based approaches for hyperthermal tumor treatment and monitoring.